

NUMERICAL INVESTIGATION OF WIND LOAD CHARACTERISTICS  
AROUND AN ISOLATED TALL BUILDING

A THESIS SUBMITTED TO  
THE GRADUATE SCHOOL OF NATURAL AND APPLIED SCIENCES  
OF  
MIDDLE EAST TECHNICAL UNIVERSITY

BY

GÖKALP DOĞUKAN DEMİRBAŞ

IN PARTIAL FULFILLMENT OF THE REQUIREMENTS  
FOR  
THE DEGREE OF MASTER OF SCIENCE  
IN  
CIVIL ENGINEERING

FEBRUARY 2021



Approval of the thesis:

**NUMERICAL INVESTIGATION OF WIND LOAD CHARACTERISTICS  
AROUND AN ISOLATED TALL BUILDING**

submitted by **GÖKALP DOĞUKAN DEMİRBAŞ** in partial fulfillment of the requirements for the degree of **Master of Science in Civil Engineering, Middle East Technical University** by,

Prof. Dr. Halil Kalıpçılar  
Dean, Graduate School of **Natural and Applied Sciences**

\_\_\_\_\_

Prof. Dr. Ahmet Türer  
Head of the Department, **Civil Engineering**

\_\_\_\_\_

Prof. Dr. Mete Köken  
Supervisor, **Civil Engineering, METU**

\_\_\_\_\_

Prof. Dr. Özgür Kurç  
Co-Supervisor, **Civil Engineering, METU**

\_\_\_\_\_

**Examining Committee Members:**

Prof. Dr. İsmail Aydın  
Civil Engineering, METU

\_\_\_\_\_

Prof. Dr. Mete Köken  
Civil Engineering, METU

\_\_\_\_\_

Assoc. Prof. Dr. Elif Oğuz  
Civil Engineering, METU

\_\_\_\_\_

Assoc. Prof. Dr. Nilay Sezer Uzol  
Aerospace Engineering, METU

\_\_\_\_\_

Assoc. Prof. Dr. Müsteyde Baduna Koçyiğit  
Civil Engineering, Gazi University

\_\_\_\_\_

Date: 10.02.2021

**I hereby declare that all information in this document has been obtained and presented in accordance with academic rules and ethical conduct. I also declare that, as required by these rules and conduct, I have fully cited and referenced all material and results that are not original to this work.**

Name, Last name : Gökalp Doğukan Demirbaş

Signature :

## ABSTRACT

### NUMERICAL INVESTIGATION OF WIND LOAD CHARACTERISTICS AROUND AN ISOLATED TALL BUILDING

Demirbař, Gökalp Dođukan  
Master of Science, Civil Engineering  
Supervisor: Prof. Dr. Mete Köken  
Co-Supervisor: Prof. Dr. Özgür Kurç

February 2021, 189 pages

As a common practice, wind loads on tall buildings are calculated using empirical formulas with several assumptions described within Turkish Standards: TS498 and TS EN 1991-1-4. Since these standards are mainly based on past site experiences and wind tunnel tests, these formulas become invalid with distinctive designs and the increase in the building height. With the development of computer technology, computational fluid dynamics (CFD) tools have become common in calculating wind loads on tall buildings. Within this study's scope, wind-induced effects on an isolated 182.88 m x 45.72 m x 30.48 m tall building were investigated by utilizing Spalart-Allmaras based Detached eddy simulation (S-A DES) under inhomogeneous and anisotropic turbulent flow (i.e., strong winds) within the neutral atmospheric boundary layer. To generate inflow boundary conditions, a synthetic inflow turbulence generation technique called "Consistent Discrete Random Flow Generation" was used. An excellent agreement in mean pressure coefficients with wind tunnel data was obtained on the building's windward and crosswind surfaces. Similar but slightly underestimated mean pressure coefficients were obtained on the leeward surface. Furthermore, wind flow characteristics such as horseshoe vortex formation and recirculation zone around the building were investigated in detail.

Keywords: CFD, S-A DES, Atmospheric Boundary Layer, Synthetic Inflow Turbulence Generation, Wind Flow Characteristics Around Tall Building

## ÖZ

### TEKİL BİNA ETRAFINDAKİ RÜZGAR YÜKÜ KARAKTERİSTİKLERİNİN SAYISAL YÖNLEMLERLE İNCELENMESİ

Demirbaş, Gökalp Doğukan  
Yüksek Lisans, İnşaat Mühendisliği  
Tez Yöneticisi: Prof. Dr. Mete Köken  
Ortak Tez Yöneticisi: Prof. Dr. Özgür Kurç

Şubat 2021, 189 sayfa

Genel olarak, yüksek binalara etkiyen rüzgar yükleri, Türkiye’de TS498 ve TS EN 1991-1-4 standartlarınca önerilen birtakım varsayımlar altında ampirik formüller kullanılarak hesaplanmaktadır. Bu standartların genellikle geçmiş saha deneyimlerine ve rüzgar tüneli testlerine dayanmasından dolayı bu formüller farklı tasarımlar ve binalarının yüksekliklerindeki artış ile birlikte yetersiz kalmaktadır. Bilgisayar teknolojisinin gelişmesiyle, yüksek binalara etkiyen rüzgar yükünün hesaplanmasında hesaplamalı akışkanlar dinamiği (HAD) araçlarının kullanılması yaygınlaşmaya başlamıştır. Bu çalışma kapsamında nötr atmosferik sınır katmanında homojen olmayan anizotropik türbülanslı akım altında (güçlü rüzgarlar), izole 182,88 m x 45,72 m x 30,48 m ölçülerine sahip yüksek bir binadaki rüzgar etkileri Spalart-Allmaras tabanlı DES modeli kullanılarak incelenmiştir. Giriş sınır koşulları için sentetik türbülans tekniklerinden “Tutarlı Ayrık Rastgele Akış Üretimi” metodu kullanılmıştır. Binanın rüzgar üstü ve yan yüzeylerinde rüzgar tüneli verileri ile ortalama basınç katsayılarında mükemmel bir uyum yakalanmıştır. Binanın rüzgar altı yüzeyinde ise rüzgar tüneli verilerine benzer fakat nispeten az ortalama basınç katsayıları elde edilmiştir. Buna ek olarak, bina etrafındaki at nalı girdabı oluşumu ve sirkülasyon bölgesi gibi rüzgar akış karakteristikleri detaylı olarak incelenmiştir.

Anahtar Kelimeler: HAD, S-A DES, Atmosferik Sınır Tabakası, Sentetik Giriş Türbülansı Oluşturulması, Yüksek Bina Etrafındaki Akım Karakteristikleri

*In memory of Mustafa Burak Demirbař*

*Rest in peace, my brother.*

## ACKNOWLEDGMENTS

I would like to express my gratitude to my supervisor Prof. Dr. Mete Köken for his guidance, endless support, encouragement, and patience during the processes of my thesis. I am very thankful to him for giving me to chance to study this topic.

I am so grateful to my co-supervisor Prof. Dr. Özgür Kurç for his guidance and contributions to the study by approaching from a different perspective.

I also would like to thank the committee members of my thesis; Prof. Dr. İsmail Aydın, Assoc. Prof. Dr. Elif Oğuz, Assoc. Prof. Dr. Müsteyde Baduna Koçyiğit, and Assoc. Prof. Dr. Nilay Sezer Uzol for their time and valuable suggestions to improve the quality of the thesis.

I am also thankful to my colleagues; Serkan Gökmener (especially him), Ezgi Budak, Emre Haspolat, Abiddin Berhan Melek and Hasan Hüseyin Yıldırım for their support and valuable friendship. I am very happy to work in the same division with these people.

I would like to express my gratitude to my father Baki Demirbaş, and my brother Tolunay Demirbaş for their support and love. Special thanks to my lovely mother, Gülşah Demirbaş who always cheers me up. I am so lucky to have such a mother who always trusts me.

I would like to express my deepest gratitude to my wife Yağmur Saklı Demirbaş who is my super-secret hero, my honey badger and the meaning of my life. No matter how much I thank to her for being my side, accepting me as I am, and her support for my education in all difficulties that I have been through financially and morally, it will not be enough. Having such a wife in my life makes me very happy.

I dedicate this thesis to my brother Mustafa Burak Demirbaş who passed away untimely. I want to finish my words with his quote which has always been a source of motivation for me: "*Nerede kalmıştık?*"

## TABLE OF CONTENTS

ABSTRACT.....	v
ÖZ .....	vi
ACKNOWLEDGMENTS .....	viii
TABLE OF CONTENTS.....	ix
LIST OF TABLES .....	xiii
LIST OF FIGURES .....	xiv
LIST OF ABBREVIATIONS .....	xvii
LIST OF SYMBOLS .....	xxi
CHAPTERS	
1 INTRODUCTION .....	1
1.1 Computational Wind Engineering .....	1
1.2 Scope of the Thesis .....	4
2 THEORETICAL BACKGROUND.....	5
2.1 The Atmospheric Boundary Layer.....	5
2.1.1 Forces Behind the Wind Formation.....	5
2.1.2 Definition and Stratification of the Atmospheric Boundary Layer.....	8
2.1.3 Scales of Atmospheric Motions .....	9
2.1.4 Structure and Diurnal Cycle of the Atmospheric Boundary Layer...	10
2.1.4.1 Outer Layer .....	11
2.1.4.2 Surface Layer.....	13
2.2 Essentials and Characteristics of Turbulence in ABL Flows.....	14
2.2.1 Statistical Classification of Turbulence in ABL .....	14

2.2.2	Decomposition of Turbulent Flow Fields.....	15
2.2.2.1	Types of Averaging for Mean Components.....	16
2.2.2.2	Description of Vertical Mean Wind Speed Profiles.....	18
2.2.2.2.1	Mean Velocity Distribution with Logarithmic Law .....	18
2.2.2.2.2	Mean Velocity Distribution with Power Law .....	23
2.2.2.3	Variance, Standard Deviation, and Turbulence Intensities .....	27
2.2.2.4	Probability Density of Random Variations .....	30
2.2.2.5	Spectral Structure and Scales of Turbulent Motions.....	31
2.2.2.5.1	Spectral Regions of Energy Spectrum .....	31
2.2.2.5.2	Length, Time, and Velocity Scales of Eddies.....	32
2.2.2.5.3	Definitions of Wavenumber and Frequencies of Eddies .....	37
2.2.2.5.4	Spectral Density Functions for Turbulent Flows .....	39
2.2.2.6	Covariance, Correlation, and Coherence .....	43
3	COMPUTATIONAL MODELING AND SIMULATION.....	45
3.1	Governing Equations .....	45
3.1.1	Conservation of Mass .....	46
3.1.2	Conservation of Momentum.....	46
3.2	Techniques for Simulating Turbulent Flows in ABL.....	48
3.2.1	Steady and Unsteady Reynolds Averaged Navier-Stokes.....	48
3.2.2	Large Eddy Simulation (LES) .....	51
3.2.3	Hybrid Methods: Detached Eddy Simulation (DES) .....	53
3.2.4	Direct Numerical Simulation (DNS).....	53
3.3	Inflow Turbulence Generation Methods .....	54
3.3.1	Precursor Database Method.....	55

3.3.2	Recycling Method .....	57
3.3.3	Synthetic Turbulence Generation Methods with a Brief Review .....	58
3.3.3.1	Proper Orthogonal Decomposition Method (POD) .....	58
3.3.3.2	Vortex Method (VM) .....	59
3.3.3.3	Synthetic-Eddy Method (SEM) .....	59
3.3.3.4	Spectral Methods .....	60
3.3.3.4.1	Digital Filter Based Methods .....	60
3.3.3.4.2	Fourier Synthesis Based Methods .....	62
4	LITERATURE REVIEW .....	65
4.1	Wind-Tunnel Studies .....	65
4.2	Numerical Studies (CFD) .....	68
4.2.1	Pioneering Numerical Studies on Aerodynamics of Bluff Bodies ...	68
4.2.2	Numerical Studies on Aerodynamics of Tall Buildings .....	74
4.3	Comments and Inferences About Studies in Literature .....	84
5	METHODS .....	87
5.1	Description of Numerical Model .....	87
5.1.1	Spalart-Allmaras One Equation Model .....	88
5.1.2	Spalart-Allmaras Based Detached Eddy Simulation .....	89
5.2	Description of Synthetic Inflow Turbulence Generator .....	90
5.2.1	Consistent Discrete Random Flow Generation Method (CDRFG) ..	90
5.2.2	Implementation of CDRFG with Fortran and MPI .....	100
5.3	Geometric Description of Selected Tall Building for Analysis .....	105
5.4	Computational Domains and Grid Discretization Strategies .....	105
5.5	Boundary Conditions .....	115

5.5.1	Decomposition of Synthesized Turbulent Velocity Fields.....	120
6	RESULTS AND DISCUSSION.....	131
6.1	Grid Independence Study .....	131
6.2	Analysis of Mean and RMS Pressure Coefficients .....	132
6.2.1	Mean Pressure Coefficients: Study Case CD0 (0° AOA) .....	132
6.2.2	The Effects of AOA on Mean Pressure Coefficients .....	138
6.2.3	RMS Pressure Coefficients: Study Case CD0 (0° AOA).....	141
6.3	Flow Characteristics Around the Building.....	145
6.3.1	Study Case CD0: 0° Angle of Attack.....	145
6.3.2	Study Case CD45: 45° Angle of Attack.....	155
6.4	Summary and Conclusions .....	163
6.5	Challenges of This Study.....	164
6.6	Future Studies .....	168
	REFERENCES .....	169

## LIST OF TABLES

### TABLES

Table 2.1 Davenport's roughness classification revised by Wieringa (1992) .....	20
Table 2.2 Power-law coefficients for different terrains by Davenport (1960).....	25
Table 5.1 Model constants .....	89
Table 5.2 Total grid points and hexahedron cells of computational domains .....	110
Table 5.3 Meshing parameters about computational domains.....	110
Table 5.4 Parameters used for the generation of the turbulent velocity field .....	117
Table 5.5 Statistical observation points and their statistical descriptors.....	120
Table 6.1 Time spent on synthesizing velocity fields for each study case .....	166
Table 6.2 Time spent on S-A DES simulations for each study case.....	167

## LIST OF FIGURES

### FIGURES

Figure 1.1. Regions of high surface winds around a tall building.....	2
Figure 2.1. Wind circulations in cyclone and anticyclone .....	6
Figure 2.2. General patterns of atmospheric circulation .....	7
Figure 2.3. Spatial and temporal scales of atmospheric motions .....	10
Figure 2.4. Structure of the atmospheric boundary layer .....	11
Figure 2.5. Components of the outer layer and flow patterns in a diurnal cycle.....	13
Figure 2.6. Representative mean wind speed profiles for different terrains.....	21
Figure 2.7. Typical mean wind velocity profiles of different stabilities in SL.....	22
Figure 2.8. Power-law wind speed profiles for different terrains.....	24
Figure 2.9. Spectral regions of the energy spectrum with their length scales .....	32
Figure 2.10. Energy cascade in turbulent flows with very high Reynold numbers.	36
Figure 2.11. Taylor’s frozen turbulence hypothesis .....	38
Figure 2.12. Spectral regions with their representative periodic patterns .....	39
Figure 2.13. Energy spectrum at high Reynold numbers with spectral models .....	41
Figure 3.1. Turbulence models based on resolved and modeled scales .....	49
Figure 3.2. Closure models of RANS/URANS .....	50
Figure 3.3. Representation of flow captured by experiments, LES, and RANS .....	52
Figure 3.4. Wind Tunnel Replication (WTR) and Precursor Database methods ....	56
Figure 3.5. Recycling Method .....	57
Figure 3.6. Processes of Digital Filter method .....	61
Figure 4.1. Schematic airflow pattern around a bluff body.....	70
Figure 5.1. Structure and generation of frequency domain of CDTRFG .....	91
Figure 5.2. Illustration of correction procedure of wavenumber domain.....	96
Figure 5.3. Sample velocity-time traces for a single segment frequency.....	98
Figure 5.4. Sample velocity-time histories.....	98
Figure 5.5. Flowchart of CDTRFG technique .....	99
Figure 5.6. Flowchart of CDTRFG used in this study .....	104

Figure 5.7. Full-scale dimensions of CAARC standard tall building model .....	105
Figure 5.8. Blockage ratio of the computational domain.....	106
Figure 5.9. Dimensions of computational domains for each study case.....	107
Figure 5.10. Approaching angle of grid lines to the building walls.....	109
Figure 5.11. Grid distribution on building surfaces .....	110
Figure 5.12. Overall grid distribution of computational domains.....	111
Figure 5.13. Meshing strategy for CD0 .....	112
Figure 5.14. Meshing strategy for CD0R.....	113
Figure 5.15. Meshing strategy for CD45 .....	114
Figure 5.16. Assigned boundary conditions for computational domains .....	115
Figure 5.17. Profiles used for generation of the turbulent velocity field.....	118
Figure 5.18. The synthesized velocity field at $t=24 D/U$ .....	119
Figure 5.19. Velocity-time histories at SOP-1 for CD0 and CD0R.....	122
Figure 5.20. Velocity-time histories at SOP-1 for CD45.....	123
Figure 5.21. Comparison of along-wind mean velocity profiles .....	124
Figure 5.22. Comparison of velocity-time histories .....	126
Figure 5.23. Comparison of turbulence intensity profiles .....	127
Figure 5.24. Comparison of along-wind spectra with von Karman spectrum .....	128
Figure 5.25. Comparison of across-wind spectra with von Karman spectrum .....	129
Figure 5.26. Comparison of vertical-wind spectra with von Karman spectrum ...	130
Figure 6.1. Non-dimensional mean velocity field of CD0 (a) and CD0R (b).....	132
Figure 6.2. Mean $C_p$ distributions on the windward surface ( $0^\circ$ AOA) .....	133
Figure 6.3. Comparison of mean $C_p$ on the windward surface ( $0^\circ$ AOA).....	134
Figure 6.4. Comparison of mean $C_p$ on the leeward surface ( $0^\circ$ AOA).....	136
Figure 6.5. Mean $C_p$ distributions over the horizontal section ( $0^\circ$ AOA).....	137
Figure 6.6. Nomenclature of building surfaces for $0^\circ$ AOA (a) and $45^\circ$ AOA (b). 138	
Figure 6.7. The effect of AOA on positive pressure coefficients .....	139
Figure 6.8. The effect of AOA on negative pressure coefficients .....	140
Figure 6.9. Comparison of RMS $C_p$ distributions ( $0^\circ$ AOA) .....	142
Figure 6.10. RMS $C_p$ distributions over the horizontal section ( $0^\circ$ AOA).....	143

Figure 6.11. RMS pressure coefficient distributions from several studies.....	144
Figure 6.12. Characteristic mean flow patterns around the building (0° AOA)....	146
Figure 6.13. Mean streamline patterns with pressure distribution (0° AOA) .....	147
Figure 6.14. Separations and corner streams captured by S-A DES (0° AOA) ....	149
Figure 6.15. Comparison of wake flow patterns (0° AOA) .....	149
Figure 6.16. Comparison of mean flow patterns (0° AOA) .....	152
Figure 6.17. Mean out-of-plane vorticities obtained by S-A DES (0°AOA) .....	153
Figure 6.18. Non-dimensional TKE distributions (0° AOA) .....	154
Figure 6.19. The effect of AOA on mean flow patterns around the building .....	156
Figure 6.20. Comparison of mean flow patterns with pressure distributions.....	157
Figure 6.21. Isosurface plots of mean vortices captured by S-A DES .....	158
Figure 6.22. Comparison of wake flow patterns with mean vertical velocities ....	159
Figure 6.23. The effect of incidence angle on flow patterns captured by DES.....	160
Figure 6.24. Mean out-of-plane vorticities obtained by S-A DES (45°AOA) .....	161
Figure 6.25. Non-dimensional TKE distribution (45° AOA).....	162

## LIST OF ABBREVIATIONS

### ABBREVIATIONS

ABL/PBL	: Atmospheric Boundary Layer or Planetary Boundary Layer
ADI	: Alternating Direction Implicit Method
AIJ	: Architectural Institute of Japan
AMS	: American Meteorological Society
AOA	: Angle of Attack
ARFG	: Adjusted Random Flow Generator
ASM	: Algebraic Second-moment Model
BLWT	: Boundary Layer Wind Tunnel
CAARC	: Commonwealth Advisory Aeronautical Council
CD	: Computational Domain
CDRFG	: Consistent Discrete Random Flow Generation
CFD	: Computational Fluid Dynamics
COST	: The European Cooperation in Science and Technology
CPU	: Central Processing Unit
CS	: Current Slice
CWE	: Computational Wind Engineering
CWLV	: Crosswind Left Vortex
CWRV	: Crosswind Right Vortex
DDES	: Delayed Detached Eddy Simulation
DES	: Detached Eddy Simulation

DF	: Downwash Flow
DNS	: Direct Numerical Simulation
DSRFG	: Discretizing and Synthesizing Random Flow Generation
DV	: Direction of View
ELES	: Embedded Large Eddy Simulation
ESD	: Energy Spectral Density
ESDU	: Engineering Science Data Unit
FFT	: Fast Fourier Transform
FORTTRAN	: Formula Translation
FSI	: Fluid-structure Interaction
FSL	: Free Shear Layer
GPU	: Graphics Processing Unit
HAWT	: Horizontal Axis Wind Turbine
HSV	: Horseshoe Vortex
ISL	: Inertial Sublayer
LES	: Large Eddy Simulation
MDOF	: Multi Degree of Freedom
MDSRFG	: Modified Discretizing and Synthesizing Random Flow Generation
MKL	: Math Kernel Library
ML/CBL	: Mixed Layer or Convective Boundary Layer
MPI	: Message Passing Interface
NASA	: National Aeronautics and Space Administration

HAD	: Hesaplamalı Akışkanlar Dinamiği
OPENMP	: Open Multi-processing
PIV	: Particle Image Velocimetry
POD	: Proper Orthogonal Decomposition Method
PRFG	: Prescribed-wavevector Random Flow Generator
PSD	: Power Spectral Density
RANS	: Reynolds-averaged Navier-Stokes
RF	: Reverse Flow
RL	: Residual Layer
RMS	: Root Mean Square
RNG	: Random Number Generator
RSL	: Roughness Sublayer or Interfacial Sublayer
RxL	: The Radix Layer
S-A	: The Spalart – Allmaras Closure Model
SBL/NBL	: Stable Boundary Layer or Nocturnal Boundary Layer
SDOF	: Single Degree of Freedom
SDP	: Saddle Point (Elevated free stagnation point)
SEM	: Synthetic-Eddy Method
SGS	: Sub-grid Scale
SL	: Surface Layer
SOP	: Statistical Observation Point
SP	: Stagnation Point

SRANS : Steady Reynolds-averaged Navier-Stokes

TKE : Turbulence Kinetic Energy

TÜBİTAK : Scientific and Technological Research Council of Turkey

TR : Trust – Region Algorithm

TRUBA : Turkish National e-Science e-Infrastructure

UPS : Upward Separation

URANS : Unsteady Reynolds-averaged Navier-Stokes

VM : Vortex Method

WAWS : Weighted Amplitude Wave Superposition

WTR : Wind Tunnel Replication Method

WV1 : Primary Wake Vortex

WV2 : Secondary Wake Vortex

WV3 : Tertiary Wake Vortex

XC : Xie and Castro’s Method

XCDF : Xie and Castro’s Divergence-Free Method

ZDES : Zonal Detached Eddy Simulation

## LIST OF SYMBOLS

### SYMBOLS

$L_v$	: Across-wind Integral Turbulence Length Scale	[m]
$S_v$	: Across-wind Power Spectral Density	[m <sup>2</sup> /s]
$\sigma_v$	: Across-wind Standard Deviation	[m/s]
$I_v$	: Across-wind Turbulence Intensity	[-]
$L_u$	: Along-wind Integral Turbulence Length Scale	[m]
$S_u$	: Along-wind Power Spectral Density	[m <sup>2</sup> /s]
$\sigma_u$	: Along-wind Standard Deviation	[m/s]
$I_u$	: Along-wind Turbulence Intensity	[-]
$\omega$	: Angular Frequency	[rad/s]
$k_a$	: Angular Wavenumber	[rad/m]
$A_{DS}$	: Area of Inflow Plane	[m <sup>2</sup> ]
$A_{BS}$	: Area of Building's Front Surface	[m <sup>2</sup> ]
$\rho_u$	: Autocorrelation Function	[-]
$\Psi_s$	: Atmospheric Stability Function	[m/s]
$U_m$	: Average Velocity of Inflow Plane	[m/s]
$\delta_{BR}$	: Blockage Ratio	[-]
$\delta$	: Boundary Layer Depth or Gradient Height ( $z_G$ )	[m]

$\ell$	: Characteristic Eddy Size	[m]
$C_c$	: Coherence Decay Constant	[-]
$\gamma$	: Coherency Tuning Factor	[-]
$f$	: Coriolis Parameter	[rad/s]
$k$	: Non-dimensional Wavenumber	[-]
$\rho$	: Correlation Coefficient	[-]
$f_{v1}$	: Damping Function for Turbulent Eddy Viscosity	[-]
$C$	: Decay Parameter	[-]
$\nabla$	: Del Operator	[-]
$\rho_f$	: Density of Fluid	[kg/m <sup>3</sup> ]
$C_{DES}$	: DES Model Constant	[-]
$\varepsilon$	: Dissipation Rate of Turbulence Kinetic Energy	[m <sup>2</sup> /s <sup>3</sup> ]
$\mu$	: Dynamic Viscosity	[N.s/m <sup>2</sup> ]
$k_s$	: Equivalent Roughness Height	[m]
$u'$	: Fluctuating Component of Longitudinal Velocity (Along-wind)	[m/s]
$v'$	: Fluctuating Component of Transverse Velocity (Across-wind)	[m/s]
$w'$	: Fluctuating Component of Vertical Velocity	[m/s]
$f_n$	: Frequency	[Hz]
$p, q$	: Frequency-based Amplitudes	[m/s]
$u_*$	: Friction or Shear Velocity	[m/s]

$U_\infty$	: Gradient Velocity	[m/s]
$Z_{CD}$	: Height of Computational Domain	[m]
$z_s$	: Height of Lower ABL Layer	[m]
$H$	: Height of Tall Building	[m]
$u$	: Instantaneous Longitudinal Velocity (Along-wind)	[m/s]
$v$	: Instantaneous Transverse Velocity (Across-wind)	[m/s]
$w$	: Instantaneous Vertical Velocity	[m/s]
$L$	: Integral Length Scale	[m]
$\nu$	: Kinematic Viscosity	[m <sup>2</sup> /s]
$\eta$	: Kolmogorov Length Scale	[m]
$\tau_\eta$	: Kolmogorov Time Scale	[s]
$u_\eta$	: Kolmogorov Velocity Scale	[m/s]
$Re_\eta$	: Kolmogorov-scale Reynold Number	[-]
$L_{CD}$	: Length of Computational Domain	[m]
$D$	: Length of Tall Building	[m]
$\tilde{S}$	: Magnitude of Vorticity	[1/s]
$f_{\max}$	: Maximum Frequency	[Hz]
$\bar{u}$	: Mean Component of Longitudinal Velocity (Along-wind)	[m/s]
$\bar{v}$	: Mean Component of Transverse Velocity (Across-wind)	[m/s]
$\bar{w}$	: Mean Component of Vertical Velocity	[m/s]

$f_{\min}$	: Minimum Frequency	[Hz]
$C_p$	: Mean Pressure Coefficient	[-]
M	: Number of Segment Frequencies	[-]
N	: Number of Sub-frequencies for Each Segment Frequency	[-]
$L_s$	: Obukhov Stability Length	[m]
$P$	: Period	[s]
$\lambda_R$	: Plan-area Density Ratio of Surface Roughness Elements	[-]
$\alpha$	: Power-law Coefficient	[-]
p	: Pressure	[N/m <sup>2</sup> ]
$z_{ref}$	: Reference Height	[m]
$z_B$	: Reference Height for Numerical Models	[-]
Re	: Reynolds Number of Turbulent Flow	[-]
$C_{p_{rms}}$	: RMS Pressure Coefficient	[-]
$f_m$	: Segment Frequency	[Hz]
S	: Strain Rate	[-]
$f_{m,n}$	: Sub-frequency	[Hz]
$z_0$	: Surface Roughness Length	[m]
$\lambda$	: Taylor Microscale	[m]
$Re_\lambda$	: Taylor-scale Reynolds Number	[-]
t	: Time	[s]

$\tau_0$	: Time Scale of Largest Eddies	[s]
$\sigma_{u_1 u_2}$	: Velocity Covariance	[m <sup>2</sup> /s <sup>2</sup> ]
$u_0$	: Velocity Scale of Largest Eddies	[m/s]
$L_w$	: Vertical-wind Turbulence Integral Length Scale	[m]
$S_w$	: Vertical-wind Power Spectral Density	[m <sup>2</sup> /s]
$\sigma_w$	: Vertical-wind Standard Deviation	[m/s]
$I_w$	: Vertical-wind Turbulence Intensity	[-]
$\kappa$	: Von Karman Constant	[-]
$k_w$	: Wavenumber	[m <sup>-1</sup> ]
$W_{CD}$	: Width of Computational Domain	[m]
$W$	: Width of Tall Building	[m]
$z_d$	: Zero Plane Displacement	[m]



# CHAPTER 1

## INTRODUCTION

### 1.1 Computational Wind Engineering

Computational Fluid Dynamics (CFD) is a growing field of fluid mechanics that involves a group of computational methodologies (i.e., numerical analysis and discretization methods.) to solve and analyze fluid flow problems such as heat transfer or turbulence. Based on the problem to be solved, conservation laws, Navier-Stokes equations, Euler Equations, acoustic wave equations, shallow water equations, and boundary layer equations may be used with various discretization methods for different branches of science and industrial purposes. The efficiency of CFD simulations are dependent on computational resources such as central processing units (CPU), memory capacity, and graphics processing units (GPU) that lead to better parallel algorithms. Therefore, in company with current improvements in computational resources, this field provides many engineering tools that come with potential benefits. Furthermore, there is a subfield of CFD called Computational Wind Engineering that focuses mainly on atmospheric boundary layer-related phenomena explained in Chapter (2) briefly, including wind characteristics for structural designs, pedestrian level comfort, air pollutant dispersion-deposition, wind-driven rain, and building ventilation.

As a common practice, wind loads on tall buildings are calculated using empirical formulas with some simplifying assumptions described within Turkish Standards: TS498 and TS EN 1991-1-4 in Turkey. Since the existing building codes for wind loads are mainly based on performed boundary layer wind tunnel tests earlier with past site experiences, these formulas and assumptions become invalid with the increase in the building height, similar to other building codes. For instance, Turkish (TS EN 1991-1-4), Australian (AS/NZS-1170.2), and European (EN 1991-1-4:2005)

standards are applicable for buildings or civil engineering works with heights up to 200 m and for bridges having no span greater than 200 m. Moreover, these standards are generalized with limited types of cross-sections, aspect ratios, and analytical methods, which are insufficient to use in tall buildings' design process considering across-wind effects, vortices, and turbulent flow fluctuations, that can result in fluctuating motions, especially for flexible structures. (e.g., vibrations which may be enhanced by resonance). (Parv et al., 2012) Even though structures are adequately designed to handle wind-induced forces within structural safety, pedestrian-level wind conditions are also essential for proper configuration. High rise buildings may cause higher wind speeds at a pedestrian level, leading to vortex flows near the ground, corner streams, and suction due to the through-flows, as shown in figure (1.1). Based on the many factors such as relative location, the dimensions, the shapes, the roughness, topographical features of the construction terrain, and the existence of one or more tall buildings, wind flow around the surface may change significantly due to the complex dependency. (Simiu & Yeo, 2019)

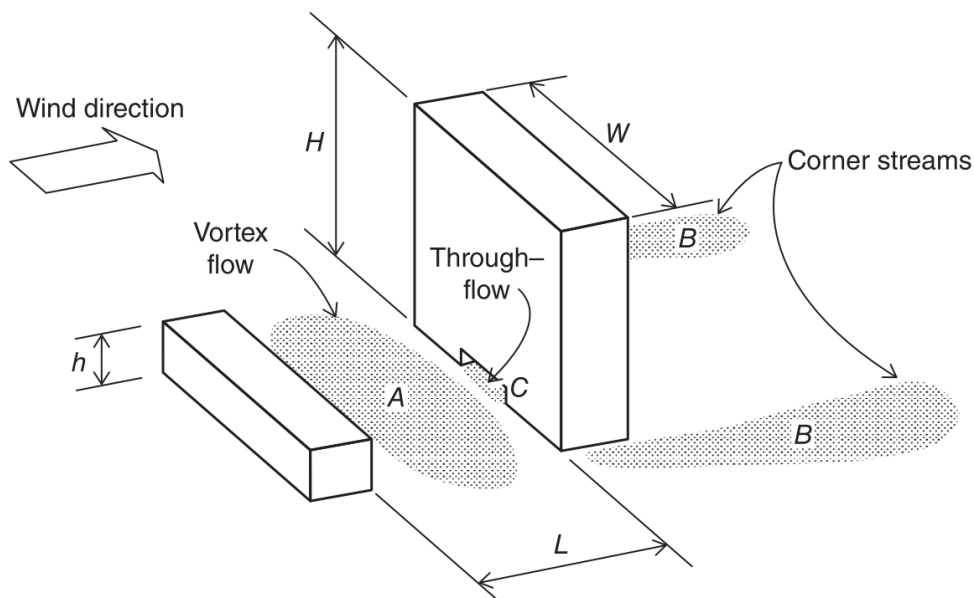


Figure 1.1. Regions of high surface winds around a tall building

Note: Reprinted from *Wind Effects on Structures: Modern Structural Design for Wind* (4th ed., p.230), by Authors E. Simiu and Y. Donghun, 2019, John Wiley & Sons, Ltd. Copyright 2019 by John Wiley & Sons, Ltd.

For these reasons, all codes/standards suggest using wind tunnel experiments for tall buildings with heights above the specified limits and distinctive design. As an experimental approach, wind tunnel tests yield more realistic, reliable results and even direct observation of applied conditions on the target design. However, considering difficulties of wind tunnels such as;

- longer lead times,
- costs of a model, measuring equipment such as laser Doppler velocimetry, hot-wire velocity probes, and total pressure rakes, maintenance and running,
- initial and boundary conditions such as wall effects, free stream turbulence matching,
- simulating full-scale Reynolds numbers experimentally,
- their applicability-availability for the engineers,

the numerical determination of wind loads using computational fluid dynamics provides excellent convenience for studies on scaled models in the atmospheric boundary layer. The main advantages of the computational fluid dynamics are matching target Reynold's number, absence of wall effects, cheaper-faster modeling, and obtaining more detailed/unlimited data about related parameters such as pressure and velocity for each target point of the computational domain. On the other hand, due to the disadvantages, for instance;

- truncational or discretization errors,
- lack of reliable turbulence models,
- increasing mesh points with a complex geometry that leads to longer convergence times,
- difficulties of results verification,

one may conclude that both experimental and computational approaches have their advantages and disadvantages. When analyzing projects of some industries and the studies about wind-induced forces conducted up to the present, it can be seen that

some researchers use their CFD models as preliminary work to eliminate an excessive number of wind tunnel tests, while others are using wind tunnel test data to calibrate or validate their CFD models. Therefore, it can be said that there is an undeniable synergy between these two approaches.

## **1.2 Scope of the Thesis**

The aim of this study is to analyze wind flow characteristics such as horseshoe vortex formation and recirculation region around an isolated 182.88 m x 45.72 m x 30.48 m standard tall building model (CAARC) and examine wind-induced effects in terms of pressure coefficients on that building. Simulations were performed by micro-scale modeling under the conditions of inhomogeneous and anisotropic turbulent flows that occur in strong winds within the lower layer of the neutral atmospheric boundary layer. Spalart-Allmaras based Detached Eddy Simulation (S-A DES) model with high resolution was used to simulate flows around target building at 0° and 45° angles of wind attack under the open-terrain conditions. One of the synthetic turbulence generation methods called “Consistent Discrete Random Flow Generation” (CDRFG) was utilized to generate inflow boundary layer conditions that represent strong winds for the S-A DES numerical model. This technique was handled with an algorithm compiled using the Fortran programming language with math kernel libraries and MPI implementations. Synthetic methods were mainly proposed for the LES numerical model, and a limited number of studies on tall building aerodynamics in the literature used one of them with hybrid methods to generate inflow boundary conditions. Thus, within this study, it is also aimed to investigate the DES model's performance with one of the inflow generation techniques. Besides, to observe the differences between the S-A RANS and S-A DES model, the same flows were also simulated using the S-A RANS numerical model. Since RANS numerical models resolve mean properties of flow, effects of the synthesized turbulent velocity field on results were also revealed and observed by comparing these two numerical models.

## **CHAPTER 2**

### **THEORETICAL BACKGROUND**

Due to the structure of the atmospheric boundary layer and its diurnal cycle, the characteristics of air movements within this layer, such as winds, differ significantly. Therefore, fundamental knowledge is required before modeling the turbulent flows in this layer caused by these movements. Consequently, in this chapter, the forces behind the wind formation, the definition, and the atmospheric boundary layer structure are explained to clarify this study's scope, which is given in Section (1.2), more clearly. Furthermore, it is aimed to mention several statistical descriptors, models, and theories used in the synthetic inflow turbulence generation method described in Section (5.2).

#### **2.1 The Atmospheric Boundary Layer**

##### **2.1.1 Forces Behind the Wind Formation**

With a wide range of scales (both local and worldwide), wind formation occurs due to pressure gradient force, the Coriolis force, and friction force. (Simiu & Yeo, 2019) This formation may arise from all of these forces or one of them in the atmosphere. Pressure gradient force originates from the variation of the strike angle and amount of Sun's rays hitting the surface of Earth and the terrain's energy holding capabilities (e.g., land or water). This variation leads to the differential amount of solar energy within the form of radiated heat. It results in the change of air density (i.e., temperature differences), which creates high and low atmospheric pressure zones in the atmosphere both in time and space with pressure gradient force. Air flows from higher-pressure zones to lower-pressure zones with this force either in the vertical or the horizontal direction. Regardless of the direction, air movement caused by the

pressure difference follows a spiral path rather than a straight path. The reason for that is Earth's rotational motion, which leads to Coriolis Effect/Force that deflects air movement over the Earth's surface with respect to the flow location. This deflection has the direction to the right in the Northern hemisphere, and it has the direction to the left in the Southern hemisphere. On the other hand, there is no deflection on the equator where the Coriolis Effect does not exist. Under the influence of both pressure gradient force and Coriolis force, the wind systems that rotate around low and high-pressure zones are called cyclones and anticyclones, respectively, as given in figure (2.1).

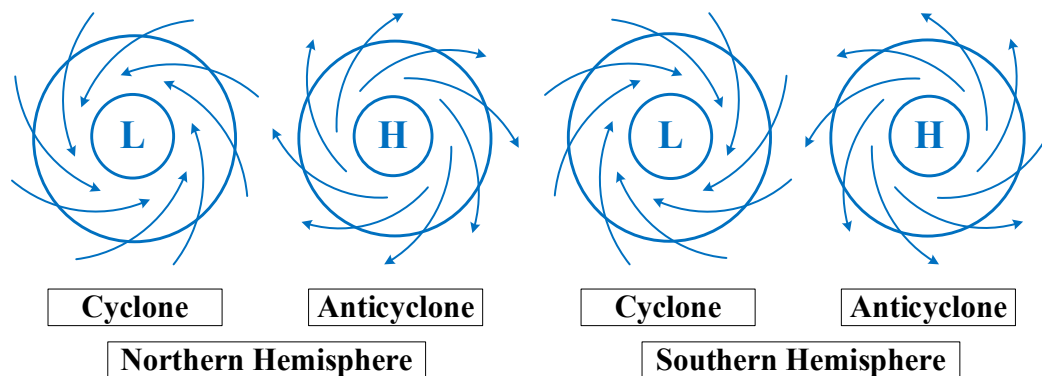


Figure 2.1. Wind circulations in cyclone and anticyclone

Furthermore, the friction force between air and Earth's surface has a retarder effect, which increases as getting closer to the surface on the airflow horizontally. Theoretically, in the absence of this force, the airflow direction is parallel to isobars. Isobars are the lines with constant pressure at a given height when both pressure gradient and Coriolis forces balance each other. In addition, this air motion is called *geostrophic wind*. However, it is quite rare because isobars are generally curved, which introduces centrifugal force. Winds rotating around the low and high-pressure zone create centrifugal force that disturbs the balance between pressure gradient force and Coriolis force. Within the presence of a centrifugal force, *gradient winds* arise from the balance of these three forces. In the rotational air motion around the low-pressure zone, centrifugal force acts in the same direction with Coriolis force to direct flow from the low-pressure zone to high, which is not possible. Therefore the

Coriolis force reduces to bring force balance with constant pressure gradient force that leads to the *sub-geostrophic wind*. Since less force acting on flow, these winds are slower than geostrophic winds. On the contrary, in air motion around the high-pressure zone, centrifugal force acts in the same direction with the pressure gradient force result in stronger Coriolis force for balance in the opposite direction. This lead to the formation of *super-geostrophic* winds, which are relatively faster than geostrophic winds.

In brief, the horizontal motion of the air is formed by the Coriolis Effect, friction force, and the horizontal pressure gradient force that results from spatial variation of the horizontal pressures, while buoyancy force determines the vertical motion of air. (Simiu & Yeo, 2019) As a consequence of this formation, *atmospheric circulation* occurs, and together with ocean circulation, thermal energy is redistributed throughout the earth's surface. Figure (2.2) represents this large-scale air movement, which is also known as “*global circulation.*”

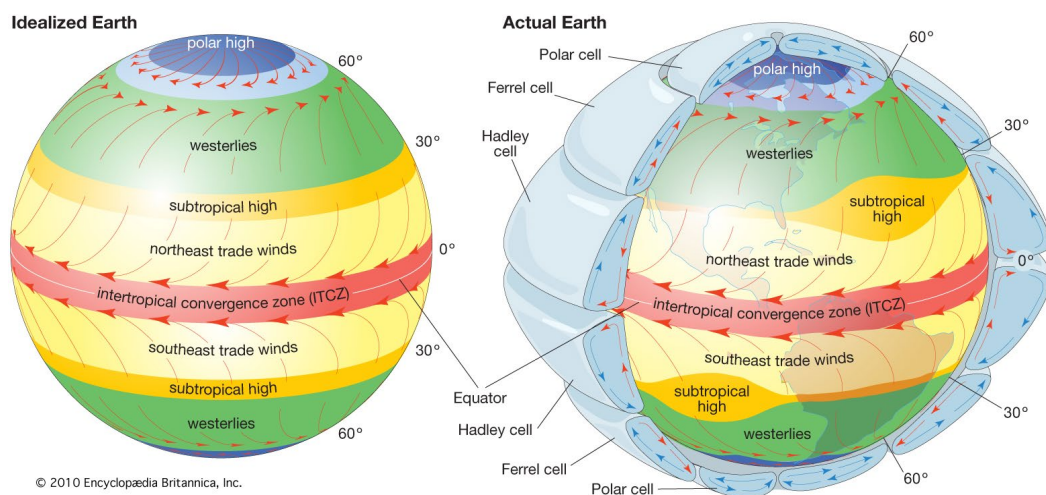


Figure 2.2. General patterns of atmospheric circulation

Note: Reprinted from Atmospheric Circulation, In *Encyclopædia Britannica*, by The Editors of Encyclopædia Britannica, Retrieved February 12, 2020, from <https://www.britannica.com/science/atmospheric-circulation>. Copyright 2019 by Encyclopædia Britannica

### 2.1.2 Definition and Stratification of the Atmospheric Boundary Layer

The friction force that is mentioned previously in Sub-section (2.1.1) decreases as the elevation from the surface of the Earth increases until it becomes negligible at a specific height named *gradient height* denoted by  $z_G$  or  $\delta$ . Since this force has a retarder effect on horizontal air motion, the flow velocity is also increasing as a function of height. Flow velocity at that specific height is called “*gradient velocity*.” The part of the atmosphere where the airflow is under the influence of this frictional force of the planetary surface is called “*the planetary boundary layer (PBL)*” or “*the atmospheric boundary layer (ABL)*.” This region is directly modified by the exchange of momentum, heat, and water vapor between the underlying Earth’s surface and the gradient height. (Kaimal & Finnigan, 1994; Simiu & Yeo, 2019) The atmosphere above the gradient height is named “*the free atmosphere*.” While the height of the atmospheric boundary layer varies from several meters to kilometers in both time and space, the free atmosphere's thickness is less variable.

Furthermore, in the atmospheric boundary layer, air and Earth's surface interact in two primary forms, which are mechanical and thermal. While mechanical interaction occurs due to the friction force that results in vertical wind shear, thermal interaction is caused by solar radiation differentiation. These interactions are the main mechanisms that make the atmospheric flow in ABL dominated by almost consistent turbulent motions with rapid turbulent mixing in both vertical and horizontal directions. Therefore, mechanical and thermal interactions can be identified with shear production of turbulence and buoyancy production/destruction of turbulence, respectively. Based on the buoyancy force's direction or absence of this force, the atmospheric boundary layer can be classified by its stratification as unstable, stable, and neutral. While the buoyancy force acts upward, stratification is *unstable*. On the other hand, if it acts downward, stratification is *stable*. In the case of the absence of this force, stratification is *neutral*. In contrast, the free atmosphere is generally laminar with small molecular diffusion, usually in a horizontal direction.

Correspondingly, while winds in ABL are mainly sub-geostrophic, winds in the free atmosphere are almost geostrophic.

From the structural point of view, the effect of strong winds is of great priority. In strong winds, turbulent mixing tends to form neutral ABL since turbulent transport dominates heat convection. (Simiu & Yeo, 2019) For this reason, studies within the scope of this thesis were conducted by considering the neutral stratification of ABL.

### **2.1.3 Scales of Atmospheric Motions**

Computational wind engineering applications focus on atmospheric phenomena with various scales that differ based on time and length scales within a whole depth of atmosphere. These scales are categorized under three main groups, which are macro-scale (i.e., synoptic-scale), meso-scale, and micro-scale. Based on The American Meteorological Society (AMS), Blocken (2015) defines these scales as follows.

- Macro-scale modeling: deals with the largest scale of atmospheric motions such as global circulations, cyclones, and weather types with a typical range of hundreds of kilometers.
- Meso-scale modeling: considers atmospheric phenomena with horizontal scales ranging from a few to several hundred kilometers, including thunderstorms, squall lines, fronts, precipitation bands in tropical and extratropical cyclones topographically generated weather systems such as mountain waves and sea or land breezes.
- Micro-scale modeling: intends to simulate atmospheric motions including large scale turbulence, thermals, and building wakes with the scale where Lagrangian Rossby number (dimensionless number as the ratio of inertial force to Coriolis force to identify a fluid flow) greater than two hundred or spatial scales up to two km or less.

Figure (2.3) represents these main groups with their spatial and temporal scales of atmospheric motions.

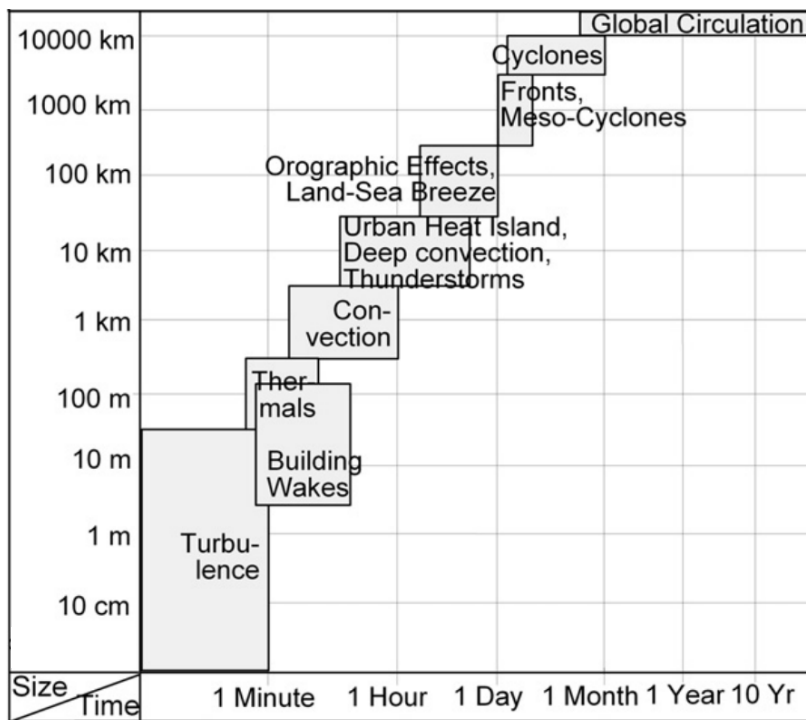


Figure 2.3. Spatial and temporal scales of atmospheric motions

Note: Adapted from “Joint modeling of obstacle induced and mesoscale changes- Current limits and challenges” by Authors K. H. Schlünzen, D. Grawe, S. I. Bohnenstengel, I. Schlüter, and R. Koppmann, 2011, *Journal of Wind Engineering and Industrial Aerodynamics*, 99, 217–225, Copyright by Elsevier

#### 2.1.4 Structure and Diurnal Cycle of the Atmospheric Boundary Layer

As already mentioned before in Sub-section (2.1.2), the height of the atmospheric boundary layer varies from several meters to kilometers in both time and space. This variation is directly under the influence of shape, friction, and thermal effects resulting from the Earth's surface and motion. (Weerasuriya, 2013) In other words, it depends on wind speed, the roughness of the terrain, the angle of latitude, and the degree to which the stratification of the free flow. (Simiu & Yeo, 2019) Considering these factors, the governing equations and the accuracy of CFD simulations strictly depend on a selected approach to handle turbulent motions within their complexity throughout the structure of the atmospheric boundary layer. As shown in figure (2.4), the atmospheric boundary layer can be divided into two prominent layers that are the

inner (or surface, or wall) layer and the outer layer. Besides, the inner or surface layer also has two sublayers, which are the inertial sublayer and interfacial sublayer (also known as roughness sublayer or microlayer). (Garratt, 1994; Kaimal & Finnigan, 1994; R. B. Stull, 1988)

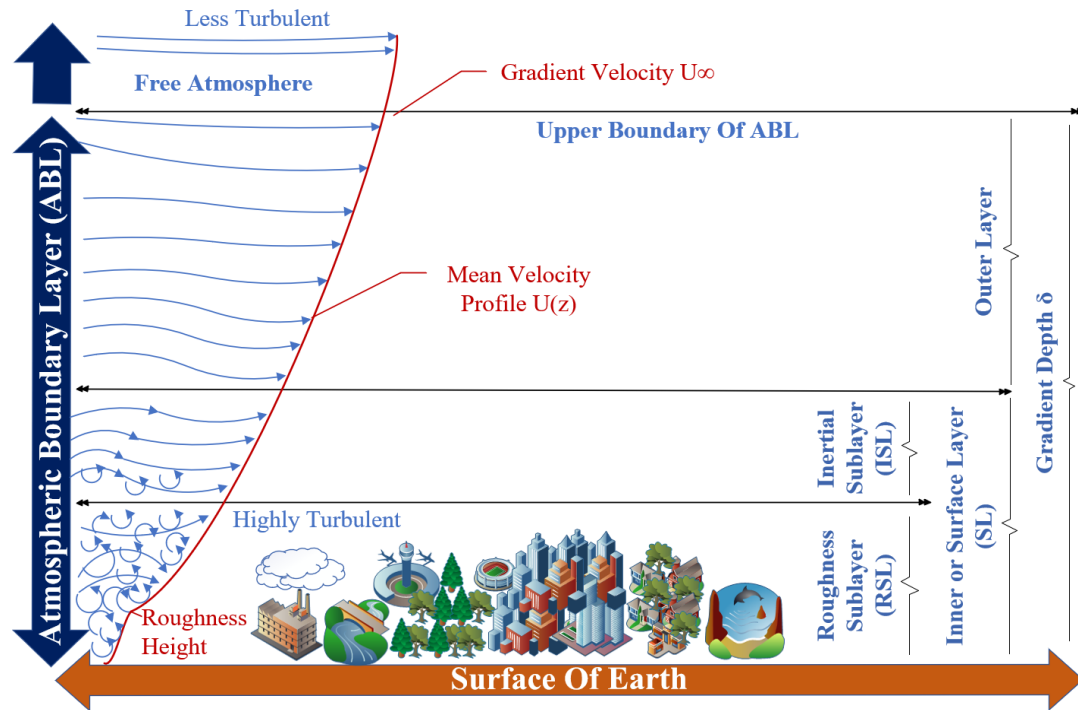


Figure 2.4. Structure of the atmospheric boundary layer

#### 2.1.4.1 Outer Layer

The outer layer is defined as the transitional region, where variable shear-stress exists above the inner layer. In this layer, airflow is under the influence of temperature gradient, Coriolis force, and surface friction. However, comparing the inner layer, the effect of surface friction is less. (Garratt, 1994; Kaimal & Finnigan, 1994; R. B. Stull, 1988) The structure of the atmospheric boundary layer, especially in the outer layer, depends on the thermal interaction between air and surface, which changes dramatically within a diurnal cycle. This cycle leads to the formation of three major components of ABL, which are *the mixed layer (ML)*, *residual layer (RL)*, and *the stable boundary layer (SBL)*. (R. B. Stull, 1988)

The mixed layer is an unstably stratified layer that follows the terrain's topography and enlarges with air entrainment above. It develops in the middle of the day between sunrise and sunset when heat transfer and radiative cooling, which are convective sources, produce thermal instability. In more detail, the virtual potential temperature, which is a potential temperature without variations result from pressure changes, increases with height (sub-adiabatic) at the top of this layer. In contrast, it decreases with height at the bottom as closer to the surface (super-adiabatic) while the adiabatic process appears in the middle. Consequently, nearly homogeneous (similar) ascending-descending air motions in the vertical direction between the surface and top of the cloud layer occur, and sub-geostrophic winds are observed. Although wind shear is another source for turbulence generation, these motions mix air uniformly across the whole layer and make the turbulence convectively driven (Large eddies). Therefore, ML is also referred to as the convective boundary layer (CBL). In the first 10% of CBL, the variation of mean wind speed, wind direction, and temperature arises with the steepest gradient. On the other hand, they are almost flattened by intense convective mixing in the vertical direction. (Kaimal & Finnigan, 1994)

Within a short period before sunset and throughout the night, both the residual and stable boundary layers exist in the absence of air motions related to convective sources. Stull (1988) defines the residual layer as the neutrally stratified layer (nearly equal turbulence in all directions) with the same mean state and concentration variables of the recently-decayed mixed layer. It is separated from the surface by the stable boundary layer (SBL), also known as the nocturnal boundary layer (NBL), which evolves with a surface inversion at the RL's bottom. This evolution is statically stable with relatively weak turbulence along with SBL, although super-geostrophic winds (low-level jet or nocturnal jet) infrequently result in shear-generated turbulence formation. Strong wind shear, small eddies, and occasional wave activity characterize the flow in this layer. (Kaimal & Finnigan, 1994) Figure (2.5) represents components of the outer layer in a diurnal cycle with their flow patterns.

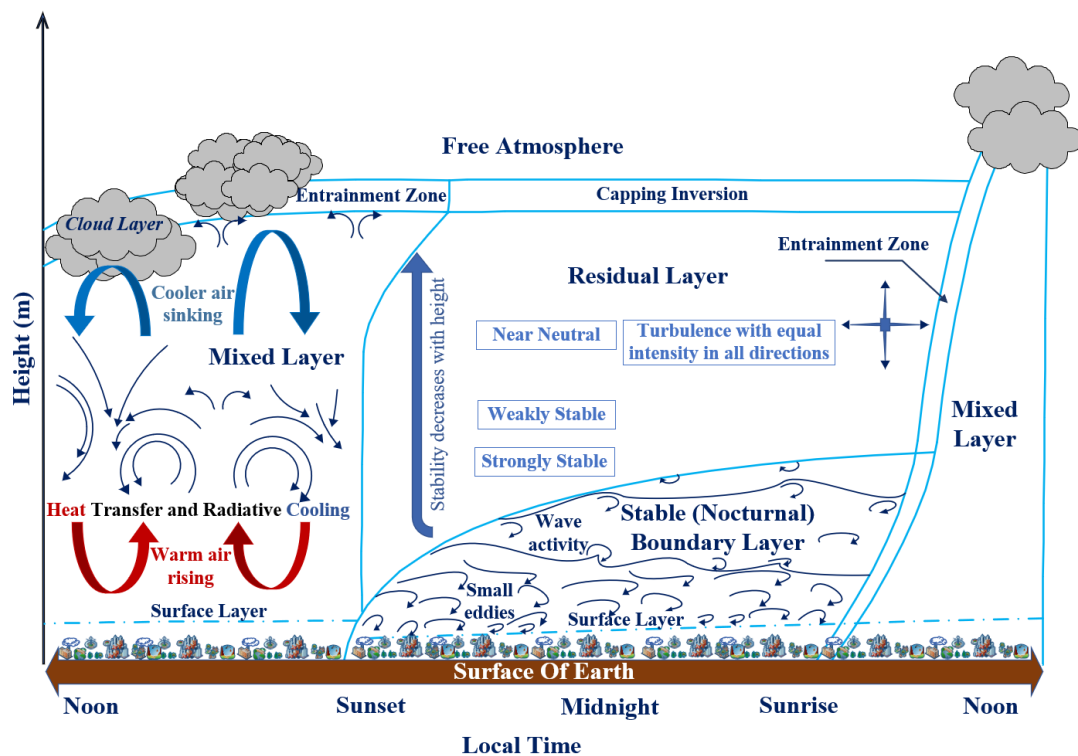


Figure 2.5. Components of the outer layer and flow patterns in a diurnal cycle  
 Note: Adapted from (Garratt, 1994; Kaimal & Finnigan, 1994; R. B. Stull, 1988)

#### 2.1.4.2 Surface Layer

While Kaimal and Finnigan (1994) define the inner layer based on Sutton (1977) with the term “surface layer” as a region with constant vertical shear stress and with a depth of 50 to 100 m from the surface where wind structure is mainly dominated by surface friction and vertical temperature gradient. On the other hand, Stull (1988) describes this layer as the bottom 10% of the ABL where the variation of turbulent fluxes and stresses are less than 10% of their magnitude even if it is part of the mixed layer or stable boundary layer. In the bottom part of SL, which is referred to as the interfacial or the roughness sublayer (RSL), the surface characterizes the flow depending on the roughness elements on it, either with the domination of molecular transportation or molecular diffusion over turbulent motions. (Garratt, 1994; R. B. Stull, 1988) Stull (1988) also introduces this thin layer in his book with the term “*microlayer*.” Moreover, the upper part of the SL is the inertial sublayer. In this

sublayer, turbulent motions' characteristics mainly depend on the height from the surface, and they have almost the same properties in the horizontal direction.

## **2.2 Essentials and Characteristics of Turbulence in ABL Flows**

In fluid dynamics, turbulent flow is defined as the flow regime that occurs when inertial forces dominate over viscous forces. It is characterized by irregular, quasi-random motions of fluid particles with a highly diffusional, dissipative, and rotational nature. Except for strong thermal stratification, turbulent motions are usually omnipresent in the atmospheric boundary layer. (Garratt, 1994) These motions are responsible for energy dissipation/transformation, rapid mixing, and transportation of enhanced rates of mass, momentum, and energy between the underlying surface and atmosphere. In a diurnal cycle, turbulence generation in ABL occurs as a result of thermal, mechanical, and inertial interactions that lead to chaotic behavior in the flow field. Therefore, these motions are described with theories based on statistical approaches with stochastic processes rather than a deterministic approach.

### **2.2.1 Statistical Classification of Turbulence in ABL**

In Sub-section (2.1.2), stratification of ABL is mentioned based on the buoyancy force directly related to turbulence production and destruction. On the other hand, from the point of statistics, turbulence in ABL is classified with several concepts such as homogeneous, stationary, isotropic, or their definitional inverse, based on statistical dependency. If the turbulent flow's statistical properties are the same at every point in space, or in other words, if the averaged turbulence characteristics of the flow have no relation with the translation of the spatial axes, then the flow is termed *homogeneous turbulence*. Under the circumstance that turbulent flow has statistical distinctness throughout the vertical direction but not in a horizontal direction, it is referred to as *horizontally homogeneous*. (Garratt, 1994; R. B. Stull,

1988) This type of turbulent flow in ABL exists with a balance between vertical mean wind speed and turbulence profiles with ground roughness characteristics. (Blocken et al., 2007)

Similarly, turbulent flow can also be described with respect to the time in which averaging is made. If its statistical qualities do not vary with time, then turbulence is called *stationary*. In the case of *isotropic turbulence*, turbulent flow is statistically uniform with the independence of translation, reflection, and rotation of the spatial axes. According to this definition, isotropic turbulence can also be classified as homogeneous. (Garratt, 1994)

Since turbulent flows in ABL are usually inhomogeneous and anisotropic, studies were conducted considering these properties within this thesis's scope.

### 2.2.2 Decomposition of Turbulent Flow Fields

Stull (1988) states that winds can be separated into the mean wind, turbulence, and waves, whether they can exist in separate or superimposed form. In a similar manner, if the literature is reviewed, one may conclude that ABL's turbulent flow field is suggested to be analyzed within two components: the mean component and the fluctuating or perturbation component. The fluctuating component is also known as the eddy component. Hence, turbulent flow in a three-dimensional domain can be decomposed in terms of turbulence quantities such as velocity or pressure that consist of these mean and fluctuating components by denoting the mean component with an overbar and eddy component with prime based on a mathematical technique called *Reynolds decomposition*. Accordingly, the velocity term for any three-dimensional flow would be decomposed, as given below;

$$u = \bar{u} + u' \quad , \quad v = \bar{v} + v' \quad , \quad w = \bar{w} + w' \quad (2.2.1)$$

However, specific rules known as *Reynolds averaging conditions* must be fulfilled to implement the formulation (2.2.1), and these are given below in accordance with the reference (Kaimal & Finnigan, 1994).

- The average of the averaged component must give the same value.

$$\overline{\overline{u}} = \overline{u}, \quad \overline{\overline{v}} = \overline{v}, \quad \overline{\overline{w}} = \overline{w} \quad (2.2.2)$$

- Since fluctuating components are defined as deviating values around a mean value, these quantities' average values must always be zero.

$$\overline{u'} = \overline{v'} = \overline{w'} = 0 \quad (2.2.3)$$

- The effect of constants, which are taken as correlation factors between mean and eddy components, must be eliminated.

$$\overline{\overline{Cu'}} = 0, \quad \overline{\overline{Cv'}} = 0, \quad \overline{\overline{Cw'}} = 0 \quad (2.2.4)$$

- Averaged partial derivative of component, whether in space or time, must be the same as derivative of the averaged component.

$$\overline{\frac{\partial u(x_i)}{\partial x_i}} = \frac{\partial \overline{u(x_i)}}{\partial x_i}, \quad \overline{\frac{\partial u(x_i)}{\partial t}} = \frac{\partial \overline{u(x_i)}}{\partial t} \quad (2.2.5)$$

### 2.2.2.1 Types of Averaging for Mean Components

There are several averaging types that are used for defining the mean component of decomposed turbulent flow, and these are *ensemble average*, *spatial average*, and *time average*. Ensemble average is the most convenient characterization of any target system that can be performed with the aid of theoretical analysis and probability density functions by repeating N identical experiments or synthesizing data to reduce errors due to randomness. (Garratt, 1994; R. B. Stull, 1988) With another definition, as Kaimal and Finnigan (1994) stated, the ensemble average is “*averaging over many realizations under identical conditions.*” Then, for any statistical quantity, “A,” such

as velocity that is a function of both time, “t,” and space, “s,” the ensemble average can be formulated as given below.

$$\bar{A}(s,t) = \frac{1}{N} \sum_{i=0}^{N-1} A_i(s,t) \quad (2.2.6)$$

Even if the ensemble average satisfies all conditions which are given for Reynolds averaging, difficulties coming from observing recursive atmospheric events make it unable to use, unlike laboratory works. Therefore, spatial and time averaging are deployed with respect to flow's statistical dependency by considering the ergodic hypothesis or condition. (Garratt, 1994; Kaimal & Finnigan, 1994; R. B. Stull, 1988) In accordance with this hypothesis, spatial averaging is considered the same as the ensemble average when turbulent flow in ABL is homogeneous. It is obtained for an instant time by dividing the summation or integration of target quantity with a spatial domain “S” that may represent a line, area, or volume. (R. B. Stull, 1988)

$$\bar{A}(t) = \frac{1}{N} \sum_{i=0}^{N-1} A(i,t) \quad \text{or} \quad \bar{A}(t) = \frac{1}{S} \int_{t=0}^S A(s,t) ds \quad \text{where } s=i\Delta s \text{ (discrete)} \quad (2.2.7)$$

Considering the fact that most flows in ABL are inhomogeneous, time-averaging is a more common way to describe the mean properties of turbulent flow rather than spatial averaging. However, spatial averaging may also be used by combining with time-averaging for flows such as a horizontally homogeneous turbulent flow with at least one directional homogeneity to achieve faster convergence in statistical operations. (Gatski & Bonnet, 2013) Time averaging is the arithmetic mean of a statistical parameter over a certain period, “P,” and it is taken as ensemble average for statistically stationary turbulent flows.

$$\bar{A}(s) = \frac{1}{N} \sum_{i=0}^{N-1} A(s,i) \quad \text{or} \quad \bar{A}(s) = \frac{1}{P} \int_{t=0}^P A(t,s) dt \quad \text{where } t=i\Delta t \text{ (discrete)} \quad (2.2.8)$$

Principally for a definition of basic wind velocity and wind-induced responses, the averaging period varies with certain assumptions, approaches, and procedures. To be more precise, while hourly mean speed that refers to averaged speed over 1 hour is

used mainly as a reference wind speed for wind tunnel simulations, shorter averaging periods are used for building codes and standards. (Kwon & Kareem, 2013; Simiu & Yeo, 2019)

### 2.2.2.2 Description of Vertical Mean Wind Speed Profiles

Several factors and their uncertainties with the diurnal cycle of ABL, such as atmospheric stability, statistical dependencies, surface roughness (which depends on terrain category and topography features), directly impact the shape, speed, and direction of wind profile in both time and space. Therefore, it is not easy to define the actual mean wind velocity profile without consuming money and time-related sources for both simulating winds in ABL with either numerical (CFD) or experimental (e.g., Wind Tunnels) processes and calculating wind responses based on specific procedures provided by building codes/standards. (Thordal et al., 2019; Weerasuriya, 2013) As a consequence, the description of the mean wind velocity profile (i.e., the vertical extrapolation of mean wind speeds) that represents target layers of ABL is done by empirical formulations, which may be relied on either logarithmic law or power-law under some classifications with respect to frictional force/velocity, roughness length, and shear stresses.

#### 2.2.2.2.1 Mean Velocity Distribution with Logarithmic Law

Mean wind velocity profile with logarithmic law (also known as the logarithmic law of the wall) is scale-dependent velocity distribution with a theoretical basis in terms of Von Karman constant  $\kappa$ , surface roughness length  $z_0$ , friction velocity  $u_*$ , and Coriolis parameter  $f$  as follows.

$$\bar{u}(z) = \frac{u_*}{\kappa} \ln \left( \frac{z}{z_0} \right) \quad (2.2.9)$$

However, equation (2.2.9) is not applicable along with the entire depth of ABL, and it is valid for the height within the interval between roughness length and height of the lower layer of ABL denoted by  $z_s$ . (Simiu & Yeo, 2019)

$$u_* = \frac{u(z)}{2.5 \ln(z / z_0)} \quad \text{where } z_0 < z < \left( z_s \approx 0.02 \frac{u_*}{f} \right) \quad (2.2.10)$$

Generally, friction velocity is acquired with fitting procedures, and it is defined as a measure of drag force per unit surface area of the ground. (R. Stull, 2017) On the other hand, the Von Karman constant is a universal dimensionless parameter that is often used with boundary layer turbulence modeling with a value of approximately 0.40. Surface roughness length is the integrational constant that is used to represent terrain influence as the retarder effect of surface roughness elements with respect to their height, shape, and density. In logarithmic law, this length corresponds to the level in a vertical direction where mean wind speed is zero and approximately equals 1/30 of the height of the roughness elements in laboratory measurements. (Kaimal & Finnigan, 1994) Typical roughness heights are classified and provided for different terrains by building codes/standards and studies in literature, with relatively different values and terrain definitions. Engineering Science Data Unit (ESDU) provides typical values for surface roughness height within the data items (ESDU 82026, 2002; ESDU 84011, 1993; ESDU 85020, 2001). Besides, even if it is not given here, ESDU 84011 (1993) also depicts these values and their terrains with several figures, while ESDU 82026 (2002) comes up with a more comprehensive table that comprises a range from  $10^{-5}$  m to 10 m for this parameter with detailed landscape description.

Table (2.1) introduces Davenport's roughness classification (Alan G. Davenport, 1960) that was later revised by Wieringa (1992), according to a considerable amount of field experiments.

Table 2.1 Davenport’s roughness classification revised by Wieringa (1992)

$z_0$ (m)	<i>Classification</i>	<i>Landscape Description</i>
0.0002	Sea	Open sea or lake (irrespective of the wave size), tidal flat, snow-covered flat plain, featureless desert, tarmac and concrete, with a free fetch of several kilometers.
0.005	Smooth	Featureless land surface without any noticeable obstacles and with negligible vegetation; e.g., beaches, pack ice without large ridges, morass, and snow-covered or fallow open country.
0.03	Open	Level country with low vegetation (e.g., grass) and isolated obstacles with separations of at least 50 obstacle heights; e.g., grazing land without windbreaks, heather, moor and tundra, runway area of airports.
0.10	Roughly open	Cultivated area with a regular cover of low crops or moderately open country with occasional obstacles (e.g., low hedges, single rows of trees, isolated farms) at relative horizontal distances of at least 20 obstacle heights.
0.25	Rough	Recently-developed “young” landscape with high crops or crops of varying height and scattered obstacles (e.g., dense shelterbelts, vineyards at relative distances of about 15 obstacle heights.
0.5	Very rough	“Old” cultivated landscape with many rather large obstacle groups (large farms, clumps of a forest) separated by open spaces of about 10 obstacle heights. Also low large vegetation with small interspaces, such as bushland, orchards, young densely-planted forest.
1.0	Closed	Landscape totally and quite regularly covered with similar-size large obstacles, with open spaces comparable to the obstacle heights; e.g., mature regular forests, homogeneous cities, or villages.
$\geq 2$	Chaotic	Centres of large towns with a mixture of low-rise and high-rise buildings. Also irregular large forests with many clearings.

When table (2.1) is examined, it can be seen that the roughness coefficient increases from open terrains to city centers. Accordingly, by the definitions of surface roughness length and gradient height, one may easily conclude that gradient height and gustiness also increase in the same way with roughness length as represented in figure (2.6). (Cochran & Derickson, 2005; Alan G. Davenport, 1960; Mendis et al., 2007)

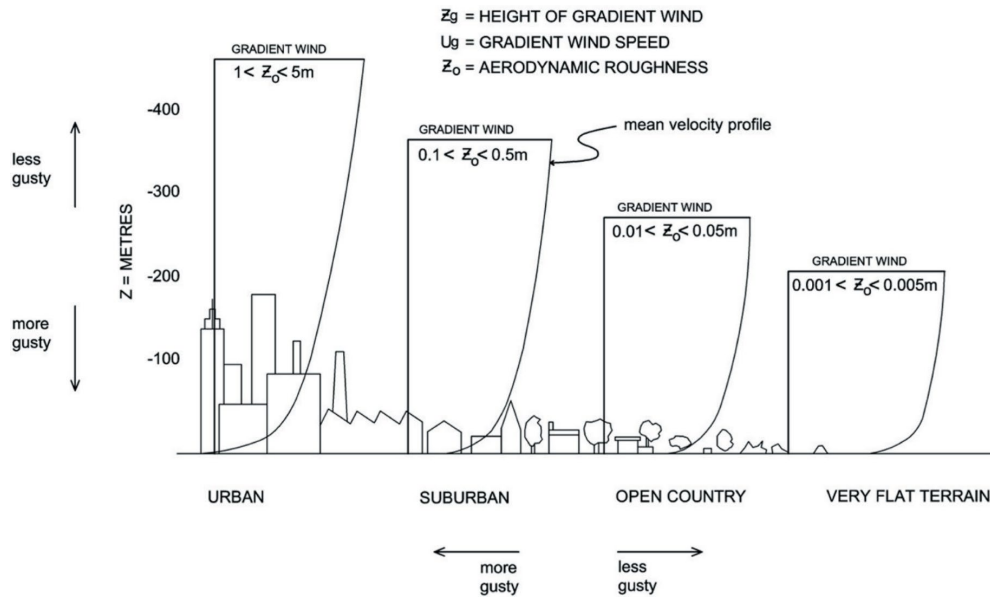


Figure 2.6. Representative mean wind speed profiles for different terrains  
 Note: Reprinted from “Low-rise Buildings and Architectural Aerodynamics” by Authors L. Cochran and R. Derickson, 2005, *Architectural Science Review*, 48:3, 265–276, Copyright by Taylor & Francis

In the case of very rough terrains (i.e., urban areas and forests), equation (2.2.9) is modified to equation (2.2.11) by replacing the height “z” with the effective length  $(z - z_d)$  where  $z_d$  is zero plane displacement. Zero plane displacement depends on the plan-area density of surface roughness elements to account for uncertainties of wind speed predictions due to the complicated behavior of flows between obstacles near ground level. (ESDU 82026, 2002; Holmes, 2001; Simiu & Yeo, 2019)

$$\bar{u}(z) = \frac{u_*}{\kappa} \ln \left( \frac{z - z_d}{z_0} \right) \quad (2.2.11)$$

According to Holmes (2001), zero plane displacement can be taken as about three-quarters of the general rooftop height, while Simiu and Yeo (2019) provide equation (2.2.12) that may be used to achieve reasonable values for it.

$$z_d = \bar{h} - \frac{z_o}{\kappa} \text{ where } \bar{h} \text{ is the general roof-top level} \quad (2.2.12)$$

On the other hand, ESDU 82026 (2002) suggests equations (2.2.13) and (2.2.14) in terms of general height  $H$ ,  $z_0$  and  $\lambda$  based on various wind tunnel experiments.

$$z_d = H - z_0[4.3(1 - \lambda_R) + 10 \exp(-90\lambda_R^{1.5})] \quad (2.2.13)$$

$$z_d = H - 4.3z_0(1 - \lambda_R) \text{ for } 0.2 < \lambda_R < 0.8 \quad (2.2.14)$$

Where,  $\lambda_R$  is defined as the density ratio of ground obstructions that is the ratio of plan area of ground obstacles to the total ground area containing obstacles.

Logarithmic definition of mean wind velocity profile with height is accurately applicable for the neutral atmosphere over a uniform surface, and wind profile differs relatively depending upon other stabilities as shown in figure (2.7). (Kaimal & Finnigan, 1994; R. Stull, 2017)

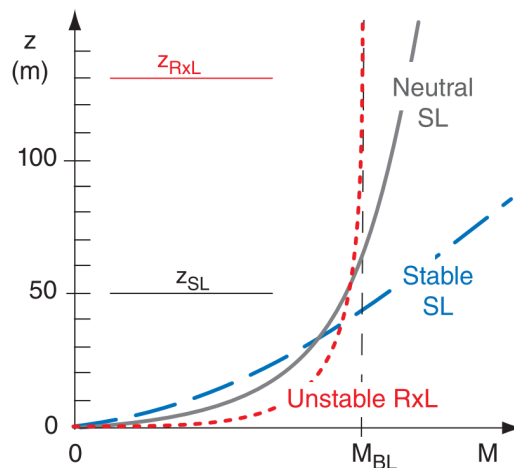


Figure 2.7. Typical mean wind velocity profiles of different stabilities in SL  
 Note: Reprinted from *Practical Meteorology: An Algebra-based Survey of Atmospheric Science* (Version 1.02b, p.700) by Author R. Stull, 2017, Copyright 2017 by Roland Stull, Reprinted under CC BY 4.0

In figure (2.7), R. Stull (2017) defines the bottom of 20% of the convective boundary layer as the radix layer (RxL), and the average wind speed is denoted with  $M_{BL}$ . However, Kaimal and Finnigan (1994) also stated that wind profile for the height of fewer than *10 meters* (generally, reference wind speed measurements are taken at this elevation.) can be defined presumptively with logarithmic formulation regardless of the stability of the atmosphere for most applications.

To consider the effect of atmospheric stability on the mean wind speed profile, equation (2.2.9) is transformed into equation (2.2.15) by adding the stability correction term  $\Psi_s$ , which is a function in terms of the ratio of the height to the Obukhov stability length  $L_s$ . (D. A. Spera, 2009)

$$\bar{u}(z) = \frac{u_*}{\kappa} \ln\left(\frac{z}{z_0}\right) + \Psi_s\left(\frac{z}{L_s}\right) \quad \text{for } z \gg z_0 \quad (2.2.15)$$

It is essential to inform that parameter  $L_s$  is also known as the Monin-Obukhov similarity length in the literature since it forms the basis of the similarity hypothesis proposed by Monin and Obukhov (1954). This hypothesis suggests the formulation of various atmospheric parameters and statistics in terms of buoyancy parameter ( $z/L_s$ ) under normalization of them with appropriate powers of the friction velocity and the scaling temperature. (Kaimal & Finnigan, 1994) Since this thesis study focused on neutral atmospheric boundary layer conditions, no further investigation has been done for other stabilities.

#### 2.2.2.2.2 Mean Velocity Distribution with Power Law

Contrary to logarithmic law, the power-law definition of the mean wind velocity profile is scale-independent and strictly empirical. (Simiu & Yeo, 2019; Thordal et al., 2019) It is a velocity distribution in the vertical direction with no theoretical basis and associated with the reference mean wind speed  $\bar{u}(z_{ref})$  at the reference height  $z_{ref}$  and coefficient  $\alpha$ . (Holmes, 2001; Simiu & Yeo, 2019)

The power-law distribution of mean wind velocity may be formulated as given below with the equation (2.2.16).

$$\bar{u}(z) = \bar{u}(z_{ref}) \left( \frac{z}{z_{ref}} \right)^\alpha \quad (2.2.16)$$

The coefficient  $\alpha$  varies with the range of height, surface roughness, averaging time, temperature, season, time of day, and thermal & mechanical mixing parameters. While the mean wind speed profile obtained by power-law becomes flatter as the averaging time decreases, the velocity with height increases more gradually within the thickening of the affected layer (i.e., gradient height) that results from increasing roughness length, as illustrated in figure (2.8). In other words, the power-law coefficient  $\alpha$  takes an increasing value from open terrains to city centers. (Blocken, 2015; Foken, 2017; Plate, 1971)

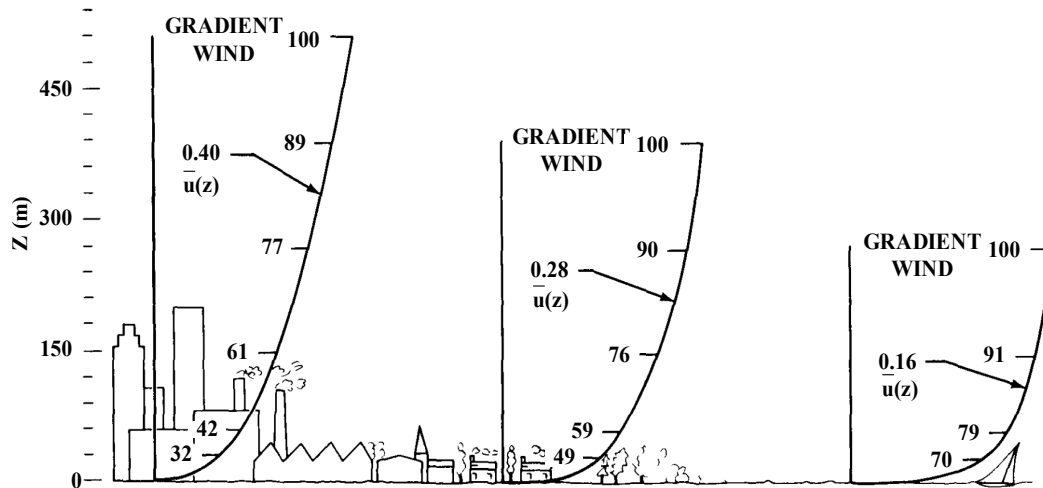


Figure 2.8. Power-law wind speed profiles for different terrains  
 Note: Reprinted from *Aerodynamic Characteristics of Atmospheric Boundary Layers* (p.40) by Author E. J. Plate, 1971, U.S. Atomic Energy Commission, Division of Technical Information

Power law coefficients for different types of terrain gathered by Davenport (1960) based on many experimental studies, measurements, and observations are given in table (2.2) to show the influence of surface roughness on the power-law coefficient.

Table 2.2 Power-law coefficients for different terrains by Davenport (1960)

Landscape Description	$\alpha$
Coastal waters of an inland sea	0.095
Flat shore on “Ocean of Small Islands”	0.121
Open grassland without hedgerows or trees	0.130 – 0.143
Open slightly rolling farmland	0.143
Open level agricultural land with only isolated trees	0.128 – 0.170
Gently rolling grazing land with few trees	0.160
Open fields divided by low stone walls and hedges	0.170
Rough coast	0.200
Gently rolling country with many bushes and small trees	0.220
Relatively level meadowland but with numerous hedges and trees around the small fields	0.230
Level country uniformly covered with scrub oak and pine to the height to a height of 9.144 meters	0.250 – 0.345
Wooded and treed farmland	0.357
Centre of a large city	0.357 – 0.625

In order to calculate the coefficient  $\alpha$ , several relationships considering the parameters in the logarithmic/linear law have been suggested in the literature, and this approach is physically more correct, according to numerous studies. However, since these relationships come with complicated approximations that lead to a reduction in simplicity and directness of the power law, obtaining a value for this coefficient with best-fit procedures according to the available wind data bearing in mind the empirical nature of the power-law is considered as a practical approach for some specialists. (Manwell et al., 2011; D. A. Spera, 2009) Several empirical relationships that are found in the literature for the determination of coefficient  $\alpha$  are given below.

Counihan (1975) proposed equation (2.2.17) to determine this parameter based on the surface roughness parameter within the interval 0.001 m to 10 m. (Manwell et al., 2011)

$$\alpha = 0.096 \log_{10}(z_0) + 0.016(\log_{10}(z_0))^2 + 0.24 \quad (2.2.17)$$

On the other hand, according to Holmes (2001), the power-law exponent can be associated with surface roughness length and reference height, as given below:

$$\alpha = \left( \frac{1}{\ln(z_m / z_0)} \right) \quad (2.2.18)$$

The height  $z_m$  is the level where both logarithmic law and power law are matched, and it may be taken as either half of the maximum height or the average height in the range where matching is required.

Rather than relating to the surface roughness parameter, Justus et al. (1976) proposed equation (2.2.19) to handle this parameter in terms of reference velocity and reference height.

$$\alpha = \frac{0.37 - 0.088 \ln(\bar{u}(z_{ref}))}{1 - 0.088 \ln(z_{ref} / 10)} \quad (2.2.19)$$

The Spera-Richards model is another relationship proposed by Spera and Richards (1979) for the coefficient  $\alpha$  in terms of surface roughness length and reference wind speed. It was used extensively by researchers at the NASA Lewis Research Center to design large-scale horizontal axis wind turbines (HAWT) as follows. (D. A. Spera, 2009)

$$\alpha = \alpha_0 \left[ 1 - 0.55 \log(\bar{u}(z_{ref})) \right] \quad \text{where} \quad \alpha_0 = (z_0 / 10)^{0.2} \quad (2.2.20)$$

Although it is not given here in detail, alongside those who use logarithmic law with the Monin-Obukhov similarity theory for other stabilities of the atmospheric boundary layer, there are also those who suggested and used modified power-law relations with this theory. (Benoit, 1977; Businger et al., 1971; Irwin, 1979; Panofsky et al., 1960)

Reproducing the mean wind velocity profile for the lower regions of ABL by the logarithmic law is more appropriate than the power-law. (Straw et al., 2000) It is the most accurate mathematical representation in strong wind conditions that leads to

neutral stratification. (Holmes, 2001) However, the power-law provides enough accuracy for engineering purposes (Farell & Iyengar, 1997), and it is more convenient when considering the mathematical characteristics of the logarithmic law. Since logarithmic law is not applicable for heights lower than zero displacement length and the heights such that  $(z - z_d) < z_0$ . (Holmes, 2001; Lateb et al., 2016)

### 2.2.2.3 Variance, Standard Deviation, and Turbulence Intensities

As mentioned in Sub-section (2.2.2), winds that can be quite diverse are formed with three types of flow, either in individual or superimposed form, which are the mean wind, waves, and turbulence. As the name implies, the mean wind is considered relatively constant when considering its slow variations in hourly intervals. On the other hand, waves are linear oscillations with a period of ten minutes or more, while turbulence is irregular, quasi-random, and nonlinear motions with a duration of seconds to minutes. For this reason, unlike the mean wind, characteristic definitions of waves and turbulence that are examined under the perturbation part of the winds become difficult. Several parameters, which are variance, standard deviation, and turbulence intensity, are used as descriptors to deal with this difficulty. (R. Stull, 2017; R. B. Stull, 1988)

Variance (biased) is one of the commonly used statistical descriptors to measure the degree of variability from the mean. For any data set of a turbulence parameter ( $\varphi$ ) that consists of N number of variables, it is obtained as follows:

$$\sigma_{\varphi}^2 = \left( \frac{1}{N-1} \right) \sum_{t=1}^N (\varphi_t - \bar{\varphi})^2 \quad (2.2.21)$$

where  $\varphi_t$  is a data point at a time step  $t$ , while  $\bar{\varphi}$  is the mean value of the data set. All data points in a data set are identical if the variance of these variables equals zero, and it is important to quote that “*velocity variances can exist in all three directions even if there is a mean wind in only one direction.*” (R. Stull, 2017, p.706)

As formulated with the equation (2.2.22), the standard deviation that equals the square root of the variance is another common statistical descriptor. It represents the amount of mathematical dispersion within the data points in a set.

$$\sigma_{\varphi} = \sqrt{\left(\frac{1}{N-1}\right) \sum_{t=1}^N (\varphi_t - \bar{\varphi})^2} \quad (2.2.22)$$

It is also used to obtain turbulence intensity, which is a dimensionless parameter that describes the turbulence level as a measure of the magnitude of fluctuations. Turbulence intensity is defined as the ratio of the standard deviation of a set of wind speeds recorded with a certain duration (i.e., the root-mean-square of the fluctuating components of instantaneous velocities) to the mean velocity at recording height in the main wind direction. (Emes et al., 2016; ESDU 74030, 2010; Holmes, 2001; R. Stull, 2017) The duration mentioned here to calculate the fluctuating component's standard deviation is taken equal to or longer to the period of fluctuations. However, it should be shorter than the periods of other types of fluctuations that arise from the atmosphere's diurnal cycle. Typical lengths of this duration are one hour and ten minutes. (Manwell et al., 2011; Simiu & Yeo, 2019) In accordance with the definitions given in Sub-section (2.2.1), relations (2.2.23) are valid for isotropic turbulence where  $I_u$ ,  $I_v$  and  $I_w$  represent turbulence intensities in each direction, which are longitudinal, transverse, and vertical in order.

$$\sigma_u^2 = \sigma_v^2 = \sigma_w^2 \quad , \quad I_u = I_v = I_w \quad (2.2.23)$$

However, considering the diurnal cycle of ABL, turbulence is anisotropic under many circumstances, and it is formulated as given with the relations (2.2.24).

$$I_u = \frac{\sigma_u}{u} = \frac{\sqrt{\overline{(u')^2}}}{u} \quad , \quad I_v = \frac{\sigma_v}{u} = \frac{\sqrt{\overline{(v')^2}}}{u} \quad , \quad I_w = \frac{\sigma_w}{u} = \frac{\sqrt{\overline{(w')^2}}}{u} \quad (2.2.24)$$

Turbulence intensity varies depending on the roughness length and the mean wind speed profile. It tends to increase as the roughness length of related terrain increases. In contrast with this tendency, it decreases with increasing height until disappearing

near the top of the atmospheric boundary layer. (Counihan, 1975; Holmes, 2001; Leon Lyles et al., 1971; Simiu & Yeo, 2019) If each direction's intensities in anisotropic turbulence are quantitatively compared to each other, in general, the vertical intensity is the lowest while the longitudinal one is the largest. (Counihan, 1975; Holmes, 2001) Besides that, several studies for neutral atmospheric conditions indicate an almost constant relationship between friction velocity and standard deviations calculated from fluctuating components of velocities in each direction near the ground (i.e., in the constant-stress layer). In other words, standard deviations and accordingly turbulence intensities have a constant ratio among themselves at near ground levels. (Counihan, 1975; ESDU 85020, 2001; Holmes, 2001; Leon Lyles et al., 1971) Correspondingly, ESDU 85020 (2001) suggested using empirical relations (2.2.25) that represent these ratios in the neutral atmospheric boundary layer. These relations are provided since they are used very frequently in the literature. Although it is not given in detail, it is possible to find different suggestions for the relationship between intensities in the literature, such as the references (Holmes, 2001) and (R. Stull, 2017).

$$\frac{\sigma_v}{\sigma_u} = 1 - 0.22 \cos^4\left(\frac{\pi z}{2h}\right) \quad , \quad \frac{\sigma_w}{\sigma_u} = 1 - 0.45 \cos^4\left(\frac{\pi z}{2h}\right) \quad (2.2.25)$$

Gradient height is defined as the height above which hourly-mean wind speed is independent of the underlying terrain. It is denoted by  $h$  within the data items 82026 and 85020 provided by Engineering Science Data Unit with the equation (2.2.26) given below.

$$h = \frac{u_*}{6f} \quad (2.2.26)$$

After calculating longitudinal turbulence intensity for the target terrain with the provided relations with (2.2.27), turbulence intensities in both transverse and vertical directions are obtained by multiplying it with computed ratios given in (2.2.25).

$$I_u = \frac{\sigma_u u_*}{u_* u}$$

$$\text{where } \frac{\sigma_u}{u_*} = \frac{7.5\eta \left[ 0.538 + 0.09 \ln \left( \frac{z}{z_0} \right) \right]^p}{1 + 0.156 \ln \left( \frac{u_*}{fz_0} \right)} \quad \text{and} \quad \eta = 1 - \frac{6fz}{u_*}, \quad p = \eta^{16} \quad (2.2.27)$$

#### 2.2.2.4 Probability Density of Random Variations

Turbulent flows such as those occurring in the atmospheric boundary layer comprise random variations that do not recur over time by its nature. (Holmes, 2001) The main reasons for the formation of these variations are the superposition of eddies or vortices (i.e., coherent patterns of velocity, vorticity, and pressure) and the interaction of these eddies with themselves and mean flow. (Holmes, 2001; Kaimal & Finnigan, 1994) They come into existence with many different sizes throughout the flow and never exactly coincide with each other. Therefore, the requirement to use statistical methods to identify sudden changes in wind speed has arisen, and measurements that are taken with the same objective have revealed that the distribution of the magnitude of the wind speed components in the atmospheric boundary layer follows pretty close to the normal or Gaussian probability density. (ESDU 85020, 2001; Holmes, 2001) Although there are some situations at certain levels, especially those below 30 meters, where atmospheric turbulence conflicts with Gaussian probability density, it is usually sufficient to assume the probability density as Gaussian to calculate the wind loads and the reactions of buildings under these loads. (ESDU 85020, 2001) By virtue of this distribution's characteristic bell-shaped structure, which is defined by standard deviation and mean value as given with equation (2.2.28), it is possible to predict the probability of any wind speed occurrence by knowing these two fundamental parameters. (Holmes, 2001)

$$f_u(u) = \frac{1}{\sigma_u \sqrt{2\pi}} \exp \left[ -\frac{1}{2} \left( \frac{u - \bar{u}}{\sigma_u} \right)^2 \right] \quad (2.2.28)$$

### 2.2.2.5 Spectral Structure and Scales of Turbulent Motions

Turbulent eddies are spatially large structures with a specific wavenumber. They can also be described through periodic motions with a specific angular/circular frequency, amplitude, and phase, considering the relationship between spatial scales and frequency scales established by Taylor's frozen turbulence hypothesis. (Kaimal & Finnigan, 1994; Simiu & Yeo, 2019; R. B. Stull, 1988) Large-scale eddies have a lower frequency range than small-scale eddies, while small-scale eddies have a weaker structure. (R. B. Stull, 1988) These eddies, which have a wide range of scales, provide the energy based on their size. They form total kinetic energy of turbulent flow with superposition and strong interaction between them. (Garratt, 1994; Simiu & Yeo, 2019) Large eddies transfer their energy to smaller eddies by generating wind shear zones that also result in the generation of smaller eddies. On the other hand, smaller eddies continue to shrink until they have molecular scales where kinetic energy is converted to heat by viscous dissipation. This process is called *the energy cascade* and forms *the turbulent energy spectrum* itself. (Garratt, 1994; R. B. Stull, 1988)

#### 2.2.2.5.1 Spectral Regions of Energy Spectrum

The energy spectrum of turbulence is divided into two essential spectral regions: the energy-containing range and the universal equilibrium range. (Foken, 2017; Kaimal & Finnigan, 1994) The energy-containing range is the spectral region of low-frequency eddies that have a large part of the turbulent flow's total energy resulting from buoyancy and shear forces. The universal equilibrium range also consists of two subranges, which are the inertial subrange and the dissipation range. The inertial subrange is where energy is delivered to smaller scales without any specific production or dissipation. On the other hand, high-frequency eddies' kinetic energy is converted into heat in viscous forces' dominance throughout the dissipation range. (Kaimal & Finnigan, 1994)

### 2.2.2.5.2 Length, Time, and Velocity Scales of Eddies

Each spectral region, which is part of the energy spectrum, has a different turbulence length scale due to the different sizes of the eddies they contain densely. Turbulence scales are physical measurements that are taken over the sizes of eddies. (Pope, 2000) The sizes of eddies that play a prominent role in identifying flows with high Reynolds Numbers have a wide range limited by both the flow field's dimensions and the diffusive effect of molecular viscosity. (Tennekes & Lumley, 1972) Within the framework of this range, three different length scales, which are the integral length scale, Taylor microscale, and Kolmogorov scale, are used to characterize the size of eddies, as shown in figure (2.9) together with the spectral regions of the energy spectrum.

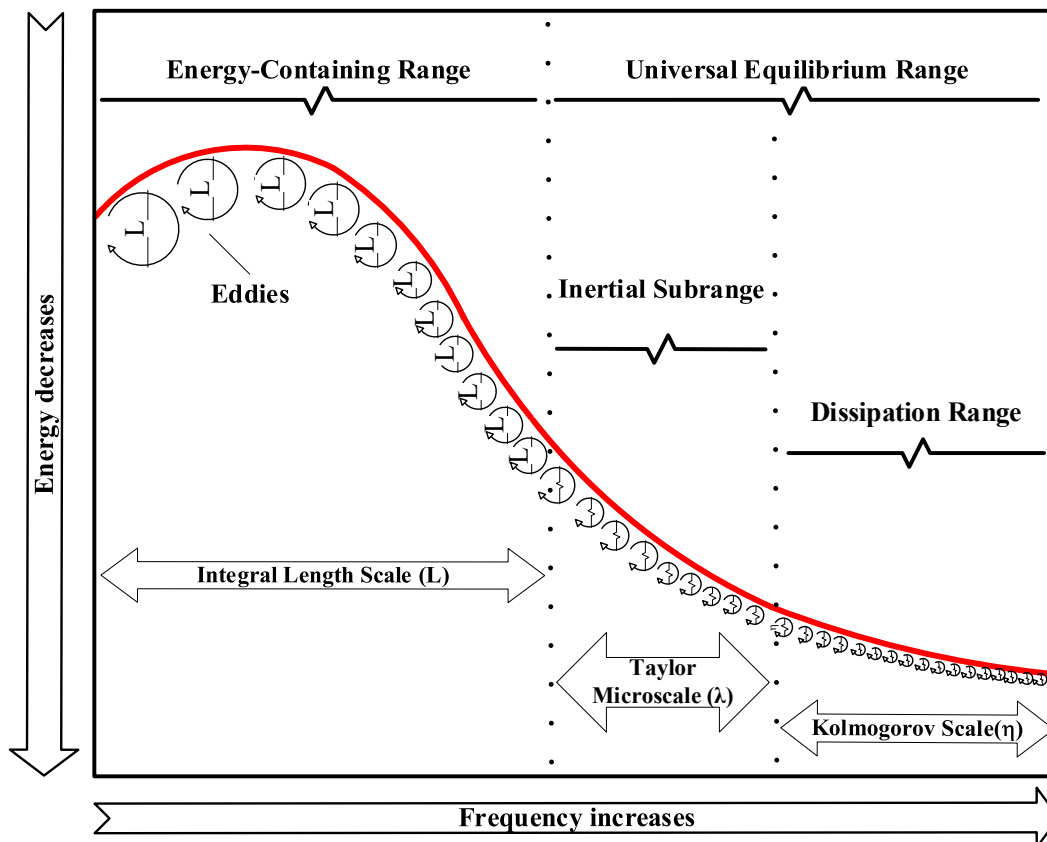


Figure 2.9. Spectral regions of the energy spectrum with their length scales

Large eddies have a characteristic velocity and time scale of their own. These eddies' characteristic velocities are in the same order as the root-mean-square values of the turbulent flow's fluctuating velocity components. (Pope, 2000; Tennekes & Lumley, 1972) This statement also means that large eddies have higher Reynolds numbers; therefore, the direct effect of viscosity on them is negligible. These eddies, which are generally anisotropic, are affected and restricted by the flow field's physical and boundary conditions. (Pope, 2000) Furthermore, since large eddies are as large as the flow field's width, Tennekes and Lumley (1972) propose considering the length scale of these eddies in analyzing the relationship between turbulence and the main flow. Accordingly, the integral length scale ( $L$ ) is used to define both the flow field's width and the average size of the eddies in the energy-containing range as a measure of the flow's largest turbulent eddies. (Kaimal & Finnigan, 1994; Pope, 2000; Simiu & Yeo, 2019; Tennekes & Lumley, 1972) Furthermore, this length scale can be obtained with statistical methods considering large eddies' relationship to the turbulent flow's fluctuating velocity components. (Tennekes & Lumley, 1972)

Unlike large eddies that are unstable and friable, small eddies in the equilibrium range are relatively stable with smaller time scales (i.e., higher frequencies). Thus, they tend to maintain dynamic balance by quickly adapting to the energy transferred by large scale eddies. Additionally, due to the fact that large eddies lose their geometry, which depends on the main flow and its boundary conditions while transferring their energy, small eddies are statistically independent of the mean flow and relatively large-scale turbulent motions. In other words, small-scale eddies or motions have statistically similar properties in all flows that have a high Reynolds number. To define these similar properties under certain assumptions, it is necessary to consider two important processes, which are energy transfer and viscous dissipation, that take place within the energy cascade. The net rate of energy change that depends on the time scale of flow is considerably smaller than the dissipation of energy into heat in small scales. Therefore, the energy supply rate of large eddies

and dissipation rate, which depends on the energy supply, can be assumed as equal to each other. Consequently, small-scale eddies, especially in the viscous dissipation range, can be defined universally with the energy transfer rate and kinematic viscosity. This statement is called Kolmogorov's first similarity hypothesis and forms Kolmogorov's universal equilibrium theory. In accordance with this hypothesis, the length, velocity, and time scales, which are formulated below, are used to characterize dissipative turbulent eddies, and these scales are called Kolmogorov scales. (Pope, 2000; Tennekes & Lumley, 1972)

$$\eta \equiv (\nu^3 / \varepsilon)^{1/4} \quad , \quad u_\eta \equiv (\varepsilon \nu)^{1/4} \quad , \quad \tau_\eta \equiv (\nu / \varepsilon)^{1/2} \quad (2.2.29)$$

The Kolmogorov length scale ( $\eta$ ) describes the smallest turbulent motions in the flow. It is a measure of which eddies with their energies will be converted into heat by molecular viscosity. Additionally, both Kolmogorov length and time scales decrease as the mean velocity increases since these scales depend on the dissipation rate, which is proportional to the velocity in the main direction of the flow. As given with the equation (2.2.30), the Reynolds number of small eddies is always equal to one according to the formulation of Kolmogorov scales. This fact indicates that viscous dissipation adjusts itself through the length scales of small eddies to the energy transferred by larger eddies. In other words, Kolmogorov scales show consistency with the shrinking of eddies down to molecular sizes along the energy cascade. (Pope, 2000; Tennekes & Lumley, 1972)

$$\text{Re}_\eta = (\eta u_\eta / \nu) = 1 \quad (2.2.30)$$

Although large eddies lose some of their energy under the direct effect of viscous dissipation, this loss has a value that can be ignored in flows with high Reynolds numbers. For this reason, the energy transferred by large eddies to the smaller ones is in the same order with the square of their velocity on their scale. Within the scope of Kolmogorov's first similarity hypothesis, using the assumption that the energy transfer rate and dissipation rate are the same, the dissipation rate ( $\varepsilon$ ) can be expressed approximately with the equation (2.2.31). (Tennekes & Lumley, 1972)

$$\varepsilon \sim (u_0^3 / L) \quad (2.2.31)$$

When the equation (2.2.31) is used with the relations given with (2.2.29) for Kolmogorov scales, the ratios of turbulence scales of large and small eddies are as follows, where  $Re$  represents the Reynolds number of the flow.

$$(\eta / L) \sim Re^{-3/4} \quad , \quad (u_\eta / u_0) \sim Re^{-1/4} \quad , \quad (\tau_\eta / \tau_0) \sim Re^{-1/2} \quad (2.2.32)$$

It can be concluded with the relations above that the turbulence scales of small eddies are quite small compared to the turbulence scales of large eddies. The difference between the scales of these eddies increases with the increasing Reynolds number of the flow. Therefore if the flow has a Reynolds number that high enough to produce this difference, eddies that are considerably larger than the Kolmogorov length scale and smaller than the integral length scale occur in the inertial subrange within the transition from large eddies to smaller eddies through the energy cascade as shown in figure (2.10). (Pope, 2000; Tennekes & Lumley, 1972) With this similarity hypothesis, Kolmogorov also states that in each flow with a sufficiently high Reynold number, the eddies' statistical definition in the range covered by the length scale ( $\ell$ ) can be made in a universal way that depends on dissipation rate and independent of kinematic viscosity. However, since the turbulence scales of the eddies within this range cannot be formulated with only the dissipation rate ( $\varepsilon$ ), the time and velocity scales are defined as a function of the length scale of these eddies and dissipation rate as follows. (Pope, 2000)

$$\begin{aligned} \tau(\ell) &= \left( \frac{\ell^2}{\varepsilon} \right)^{1/3} = \tau_\eta \left( \frac{\ell}{\eta} \right)^{2/3} \sim \tau_0 \left( \frac{\ell}{L} \right)^{2/3} \\ u(\ell) &= (\varepsilon \ell)^{1/3} = u_\eta \left( \frac{\ell}{\eta} \right)^{1/3} \sim u_0 \left( \frac{\ell}{L} \right)^{1/3} \end{aligned} \quad (2.2.33)$$

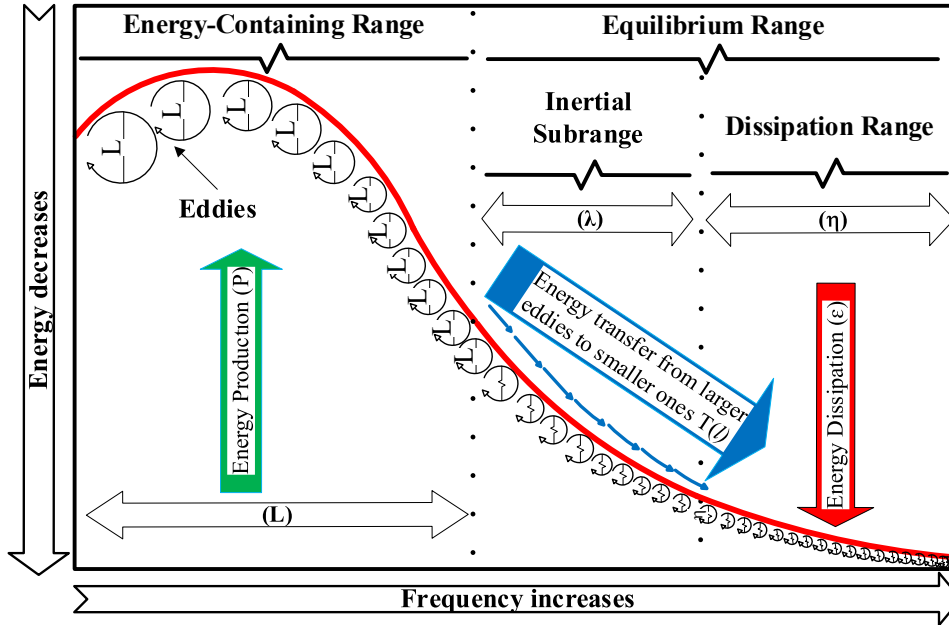


Figure 2.10. Energy cascade in turbulent flows with very high Reynold numbers

Although it does not have a specific physical definition as the integral length scale or Kolmogorov length scale, and it is not a scale on the lengths of eddies of a certain size, another turbulence scale is the Taylor microscale. Even though Taylor defines this scale as the size of the eddies, which responsible for energy dissipation by assuming fluctuating velocity components of the flow as the characteristic velocities of dissipative eddies, the scale that defines the smallest eddies is Kolmogorov scales. In accordance with this assumption, Taylor defined this scale and dissipation rate for isotropic turbulence as follows.

$$\varepsilon = 15\nu(\partial u' / \partial x)^2 \equiv 15\nu(u'^2 / \lambda^2) \quad (2.2.34)$$

According to Tennekes and Lumley (1972), even the value found with the equation (2.2.34) for the dissipation rate is not exactly correct, it gives a favorable estimation of this rate because the eddies in the equilibrium range are almost isotropic within the flows that have high Reynold number. The ratio between the Taylor microscale and the integral length scale may be obtained as given below. (Pope, 2000)

$$(\lambda / L) = \sqrt{10} \text{Re}^{-1/2} \quad (2.2.35)$$

When considering given relations (2.2.32) and (2.2.35), it can be concluded that the Taylor microscale is a scale between the integral length scale and the Kolmogorov length scale. For this reason, the inertial range, which contains eddies that are characterized by both their length scale and dissipation rate, is defined by the Taylor microscale. Furthermore, its relationship with spatial velocity autocorrelations and the use of the Taylor scale Reynold number ( $Re_\lambda$ ) to characterize grid turbulence make this scale also important. (Pope, 2000; Tennekes & Lumley, 1972)

$$Re_\lambda \equiv (u' \lambda / \nu) \quad (2.2.36)$$

### 2.2.2.5.3 Definitions of Wavenumber and Frequencies of Eddies

Wavenumber is a spatial frequency defined as the number of waves per meter or radian per meter as an angular wavenumber. It is formulated as given below for an eddy that has a length scale or size ( $\ell$ ).

$$k_w = \frac{1}{\ell} \quad , \quad k_a = \frac{2\pi}{\ell} \quad (\text{Angular wavenumber}) \quad (2.2.37)$$

On the other hand, frequency ( $f_n$ ) is the number of times that repeating eddies occur at a certain time interval. The frequency and angular frequency of eddies with a period ( $P$ ) at a fixed point are found as given with (2.2.38).

$$f_n = \frac{1}{T} \quad , \quad \omega = \frac{2\pi}{T} = 2\pi f_n \quad (\text{Angular frequency}) \quad (2.2.38)$$

The relationship between the wavenumber of an eddy and its angular frequency can be obtained with Taylor's frozen turbulence hypothesis. This hypothesis states that the frequency components of each fluctuating velocity resulting from the turbulence move unchanged with the flow's mean speed. (Simiu & Yeo, 2019) In other words, Taylor (1938) proposed that velocity fluctuations' sequence at any fixed point taken in the main direction of the flow is formed as a result of the passage of the eddies,

which are carried by mean flow without losing their characteristics and dimensions as shown with the figure (2.11). Hence, an eddy period with a characteristic length scale ( $\ell$ ) is the division of the flow's average velocity by this scale since it is carried by the main flow without losing its properties. (Arany et al., 2015; Simiu & Yeo, 2019) Based on this statement, the relationship between angular wavenumber and angular frequency of an eddy can be expressed as given below.

$$k_a = \frac{2\pi f_n}{u(\ell)} = \frac{\omega}{u(\ell)} \quad (2.2.39)$$

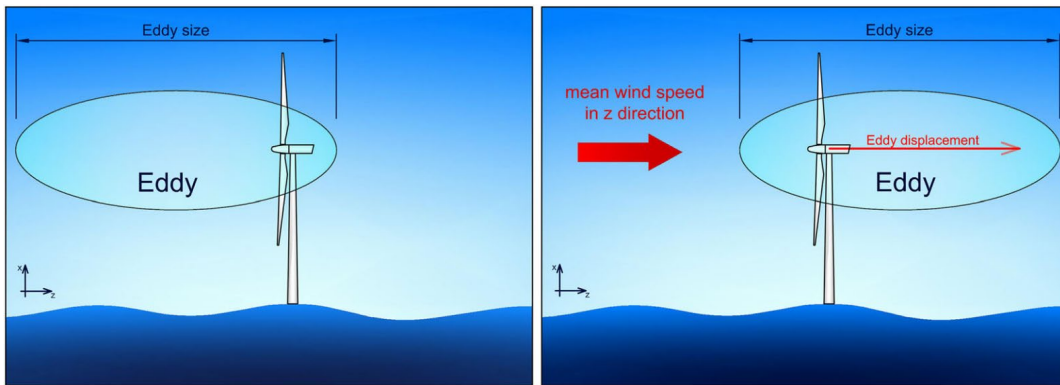


Figure 2.11. Taylor's frozen turbulence hypothesis

Note: Reprinted from "Simplified critical mudline bending moment spectra of offshore wind turbine support structures" by Authors L. Arany, S. Bhattacharya, J. Macdonald, and S.J. Hogan, 2015, *Wind Energy*, 18:12, 2171-2197, Copyright by John Wiley & Sons, Ltd.

Since large eddies have lower frequencies than smaller eddies, they have longer periods and small wavenumbers. The typical frequency range of eddies in the energy-containing range is  $f_n \sim 10^{-4}$  Hz, while eddies in the dissipation range have frequencies between 10 Hz and 30 Hz. (Foken, 2017) Figure (2.12) illustrates representative periodic patterns of eddies according to their wavenumbers and frequencies. Under Taylor's hypothesis, eddies' time and length scales are interrelated to each other within the turbulent flow's mean velocity. (Arany et al., 2015) Therefore an eddy motion can be defined by trigonometric functions that have both wavelength space ( $k_w x$ ) and frequency space ( $\omega t$ ) terms. The term ( $k_w x$ )

defines the harmonic wave when time is constant, while the term  $(\omega t)$  is a harmonic function that describes the motion for a fixed point. (Simiu & Yeo, 2019)

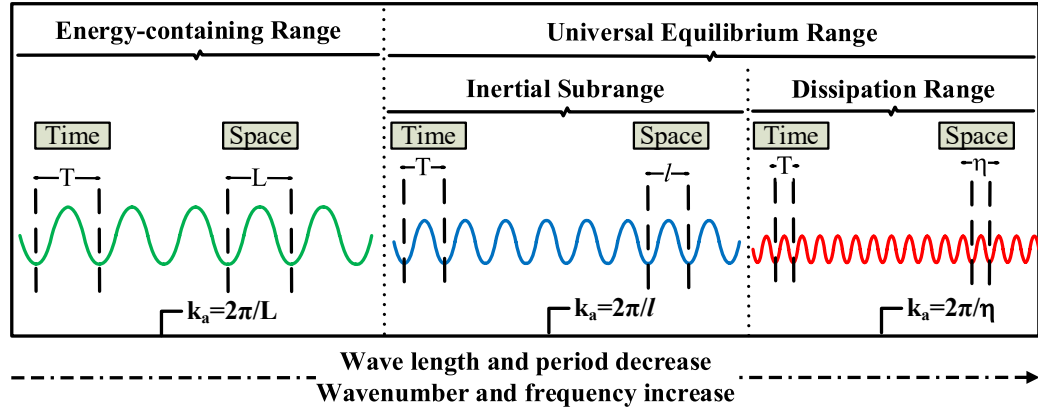


Figure 2.12. Spectral regions with their representative periodic patterns

Moreover, Taylor (1938) proposed that a particular point's turbulence spectrum is associated with the relationship between velocity measurements taken over two points. Therefore, the integral length scale ( $L_u$ ) for along wind direction can be formulated with the integral time scale ( $\tau_u$ ), which is defined by the autocorrelation function ( $\rho_u$ ) of horizontal velocity fluctuations as given in equation (2.2.40).

$$L_u = \bar{u} \cdot \tau_u = \bar{u} \int_0^{\infty} \rho_u(\xi) d\xi = \bar{u} \int_0^{\infty} \frac{\overline{u'(t)u'(t+\xi)}}{\sigma_u^2} d\xi \quad (2.2.40)$$

#### 2.2.2.5.4 Spectral Density Functions for Turbulent Flows

Although the probability density is used to describe the magnitudes of wind speed fluctuations that occur within the energy cascade, this method cannot provide any information about the variations of fluctuations with time. (Holmes, 2001) At this point, the energy spectral density (ESD) functions are used to define the energy variation of turbulent fluctuations with time or frequency in terms of eddy sizes and their relative positions in space. (Holmes, 2001; Simiu & Yeo, 2019)

In isotropic turbulence, the relationships between the spectral structure of fluctuations and their variances are the same in each direction. On the other hand, they are different for each direction in anisotropic turbulence and may be formulated as given below.

$$\begin{aligned}
\sigma_u^2 &= \int_0^{\infty} E_u(k) dk = \int_0^{\infty} S_u(f) df \\
\sigma_v^2 &= \int_0^{\infty} E_v(k) dk = \int_0^{\infty} S_v(f) df \\
\sigma_w^2 &= \int_0^{\infty} E_w(k) dk = \int_0^{\infty} S_w(f) df
\end{aligned} \tag{2.2.41}$$

Furthermore, in dynamic and stochastic analyses that the average power of turbulence in a particular frequency range or domain has importance, power spectral density (PSD) functions may also be used as shown in (2.2.41). These equations are the integration of the spectral contributions of all frequencies in the range from  $f_n$  to  $f_n + df_n$  where power spectral density functions in longitudinal, transverse, and vertical directions are denoted by  $S_u$ ,  $S_v$  and  $S_w$  respectively. (Holmes, 2001) The power spectral density of any wind can be obtained by analyzing the time series of fluctuating wind speed with Fast Fourier Transform (FFT). However, if there is not enough data and cannot be obtained, representative model spectra may be employed, especially in wind energy engineering practices. (Manwell et al., 2011) Although there are many studies and approaches in the literature that try to define the spectral regions of the energy spectrum, frequently-used ones are the Kolmogorov model, Gaussian model, and Von Karman model. These models are shown in figure (2.13) with the spectral regions of the energy spectrum, which they comprised.

The Kolmogorov model is valid only for the inertial subrange, and it is not possible to extrapolate this model to obtain sufficient assumptions for other regions. (Solsvik & Jakobsen, 2016) On the other hand, the Gaussian model has been proposed to describe the energy-containing range and ignores the energy of both inertial and dissipation range. Even if the length scales of eddies in the dissipation range may be

smaller with respect to the filtering length scale used in numerical simulations (e.g., LES/DES), this is not valid for the eddies in the inertial subrange that have the length scale between integral length scale and Kolmogorov scale which is greater than the filtering length scale. Besides, it has been revealed in previous studies that the eddies in the inertial subrange are essential for analyzing wind-induced responses of buildings. On the contrary to these models, the Von Karman model brings a definition to both energy-containing range and inertial range. In addition to this, this model matches with the real turbulence spectrum in the ABL, according to several studies. Consequently, the Von Karman model is more appropriate to take as a target spectrum in numerical simulations. (S. H. Huang et al., 2010). Therefore, the Von Karman wind turbulence model has been selected for this study.

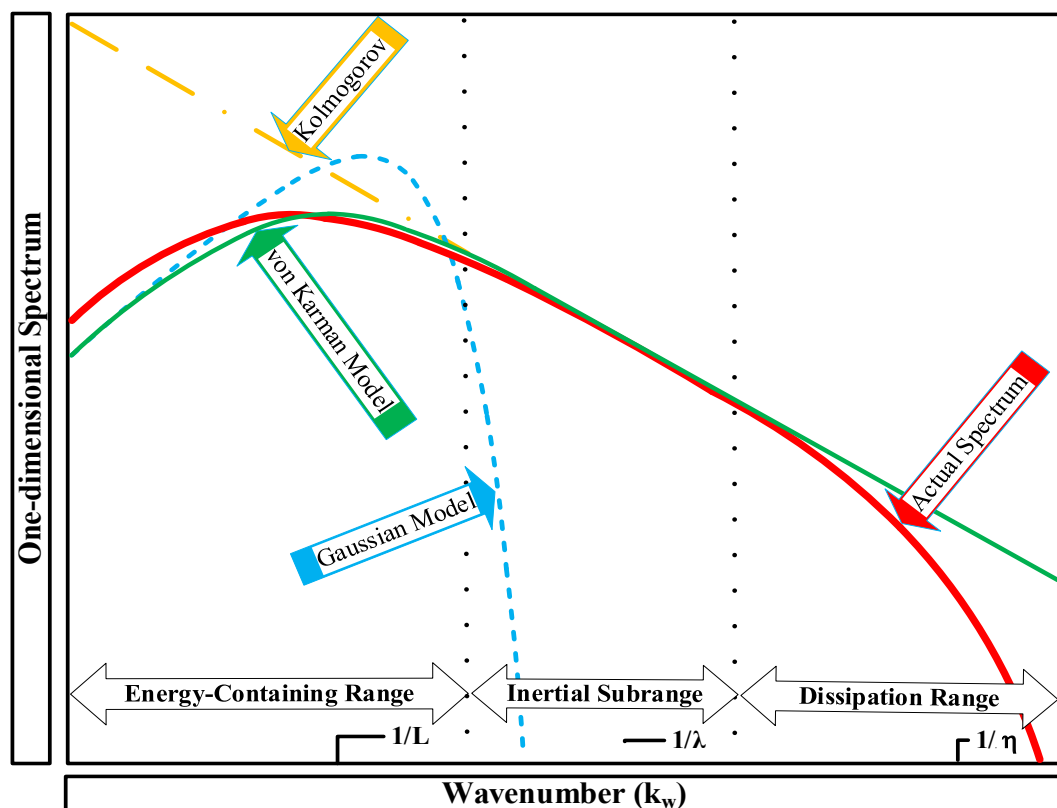


Figure 2.13. Energy spectrum at high Reynolds numbers with spectral models  
 Note: Adapted from “A general inflow turbulence generator for large-eddy simulation” by Authors S.H. Huang, Q.S. Li, and J.R. Wu, 2010, *Journal of Wind Engineering and Industrial Aerodynamics*, 98 (10-11), 600–617, Copyright by Elsevier

Power spectral density (PSD) functions for the fluctuating velocity components of isotropic turbulence are defined by the Von Karman model as follows.

$$S_u(f_n) = S_v(f_n) = S_w(f_n) = \frac{4(I\bar{u})\left(\frac{L}{u}\right)}{\left[1 + 70.8\left(\frac{f_n L}{u}\right)^2\right]^{\frac{5}{6}}} \quad (2.2.42)$$

In the case of inhomogeneous anisotropic turbulence, the spectra of velocity components for each direction are described with the provided equations from (2.2.43) to (2.2.45) where  $\bar{u}$  represents average velocity in the main wind direction at a certain height.  $L_u$ ,  $L_v$  and  $L_w$  are turbulence integral length scales in longitudinal, transverse, and vertical directions in order.

$$S_u(f_n) = \frac{4(I_u\bar{u})^2\left(\frac{L_u}{u}\right)}{\left[1 + 70.8\left(\frac{f_n L_u}{u}\right)^2\right]^{\frac{5}{6}}} \quad (2.2.43)$$

$$S_v(f_n) = \frac{4(I_v\bar{u})^2\left(\frac{L_v}{u}\right)\left(1 + 188.4\left(2f_n\left(\frac{L_v}{u}\right)\right)^2\right)}{\left[1 + 70.8\left(\frac{2f_n L_v}{u}\right)^2\right]^{\frac{11}{6}}} \quad (2.2.44)$$

$$S_w(f_n) = \frac{4(I_w\bar{u})^2\left(\frac{L_w}{u}\right)\left(1 + 188.4\left(2f_n\left(\frac{L_w}{u}\right)\right)^2\right)}{\left[1 + 70.8\left(\frac{2f_n L_w}{u}\right)^2\right]^{\frac{11}{6}}} \quad (2.2.45)$$

### 2.2.2.6 Covariance, Correlation, and Coherence

*Covariance* and *correlation* are two important features in calculating fluctuating wind loads on structures in the atmospheric boundary layer. The velocity covariance used to obtain integral length scales is statistical data belonging to the fluctuating velocity components, which averaged over two different points or heights for a certain duration, and it is defined as given below.

$$\sigma_{u(z_1)u(z_2)} = \frac{1}{T} \int_0^T \left[ \left( u(z_1, t) - \bar{u}(z_1) \right) \left( u(z_2, t) - \bar{u}(z_2) \right) \right] dt \quad (2.2.46)$$

The correlation coefficient of these points given below is calculated in explaining the statistical dependence between these two points, whose covariance is calculated above.

$$\rho = \frac{\sigma_{u(z_1)u(z_2)}}{\sigma_u(z_1)\sigma_u(z_2)} \quad (2.2.47)$$

This coefficient that varies in a range between -1 to 1 means that there is a complete statistical correlation between the fluctuating velocity components taken over the two points when it is equal to one. On the other hand, if it is equal to -1, it indicates a perfect inverse correlation. In brief, this coefficient gives information about how and at what rate the variables taken over two points increase and decrease together. Therefore it can be concluded that there is no statistical dependence when the correlation coefficient is zero. (Holmes, 2001; R. Stull, 2017; R. B. Stull, 1988) It is also possible to define this parameter approximately with the exponential decay function given in equation (2.2.48).

$$\rho \approx e^{-C|z_1 - z_2|} \quad (2.2.48)$$

Where C represents the decay parameter. Considering the above statements with this equation, one may conclude that the statistical correlation increases as the two points get closer to each other. (Holmes, 2001)

In a similar way to the correlation calculation over fluctuating velocities, it is also possible to obtain the correlation of the frequencies, and this measurement is called *coherence*. In other words, it is the frequency-based correlation of velocity fluctuations that are generated by the superposition of eddies that are expressed as harmonic movements with different frequencies. (Holmes, 2001; Simiu & Yeo, 2019) This statistical measurement is expressed with an exponential equation given below. (Holmes, 2001; Manwell et al., 2011)

$$\rho(\Delta z, f_n) = e^{\left(-\left(\frac{C_c \cdot f_n \Delta z}{u}\right)\right)} \quad (2.2.49)$$

Where  $\Delta z$  represents the distance between two points while  $C_c$  is coherence decay constant.

## CHAPTER 3

### COMPUTATIONAL MODELING AND SIMULATION

In this chapter, numerical approaches used in the aerodynamic analysis of tall buildings in the literature are mentioned with the governing equations. It is also aimed to touch briefly on several turbulence generation techniques with their advantages and disadvantages. On the other hand, synthetic turbulence generation methods are covered in more detail with a literature review to clarify why one of the spectral methods called CDRFG is chosen among these methods in this study. Therefore, this chapter is another search that has been performed to get into details of the studies in the literature as a continuation of the theoretical background.

#### 3.1 Governing Equations

The movement of any fluid along with the flow and its interaction with various surfaces or boundary conditions are in accord with the conservation laws of physics. These laws are conservation of mass, conservation of momentum (both linear and angular), and conservation of energy. There is no definite relation between mass conservation, the conservation of momentum, and energy equations since density is constant in incompressible flows. For this reason, such flows can be solved with the mass conservation and conservation of momentum, while energy conservation is important only in flows with heat transfer. (Versteeg & Malalasekera, 2007) Since CWE applications generally take into account incompressible flows, only the laws of conservation of mass and conservation of momentum are mentioned here. (Braun & Awruch, 2009; Simiu & Yeo, 2019)

### 3.1.1 Conservation of Mass

Conservation of mass is the law that states that mass change in any system is zero except for certain fluids such as nuclear reactions, and it is defined as given below. (Jayanti, 2018)

$$\frac{\partial \rho_f}{\partial t} + \nabla(\rho_f \mathbf{V}) = \frac{\partial \rho_f}{\partial t} + \frac{\partial(\rho_f u)}{\partial x} + \frac{\partial(\rho_f v)}{\partial y} + \frac{\partial(\rho_f w)}{\partial z} = 0 \quad (3.1.1)$$

The above expressions are valid for three-dimensional unsteady and compressible flows. In the case of incompressible flows, equation (2.2.50) takes the following form since the density is constant ( $\partial \rho_f / \partial t = 0$ ).

$$\nabla \cdot \mathbf{V} = \frac{\partial u}{\partial x} + \frac{\partial v}{\partial y} + \frac{\partial w}{\partial z} = 0 \quad (3.1.2)$$

### 3.1.2 Conservation of Momentum

Based on Newton's second law, the momentum conservation law implies that the total forces (external) acting on fluid particles are equal to these particles' momentum change rate. (Versteeg & Malalasekera, 2007) External forces acting on fluid particles are divided into two forces: body forces and surface forces. While surface forces such as pressure forces, viscous forces take place in momentum equations with separate terms, body forces such as centrifugal force, gravitational force (weight), Coriolis force, and electromagnetic forces are expressed in source term within these equations. Accordingly, if the momentum increase rate per unit volume of fluid-particle is defined as  $(\rho_f Du / Dt)$ ,  $(\rho_f Dv / Dt)$ , and  $(\rho_f Dw / Dt)$  for each direction in order, then momentum equations are formulated as given with the (3.1.3). (Jayanti, 2018; Versteeg & Malalasekera, 2007)

$$\begin{aligned}
\frac{\rho_f Du}{Dt} &= \frac{\partial(-p + \tau_{xx})}{\partial x} + \frac{\partial \tau_{yx}}{\partial y} + \frac{\partial \tau_{zx}}{\partial z} + S_{Mx} \\
\frac{\rho_f Dv}{Dt} &= \frac{\partial \tau_{xy}}{\partial x} + \frac{\partial(-p + \tau_{yy})}{\partial y} + \frac{\partial \tau_{zy}}{\partial z} + S_{My} \\
\frac{\rho_f Dw}{Dt} &= \frac{\partial \tau_{xz}}{\partial x} + \frac{\partial \tau_{yz}}{\partial y} + \frac{\partial(-p + \tau_{zz})}{\partial z} + S_{Mz}
\end{aligned} \tag{3.1.3}$$

In these equations, while  $(p)$  represents the pressure,  $(\tau_{ij})$  expresses the viscous stress components in the  $i$  direction and acting to the normal surface in the direction of  $j$ . Besides, the source term in the  $i$  direction is denoted by  $S_{M,i}$ . Within this form, momentum equations require additional relations since a total of nine viscous stress components in three directions are unknown. In Newtonian fluids, viscous stresses are proportional to the deformation rates; therefore, Newton's viscosity law that relates the stresses through linear deformations with dynamic viscosity and volumetric changes over secondary viscosity is used. With this law, these viscous stresses are defined as given below. (Versteeg & Malalasekera, 2007)

$$\begin{aligned}
\tau_{xx} &= 2\mu \frac{\partial u}{\partial x} + \lambda \nabla \cdot \mathbf{V}, \quad \tau_{yy} = 2\mu \frac{\partial v}{\partial y} + \lambda \nabla \cdot \mathbf{V}, \quad \tau_{zz} = 2\mu \frac{\partial w}{\partial z} + \lambda \nabla \cdot \mathbf{V} \\
\tau_{xy} = \tau_{yx} &= \mu \left( \frac{\partial u}{\partial y} + \frac{\partial v}{\partial x} \right), \quad \tau_{xz} = \tau_{zx} = \mu \left( \frac{\partial u}{\partial z} + \frac{\partial w}{\partial x} \right), \quad \tau_{yz} = \tau_{zy} = \mu \left( \frac{\partial v}{\partial z} + \frac{\partial w}{\partial y} \right)
\end{aligned} \tag{3.1.4}$$

When these equations are used with the momentum equations, they are called Navier-Stokes equations and formulated as follows.

$$\begin{aligned}
\frac{\rho_f Du}{Dt} &= -\frac{\partial p}{\partial x} + \frac{\partial}{\partial x} \left[ 2\mu \frac{\partial u}{\partial x} + \lambda \nabla \cdot \mathbf{V} \right] + \frac{\partial}{\partial y} \left[ \mu \left( \frac{\partial u}{\partial y} + \frac{\partial v}{\partial x} \right) \right] + \frac{\partial}{\partial z} \left[ \mu \left( \frac{\partial u}{\partial z} + \frac{\partial w}{\partial x} \right) \right] + S_{Mx} \\
\frac{\rho_f Dv}{Dt} &= -\frac{\partial p}{\partial y} + \frac{\partial}{\partial x} \left[ \mu \left( \frac{\partial v}{\partial x} + \frac{\partial u}{\partial y} \right) \right] + \frac{\partial}{\partial y} \left[ 2\mu \frac{\partial v}{\partial y} + \lambda \nabla \cdot \mathbf{V} \right] + \frac{\partial}{\partial z} \left[ \mu \left( \frac{\partial v}{\partial z} + \frac{\partial w}{\partial y} \right) \right] + S_{My} \\
\frac{\rho_f Dw}{Dt} &= -\frac{\partial p}{\partial z} + \frac{\partial}{\partial x} \left[ \mu \left( \frac{\partial w}{\partial x} + \frac{\partial u}{\partial z} \right) \right] + \frac{\partial}{\partial y} \left[ \mu \left( \frac{\partial w}{\partial y} + \frac{\partial v}{\partial z} \right) \right] + \frac{\partial}{\partial z} \left[ 2\mu \frac{\partial w}{\partial z} + \lambda \nabla \cdot \mathbf{V} \right] + S_{Mz}
\end{aligned} \tag{3.1.5}$$

In incompressible flows, the secondary viscosity does not matter since ( $\underline{\nabla} \cdot \underline{V} = 0$ ).

### **3.2 Techniques for Simulating Turbulent Flows in ABL**

Turbulence models are the mathematical approaches or procedures used to analyze or predict turbulent motions and their effects during the energy transfer of eddies and their dissipation into heat. When it comes to simulating turbulent flows, which turbulence model is the appropriate selection depends on the model's precision, consistency, computational cost, discretization scheme, boundary conditions, and target variables of the flow to be analyzed great importance. In other words, turbulence models that differentiate based on modeled and resolved eddy scales are considered advantageous or disadvantageous depending on the problem's definition. (Simiu & Yeo, 2019) Therefore, it is impossible to analyze all turbulent flows with a single model effectively when the mentioned criteria above are considered. Accordingly, in the literature, there are various types of turbulence models that serve their purpose and studies presented with their use. Among these turbulence models, the most frequently used ones are given in figure (3.1) based on their resolving and modeling ranges on the energy spectrum.

#### **3.2.1 Steady and Unsteady Reynolds Averaged Navier-Stokes**

Reynolds Averaged Navier Stokes (i.e., RANS or Steady RANS) model is a mathematical procedure that simulates stationary flows that are not time-dependent by solving the Navier-Stokes equations with the assumption which divides flow variables into two components as mean and fluctuating (i.e., Reynold Decomposition). With this model, all eddies are modeled approximately regardless of their scales, and only average flow values are obtained. (Bensow et al., 2006; Blocken, 2018; Simiu & Yeo, 2019) For this reason, RANS-based turbulence models are inadequate in large-scale unsteady flows, and they are not considered as models

that solve the turbulent flow in a full sense. (Baker et al., 2019; M. F. Huang et al., 2011)

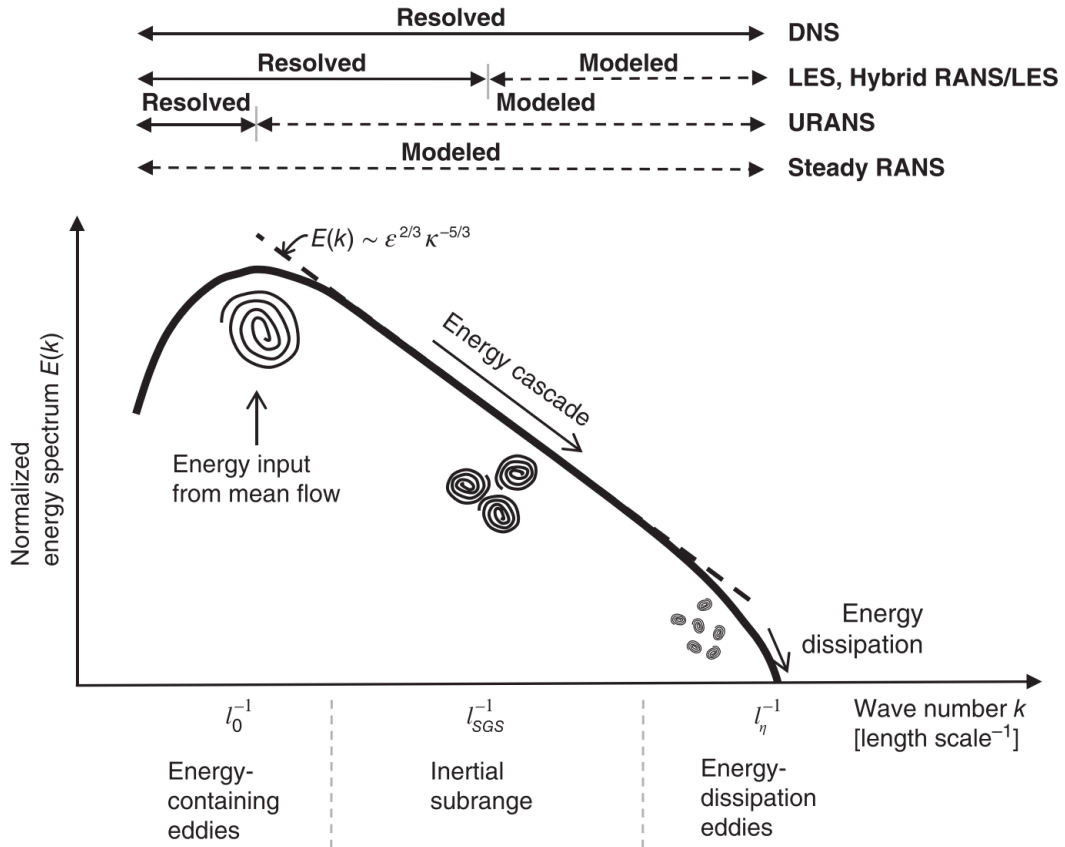


Figure 3.1. Turbulence models based on resolved and modeled scales

Note: Reprinted from *Wind Effects on Structures: Modern Structural Design for Wind* (4th ed., p.141), by Authors E. Simiu and Y. Donghun, 2019, John Wiley & Sons, Ltd. Copyright 2019 by John Wiley & Sons, Ltd.

Unlike Steady RANS, URANS (Unsteady Reynold Averged Navier Stokes) is a model that simulates time and space-dependent flows by adding transient (unsteady) terms to the same governing equations. In other words, URANS simulates time, and space-dependent flows by solving the ensemble-averaged Navier-Stokes equations rather than Reynold averaged ones. (Dagnew & Bitsuamlak, 2013; Salim & Ong, 2013; Simiu & Yeo, 2019) Although URANS models are sufficient to capture large unsteady eddies, they do not provide adequacy in capturing smaller-scale eddies. For this reason, these models have applicability in simulating periodic and semi-periodic flows with generally deterministic character. (Salim & Ong, 2013)

RANS and URANS models require additional differential equations or approaches known as closure models because of the additional unknowns that occur due to averaging over Navier-Stokes equations. These unknowns are called Reynold stresses for the momentum equations. (Blocken, 2018) The closure models that are used for Reynold Stresses are given in figure (3.2). Despite RANS and URANS models' disadvantages, their lower computational cost and simple level applicability compared to other turbulence models make them still frequently used models. (Baker et al., 2019)

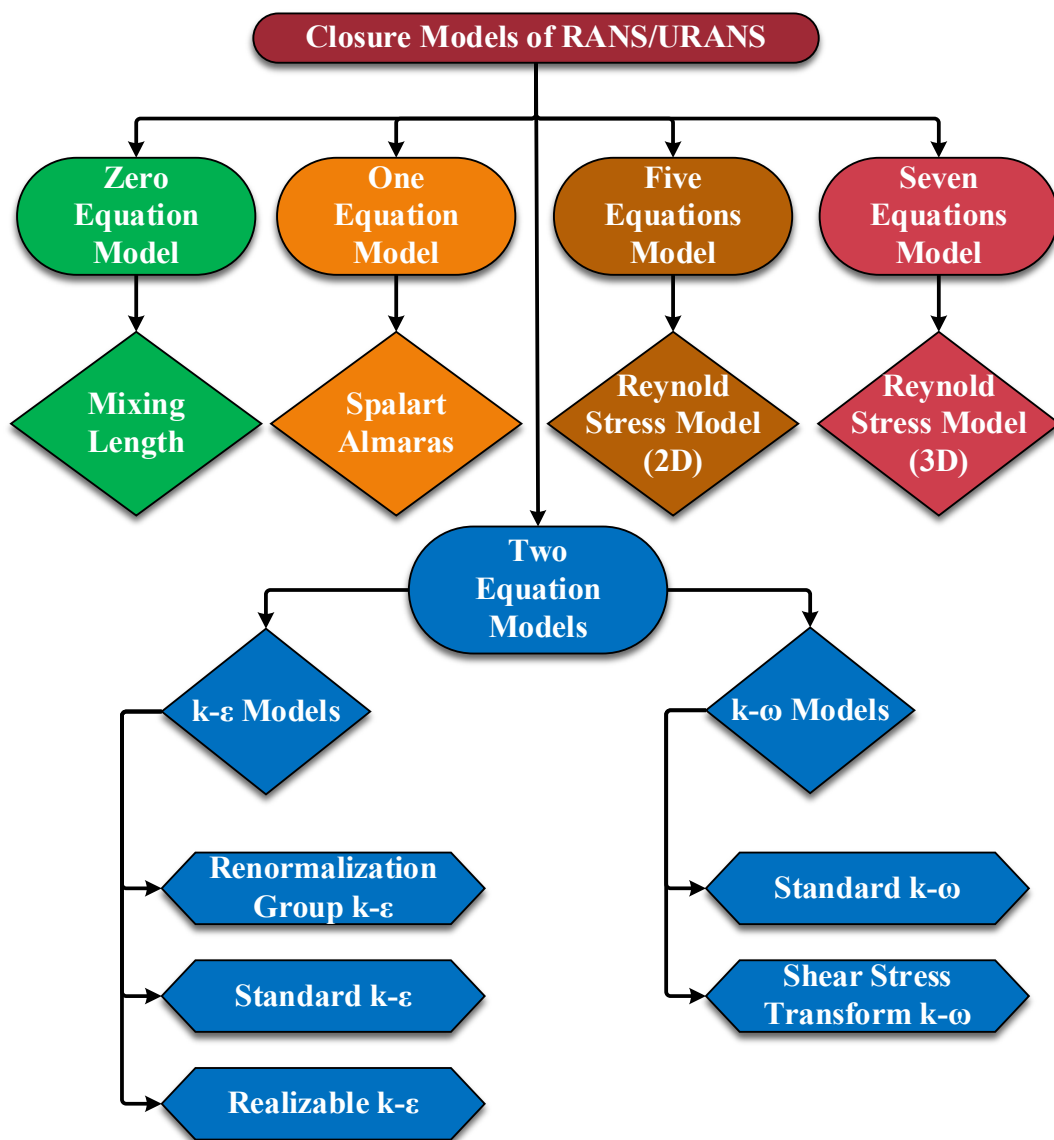


Figure 3.2. Closure models of RANS/URANS

### 3.2.2 Large Eddy Simulation (LES)

As explained earlier in Sub-section (2.2.2.5.2), large scale eddies that provide quite a large part of the kinetic energy of turbulent flow are characterized by the flow's physical and boundary conditions. On the other hand, relatively smaller eddies lose their geometry while transferring their energy. Therefore, smaller eddies are nearly universal in turbulent flows, which means that they are independent of the main flow and boundary conditions (approximately isotropic). Large-eddy simulation (LES) separates these large-scale and small-scale eddies with a certain filter size, which depends on the computational domain's cell size where the flow is simulated. While it resolves the dynamically important large and medium-sized eddies precisely in both time and space with the numerical scheme, the effect of eddies that are smaller than this filter size on resolved eddies is modeled without any resolving procedure. (Baker et al., 2019; Bensow et al., 2006; Blocken, 2018; Simiu & Yeo, 2019) In other words, the turbulence kinetic energy of the flow is analyzed by filtering the instantaneous Navier-Stokes equations, while the dissipation, which is assumed to be less effective, is modeled with the approach called sub-grid scale (SGS). Therefore, as illustrated in figure (3.3), unlike RANS and URANS models, LES offers a more comprehensive approach with reasonable computational cost to analyze unsteady flows. (Bensow et al., 2006; Blocken, 2018; Dagneu & Bitsuamlak, 2013)

SGS models are derived approaches to model additional unknowns called subgrid-scale stresses or residual stresses, which are generated by filtering the Navier-Stokes equations in the LES model. (Blocken, 2018; Dagneu & Bitsuamlak, 2013) Unlike RANS and URANS closure models, SGS models are simpler models since small scale eddies are more homogeneous and universal. (Baker et al., 2019) The standard Smagorinsky SGS model, the simplest single equation model, is the first SGS model introduced by Smagorinsky in 1963. (Baker et al., 2019; Blocken, 2018) Following this model, several models were developed, such as the Dynamic Smagorinsky-Lily subgrid-scale (SGS) model.

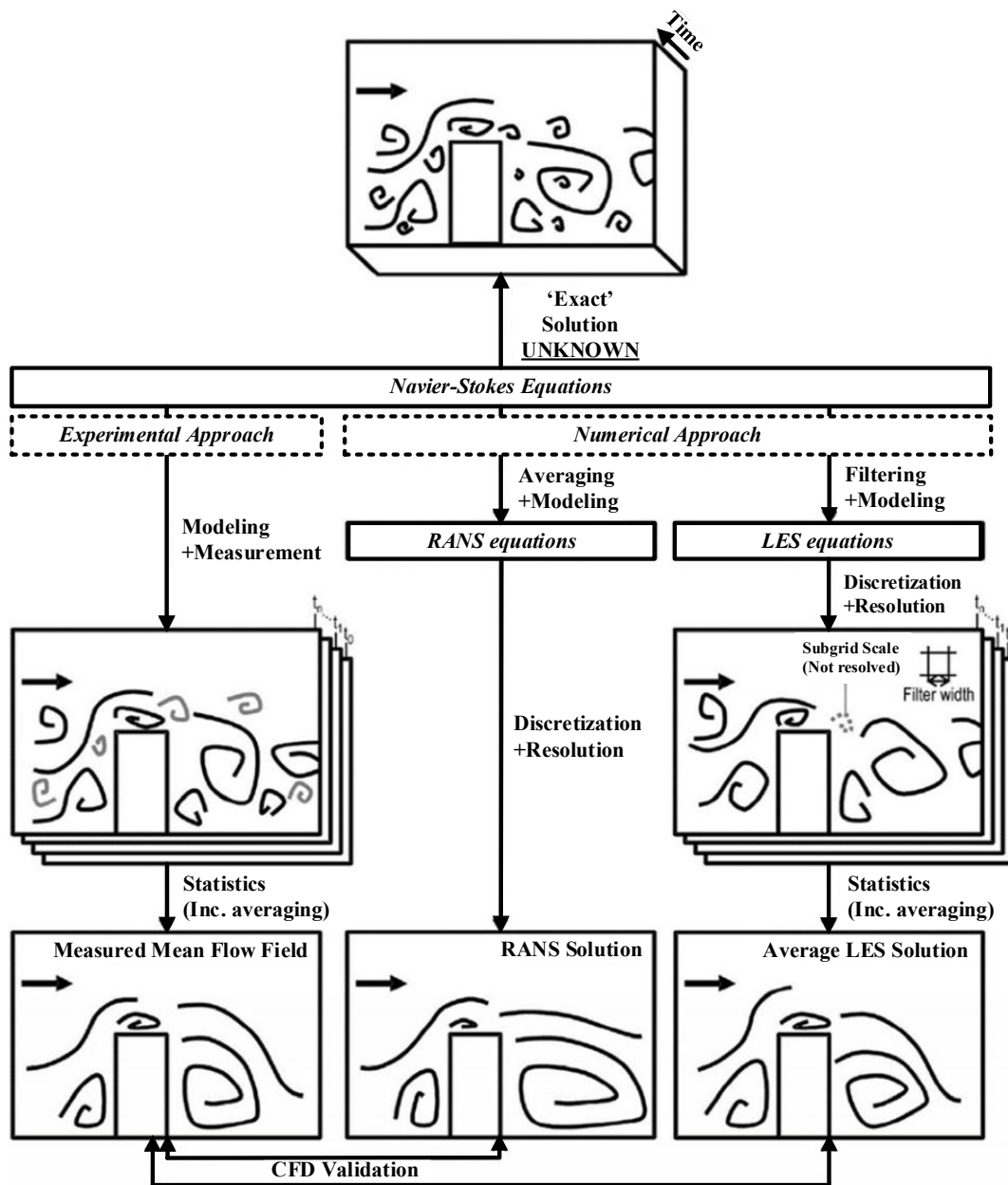


Figure 3.3. Representation of flow captured by experiments, LES, and RANS  
 Note: Reprinted from “LES over RANS in building simulation for outdoor and indoor applications: A foregone conclusion?” by Author B. Blocken, 2018, *Building Simulation*, 11, 821–870, Copyright 2018 by B. Blocken, Reprinted under CC BY 4.0

### **3.2.3 Hybrid Methods: Detached Eddy Simulation (DES)**

Although the LES approach successfully simulates flows with high Reynolds numbers, resolving the turbulent motions near the walls with LES increases computational cost since it requires quite finer mesh and smaller time steps in these regions. (Dagneu & Bitsuamlak, 2013) Consequently, using the LES approach without specific wall treatments reduces its applicability in this kind of flows. For this reason, in order to maintain a balance between solution accuracy and computational cost, hybrid methods have been proposed considering the strengths and limits of RANS/URANS and LES approaches. Hybrid methods are numerical approaches that adopt a RANS or URANS model in regions close to the walls and the LES model in the regions far from the walls.

Detached-eddy simulation, which is one of these hybrid methods, was proposed by Spalart et al. in 1997. DES is a mathematical approach that models the eddies within the boundary layers as attached eddies using the RANS approach with the single equation Spalart-Allmaras closure model and resolves the eddies as detached eddies which are independent of these layers with the LES approach. (Spalart et al., 1997) After the introduction of this approach, many DES models have been proposed with different closure models of RANS. Although hybrid methods have higher computational cost than RANS models, they provide similar accuracy with LES models with a reasonable cost lower than LES, makes these models valuable for this field.

### **3.2.4 Direct Numerical Simulation (DNS)**

Direct numerical simulation (DNS) is an approach that completely solves Navier-Stokes equations for the instantaneous motions of the turbulent flow with all eddy scales up to the smallest ones without any specific assumption and modeling. (Pope, 2000; Simiu & Yeo, 2019) However, since the smallest eddy scales that can be obtained from numerical simulations are equal to the smallest cell size in the

calculation domain to be solved, the smallest cell in this domain should be at least the same as the Kolmogorov length scale. In addition to that, the selected time step should also be smaller than the Kolmogorov timescale. (Baker et al., 2019) Therefore the computational cost will increase significantly as the Reynolds number of the flow increases. For this reason, this model remains an approach that cannot be used to analyze and simulate flows around tall buildings considering the current computer technology with the size of data to be obtained as a result of the simulation of the flow with the finest detail. (Baker et al., 2019; Pope, 2000; Simiu & Yeo, 2019)

### **3.3 Inflow Turbulence Generation Methods**

For RANS turbulence models, average quantities and integral properties with closure models are required at the inlet boundary conditions. (Kröger & Kornev, 2018; Smirnov et al., 2001) In contrast to these approaches, LES, hybrid methods, and DNS require proper inflow boundary conditions that convey the fluctuating details of turbulent motions. (S. H. Huang et al., 2010; Jarrin et al., 2006; Y. Kim et al., 2013; Kröger & Kornev, 2018; Smirnov et al., 2001) Many researchers and studies in the literature emphasize that the inflow boundary conditions are very important in the sensitivity of these models in analyzing flow patterns and turbulent flow statistics. (Aboshosha et al., 2015; Daniels et al., 2013; Elshaer et al., 2016; S. H. Huang et al., 2010; Y. Kim et al., 2013; Melaku et al., 2017; Pamiès et al., 2009; Smirnov et al., 2001; Yang et al., 2020; Yu et al., 2018) In other words, the mean wind speed profiles and turbulence quantities that are not well defined at the inlet/inflow boundary conditions cause unreasonably long execution times and erroneous or insufficient results in predicting the effects of turbulent flow on the target building such as fluctuating pressure values. (Smirnov et al., 2001; B. W. Yan & Li, 2015) Therefore it is essential to provide the necessary conditions for turbulence characteristics such as target spectra, correlations, and intensities for the inflow boundary conditions that match turbulent flows in the atmospheric boundary layer. (Aboshosha et al., 2015; S. H. Huang et al., 2010; Smirnov et al., 2001; Yang et al., 2020; Yu et al., 2018)

However, considering that the data obtained from wind tunnel tests or field measurements are insufficient and the conditions to be met for the inflow boundary conditions have similar nature to the results of turbulent flows that are analyzed, generation of inflow data which includes sufficient conditions for numerical simulations is one of the challenging issues in this field. (Pamiès et al., 2009; B. W. Yan & Li, 2015) Several techniques are proposed to handle this challenge, and they are categorized into three main groups: precursor database method, recycling method, and synthetic turbulence generation method. (Aboshosha et al., 2015; Elshaer et al., 2016; M. F. Huang et al., 2011; Melaku et al., 2017; Pamiès et al., 2009; B. W. Yan & Li, 2015; Yu et al., 2018) On the other hand, these approaches are divided into four main groups with adding wind tunnel replication method according to the Thordal et al. (2019). However, since the wind tunnel replication method is very similar to the precursor database method, this method is mentioned under the precursor database method in this thesis.

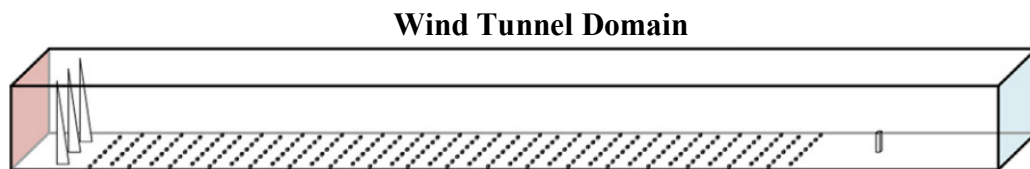
### **3.3.1 Precursor Database Method**

The Wind Tunnel Replication method (WTR) is an approach that generates turbulent inflow data by directly matching upstream conditions of numerical simulation to the upstream conditions of the wind tunnel, including its spires, roughness elements, and the test section as shown in figure (3.4). Therefore this method, which is expressed as the easiest way to create turbulent inflow conditions, gives results close to experimental methods. Nevertheless, it consumes quite a lot of time and computational power since its applicability depends on very fine mesh. (Thordal et al., 2019)

The Precursor Database method is similar to the Wind Tunnel Replication method. The only difference is that the Precursor Database method generates turbulent inflow data in two stages, as illustrated in figure (3.4). It generates the flow similar to the wind tunnels in the precursor domain created on the same basis as WTR while saving time series of upstream flow on a two-dimensional plane as a database that can be

used as turbulent inflow data for numerical simulation. This method's main advantage is that the generated database can also be used later by remapping for similar studies. (Aboshosha et al., 2015; Dagnew & Bitsuamlak, 2013; Thordal et al., 2019; B. W. Yan & Li, 2015; Yang et al., 2020; Yu et al., 2018) Numerical models with this approach also give similar results when comparing with experimental studies, and it has been used frequently in wind engineering applications in the past. (Aboshosha et al., 2015; Thordal et al., 2019; Yu et al., 2018) Moreover, it can be seen as an advantage of this method that it provides sufficient scaling for velocity fluctuations, and the generated database address a very wide range of configurations and flows with different Reynold numbers. (Aboshosha et al., 2015; Pamiès et al., 2009) However, this method has low applicability because it requires very high computing powers and storage capacities if the database is not available for flow that is planned to be simulated. (Aboshosha et al., 2015; Pamiès et al., 2009; Thordal et al., 2019; Veloudis et al., 2007; Yu et al., 2018)

**a) Wind Tunnel Replication Method**



**b) Precursor Database Method**

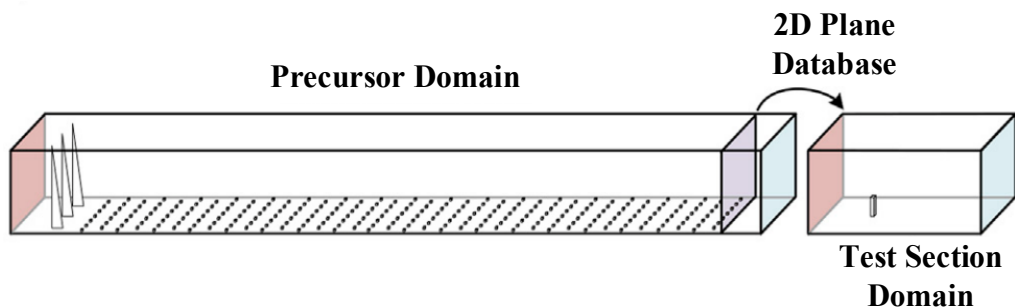


Figure 3.4. Wind Tunnel Replication (WTR) and Precursor Database methods  
 Note: Reprinted from “Review for practical application of CFD for the determination of wind load on high-rise buildings” by Authors M.S. Thordal, J.C. Bennetsen, and H.H. Koss, 2019, *Journal of Wind Engineering and Industrial Aerodynamics*, 186, 155–168, Copyright 2019 by Elsevier

### 3.3.2 Recycling Method

The Recycling method produces turbulent inflow data in two stages, similar to the Precursor Database method. The flow is cycled in the first stage until it reflects similar conditions to the atmospheric boundary layer and becomes statistically stable in the domain called the driver domain or auxiliary domain. (Aboshosha et al., 2015; Dagneu & Bitsuamlak, 2013; Thordal et al., 2019; Yu et al., 2018) This process is realized by rescaling the turbulent velocity components generated in each cycle on the specified recycling plane and remapping these scaled components to the upstream part of the driver/auxiliary domain. (Dagneu & Bitsuamlak, 2013; Thordal et al., 2019; Xiao et al., 2017; Yang et al., 2020) When the flow meets the required conditions, it is used as the inflow boundary conditions of the main computational domain, as shown in figure (3.5). One of this method's advantages is that it generates turbulent inflow data with a relatively shorter calculation domain (driver/auxiliary domain) compared to the Wind Tunnel Replication and Precursor Database methods. (Aboshosha et al., 2015; Thordal et al., 2019; Yang et al., 2020) On the other hand, this method's major disadvantage is that it cannot be used if the shape and distribution of roughness elements are unknown because generated turbulent inflow data strictly depends on these elements used in the driver/auxiliary domain. (Aboshosha et al., 2015; Yu et al., 2018)

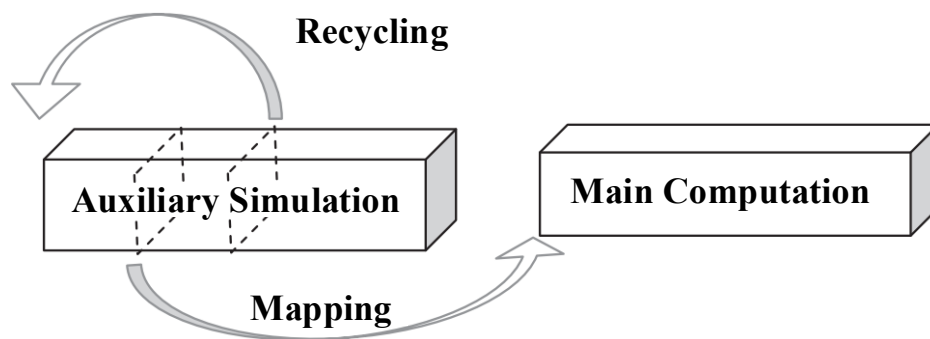


Figure 3.5. Recycling Method

Note: Reprinted from “Consistent inflow turbulence generator for LES evaluation of wind-induced responses for tall building” by Authors H. Aboshosha, A. Elshaer, G.T. Bitsuamlak, and A.E Damatty, 2015, *Journal of Wind Engineering and Industrial Aerodynamics*, 142, 198–216, Copyright 2015 by Elsevier

### **3.3.3 Synthetic Turbulence Generation Methods with a Brief Review**

Synthetic Turbulence Generation methods synthesize artificial fluctuations with statistical properties representing desired atmospheric boundary conditions by performing certain probabilistic/stochastic procedures at reasonable levels of computational cost without solving governing equations of flow. (Jarrin et al., 2006; Kröger & Kornev, 2018; Thordal et al., 2019; B. W. Yan & Li, 2015; Yang et al., 2020) The fluctuating velocity components synthesized by these methods must be spatially and temporally correlated, have the properties of the determined Reynold stresses or length scales, meet continuity condition and accurately convey the target correlation and spectral properties. However, current methods generally do not fully satisfy all of these conditions. (Kröger & Kornev, 2018) The Synthetic Turbulence Generation techniques can be categorized under four sub-groups, which are the Proper Orthogonal Decomposition method (POD), Synthetic-Eddy method (SEM), Vortex method (VM), and Spectral methods. (Yang et al., 2020)

#### **3.3.3.1 Proper Orthogonal Decomposition Method (POD)**

The Proper Orthogonal Decomposition method generates spatially and temporally correlated turbulent inflow data by applying orthogonal decomposition, linear stochastic estimation, and interpolation/extrapolation procedures to the existing turbulent flow data with an insufficient temporal or spatial resolution. This insufficient turbulent flow data is obtained either using particle-image velocimetry (PIV), resulting in low temporal resolution, or using sensors such as hot-wires rakes over a limited number of points resulting in low spatial resolution. (Druault et al., 2004; Johansson & Andersson, 2004) In this method, the signal is divided by using orthogonal decomposition into intrinsic modes representing the energetic events of the flow. By assuming that the reference signals condition the remaining ones, the flow field is estimated using these reference signals with linear stochastic approaches and the knowledge of the two-point correlation. (Druault et al., 2004) However, the

Proper Orthogonal Decomposition method is not a generally applicable approach due to the requirement of data from certain measurements of the flow and the experimental efforts. (Jarrin et al., 2006)

### **3.3.3.2 Vortex Method (VM)**

Although it has been applied in relatively few studies in the literature for tall building's aerodynamic analyses, another method under this group is the Vortex method. This approach produces inflow conditions by adding fluctuations that are determined by the positions and characteristic times of randomly distributed eddies based on the Lagrangian form of the two-dimensional vorticity equations to the average value. The input data required for this method to produce inflow boundary conditions is the average velocity distribution, turbulence kinetic energy, and turbulence dissipation rate that can be obtained through RANS simulations or wind tunnels. (Benhamadouche et al., 2006; B. W. Yan & Li, 2015)

### **3.3.3.3 Synthetic-Eddy Method (SEM)**

Familiar with the Vortex method, turbulent inflow data are produced with the Synthetic Eddy method (SEM) by superimposing randomly distributed synthetic eddies whose spatial and temporal properties are described by characteristic shape functions on the inflow plane. While these formed eddies are carried along the inflow plane until they remain active under certain numerical conditions, new ones are produced when these conditions cannot be satisfied. (Jarrin et al., 2006) Turbulent inflow values produced by this method satisfy first and second-order statistical conditions and autocorrelation functions or, in other words, prescribed average velocity values, Reynold stress tensor, and turbulence scales. The Synthetic Eddy method is a more convenient approach to use with complex geometries with the unstructured mesh, and it has a low computational cost. (Jarrin et al., 2006; Pavlidis et al., 2010) SEM, which was found for LES models by Jarrin et al. in 2006, was

improved to be used in hybrid turbulence models and to satisfy the divergent-free condition in the study conducted by Jarrin et al. in 2009. This approach also has another improved version for LES models proposed by Poletto et al. in 2011 and 2013.

### **3.3.3.4 Spectral Methods**

#### **3.3.3.4.1 Digital Filter Based Methods**

The first example of the Digital Filter method, which is also known as the Filtered Noise method, was proposed by Klein et al. in 2003. As shown in figure (3.6), this approach applies digital linear non-recursive filters to randomly distributed Gaussian white noise to generate turbulent inflow data. Then, it adjusts them with prescribed turbulence length scales to satisfy specified autocorrelation functions at each point by scaling and mapping over filtered regions. (Allegrini & Carmeliet, 2017; Klein et al., 2003; Veloudis et al., 2007) This procedure begins with a random number generation for velocity fluctuations in each direction in a region larger than the inflow plane. Subsequently, the generated region is filtered into sub-regions according to the prescribed turbulence length scales and autocorrelation function. The values in sub-regions are shifted until their mean is zero and scaled until their standard deviation is one. Finally, these values are scaled with turbulence kinetic energy ( $k_{TKE}$ ) to produce velocity fields for each period. (Kempf et al., 2012) Even if Klein et al. (2003) used this method with the Gaussian-based autocorrelation function, there are studies in the literature that used the desired space and time correlations with alternative autocorrelation functions such as exponential ones. (Allegrini & Carmeliet, 2017; di Mare et al., 2006; Y. Kim et al., 2013; Z. T. Xie & Castro, 2008) Due to its nature, this method requires memory that is proportional to the inflow plane's size. (Allegrini & Carmeliet, 2017; Kempf et al., 2012; Veloudis et al., 2007) For this reason, Veloudis et al. (2007) has implemented data interpolation techniques between domain convolution and sequential time steps to

increase the applicability of this method. Similarly, Kempf et al. (2012) eliminated excessive memory requirement, the computational cost and improved this method's parallelization with some modifications.

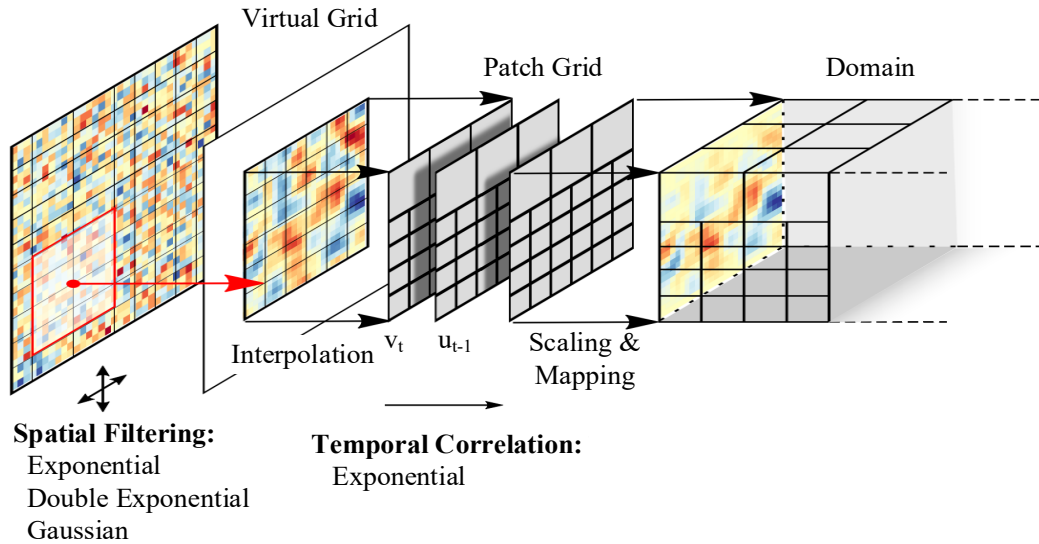


Figure 3.6. Processes of Digital Filter method

Note: Reprinted from “Evaluation of the Filtered Noise Turbulent Inflow Generation Method” by Authors J. Allegrini, and J. Carmeliet, 2016, *Flow, Turbulence and Combustion*, 98, 1087–1115, Copyright 2016 by Springer Nature

The Digital Filter method is a relatively difficult method to use due to the lack of a specific method for obtaining coefficients of filtering, and it requires experience for the input parameters. (Allegrini & Carmeliet, 2017) There are studies conducted by Veloudis et al. (2007), Allegrini & Carmeliet (2017), and especially di Mare et al. (2006) that shed light on these difficulties. Besides, the proposed version of this method by Klein et al. (2003) is not applicable for incompressible flows. (Johansson & Andersson, 2004)

Xie & Castro (2008) proposed a new approach that is easier to couple with large-scale weather codes and more effective than other Digital Filter method-based generators. This method, called ‘XC,’ uses the filtering approach with exponential correlation function to produce only spatially correlated two-dimensional fields, unlike other three-dimensional digital filter method-based approaches, while it correlates these fields with the filtered regions which are generated for the previous

time step. Considering the fact that the filtering process causes the most increase in the computational cost of the Digital Filter Methods, this approach seems more effective. Later, it was modified to satisfy the divergence-free condition by Kim et al. in 2013, and it is named ‘XCDF’ (Xie and Castro’s Divergence-Free method). This condition is met by adapting velocity-pressure coupling procedures without causing an additional increase in the computational cost.

#### **3.3.3.4.2 Fourier Synthesis Based Methods**

Based on the Fourier analysis of harmonic signals, these methods generate turbulent inflow data by superimposing sinusoidal waves of different amplitudes, frequencies, and phases. (Dagnew & Bitsuamlak, 2013; Melaku et al., 2017) Studies of this type began in 1970 after Kraichnan (1970) defined the random flow field with harmonic functions and produced an incompressible, stationary, and isotropic velocity field. Although the requirement arising from the fact that this method proposed by Kraichnan (1970) is not applicable to inhomogeneous and anisotropic flows was tried to be covered with certain filtering and scaling procedures, these procedures increased the computational cost. Therefore, Smirnov et al. (2001) has modified this approach with certain scaling and orthogonal transformation techniques to satisfy this requirement with a reasonable computational cost. They also extended this method to produce turbulent inflow data with target turbulence length and time scales. (S. H. Huang et al., 2010) This modified approach, called Spectral Synthesizer, is used in one of the commercial CFD programs based on the Gaussian spectrum model. (Castro et al., 2011; Thordal et al., 2019) However, since the Gaussian spectrum model is inadequate for numerical simulations, especially for LES with certain conditions as explained in Sub-section (2.2.2.5.4), S. H. Huang et al. (2010) proposed a new synthetic turbulence method that generates spatially correlated turbulent inflow data which satisfies divergence-free condition with any target spectrum, such as the von Karman spectrum model. This approach is called the Discretizing and Synthesizing Random Flow Generation (DSRFG) method.

DSRFG has a highly parallelizable algorithm since it produces turbulent inflow data for each point independently. On the other hand, Castro et al. (2011) pointed out that the DSRFG method was insufficient to produce turbulent inflow data in the desired statistical properties and time correlation. Therefore, they modified this method in a way that preserves prescribed statistical properties with the same computational cost. This modified technique was named Modified Discretizing and Synthesizing Random Flow Generation (MDSRFG) and provides turbulent inflow data that matches the target spectrum better than DSRFG. (Aboshosha et al., 2015; Castro et al., 2011) Aboshosha et al. (2015) emphasized that the coherence between the generated velocities was also very important in maintaining proper correlation within different frequencies, and the spectra of generated turbulent inflow data should be exactly similar to the target flow. Since generated velocities by using either DSRFG or MDSRFG do not satisfy these conditions good enough, they suggested a new approach called Consistent Discrete Random Flow Generation (CDRFG). This method satisfies the first condition by applying an exponential correlation function on frequencies based on A.G. Davenport (1995) instead of a non-frequency approach that DSRFG uses when characterizing spatial correlations and performing the same correlation for each frequency. In addition, CDRFG generates better turbulent inflow data with prescribed spectra than both DSRFG and MDSRFG. DSRFG, MDSRFG, and CDRFG approaches ensure divergent-free conditions by remapping wave numbers with certain procedures. Since these procedures require nonlinear analysis for each point, their computational cost increases as the number of grids for the inflow plane increases. To develop a more effective method to obtain a better match with target spectra by drawing attention to this computational cost, Yu et al. (2018) proposed a Narrowband Synthesis Random Flow Generation (NSRFG) technique. There are several points where this method differs from other methods. The first one is the direct calculation of wave numbers with an approach based on the spatial circular curve's parametric equation to satisfy the divergent-free condition. Using this equation instead of nonlinear equations, which brings an undeniable numerical cost in generation of turbulent inflow data with RFG methods, makes this approach

valuable. The second one is that it defines the velocity field with the trigonometric function of the simple harmonic wave (sinusoidal). In other words, NSRFG generates velocity field with sinus-based harmonic equation, while the RFG methods from Spectral Synthesizer to CDRFG define a velocity field with an equation that includes both sinus and cosine components. If it is thought that trigonometric calculations also lead increasing in computational cost, using a sinus-based harmonic equation increases the effectiveness of this method. Yu et al. (2018) stated that 20% of calculation time for turbulent inflow data generation can be saved using NSRFG after comparing the CDRFG and NSRFG. Besides, this approach is modified to adjust the spatial distribution of the generated velocity field with a target correlation function for each direction rather than one dimension. (For NSRFG, the target correlation function is based on (Hémon & Santi, 2007)) Patruno and Ricci (2017) suggested the Adjusted Random Flow Generator (ARFG) method by drawing attention to the fact that DSRFG does not provide full control over synthesized spectra and the existence of some equations that contradict Taylor's frozen turbulence hypothesis. This method was defined to obtain a direct control over a spectra and integral turbulence scales as a correction for DSRFG. Although ARFG achieved easily this purpose for isotropic turbulent flows, it does not offer the same convenience in generating anisotropic turbulent field. For this reason, in the same study they proposed a new technique called Prescribed-wavevector Random Flow Generator (PRFG) for anisotropic flow fields that differs considerably from the mentioned RFG methods. In 2018, they modified this method to generate velocity field that convey spectral properties of each direction. Modified version of PRFG is a method which satisfies the Taylor's frozen turbulence hypothesis with continuity condition, aims to control all components of the waveform and provides control over all integral scales. Moreover, Patruno and Ricci (2018) stated that PRFG satisfies divergent-free condition together with Taylor's frozen turbulence hypothesis even in generating strong anisotropic turbulent field. However, although good match was achieved between target scales and the integral scales, they emphasized that a serious study is required to validate this method before using in CFD simulations.

## CHAPTER 4

### LITERATURE REVIEW

In this chapter, studies in the literature are categorized into two sub-sections, which are wind tunnel studies and numerical studies. Numerical studies were reviewed by focusing on tall buildings and pioneering studies conducted on bluff bodies to observe the development of numerical models and common trends. Besides, although Sub-section (4.2.2) includes studies on tall building aerodynamics in general, some studies focussed on super-tall buildings, interesting structures, and several turbulence generation techniques are also mentioned. In Section (4.3), some findings from these studies are highlighted, and comments on these studies are given.

#### 4.1 Wind-Tunnel Studies

Various studies conducted in the years between 1900 and 1950 revealed that wind tunnels were not appropriate to simulate natural winds and demonstrated the requirement of proper atmospheric boundary layer flows. The first examples of wind tunnel designs to simulate ABL flows were made in the years between 1955 & 1957, and the construction process of these tunnels was completed in the years between 1960 & 1962. Between the years 1980 and 1995, some of the superior wind tunnel designs and constructions were completed. (Cermak, 2003) Wardlaw and Moss introduced a standard tall building model named CAARC in 1970 to compare the wind characteristics produced with different wind tunnel techniques, develop better approaches as a result of this comparison, and confirm the reliability of the data obtained from the measurements. (Melbourne, 1980) During this period, A.G. Davenport (1971) was measuring the responses of six tall building models with a different shape to the wind. Melbourne (1980) compared measurements of the

surface pressures and responses made on the CAARC standard tall building model conducted by six different facilities from the introduction of the CAARC model to 1975 and stated that these measurements matched with each other with acceptable experimental accuracy. He also attributed the small trends detected in pressure measurements to differences in approaching wind velocities and blockage verification requirements. In 1975, Whitbread obtained forces and base overturning moments on the CAARC building model by using the base-balance technique in his work "*The Measurement of non-steady wind forces on small-scale building models.*" (Alminhana et al., 2018; Obasaju, 1992) Blackmore (1985) conducted a study in order to compare single degree freedom (SDOF) and multi-degree of freedom (MDOF) aeroelastic models by considering responses, which were synthesized from load spectra in strong winds simulated over the CAARC building with a geometric scale of 1:500. He revealed that these aerodynamic models give quite satisfactory results in measuring the dynamic response of tall buildings. Stathopoulos (1985) examined the effects of 45° angle chamfered corners on building models' aerodynamic performance, whose full heights varied from 60 meters to 180 meters with a geometric scale of 1:400. He revealed that chamfered corners significantly reduce the area of strong winds in corner streams compared to original corners. Tanaka and Lawen (1986) compared pressure and dynamic response measurements of the 1:1000 CAARC model to the studies using larger geometric scales. As a result of this comparison, they concluded that there was no certain inconsistency arising from working with small geometric scales as long as the structural and flow parameters were kept consistent. However, they also mentioned the possibility of missing high-suction zones due to the difficulties encountered in pressure measurements on a very small size of the model. Similarly, Goliger and Milford (1988) performed wind tunnel tests with the CAARC model in various scales to investigate scale effects and stated that the geometric scale's effect is negligible on the results. They also indicated that the change in the turbulence intensities generates quite small but more noticeable effects on the results. In addition, the source of the scatter found in the results published by Melbourne (1980)

was attributed to common experimental errors and approaching wind speeds. Obasaju (1992) obtained the mean forces, RMS forces, spectra, and base overturning moments of the 1:250 CAARC building model under different angles of attack, which varied between  $0^\circ$  and  $90^\circ$  to achieve a database to be used for design purposes and defining flows. Ishizaki and Nishimura (1992) examined the basic characteristics of wind-induced vibrations on soft silicone tall building models to observe building deformations and conducted that wind-induced vibrations in tall buildings were caused by vortex shedding. Jamieson et al. (1992) studied the effects of different corner shapes, including beveled, rounded, and recessed types, on peak pressure coefficients of the 1:300 CAARC building model under different wind directions. Khanduri et al. (1998) reviewed and compared the studies about wind-induced interference effects on buildings and argued that more effort should be made on this topic. Kawai (1998) obtained results showing that corner roundness is the most effective way among different types of corners to suppress aeroelastic instability in his study on a 1:600 square prism tall building model (300 m). Similarly, Tamura et al. (1998) acquired detailed results showing that chamfered and rounded corners reduce drag forces in their experiments on the square cylinder model. Thepmongkorn et al. (2002) and Tang & Kwok (2004) examined the effects of interfering building on CAARC building's responses in multiple directions. As a result of their study, Tang and Kwok (2004) revealed that the interference effects and its mechanism directly depend on the separation distance between the two buildings and the primary building location in the wake region. Balendra et al. (2005) used a laser positioning measurement system to measure the wind-induced tip displacement of the 1:375 CAARC building model and relative displacement between two building models directly. Hideyuki Tanaka et al. (2012) conducted wind tunnel tests on several tall building configurations and provided an undeniable contribution to the literature since their study includes 28 different tall buildings models. Zhang et al. (2013) examined the effects of corner recession and double corner recession with various recession ratios on aerodynamic base moments and torque in typical wind directions. Bandi et al. (2013) performed wind tunnel tests on six different tall buildings models

with mainly triangular cross-sections to observe their aerodynamic properties by citing that there are very few studies in the literature examining the aerodynamic characteristics of tall buildings with triangular cross-sections with different configurations. J. Xie (2014) proposed a study based on studies until 2014 to guide the preliminary designs of certain aerodynamic optimizations such as tapering, twist, and stepping applied in super-tall buildings. Y. C. Kim et al. (2015) investigated the effect of building side numbers on the response characteristics for 1:1000 super tall building models (400 m) with 13 different cross-sections. As a result of this study, they concluded that as the number of sides increases, overturning moment coefficients, spectral values and responses decrease. Moreover, they obtained the data revealing that the mean and fluctuating overturning moments are mostly in triangular cross-section models. In contrast, square-section models show the largest spectral values and responses.

## **4.2 Numerical Studies (CFD)**

### **4.2.1 Pioneering Numerical Studies on Aerodynamics of Bluff Bodies**

When the literature is reviewed retrospectively, it can be concluded that numerical procedures for predicting and interpreting aerodynamics of tall buildings are based on studies dealing with the analysis of flow around simple prismatic bluff bodies with Navier-Stokes equations using certain numerical schemes. One of the pioneering studies was conducted with a prototype finite difference method by Hirt et al. (1978) to show that numerical methods have potential in interpreting and predicting the aerodynamics of a prismatic bluff body. In addition, he addressed many challenging issues that limit numerical studies, such as analyzing boundary layers in numerical studies, describing & calculating separation points, defining boundary conditions, the effect of numerical assumptions on the accuracy, numerical stability, Reynolds number of flow, and optimization. Hanson et al. (1982) analyzed the relationship between the flow around sample building model and the building's

heat loss using the Vortex method with the control volume methods and achieved promising results for two-dimensional problems. However, they emphasized that the problem should be handled over three dimensions for realistic simulation. Hanson et al. (1986) studied reverse vortex flow that can be obtained between two buildings by using the control volume method with the wind profile defined by the power-law over three dimensions. One of this study's aims was to achieve results by solving Navier-Stokes and continuity equations with a twenty percent accuracy similar to wind tunnels of that period for simulating full-scale flow. As a result of the comparison between wind-tunnel and obtained results, they showed that similar flows could be simulated numerically with target accuracy. Murakami and Mochida (1988) examined the effect of boundary conditions and mesh resolutions on results by simulating the flow around a cubic model using the  $k - \varepsilon$  turbulence (closure) model. When they compared their results with a wind tunnel, they revealed that the effect of mesh resolution behind the model on wake flow is quite large, and the accuracy of flow simulated by using the  $k - \varepsilon$  model is dependent on the mesh resolution around the target body. They also emphasized that further improvements should be made at many points, including the turbulence model, to increase accuracy. Murakami (1990) evaluated studies conducted in this field and stated that  $k - \varepsilon$  turbulence model was the most successful method for CWE applications at that time. However, it was also concluded that this method is insufficient for flows with separations or recirculation. Hence, he pointed out that using this turbulence method for simulating flows, which are characterized by stagnation, separation, and circulation zones around bluff bodies, shown in figure (4.1), may have serious deficiencies. To make up for this deficiency, it was suggested that different models such as LES and second-order closure models should be developed and expressed that the developing computer technology was promising in carrying out such studies. Moreover, Murakami (1990) addressed the problems frequently encountered in such studies and suggested that the numerical studies should be verified with experimental studies. Selvam (1992) analyzed three-dimensional flow around the Texas Tech Building (9.1x13.7x4m) by employing RANS with  $k - \varepsilon$  model. It is stated that they

found a good match when comparing obtained mean pressure values with the field and wind tunnel measurements. They also investigated the effects of different roughness coefficients on the results and stated that there is no significant difference in results. Since there was no direct calculation procedure for RMS pressure values in RANS approach, RMS pressure values were calculated theoretically. Sakamoto et al. (1993) compared the distributions of several turbulent flow terms, mean vorticity, and vorticity fluctuations obtained by two-dimensional and three-dimensional simulations of a square cylinder by using LES. It was revealed with this comparison that the results of the three-dimensional analysis provided a better match with the experimental results. They emphasized that vortex stretching, which cannot be captured in two-dimensional analyzes of unsteady flows, has great importance, especially on the square cylinder's side surfaces.

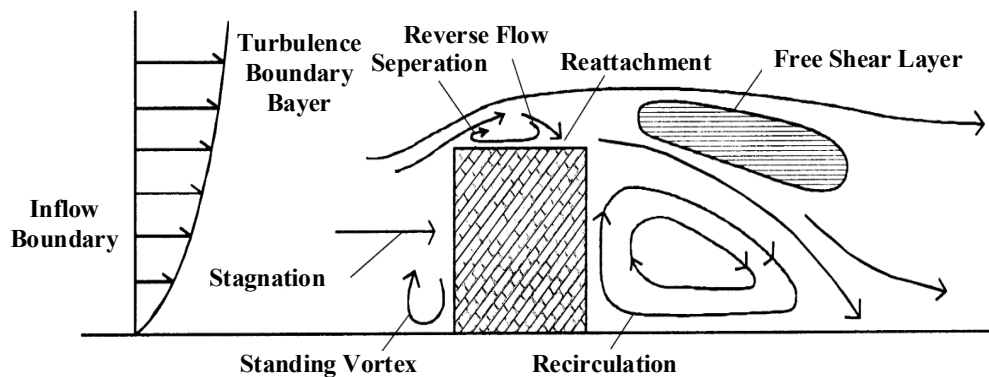


Figure 4.1. Schematic airflow pattern around a bluff body

Note: Reprinted from “Comparison of Various Turbulence Models Applied to a Bluff Body” by Author S. Murakami, 1993, *Journal of Wind Engineering and Industrial Aerodynamics*, 46-47, 21-36, Copyright 1993 by Elsevier B.V.

Mochida et al. (1993) analyzed the flow around Texas Tech Building by using LES and compare obtained velocity and pressure fields with wind tunnel data. It was concluded that LES could provide consistent results in estimating the mean and RMS pressure coefficients. Murakami (1993) compared the results obtained from flows simulated by using three different approaches, which are  $k-\varepsilon$  model, algebraic second-moment closure model (ASM), and LES around the bluff body. As a result of this comparison, he mentioned the shortcomings of the  $k-\varepsilon$  and ASM models.

Moreover, they presented a new model of LES that employs variable Smagorinsky coefficients with this study. Selvam (1996) examined the simulated flows by using  $k-\varepsilon$  and Kato-Launder  $k-\varepsilon$  models around the Texas Tech building and compared the results with existing wind tunnel tests. Although he stated that the two models gave similar results, he also emphasized that the Kato-Launder  $k-\varepsilon$  model provides more closer results to reality. Murakami et al. (1997) focused on problems based on wind-structure interaction and observed that three-dimensional LES approaches provide more accurate and closer results to experimental measurements than RANS models with closure models such as  $k-\varepsilon$ , algebraic stress model and differential stress model. Although they obtained consistent results with experiments in their study on square cylinders under free and forced oscillations, they mentioned that numerical experiments' accuracy was not similar to physical experiments. They attributed this situation to the fact that the physical experiment had no information about spatial pressure distribution compared to the numerical experiment. He and Song (1997) examined roof corner vortex phenomena with flows around Texas Tech building under two different angles of attack, which are  $215^\circ$  and  $225^\circ$  that were simulated by using LES with three different mesh systems. They noticed that numerically obtained mean values were in good agreement with field and wind tunnel measurements. They also emphasized that fluctuating eddies can be resolved at any scale, and RMS values become closer to the experimental measurements if the mesh is finer enough for LES studies. Tsuchiya et al. (1997) proposed a new model called MMK  $k-\varepsilon$  based on the  $k-\varepsilon$  model after emphasizing the erroneous or inadequate results of the standard  $k-\varepsilon$  model in simulating the flow around bluff bodies. They studied the flows simulated by using  $k-\varepsilon$ , revised  $k-\varepsilon$  (i.e., LK  $k-\varepsilon$ ) and MMK  $k-\varepsilon$  models with different wind angles around the low-rise building model and compared results with the wind tunnel. As a result of this comparison, they concluded that LK  $k-\varepsilon$  and MMK  $k-\varepsilon$  models provide better results than standard  $k-\varepsilon$  and that the MMK  $k-\varepsilon$  model gives more accurate results than the LK  $k-\varepsilon$  model at certain aspects such as the average surface pressure distribution. However, they also suggested that the MMK  $k-\varepsilon$  model

should be improved for certain cases, such as roof pressure distribution resulting from conical vortices for oblique wind angles. Tamura et al. (1998) analyzed the simulated flows by using a direct finite difference scheme without using any turbulence model at two different Reynolds numbers around square cylinders with three different corner shapes that are rounded, chamfered, and sharp corners. This study revealed that buildings' aerodynamic performance can be significantly increased if the appropriate cross-section is used. Furthermore, they emphasized that numerical calculations are reliable in estimating simple statistic data due to the computational costs and suggested examining vortex formation and flow structures for very sensitive statistics such as the correlation of unsteady pressures. Murakami (1998) drew attention to the main difficulties encountered in this field of CWE by reviewing the studies conducted using LES and RANS models and mentioned the advantages of the dynamic LES model over the standard LES. He also stated that the revised  $k - \varepsilon$  models overcome some of the problems in the standard  $k - \varepsilon$  model. Tutar and Oguz (2002) conducted a study to analyze flow simulated by using LES around two parallel cubic shape buildings (20m) under different wind directions and configurations. They affirmed that the obtained results were in good agreement with wind tunnel experiments. This study revealed that vorticities' strength decreases as the passage's width between these two parallel buildings with the same height increases. It has been found that the accuracy of the simulated flow depends on building height more than the wind direction and width of the passage. Besides, they emphasized that the RNG sub-grid scale (SGS) model used in this study could be the most suitable model for simulating flows around parallel buildings when considering the flow parameter predictions and flow physics visualizations. However, it was also stated that this model has problems in simulating these flows, especially passage entrance. Nozawa and Tamura (2002) used the LES model to examine flow around a low-rise building. One of the important aspects of this study is that they employed the recycling method, which was developed by Lund et al. (1998) for smooth walls, to generate inflow boundary conditions by improving it for rough walls. They obtained consistent mean pressure coefficients with experimental data in their studies

on several velocity profiles. However, they stated that peak pressure coefficients were underestimated at the corners and attributed this discrepancy to numerical damping, duration of the simulation, and using of small integral length scales. Senthooan et al. (2004) proposed a numerical model that generates velocity fluctuations with stochastic procedures in order to predict pressure fluctuations of bluff bodies. With this numerical model, the average quantities of the turbulent flow are estimated by solving Navier-Stokes equations over three dimensions with the aid of Kato-Launder  $k-\varepsilon$  model while synthetic velocity fluctuations are produced through a stochastic model. The Poisson equation is then solved for the fluctuating pressure field. They used this model to simulate flows around Texas Tech Building with two different wind directions which were  $60^\circ$  and  $90^\circ$ . Although the results showed a small deviation in the re-circulation regions, they stated that mean and rms pressure coefficients in critical regions were in good agreement with experimental results. The reason for the deviation in the re-circulation region was attributed to accuracy of predicted mean flow quantities. Xie and Castro (2006) simulated flows around staggered wall-mounted cubes and staggered random arrays of obstacles at different Reynold numbers by using LES and RANS models. They compared their results with both the DNS results and the wind tunnel test with the same roughness and they concluded that the results obtained from LES provided sufficient results. They also emphasized that if there was a relation between the results and Reynold number, this relation was very weak except solid walls and it was even less than the flows simulated through smooth walls or flows around isolated buildings. Additionally, they concluded that the results obtained with steady RANS provide very similar results with LES for above the canopy, but the results obtained for below the canopy were inadequate compared to LES. Therefore it was stated that unsteady RANS models cannot be applied successfully in such flows due to the absence of significant scale separation and periodicity. Stathopoulos (2006) studied on pedestrian level winds and outdoor human comfort. In this study, the flow was simulated considering temperature and relative humidity parameters around a group of buildings with a geometric scale of 1:200 by using RANS and performing wind

tunnel tests. Although, they could not achieve a good agreement between obtained and experimental results in the wake region, they mentioned that the results were similar to the wind tunnel tests in general. It has been shown that mean velocity values can be obtained in urban regions considering relative humidity and temperature by using CFD techniques with the proposed approach.

#### **4.2.2 Numerical Studies on Aerodynamics of Tall Buildings**

S. Huang et al. (2007) examined flows around CAARC standard tall building using standard  $k-\varepsilon$ , LK  $k-\varepsilon$ , MMK  $k-\varepsilon$  models with RANS and dynamic SGS-LES. After comparing the results of these numerical models with each other and existing seven wind tunnel data, they concluded that the dynamic SGS-LES model provided better results than other approaches in mean pressure coefficients and power spectral densities of wind-induced forces. In cases that require fast solutions, they emphasized that the MMK  $k-\varepsilon$  model gives more accurate results than other RANS models, although MMK  $k-\varepsilon$  also has shortcomings. Another important finding of this study was that described velocity profile, and turbulence intensity parameters in boundary conditions have great importance to obtain results with similar accuracy to wind tunnels. Obtained results indicated that the mean velocity profile affects the mean pressure coefficients, while RMS pressure coefficients are very sensitive to turbulence intensities. Yoshie et al. (2007) conducted multiple comparative studies using standard  $k-\varepsilon$ , modified  $k-\varepsilon$ , and LES models to examine flows around tall buildings with several configurations and predict pedestrian wind environment conditions. This article is one of the studies that form the basis of the Architectural Institute of Japan (AIJ) guideline. After comparing results obtained by numerical approaches with wind tunnel tests, it was found that they were at an acceptable level. Mochida and Lun (2008) reviewed CWE studies' developments and mentioned that the revised  $k-\varepsilon$  models give more accurate results than the standard  $k-\varepsilon$  model, but all  $k-\varepsilon$  models are insufficient since they are incapable of resolving the vortex shedding phenomena. Although there is no such problem in the LES model, they

stated that it is necessary to adapt hybrid RANS/LES models to this field due to LES's relatively high computational cost. Nozu et al. (2008) simulated the flow over an entire urban region (Center of metropolitan Tokyo) by employing LES with nested grid technique and geographic information system (GIS) data. Although this study showed that the flow around a target building in urban areas could be simulated using LES, it also revealed the difficulties in applying proper mesh of building in an urban area with an optimum way. Tominaga et al. (2008) compared standard  $k-\varepsilon$ , LK  $k-\varepsilon$ , modified LK  $k-\varepsilon$ , MMK  $k-\varepsilon$ , Durbin  $k-\varepsilon$ , differential stress, and LES models by using them to simulate wind flow around a high-rise building. They revealed that the standard  $k-\varepsilon$  model could not produce reverse flow in roofs and all other revised  $k-\varepsilon$  models overcome this problem. However, they concluded that all  $k-\varepsilon$  models overestimated the reattachment lengths even if the results closest to the experimental data among all  $k-\varepsilon$  models were obtained using the Durbin  $k-\varepsilon$  model. In addition, due to the overestimated results of velocity fluctuations in the lateral direction within the wake region obtained using LES without proper inflow boundary conditions, they observed a lot of vortex shedding behind the building, and some obtained results were incompatible with the wind tunnel data. Tominaga, Mochida, and Yoshie, et al. (2008), as a working group of AIJ, published a guideline for this field based on the data obtained from many experimental and numerical studies. Dagneu et al. (2009) studied the aerodynamic properties of the CAARC building for both isolated and several adjacent building configurations under different velocity profiles with the standard  $k-\varepsilon$ , RNG  $k-\varepsilon$ , and LES models. In their study cases using LES, they achieved results on the building's windward face that were in agreement with the data obtained from literature and wind tunnel tests. On the other hand, this agreement deteriorated on other surfaces. They also stated that the pressure coefficients obtained using  $k-\varepsilon$  models at the stagnation point and flow separation point were predicted higher than normal. In addition, they analyzed the average pressure values on the building surfaces depending on the height and location of the neighboring building and reported differences. Lim et al. (2009) analyzed the flow around the bluff body by using LES with the boundary conditions

which were generated by the Precursor Database method. When they compared the average and RMS surface pressures with wind tunnel data, they stated that they were consistent except for a few regions where the velocity shears high. They concluded that the Precursor Database model and numerical scheme they used are sufficient to capture the turbulent flow's main properties. They also mentioned that the LES approach is the most applicable turbulence model for this type of studies, although it requires appropriate inflow boundary conditions. Xie and Castro (2009) simulated a street-scale flow (DAPPLE site) with LES and the inflow turbulence generation technique developed based on the Digital Filtering method. After comparing their results with the wind tunnel results, it was revealed that defining proper boundary conditions for such studies is very important to obtain accurate results. Dagnew and Bitsuamlak (2010) examined the CAARC building model's aerodynamic properties for isolated and several adjacent configurations by using LES with and without inflow turbulence data. In light of each case's results, it was stated that LES with inflow turbulence data showed better performance and captured the velocity fluctuations faster. Besides, they also concluded that near-wall treatment has also effect the accuracy of numerical simulation. S. H. Huang et al. (2010) proposed the DSRFG synthetic turbulence generation technique for LES and examined the flow around a square cylinder to compare DSRFG with Simirnov's RFG. They stated that better results in many aspects were obtained by using DSRFG than the RFG method and emphasized that proper boundary conditions increase the accuracy of LES. However, they suggested that more efforts should be made to improve the LES models' accuracy because of the limitations of the SGS-LES models and procedures such as wall treatment procedures, which can lead to computational errors. Lu et al. (2012) simulated the flow around a long-span complex roof of the Shenzhen train station by using LES with the DSRFG method and stated that the obtained mean and RMS pressure coefficients were similar to the wind tunnel measurements. Daniels et al. (2013) observed high correlations between surface pressures and local wall-normal forces on the side faces of CAARC building by adopting the LES model and the synthetic turbulence method XCDF. They stated that the obtained mean pressure

coefficients were consistent with other measurements in the literature. In RMS pressure coefficients, they obtained higher magnitudes of fluctuations on the side surfaces, although their numerical approach captured high fluctuations in the building model's rear corners. They mentioned that this situation might be due to the differences in power-law coefficients for defining the mean wind velocity profile, turbulence intensities provided in the inflow boundary conditions which were taken from the literature and employed approaches for Reynold Stress components. Furthermore, it was revealed with this study that inflow turbulence intensities affect pressure fluctuations significantly. In contrast, turbulence integral scales have no significant effect on pressure fluctuations as long as they are within an appropriate range. Montazeri et al. (2013) examined the wind comfort on the balconies of the high-rise Park Tower building (Antwerp, Belgium) with the façade details (balconies, façade skin, etc.) by using RANS with the realizable  $k - \varepsilon$  model. As a result of this study, a new façade concept was proposed to reduce win-induced discomfort and danger in high-rise buildings' balconies. S. Huang et al. (2013) examined wind-induced responses of both the CAARC standard tall building model and the Taipei101 (Taiwan skyscraper with 508m height) building model under conditions of flows at High Reynold numbers by using FSI (Fluid-structure interaction) method, CSD (computational structure dynamics) and CFD solver. They used a dynamic SGS-LES model with DSRFG method for CFD analysis, and stated that obtained results were in good agreement with the experimental and numerical data. Dagneu and Bitsuamlak (2013) reviewed the CFD studies on buildings from many aspects and stated that LES and hybrid RANS/LES models provide more accurate results than other numerical models when comparing with wind tunnel data. They also emphasized that the computational cost of LES models is higher than the BLWT (Boundary Layer Wind Tunnel) tests and that hybrid RANS/LES models have a promising future in the field of CWE. Dagneu and Bitsuamlak (2014) examined aerodynamic performance of CAARC tall building model by using LES with three different inflow boundary layer generation technique that are synthetic method which is based on Smirnov et al. (2001), Recycling method based on Lund

et al. (1998) and synthetic random flow generation method which was explained in this article. They also studied the interference effect on CAARC building with another full height and half height CAARC building models. They concluded that results obtained with synthetic random flow generation method were more accurate than Smirnov's RNG method and Recycling method. Besides, they emphasized that the LES model is a suitable tool for such studies if proper boundary conditions are provided. It was also stated that required simulation time and numerical cost of LES model are still higher than BLWT tests. Yan and Li (2015) used LES with four different inflow turbulence generation techniques, which are the Recycling method, Smirnov's RNG method, Vortex method, and DSRFG method, to examine flow around the CAARC tall building model. They concluded that the DSRFG method's performance is generally more satisfactory and suitable for the LES model in predicting dynamic wind loads on tall buildings. They also argued that in the Recycling method, the driver section or subdomain between the inlet plane and building should be meshed fine enough to produce high-frequency components of the fluctuating velocities and suggested that a suitable wind flow spectrum should be adopted for this method. Aboshosha et al. (2015) used LES with CDRFG which was proposed due to the inadequacies of DSRFG which are explained in Sub-section (3.3.3.4.2), and DSRFG to analyze aerodynamic performance of square cylinder model with similar height of CAARC building. They stated that results obtained by using CDRFG were better compared to the DSRFG. Tominaga (2015) compared steady and unsteady RANS techniques with several closure models which are standard  $k-\varepsilon$ , RNG  $k-\varepsilon$ , realizable  $k-\varepsilon$ , standard  $k-\omega$ , SST  $k-\omega$  and RNG  $k-\varepsilon$  with modified  $k-\varepsilon$  equation for an aerodynamic analyzes on high-rise building model that has 1:1:2 geometric ratios. He concluded that among these closure models with URANS, only SST  $k-\omega$  model can produce unsteady fluctuations behind the building. However, it was also mentioned that this closure model with URANS underestimates the turbulence kinetic energy behind the building and predicts flow separation at the building corners more than normal. Moreover, he also emphasized that traditional RANS models cannot reproduce

energy transfer from large scale fluctuations to small scale fluctuations. Lastly, although they revealed that URANS with RNG  $k-\varepsilon$  model are better than the URANS with SST  $k-\omega$  in the estimation of certain values, they observed that RNG  $k-\varepsilon$  model resulted in longer reattachment lengths behind the building and on the roof than experimental results. Zhang et al. (2015) conducted a study on both aerodynamic and wind-induced vibration on CAARC building by using Zonal Detached Eddy Simulation (ZDES) with DSRFG technique. Although their mean pressure coefficients were in well agreement with experimental data, they observed overestimated rms values of pressure coefficients. Besides, they also concluded that defining proper inflow boundary conditions is very important for these studies. Bazdidi-Tehrani et al. (2016) reviewed inflow boundary generation techniques in detail and compared four different boundary conditions, which were obtained by using the Precursor Database method, Vortex Method, Smirnov's RNG method and without any turbulent field for a flow around a cubic model. They showed that the accuracy of LES is highly dependent on proper inflow boundary conditions. It was also concluded that these techniques have important effects on the flow field's eddy structures, frequency components of velocity fluctuations, and recirculation zones. Elshaer et al. (2016) conducted a study to analyze the CAARC tall building model's aerodynamics with and without surrounding buildings by using LES and CDRFG under the conditions of a wind tunnel experiment performed by Dragoiescu et al. in 2006. After comparing the obtained results with the BLWT data, they stated that more accurate results were obtained than other studies, especially in mean and RMS values on the building's leeward and side surfaces. Moreover, obtained base moment spectra and building responses were in good agreement with experimental data. When they compared the isolated CAARC model and CAARC building with surrounding buildings, they observed that mean pressure forces decreased by 50% or more in the surrounding case, and RMS pressure values increased by an average of 40% compared to the isolated case. Liu and Niu (2016) simulated flow around a high-rise model with a geometric ratio of (1:1:2) by using numerical methods, which were Steady RANS with RNG  $k-\varepsilon$ , LES, and DDES. They observed that all

numerical models could provide mean velocity fields on the building's windward side in good agreement with experimental data. However, they also mentioned that LES and DES models gave closer results to the wind tunnel data on the side surfaces and wake region and attributed the differences between LES and DES models to DES's mode transition. This study also proved that it is also possible to obtain similar accuracy to LES by using DES with lower mesh requirement and computational cost. B. Yan and Li (2016) examined surrounding buildings' effects on a super-tall building, which has a full-scale height of 420 m in Central Hongkong by using LES and DSRFG method. They stated that the obtained results were comparable with wind tunnel and field measurements. It was also mentioned that the DSRFG method could generate turbulent inflow data with prescribed spectra and turbulence properties. Besides, they suggested conducting sensitivity analysis in the empty computational domain because insufficient meshing of the region between the inlet and area of interest may cause low turbulence levels in that area. Elshaer et al. (2017) focused on the effects of urban development on wind-induced forces on tall buildings by using LES and CDRFG. They concluded that mean pressure values decrease and RMS pressure values increase as the density of buildings increases. Although this study seems to be similar to the study conducted by Elshaer et al. in 2016, effects of urban developments were also observed in this study by modeling and comparing the built environments of the Financial District, Toronto in 1980, 2000, and 2015. Melaku et al. (2017) employed LES with DSRFG, MDSRFG, and CDRFG to simulate flows around the CAARC building model and concluded that pressure coefficients obtained with all generation techniques were in good agreement with wind tunnel data. However, as a result of statistical comparison, it was concluded that the CDRFG method matched the spectra with the standard deviation of the fluctuations more precisely than other models. Moreover, he suggested investigating parameters that differ for these inflow turbulence generation techniques to control velocity fields, and their effects on flow in more detail. B. W. Yan and Li (2017) carried out both wind tunnel tests and numerical simulations with three different approaches which are STT  $k-\omega$  with DES, S-A with DES and SGS-LES in order

to analyze the effects of wind on the aero control tower structure that has an elliptical cross-section and height of 114 meters. In generation of inflow boundary conditions, they used WAWS (Weighted Amplitude Wave Superposition) method together with recycling method to avoid improper turbulence levels in the upper regions of the computational domain where the recycling method is insufficient to create proper turbulence levels. They also investigated the effect of surface roughness in their study cases with DES. They mentioned that they achieved proper inflow boundary conditions with the combination of WAWS and Recycling method and obtained mean pressure values by either DES or LES were in good agreement with wind tunnel test except visible differences in negative mean pressure values. On the other hand, all calculated fluctuating pressure values were overestimated compared to the experimental data. They emphasized that the negative pressure values in the separation region decreased when the surface roughness was taken into account, while the effect of different roughness values on the results was not very important. Yu et al. (2018) simulated flow around a CAARC standard tall building model by using both CDRFG and NSRFG methods with LES. They concluded that obtained mean pressure coefficients either by using CDRFG or NSRFG with LES were in good agreement with experimental data. When the RMS pressures were examined, they stated that except for certain inconsistencies, NSRFG method gives better results than CDRFG method. Alminhana et al. (2018) investigated the effects of modified corners which were chamfered and recessed corners on aerodynamic performance of CAARC building under different wind angles of attack by using LES and Fourier based inflow boundary generation technique which was proposed by Davidson in 2007. They stated that obtained responses were very similar to the experimental measurements and revealed that drag and lift coefficients can be decreased significantly with small modifications on the original shapes of the buildings. Ricci et al. (2018) studied the effects of wind angles of attack on high-rise building model (200 m) with a geometric scale of 1:400 by using LES and MDSRFG approaches. They simulated flow under  $0^\circ$ ,  $45^\circ$  and  $90^\circ$  angles of attacks and stated that calculated mean pressure coefficients were in good agreement with wind tunnel

data for all wind directions. On the other hand, they mentioned that obtained fluctuating pressure values were relatively less accurate and they were more erroneous for wind direction of  $45^\circ$  and  $90^\circ$  cases in regions where pressures are small. Meng et al. (2018) stated that the effect of geometric and computational parameters used in CFD simulations on wind pressures had not been studied much and therefore they studied the effects of several parameters such as turbulence models, wind approaching speeds and grid types on wind-induced responses of CAARC building model. They emphasized that among standard  $k-\varepsilon$ , RNG  $k-\varepsilon$ , Realizable  $k-\varepsilon$ , and SST  $k-\varepsilon$  closure models, more accurate results were obtained using Realizable  $k-\varepsilon$  and SST  $k-\varepsilon$  models. They also mentioned that the increase in the wind profile coefficients causes a gradual decrease in the mean pressure coefficients and that the large blockage ratio may cause greater wind pressures on leeward surface of the building. In addition, it was observed that approaching wind speeds and grid types do not affect the distribution of wind pressure coefficients, and motions such as fluid separation, vortex, wake effect, and reattachment are very sensitive to the wind direction. Sharma et al. (2019) investigated interference effects on high rise buildings in tandem arrangement by using DDES and Vortex methods. They performed validation studies on the CAARC building and obtained results which were in good agreement with retrieved data in literature except minor discrepancies. They stated that these discrepancies may arise from differences in generated inflow boundary conditions. It was concluded that presence of second building varies wind conditions surrounding the target building at the pedestrian level. They also defined separation ratio which is calculated by dividing the distance between the two building centers to the building width and investigated that wind conditions are better than isolated case when this ratio is greater than four. Therefore, they suggested that this ratio should be at least four to positioning such buildings. Mohotti et al. (2019) conducted a study on aerodynamic performance of super-tall slender tower with circular cross-section which has a full-scale height of 406 m to compare the results obtained by using RANS with different closure models which were realizable  $k-\varepsilon$ ,  $k-\omega$  and SST  $k-\omega$ . As a result of

this comparison, they concluded that SST  $k-\omega$  with RANS provides more closer results to the wind tunnel data. In addition, when they compared the obtained pressure values with Eurocode-1, they concluded that Eurocode-1 is quite conservative especially for flows at low Reynold numbers. In addition, they stated that pressure values and distributions which obtained based on Eurocode-1 were quite different when compared with numerical and experimental data and suggested that Eurocode-1 should not be used in the analysis of such tall buildings. Although the pressure values which were obtained from full scale CFD analysis with the unchanged Reynold number were not closer considering side suction to the wind tunnel data, they reported that results obtained by matching Reynold number to the wind tunnel scale were in good agreement with the experimental results. They suggested that RANS models should be used in the preliminary design of high-rise buildings only since these models provide time-averaged solution that does not allow to observe instantaneous pressure fluctuations. They suggested to use transient simulation models such as DDES in the investigation of dynamic behavior of buildings and stated that CFD can be used as an effective tool for structural design with correct modeling. As an additional study to that, Wijesooriya et al. (2019) used LES, hybrid ELES (Embedded LES) and DDES models to analyze aerodynamics of same structure and stated that they obtained results by using ELES with lower computational cost which were similar to the results obtained by using LES. Thordal et al. (2020) examined the CAARC building with surrounding buildings under five different wind angles of attack by using LES and Precursor Database method. They stated that obtained mean pressure coefficients were consistent with wind tunnel data for all angles. On the other hand, they also mentioned that there were small inconsistencies in fluctuating pressure values. In addition to this study, Thordal, Bennetsen, Capra and Kragh, et al. (2020) focused on the effect of chamfered and rounded corner modifications on the aerodynamic performance of the CAARC building with more than one angle of attack.

### 4.3 Comments and Inferences About Studies in Literature

When the studies from 1978 to the present are examined, it is seen that numerical studies are progressing and forming with respect to several challenges such as technological possibilities of the current period, defining the chaotic nature of turbulence, high Reynolds numbers of flow, and numerical methods that converge inconsistent results due to the numerical assumptions. Therefore, it is observed that suggestions and comments made on matching results with experimental data and targeted accuracy have changed depending on the period. For instance, when mean pressure coefficients found in numerical studies were examined, it is concluded that mean pressure coefficients on the windward surface of the building were predicted more accurately than other side and leeward surfaces. In these kinds of results, researchers generally mentioned that obtained results were in good agreement with wind tunnel data or field measurements and suggested that numerical methods needed further improvements by mentioning the shortcomings. Especially until the 2000s, RANS with closure models were generally used to simulate flows around bluff bodies, and the deficiencies identified as a result of these models were tried to be remedied. RANS models have been replaced by the LES model from time to time when the computer technologies make the LES model possible to use. Nevertheless, it is seen that RANS models were used in studies up to now for many purposes considering their faster solution performances with lower numerical costs. It is concluded from these studies that RANS models have some drawbacks, such as underestimating TKE behind the building, resolving vortex-shedding phenomena insufficiently, resulting in small deviations in the re-circulation regions and higher prediction of pressure coefficients at the stagnation and flow separations. Besides, energy transfer from large scale fluctuations to small scale fluctuations cannot be reproduced with traditional RANS models. (Tominaga, 2015) Since they provide time-averaged solutions that do not allow to observe instantaneous pressure fluctuations, it is suggested to use RANS models for the preliminary design of high-rise buildings. (Mohotti et al., 2019)

There are also some studies in the 1990s in which researchers used the LES method to overcome the shortcomings of RANS models. Based on the studies examined in Sub-chapter (4.2), in the period from 2000 to 2009, LES models' accuracy was increased with several modifications and frequently used. Besides, it is observed that the importance of inflow boundary conditions on LES accuracy has been revealed with some of the studies, while several studies focused on comparing LES and RANS models. Many studies revealed that LES models provide more accurate and consistent results comparing RANS models. However, some studies suggested that more efforts are needed to increase LES models' accuracy in the following years. With the fact that proper inflow boundary conditions increase the accuracy and performance of LES, lots of studies since 2009 focused on inflow turbulence generation techniques with LES.

Moreover, several inferences have been made in many studies regarding the effects of several properties of the turbulent boundary layer flows on the results of tall building aerodynamics. These inferences are given below in order to highlight them.

- Using small geometric scales does not significantly affect results as long as structural, and flow parameters are used consistently. (Goliger & Milford, 1988; Tanaka & Lawen, 1986)
- Change in turbulence intensity profiles has noticeable effects on the results. (Goliger & Milford, 1988) Describing flow parameters in boundary layer conditions is essential to simulate flows with an accuracy similar to wind tunnels. Mean pressure coefficients are affected substantially by the mean velocity profile, while fluctuating pressure components (i.e., RMS pressure coefficients) are more sensitive to turbulence intensities. Although the mean pressure distribution behind the building mainly depends on the mean velocity profile, it is also affected by turbulence intensities with relatively less dependency. (S. Huang et al., 2007) The distribution of pressure coefficients is not sensitive to the approaching wind speeds and grid types. Fluid separations, vortices, wake effects, and reattachments are directly

affected by the wind direction. (Meng et al., 2018) Once flow parameters are defined for numerical methods, different roughness coefficients affect mean pressure coefficients negligibly. (Selvam, 1992; Yan & Li, 2017)

- The accuracy of flow simulation around a building depends on building height more than wind direction. (Tutar & Oguz, 2002)
- Defining proper boundary conditions for LES studies is very important to obtain accurate results. (Bazdidi-Tehrani et al., 2016; S.H. Huang et al., 2010; Xie & Castro, 2009; Zhang et al., 2015) This statement is also mentioned in Section (3.3) with other reference studies. LES simulations with proper inflow data capture velocity fluctuations faster with better accuracy. (Dagneu & Bitsuamlak, 2010) Inflow boundary generation techniques greatly impact the flow eddy structure, frequency components of velocity fluctuations, and recirculation zones. (Bazdidi-Tehrani et al., 2016)
- DSRFG method provides the most suitable and accurate results with LES to predict dynamic wind loads in tall buildings, among other turbulence generation techniques: Recycling method, Smirnov's RNG method, and Vortex method. (Yan & Li, 2015) CDRFG method gives more precise results than DSRFG and MDSRFG methods considering matching spectra and target flow statistics. (Melaku et al., 2017)
- A large blockage ratio may cause greater wind pressures. (Meng et al., 2018)
- Compared to isolated tall buildings, the mean pressure forces act less on the tall buildings surrounded by other buildings, while RMS pressure coefficients are observed more in these surrounded buildings. (Elshaer et al., 2016)
- Corner modifications of tall buildings such as chamfered and rounded corners reduce drag and lift forces. If appropriate cross-sections are used for buildings, the aerodynamic performance of them increased significantly. (Alminhana et al., 2018; Tamura et al., 1998)

## CHAPTER 5

### METHODS

In the literature review, several studies conducted on tall building aerodynamics by using DES and DES-based models were found between the years 2015 and 2020. These studies seem to be less than the studies which were conducted by using LES and RANS numerical models. Considering that the LES models are still expensive methods computationally and more time consuming than BLWT studies, numerical studies based on DES are of great importance. (Dagneu & Bitsuamlak, 2013, 2014) Therefore, the S-A-based DES model with CDRFG was used in this study to examine both tall building aerodynamics, and performance of DES with one of the synthetic turbulence generation techniques. Besides, to observe the differences between DES and RANS, another simulation has also been performed using RANS with the S-A closure model for each study case. Therefore, in this chapter, the DES numerical model with this closure model is briefly mentioned, and the CDRFG technique is described in detail. In order to show CDRFG technique's accuracy, certain analyses over the synthesized velocity fields for inflow boundary conditions of computational domains are given. Furthermore, the selected tall building model's geometric description, grid discretization strategies, and boundary conditions are also included.

#### 5.1 Description of Numerical Model

As mentioned before in Sub-section (3.2.3), S-A based DES is a hybrid method that uses Spalart-Allmaras one equation eddy viscosity model with RANS mode for the attached boundary conditions and Smagorinsky-type SGS model with LES mode for the regions away from these boundaries. With this approach, the DES model has applicability comparable with RANS models for flows at high Reynold's numbers while analyzing time-dependent 3D turbulent flow motions in a way similar to LES.

(Constantinescu & Squires, 2004) Within this numerical model, Navier-Stokes equations were integrated with the fully-implicit fractional-step method. The viscous sublayer was solved directly without certain wall function by applying sufficiently small grid spacing near the solid walls. The convective terms in the momentum equations were discretized by blending with the fifth-order accurate upwind biased scheme and the second-order central scheme to reduce the level of numerical dissipation that occurs as moving away from the solid walls. The remaining terms and pressure-Poisson equations were handled with second-order central differences. In addition, an alternate direction implicit (ADI) scheme was used to integrate discrete momentum and turbulent model equations in pseudo-time. For further details, one may want to examine the studies conducted by Constantinescu et al. (2011), Constantinescu & Squires (2004), and Koken & Constantinescu (2011).

### 5.1.1 Spalart-Allmaras One Equation Model

Spalart-Allmaras model is an approach based on the formation of turbulent eddy viscosity  $\nu_t$  by the modified eddy viscosity  $\tilde{\nu}$  that is obtained with solving differential transport equation derived by using “*empiricism and arguments of dimensionless analysis, Galilean invariance and selected dependence on the molecular viscosity.*” (Spalart et al., 1992) The transport equation for modified viscosity is formulated as follows. (Koken & Constantinescu, 2011)

$$\frac{\partial \tilde{\nu}}{\partial t} + u^j \frac{\partial \tilde{\nu}}{\partial \xi^j} = C_{b1} \tilde{S} \tilde{\nu} + \frac{1}{\sigma} \left( \nabla \cdot \left( (\nu + \tilde{\nu}) \nabla \tilde{\nu} \right) + C_{b2} (\nabla \tilde{\nu})^2 \right) - C_{w1} f_w \left( \frac{\tilde{\nu}}{d} \right)^2 \quad (5.1.1)$$

Where  $t$  is time,  $\nu$  is molecular viscosity,  $\xi^j$  is the curvilinear coordinate, and  $u^j$  is the contravariant resolved velocity in the  $j$  direction. Turbulent eddy viscosity  $\nu_t$  with damping function  $f_{v1}$  is defined as given with the equation (5.1.2).

$$\nu_t = \tilde{\nu} f_{v1} \quad \text{where} \quad f_{v1} = \frac{\chi^3}{\chi^3 + C_{v1}^3}, \quad \chi = \frac{\tilde{\nu}}{\nu} + 0.5 \frac{k_s}{d} \quad (5.1.2)$$

The turbulence length scale  $d$  is obtained as follows.

$$d = d_{\min} + 0.03k_s \quad (5.1.3)$$

In the above equation,  $d_{\min}$  is the distance to the nearest wall and  $k_s$  is defined as the equivalent roughness height. The magnitude of vorticity  $\tilde{S}$  with the function  $f_{v2}$  is defined with the equation (5.1.4), where  $S$  is the strain rate.

$$\tilde{S} \equiv S + \left( \frac{\tilde{v}}{\kappa^2 d^2} \right) f_{v2} \quad \text{where} \quad f_{v2} = 1 - \frac{\tilde{v}}{\tilde{v} + \tilde{v} f_{v1}} \quad (5.1.4)$$

$f_w$  and  $C_{w1}$  are obtained as provided below.

$$f_w = g_f \left[ \frac{1 + C_{w3}^6}{g_f^6 + C_{w3}^6} \right]^{\frac{1}{6}} \quad \text{where} \quad g_f = r + C_{w2}(r^6 - r) \quad \text{and} \quad r \equiv \frac{\tilde{v}}{\tilde{S}\kappa^2 d^2} \quad (5.1.5)$$

$$c_{w1} = \frac{C_{b1}}{\kappa^2} + \frac{1 + C_{b2}}{\sigma} \quad (5.1.6)$$

The coefficients which are used in the above procedure are given in table (5.1).

Table 5.1 Model constants

Coefficient	$C_{b1}$	$C_{b2}$	$C_{v1}$	$\kappa$	$\sigma$	$C_{w2}$	$C_{w3}$
Value	0.135	0.622	7.1	0.41	0.67	0.3	2.0

### 5.1.2 Spalart-Allmaras Based Detached Eddy Simulation

The formulation of the Spalart-Allmaras based DES model is obtained by using the modified length scale  $d_{DES}$  as described in (5.1.7) instead of the turbulence length scale  $d$ , which is used in the production and destruction parts of the Spalart-Allmaras one equation closure model.

$$d_{DES} = \min[d, C_{DES}\Delta] \quad (5.1.7)$$

In equation (5.1.7),  $\Delta$  is local spacing or grid size, which is defined as follows.

$$\Delta = \min[\Delta x, \Delta y, \Delta z] \quad (5.1.8)$$

Model constant  $C_{DES}$  is taken as (0.65). The prediction of the boundary layer separation is performed in the DES model's RANS mode, and as long as the condition of  $d_{DES} = d$  satisfies, the S-A RANS model is used. As moving away from the wall boundary conditions, the turbulence length scale  $d$  becomes larger than  $C_{DES}\Delta$  so that  $d_{DES} = C_{DES}\Delta$  is provided in these regions, and Smagorinsky eddy viscosity ( $\tilde{\nu} \propto S\Delta^2$ ) is yielded. In these regions, the LES mode of the DES model is used. (Constantinescu & Squires, 2004; Koken & Constantinescu, 2011)

## 5.2 Description of Synthetic Inflow Turbulence Generator

### 5.2.1 Consistent Discrete Random Flow Generation Method (CDRFG)

As described earlier in Sub-section (3.3.3.4.2) with their developmental process, Fourier synthesis – based synthetic turbulence generation techniques generate turbulent flow fields by superimposing sinusoidal waves (i.e., harmonic functions), which have different amplitudes, frequencies, and phases. The fundamental concepts of the logic behind these harmonic functions are explained in Sub-section (2.2.2.5). According to Aboshosha et al. (2015), the Consistent Discrete Random Flow Generation (CDRFG) technique synthesizes the turbulent flow velocity fluctuations at any point in the inflow plane for a certain frequency domain with the harmonic function as given below.

$$u_i(x_j, t, f_m) = \sum_{m=1}^M \sum_{n=1}^N p_i^{m,n} \cos(k_j^{m,n} \tilde{x}_j^m + 2\pi f_{m,n} t) + q_i^{m,n} \sin(k_j^{m,n} \tilde{x}_j^m + 2\pi f_{m,n} t) \quad (5.2.1)$$

If the equation (5.2.1) is examined considering Taylor's frozen turbulence theory, one may conclude that the expression  $(k_j^{m,n} \tilde{x}_j^m)$  defines the eddy motion in the

wavelength space in which the time is constant, while the expression  $(\omega t = 2\pi f_{m,n}t)$  expresses the eddy motion in the frequency space for a fixed point. Besides, while x, y, and z directions are stated by  $j=1, 2,$  and  $3$  in order,  $u_j$  represents along-wind, across-wind, and vertical velocities for  $i=1, 2,$  and  $3,$  respectively.  $x_j$  is the location coordinate in the  $j$  direction where the synthesis process is performed, and time is denoted by  $t$ . In this approach, fluctuating velocity components for a certain segment frequency  $f_m$  are generated by superimposing the contributions of sub-frequencies  $f_{m,n}$  of that segment to these components. Therefore, the frequency domain is formed over  $M$  number of spectral segment frequencies with their sub-domains that contain  $N$  number of random frequencies, as shown in figure (5.1). These random frequencies are picked from normally distributed pseudo-random numbers with zero mean and unit standard deviation for each sub-domain. Then, shifting & scaling procedures are applied such that each sub-frequency set has a  $f_m$  mean and  $\Delta f$  standard deviation. The reason why sub-frequencies have this distribution is mentioned in Sub-section (2.2.2.4). After determining the range of segment frequencies according to represent target spectra, frequency bandwidth  $\Delta f$  is obtained with equation (5.2.2).

$$\Delta f = (f_{\max} - f_{\min}) / (M - 1) \quad (5.2.2)$$

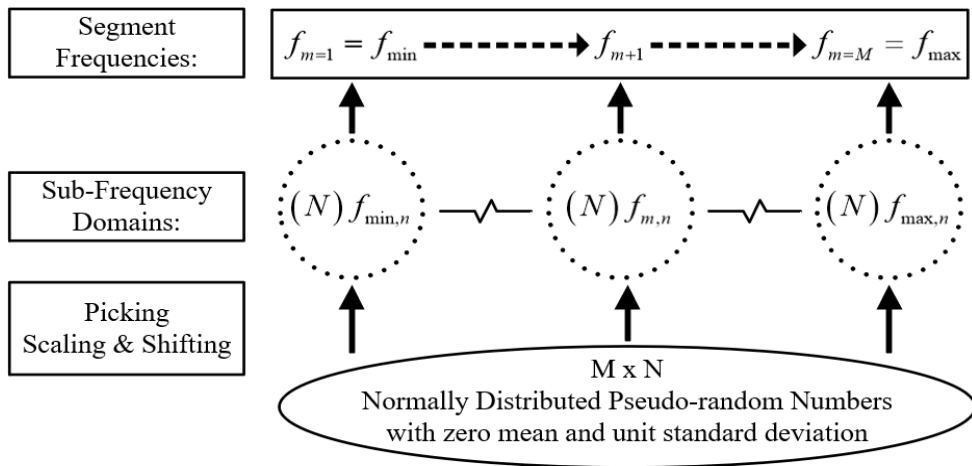


Figure 5.1. Structure and generation of frequency domain of CDRFG

$p_i^{m,n}$  and  $q_i^{m,n}$  are the parameters that indicate the spectral contributions of the segment frequencies with their sub-frequencies to the variance in the specified frequency bandwidth  $\Delta f$ . (Please see relations given with (2.2.41)) In other words, these parameters represent amplitudes of the harmonic motions by following target PSD functions, and derived from the RMS values of velocities, as given below.

$$\begin{aligned}
u_{rms,i}^2(x_j, t, f_m) &= S_i(f_m) \Delta f \\
u_{rms,i}^2(x_j, t, f_m) &= \lim_{T \rightarrow \infty} \left[ \frac{1}{T} \int_0^T (u_i(x_j, t, f_m))^2 dt \right] \\
&= \lim_{T \rightarrow \infty} \left[ \frac{1}{T} \int_0^T \left( \sum_{n=1}^N p_i^{m,n} \cos(k_j^{m,n} \tilde{x}_j + 2\pi f_{m,n} t) + q_i^{m,n} \sin(k_j^{m,n} \tilde{x}_j + 2\pi f_{m,n} t) \right)^2 dt \right] \\
&= \lim_{T \rightarrow \infty} \left[ \frac{1}{T} \sum_{n=1}^N \left( \int_0^T (p_i^{m,n} \cos(k_j^{m,n} \tilde{x}_j + 2\pi f_{m,n} t))^2 dt + \int_0^T (q_i^{m,n} \sin(k_j^{m,n} \tilde{x}_j + 2\pi f_{m,n} t))^2 dt \right) \right] \\
&= \sum_{n=1}^N \frac{(p_i^{m,n})^2}{2} + \sum_{n=1}^N \frac{(q_i^{m,n})^2}{2} = S_i(f_m) \Delta f
\end{aligned} \tag{5.2.3}$$

Where  $S_i(f_m)$  represents the longitudinal, transverse, and vertical power spectral densities at segment frequency  $f_m$  for  $i=1, 2,$  and  $3,$  respectively. These densities are defined for each direction with the equations from (5.2.4) to (5.2.6) for inhomogeneous and anisotropic turbulent flow.

$$S_u(f_m) = \frac{4(I_u \bar{u})^2 \left( \frac{L_u}{u} \right)}{\left[ 1 + 70.8 \left( \frac{f_m L_u}{u} \right)^2 \right]^{\frac{5}{6}}} \tag{5.2.4}$$

$$S_v(f_m) = \frac{4(I_v \bar{u})^2 \left( \frac{L_v}{u} \right) \left( 1 + 188.4 \left( 2f_m \left( \frac{L_v}{u} \right) \right)^2 \right)}{\left[ 1 + 70.8 \left( \frac{2f_m L_v}{u} \right)^2 \right]^{\frac{11}{6}}} \tag{5.2.5}$$

$$S_w(f_m) = \frac{4(I_w \bar{u})^2 \left(\frac{L_w}{u}\right) \left(1 + 188.4 \left(2f_m \left(\frac{L_w}{u}\right)\right)^2\right)}{\left[1 + 70.8 \left(\frac{2f_m L_w}{u}\right)^2\right]^{\frac{11}{6}}} \quad (5.2.6)$$

Since the relation derived in the procedure given with (5.2.3) cannot be solved directly for parameters  $p_i^{m,n}$  and  $q_i^{m,n}$ , these parameters are calculated as follows.

$$p_i^{m,n} = \text{sign}(r_i^{m,n}) \sqrt{\frac{2}{N} S_i(f_m) \Delta f \frac{(r_i^{m,n})^2}{1 + (r_i^{m,n})^2}} \quad (5.2.7)$$

$$q_i^{m,n} = \text{sign}(r_i^{m,n}) \sqrt{\frac{2}{N} S_i(f_m) \Delta f \frac{1}{1 + (r_i^{m,n})^2}} \quad (5.2.8)$$

$r_i^{m,n}$  is a number that is selected from three-dimensional normally distributed pseudo-random numbers with zero mean and unit standard deviation. If the above equations are checked whether they satisfy the relation (5.2.3) or not:

$$\sum_{n=1}^N (p_i^{m,n})^2 + \sum_{n=1}^N (q_i^{m,n})^2 = \frac{2}{N} S_i(f_m) \left[ \sum_{n=1}^N \left( \frac{(r_i^{m,n})^2}{1 + (r_i^{m,n})^2} \right) + \sum_{n=1}^N \left( \frac{1}{1 + (r_i^{m,n})^2} \right) \right] \quad (5.2.9)$$

Non-dimensional wavenumber is denoted by  $k_j^{m,n}$ , and the statistical distribution of this parameter's domain directly affects how the energy will be distributed in space. Therefore, this distribution should represent the desired levels of inhomogeneity and anisotropy for synthesizing. However, S. H. Huang et al. (2010) stated that there is no direct formulation for this distribution. For this reason, to satisfy the divergent-free condition, which is given with equation (5.2.10) for incompressible flows and a target level of energy distribution, this domain is obtained under the conditions derived within the following equations.

$$\nabla \cdot u(x_j, t) = \left( \partial u_1(x_j, t) / \partial x \right) + \left( \partial u_2(x_j, t) / \partial y \right) + \left( \partial u_3(x_j, t) / \partial z \right) = 0 \quad (5.2.10)$$

For velocity  $u(x_j, t)$ , the divergent-free condition becomes:

$$\begin{aligned}
\nabla \cdot u(x_j, t) &= \sum_{m=1}^M \sum_{n=1}^N \left( p_1^{m,n} \left( -k_1^{m,n} \sin(k_j^{m,n} \tilde{x}_j^m + 2\pi f_{m,n} t) \right) + q_1^{m,n} \left( k_1^{m,n} \cos(k_j^{m,n} \tilde{x}_j^m + 2\pi f_{m,n} t) \right) \right) \\
&+ \sum_{m=1}^M \sum_{n=1}^N \left( p_2^{m,n} \left( -k_2^{m,n} \sin(k_j^{m,n} \tilde{x}_j^m + 2\pi f_{m,n} t) \right) + q_2^{m,n} \left( k_2^{m,n} \cos(k_j^{m,n} \tilde{x}_j^m + 2\pi f_{m,n} t) \right) \right) \\
&+ \sum_{m=1}^M \sum_{n=1}^N \left( p_3^{m,n} \left( -k_3^{m,n} \sin(k_j^{m,n} \tilde{x}_j^m + 2\pi f_{m,n} t) \right) + q_3^{m,n} \left( k_3^{m,n} \cos(k_j^{m,n} \tilde{x}_j^m + 2\pi f_{m,n} t) \right) \right) \\
&= \left( p_1^{m,n} k_1^{m,n} + p_2^{m,n} k_2^{m,n} + p_3^{m,n} k_3^{m,n} \right) \left( -\sin(k_j^{m,n} \tilde{x}_j^m + 2\pi f_{m,n} t) \right) \\
&+ \left( q_1^{m,n} k_1^{m,n} + q_2^{m,n} k_2^{m,n} + q_3^{m,n} k_3^{m,n} \right) \left( \cos(k_j^{m,n} \tilde{x}_j^m + 2\pi f_{m,n} t) \right) = 0
\end{aligned} \tag{5.2.11}$$

Correction of the non-dimensional wavenumber domain to satisfy the divergent-free condition is performed under the above conditions.

$$\left( p_1^{m,n} k_1^{m,n} + p_2^{m,n} k_2^{m,n} + p_3^{m,n} k_3^{m,n} \right) = 0 \tag{5.2.12}$$

$$\left( q_1^{m,n} k_1^{m,n} + q_2^{m,n} k_2^{m,n} + q_3^{m,n} k_3^{m,n} \right) = 0 \tag{5.2.13}$$

Since the non-dimensional wavenumbers take values between zero and one when they are normalized with the Kolmogorov length scale, another condition to be met is given below.

$$k^{m,n} = \left| \overrightarrow{k^{m,n}} \right| = \sqrt{\left( k_1^{m,n} \right)^2 + \left( k_2^{m,n} \right)^2 + \left( k_3^{m,n} \right)^2} = 1 \tag{5.2.14}$$

According to S. H. Huang et al. (2010), isotropic and homogeneous turbulent flows can be obtained with a uniform (i.e., isotropically) distribution of wavenumbers on a sphere with a unit radius. Since the desired levels of anisotropy and inhomogeneity are defined together with the domain of pseudo-random number  $r_i^{m,n}$ , the non-dimensional wavenumber domain is distributed uniformly on a sphere with a unit radius at the first stage. Following that, this domain is subjected to conditions from (5.2.12) to (5.2.14). In other words, these wavenumbers are corrected as pseudo-random Gaussian values with zero mean and unit standard deviation on a sphere for

target anisotropy and inhomogeneity. The procedure for uniform distribution of non-dimensional wavenumbers on a sphere with unit radius is given with (5.2.15).

$$\begin{aligned}
k_{uniform,3}^{m,n} &= \sin(U_{a_1}) \\
R_{sphere}^{m,n} &= \sqrt{1 - (k_{uniform,3}^{m,n})^2} \\
k_{uniform,1}^{m,n} &= R_{sphere}^{m,n} \cos(U_{a_2}) \\
k_{uniform,2}^{m,n} &= R_{sphere}^{m,n} \sin(U_{a_2})
\end{aligned} \tag{5.2.15}$$

Where,  $U_{a_1}$  and  $U_{a_2}$  are two uniformly distributed arrays in the range  $[0, 2\pi]$ . The value  $k_{uniform,j}^{m,n}$  represents the initial uniform wavenumbers on a sphere in u, v, and w directions for  $j=1, 2, 3$ , respectively. The aforementioned conditions are handled as given below.

$$\begin{pmatrix} p_x^{m,n} & p_y^{m,n} & p_z^{m,n} \\ q_x^{m,n} & q_y^{m,n} & q_z^{m,n} \\ k_x^{m,n} & k_y^{m,n} & k_z^{m,n} \end{pmatrix} \begin{pmatrix} k_x^{m,n} \\ k_y^{m,n} \\ k_z^{m,n} \end{pmatrix} = \begin{pmatrix} 0 \\ 0 \\ 1 \end{pmatrix} \tag{5.2.16}$$

Figure (5.2) represents both the initial uniform distribution of wavenumbers and their corrected distribution for a sample segment frequency to illustrate this procedure.

Another important procedure is the frequency-based correlation of the generated turbulence flow field, as explained in Sub-section (2.2.2.6). This correlation is characterized by the parameter  $L_j^m$  which is obtained with the equation (5.2.16).

$$L_j^m = \frac{\bar{u}}{\gamma C_c f_m} \tag{5.2.17}$$

In the above equation,  $\bar{u}$  is the mean velocity and  $C_c$  is the coherency decay constant. This constant is taken as 10 for each direction in this study, the same as reference studies. (Aboshosha et al., 2015; Elshaer et al., 2016) The tuning factor  $\gamma$  is the constant used to match the synthesized velocities' coherency function with the target coherency function.

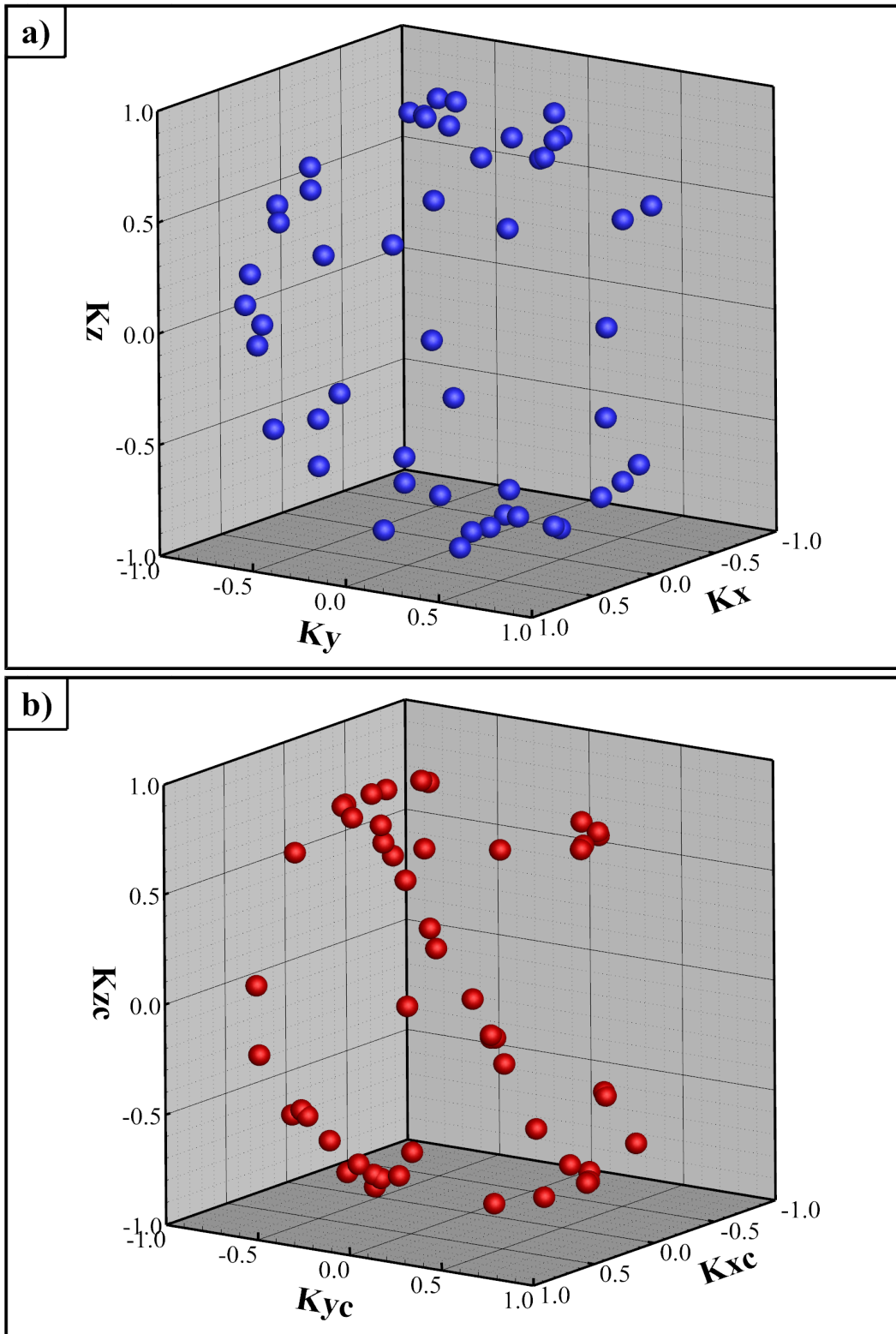


Figure 5.2. Illustration of correction procedure of wavenumber domain  
 a) Initial uniform wavenumber domain, b) Corrected wavenumber domain

While the coherency function of synthesized velocities is obtained as follows, the target coherence function is defined as in the equation (5.2.19) by Aboshosha et al. (2015) based on the study conducted by A.G. Davenport in 1995.

$$Coh_{u_1, u_2}(f_m) = \frac{|\sigma_{u_1 u_2}|}{\sigma_{u_1} \sigma_{u_2}} = \sum_{n=1}^N \cos(\gamma k_j^{m,n} C_f) \quad (5.2.18)$$

$$e^{\left(\frac{C_c f_m dx_j}{u}\right)} \quad (5.2.19)$$

Where  $\sigma_{u_1 u_2}$  is the covariance between the synthesized velocities of two points, and it is described briefly in Sub-section (2.2.2.6). The distance between these two points is expressed as  $d$ , while  $C_f$  is obtained as given below.

$$C_f = \frac{C_c f d}{u} \quad (5.2.20)$$

Conditional statements for tuning factor  $\gamma$ , which were obtained through the preliminary study performed by Aboshosha et al. (2015), are given below.

$$\gamma = \begin{cases} 3.7\beta^{-0.3} & \beta < 6.0 \\ 2.1 & \beta \geq 6.0 \end{cases} \text{ where } \beta = \frac{C_c D}{L_u} \quad (5.2.21)$$

In equation (5.2.21),  $\beta$  is a non-dimensional length scale and  $L_u$  is the longitudinal integral turbulence length scale.  $D$  is the distance to which the correlation procedure is tuned. For a good correlation,  $D$  is suggested to be taken between  $0.5H$  and  $1H$  for tall buildings with a height of  $H$ . (Aboshosha et al., 2015)  $\tilde{x}_j^m$  is the dimensionless location coordinate where the synthesizing is performed and calculated as follows.

$$\tilde{x}_j^m = \frac{x_j}{L_j^m} \quad (5.2.22)$$

When all procedures of CDRFG are completed for a certain segment frequency, synthesized fluctuating velocity-time traces at that frequency appear as given in figure (5.3).

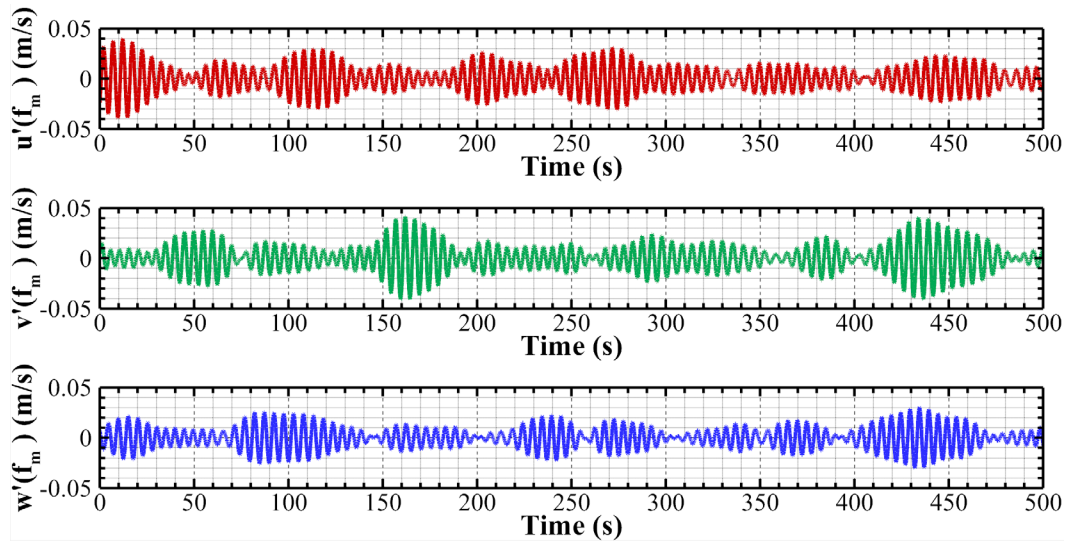


Figure 5.3. Sample velocity-time traces for a single segment frequency

After the velocity components are formed for each segment frequency, synthesized velocities in the along-wind direction are summed with the mean velocities. Consequently, the generation of the inflow boundary conditions is completed, and velocity-time traces in figure (5.3) become as in figure (5.4) for a specific point.

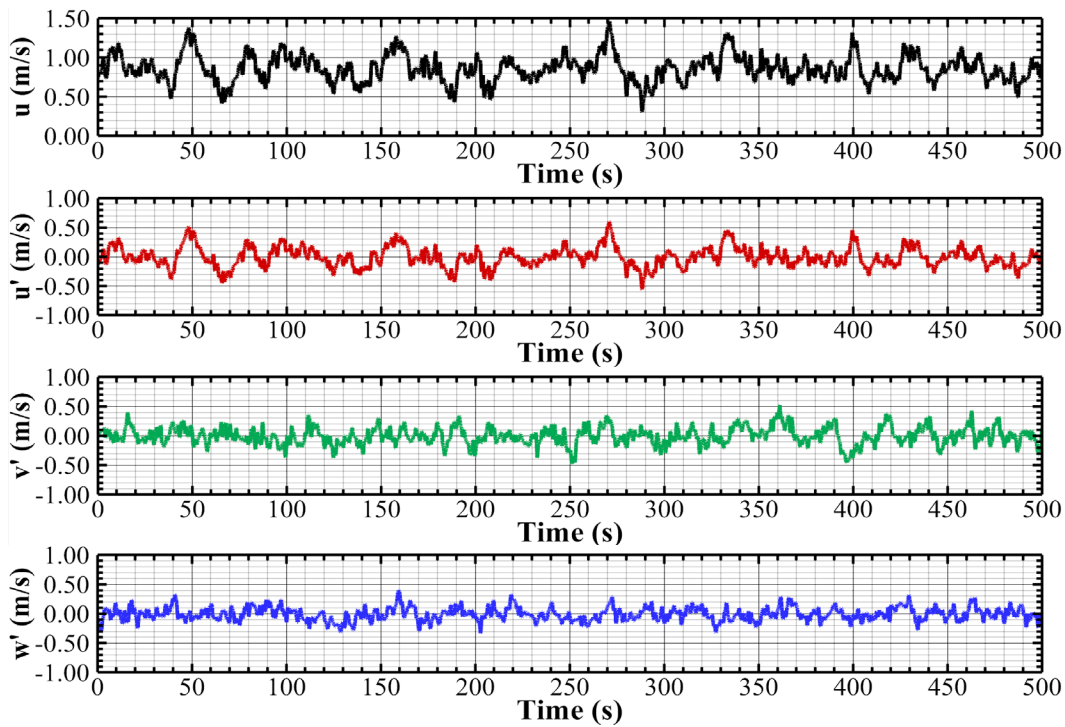


Figure 5.4. Sample velocity-time histories

In brief, the CDRFG technique needs frequencies representing the target spectrum, mean velocity profile, turbulence length scales, and turbulence intensities as input values for generating the desired turbulent velocity fields. The flow chart of this technique is given in figure (5.5).

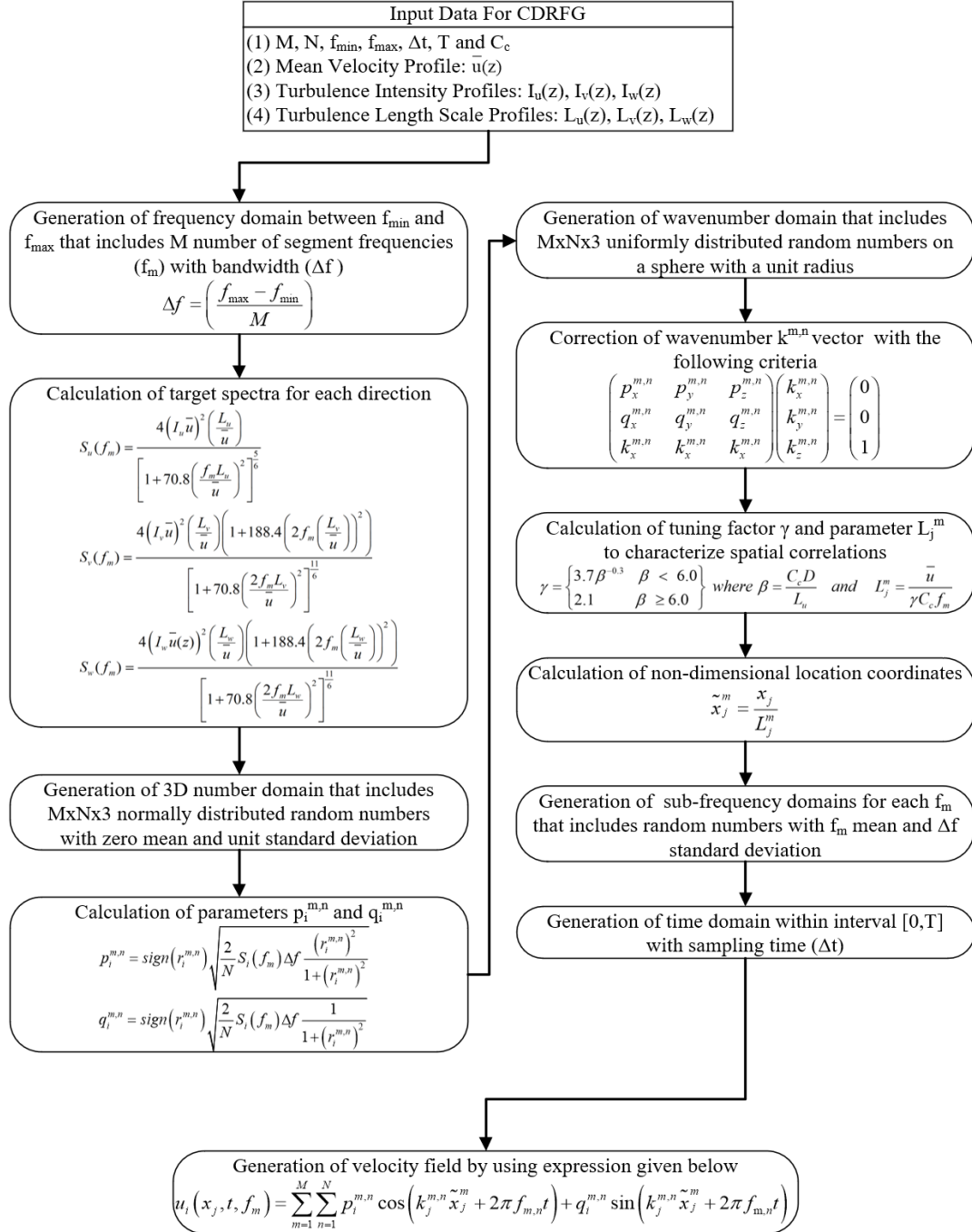


Figure 5.5. Flowchart of CDRFG technique

### 5.2.2 Implementation of CDRFG with Fortran and MPI

The CDRFG method, whose general discretization is mentioned in Sub-section (5.2.1), has been compiled in this study with Fortran 90-95 programming language using Intel Parallel Studio XE. The purposes of using this language are obtaining full control over the statistical operations required for CDRFG and employing Message-passing Interface Standards (MPI) to minimize the numerical cost of mathematical procedures such as solving non-linear equations for wavenumber corrections. Under this section, it is mentioned how some of the procedures stated in figure (5.5) are handled and how the numerical scheme is constructed considering the memory requirement and performance that highly depend on the inflow plane's size and the number of frequency segments with their sub-domains.

To reflect the chaotic nature of strong winds as well as possible, the random number sets that should be formed under certain distributions within the body of CDRFG are of great importance. These random number sets are generated in this study using certain seeds to obtain the same velocity fields when the same input parameters are used without disturbing chaotic nature. As mentioned earlier, one of these random number sets is the  $r_i^{m,n}$  parameter, which has a very important role in determining the spectral contributions of segment frequencies to variance or, in other words, in obtaining the desired inhomogeneity and anisotropy levels. Required three-dimensional normally distributed random number domain with zero mean and unit standard deviation for this parameter is generated by using the Box-Muller Transform method, whose equation is given below.

$$r_i^{m,n} = \sqrt{-2 \ln(u_1)} \sin(2\pi u_2) \quad (5.2.23)$$

The Box-Muller Transform is an approach that converts two uniformly distributed random number sets produced within the range [0,1] to a normally distributed (i.e., Gaussian Distribution) random number set. These two pseudorandom uniformly distributed number sets are produced by using the Mersenne-Twister random number generation technique. Similarly, these techniques are used by defining different seeds

to form a random number set for the frequency domain. This set of numbers for the frequency domain is separated by random picking into sub-domains, and scaling & shifting procedures are applied as given below.

$$\begin{aligned}
\overline{f_m} &= \left( \sum_{n=1}^N f_{m,n} \right) / N \\
\sigma_{f_m} &= \sqrt{\left( \sum_{n=1}^N (f_{m,n} - \overline{f_m})^2 \right) / (N-1)} \\
f_{m,n} = f_{m,n} - \overline{f_m} &\rightarrow f_{m,n} = f_{m,n} / \sigma_{f_m} \\
f_{m,n} = f_{m,n} \Delta f &\rightarrow f_{m,n} = f_{m,n} + f_m
\end{aligned} \tag{5.2.24}$$

Since only uniform random number sets are required for the non-dimensional wavenumber  $k_j^{m,n}$  domain, Mersenne-Twister random number generation technique is used only by defining different seeds for this domain. Intel Math Kernel Libraries currently incorporates multiple RNG techniques and simple generators for Intel Fortran and C programming languages, including these methods. These techniques are well optimized with OpenMP, especially for Intel processors. It is important to mention that if such processes are used with MPI, each core prone to generate the same numbers unless a different seed is specified for each core. Therefore, in algorithms designed to run on any number of processors instead of a specific number of cores, seed numbers should be assigned carefully and differently for each core considering that fact. However, in such a use, generated velocity fields inherently correct but difficult to follow since these fields change depending on the number of cores. Thus, the generation of these number sets was assigned only to the master node and then distributed to worker cores for this study. Consequently, the differences in the velocity fields depending on the number of seeds have been eliminated. When the duration needed for these processes was examined, it was observed that this approach does not cause any increase in numerical cost. The most time-consuming part of the CDRFG is the correction of wave numbers by solving non-linear equations given with (5.2.16). These equations were handled with the Trust-Region (TR) algorithm in this study, and it has been integrated into the code

using Intel MKL. The accuracy chosen for this algorithm is  $10^{-12}$ , and the initial size chosen for the trust-region was specified as 100. In this algorithm, the converging criteria are defined not only on the certain accuracy but also on the given number of iterations. A sufficient number of iterations were provided to reach the target accuracy to satisfy the divergent-free condition strictly. Furthermore, TR also requires the Jacobian matrix of the conditions given in (5.2.16). Although MKL provides the necessary routine for this calculation step, this condition was defined as follows to minimize numerical cost and prevent over-iteration.

$$\begin{aligned}
f_1 &= (p_1^{m,n} k_1^{m,n} + p_2^{m,n} k_2^{m,n} + p_3^{m,n} k_3^{m,n}) \\
f_2 &= (q_1^{m,n} k_1^{m,n} + q_2^{m,n} k_2^{m,n} + q_3^{m,n} k_3^{m,n}) \\
f_3 &= (k_1^{m,n})^2 + (k_2^{m,n})^2 + (k_3^{m,n})^2 - 1
\end{aligned}$$

$$J = \begin{pmatrix} \frac{\partial f_1}{\partial k_1} & \frac{\partial f_1}{\partial k_2} & \frac{\partial f_1}{\partial k_3} \\ \frac{\partial f_2}{\partial k_1} & \frac{\partial f_2}{\partial k_2} & \frac{\partial f_2}{\partial k_3} \\ \frac{\partial f_3}{\partial k_1} & \frac{\partial f_3}{\partial k_2} & \frac{\partial f_3}{\partial k_3} \end{pmatrix} = \begin{pmatrix} p_1^{m,n} & p_2^{m,n} & p_3^{m,n} \\ q_1^{m,n} & q_2^{m,n} & q_3^{m,n} \\ 2k_1^{m,n} & 2k_2^{m,n} & 2k_3^{m,n} \end{pmatrix} \quad (5.2.25)$$

This iterative procedure is resolved for each sub-frequency on each point. Consequently, depending on the number of grid points on the inflow plane and selected frequencies with their sub frequencies, numerical cost increases. Therefore, the numbers M and N should be chosen very carefully. In this study, 100 segment frequencies and 50 sub-frequencies are used, same as reference studies. In addition, relatively high accuracy for wavenumber correction has been selected. Depending on the inflow plane size to be studied, this accuracy can be changed.

Another part that increases the numerical cost is the intrinsic trigonometric functions that are included in the equation (5.2.1), where velocities are synthesized. Since these functions are performed MxN times for each point and each time step, it is important how these operations are handled. For this reason, Intel MKL vector trigonometric functions were used for these operations.

In the S-A based DES model, a non-dimensional analysis is performed on the molecular viscosity and the target Reynold's number of the flow. Based on this analysis, synthesized velocities are required as non-dimensional for inflow boundary conditions. Therefore, taken reference turbulence length scales were normalized by a certain length, and mean velocities were made non-dimensional with the procedure (5.2.26). On the other hand, frequencies were scaled as given in (5.2.27). In this way, the desired turbulence intensities or deviations and related input conditions (written as 'reference') were kept the same for DES.

- Calculation process for non-dimensional mean velocity profile:

$$\begin{aligned}
\Delta y_{jk} &= \frac{(y(j+1,k) - y(j,k)) + (y(j+1,k+1) - y(j,k+1))}{2} \\
\Delta z_{jk} &= \frac{(z(j,k+1) - z(j,k)) + (z(j+1,k+1) - z(j+1,k))}{2} \\
u_{jk} &= \frac{(\bar{u}(j,k) + \bar{u}(j+1,k) + \bar{u}(j,k+1) + \bar{u}(j+1,k+1))}{4} \\
A_{jk} &= \Delta y_{jk} \Delta z_{jk} \quad , \quad Q_{jk} = u_{jk} \cdot A_{jk} \\
\sum Q_{\text{inflow}} &= \sum_{y=1}^{N_y-1} \sum_{z=1}^{N_z-1} Q_{jk} \rightarrow U_m = \frac{Q_{\text{inflow}}}{A_{\text{inflow plane}}} \rightarrow u_{\text{non-dimensional}} = \frac{\bar{u}}{U_m}
\end{aligned} \tag{5.2.26}$$

- Determination of frequency range based on non-dimensional parameters:

$$\begin{aligned}
\frac{f_{\text{reference}} L_{\text{reference}}}{u_{\text{reference}}} &= \frac{f_{\text{DES}} L_{\text{DES}}}{u_{\text{DES}}} \rightarrow f_{\text{DES}} = \frac{(u_{\text{DES}} L_{\text{reference}})}{(u_{\text{reference}} L_{\text{DES}})} f_{\text{reference}} \\
\frac{f_{\text{reference}} S_{i,\text{reference}}}{(\sigma_{i,\text{reference}})^2} &= \frac{f_{\text{DES}} S_{i,\text{DES}}}{(\sigma_{i,\text{DES}})^2} \quad , \quad \sigma_{i,\text{reference}} = \frac{I_{i,\text{reference}}}{u_{i,\text{reference}}} \quad , \quad \sigma_{i,\text{DES}} = \frac{I_{i,\text{reference}}}{u_{i,\text{DES}}} \\
\frac{f_{\text{reference}} S_{i,\text{reference}}}{\left(\frac{I_{i,\text{reference}}}{u_{i,\text{reference}}}\right)^2} &= \frac{f_{\text{DES}} S_{i,\text{DES}}}{\left(\frac{I_{i,\text{reference}}}{u_{i,\text{DES}}}\right)^2} \rightarrow \frac{f_{\text{reference}} S_{i,\text{reference}}}{f_{\text{DES}} S_{i,\text{DES}}} = \left(\frac{u_{i,\text{DES}}}{u_{i,\text{reference}}}\right)^2
\end{aligned} \tag{5.2.27}$$

Considering the mentioned statements in this sub-section and RNG methods, the flowchart of the CDRFG code compiled for this study is given in figure (5.6).

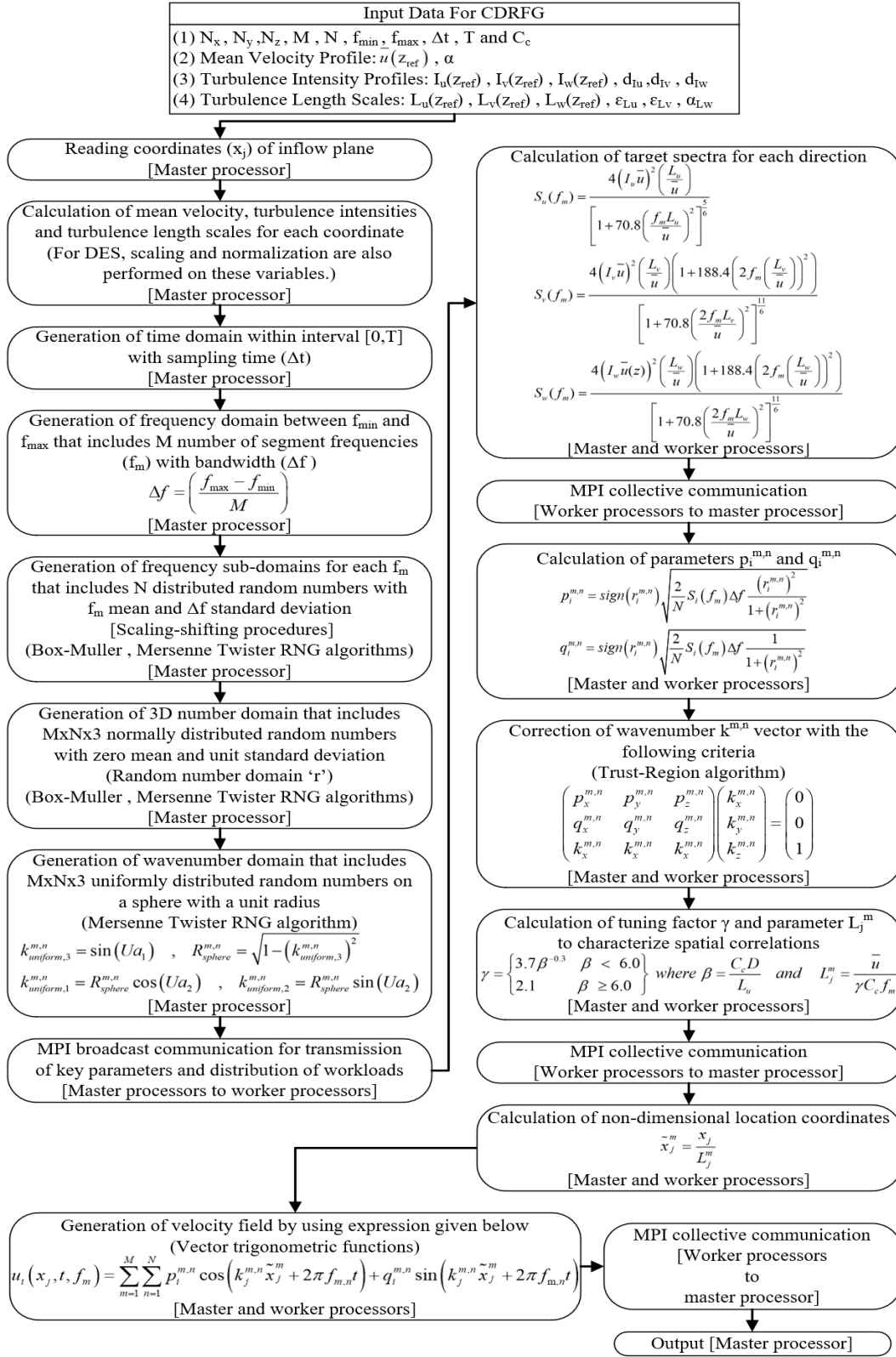


Figure 5.6. Flowchart of CDRFG used in this study

### 5.3 Geometric Description of Selected Tall Building for Analysis

The tall building chosen to perform the aerodynamic analysis is the CAARC standard tall building model proposed by Wardlaw and Moss in 1970 to compare different wind tunnels' techniques and determine the reliability of the data obtained from these tunnels as mentioned earlier in Section (4.1). If Chapter (4) is examined, it can be concluded that it is a highly used tall building model in both wind tunnel tests and numerical studies. The full-scale dimensions of this model, which has a prismatic structure, are given below.

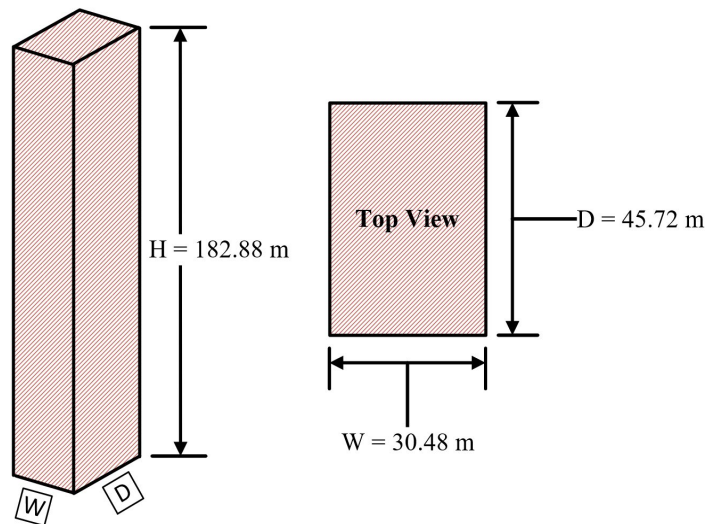


Figure 5.7. Full-scale dimensions of CAARC standard tall building model

### 5.4 Computational Domains and Grid Discretization Strategies

Aerodynamic analysis of the CAARC standard tall building model was conducted at  $0^\circ$  and  $45^\circ$  angles of attack under the name of CD0 (study case-1) and CD45 (study case-2), respectively. Besides, to examine grid dependency, another simulation named CD0R was performed with a coarser mesh for study case-1. Since the reference numerical (Elshaer et al., 2016) and experimental studies (Dragoiescu et al., 2006) contain results regarding the aerodynamic analysis of CAARC building under the  $0^\circ$  angle of attack, CD0 was compared with these studies. CD45 was

carried out as an additional study to observe the effects of a different angle of attack. For each study case, computational domains were discretized within the framework of several suggestions given by AIJ (Tominaga, Mochida, Yoshie, et al., 2008) and COST (Franke et al., 2007) guidelines. These guidelines are referred to as AIJ and COST from now on for integrity. For the dimensions of the computational domains, COST and AIJ guidelines provide several values considering the blockage ratio. The blockage ratio is defined by COST as the ratio of the computational domain surface area perpendicular to the flow direction to the area of the building surface perpendicular to the flow direction. It is calculated as given below and shown in figure (5.8). While COST and AIJ guidelines suggest that this ratio should be below 3%, the COST guideline also states that this value should be a maximum of 10%.

$$\delta_{BR} = A_{BS} / A_{DS} \quad (5.4.1)$$

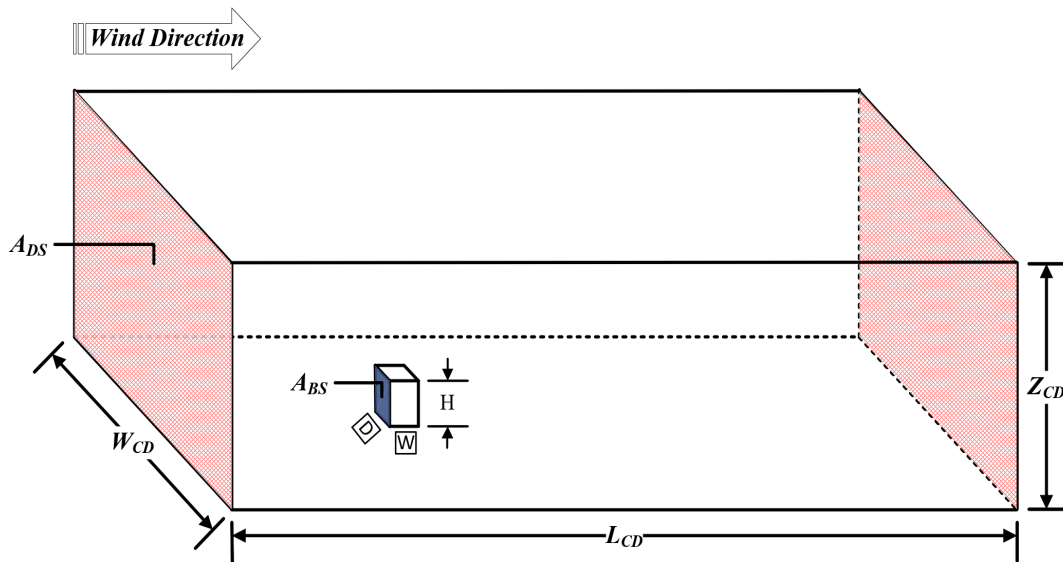


Figure 5.8. Blockage ratio of the computational domain

Both AIJ and COST recommended that the inlet, lateral and top boundaries of the computational domain for individual tall building studies should have a distance from the target building at least five times larger than the height of the target building H to keep this ratio at an optimum level. COST emphasized that these distances are needed to avoid artificial accelerations on the building and around it.

In addition to that, COST proposed this  $5H$  distance between the inflow boundary and the building when the approaching flow profiles are well known and stated that this distance should be kept longer in cases where the flow profiles are not known. Since related wind profiles were directly taken from the reference studies and used with CDRFG, this distance was taken as  $5H$  in this study. Furthermore, the outflow boundary was suggested by these guidelines to be far away from the target building, at least  $15H$ , to make flow fully developed behind the building. Considering these recommendations, the following dimensions, as shown in figure (5.9), were used for computational domains.

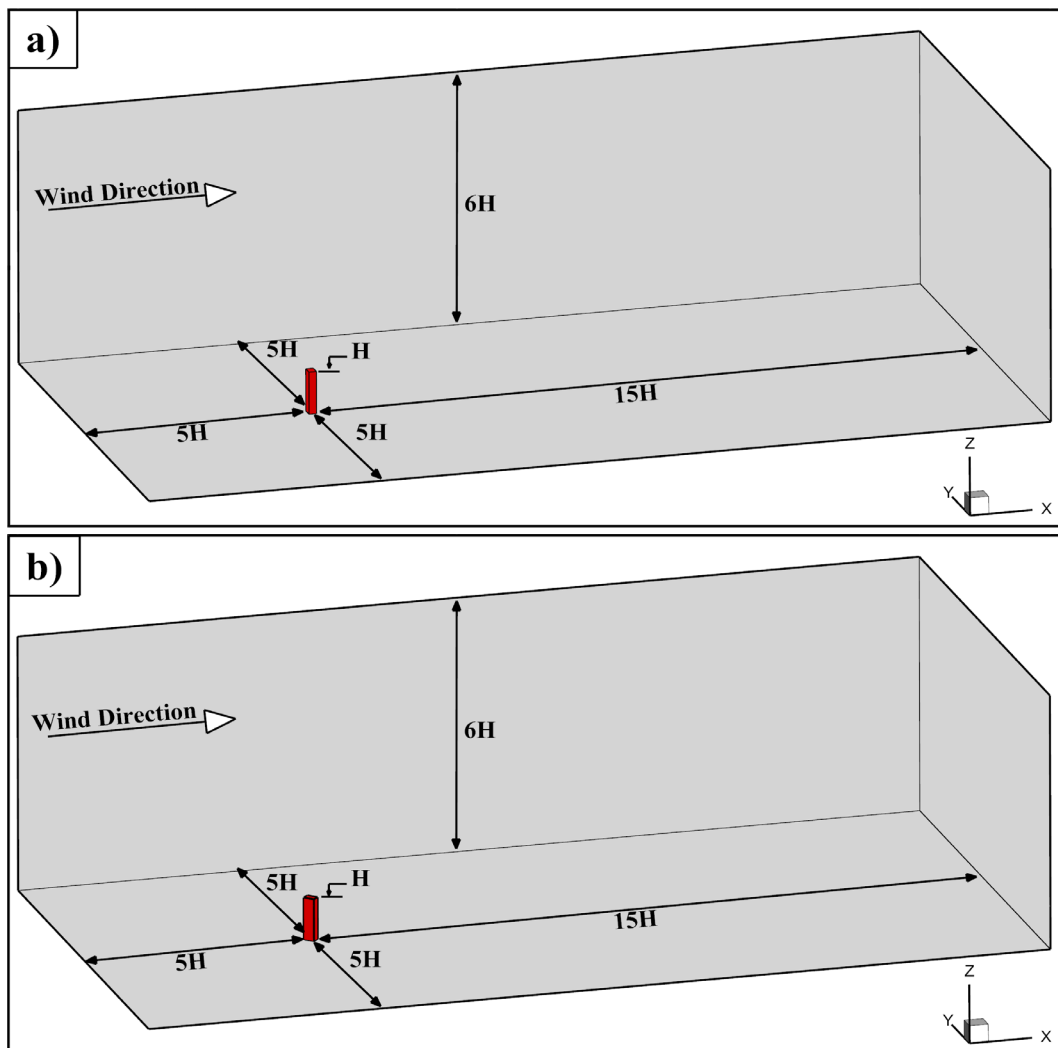


Figure 5.9. Dimensions of computational domains for each study case  
a) CD0-CD0R, b) CD45

With the numerical scheme used, the working conditions were analyzed by making them non-dimensional with the larger length of the CAARC cross-section  $D$ , which is 45.72 m, and the average mean wind velocity of the inflow plane  $U_m$  that is calculated by using the reference mean wind velocity  $\bar{u}(z_B)$ , which is 10 m/s for the reference height  $H$ . Therefore, the reference height  $Z_B$  results in  $(H/D)=4$  for non-dimensional computational domains. Correspondingly, when the blockage ratios of computational domains are calculated with the dimensions given in figure (5.9), these values correspond to approximately 0.41% for both study cases.

Another criterion in the computational domains' discretization is proposed to analyze flow around the building or buildings with sufficient accuracy is the stretching ratio or expansion ratio. It is defined as a ratio between the neighboring cells' sizes one after to another. It was suggested by COST and AIJ that this ratio, which is also important to provide sufficiently fine grid refinement considering numerical costs for the regions where separating flows occurs, such as near the corners, wall, and roofs, should be less than 1.3. Although COST cited several studies suggesting that this value should not be greater than 1.2, it was also mentioned that it would not be a problem if this value is a little higher in studies using the higher-order numerical schemes. Since a higher-order numerical scheme was used in this study, the value of 1.3 was accepted as a limiting criterion in discretizing the computational domains, which was not exceeded. In more detail, domains of CD0 and CD45 cases were discretized by aiming the value of 1.2 for this ratio as the maximum in general, although cells around the building have 1.3 stretching ratios. On the other hand, for the domain of CD0R, this ratio was taken as 1.3 predominantly.

According to COST, grid lines should approach to the building walls in a way perpendicular. To provide that, a small region around the building with an area of  $(0.025Z_B)^2$  were meshed without any strategy, as shown in figure (5.10). Since the viscous sublayer was solved directly without using a certain wall function approach,

the discretization of computational domains was done so that the first node's distance to the walls is  $y^+ = 1$ .

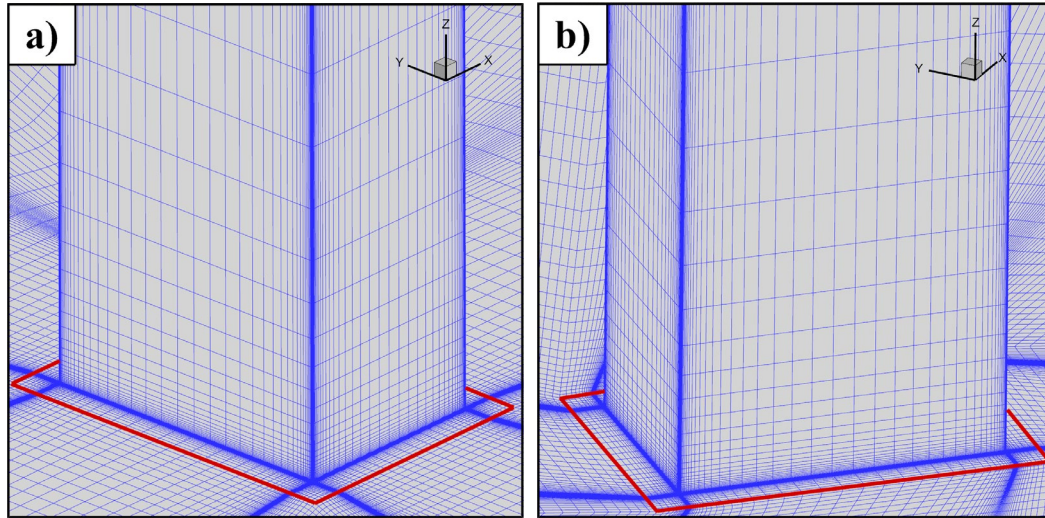


Figure 5.10. Approaching angle of grid lines to the building walls  
a) CD0~CD0R, b) CD45

Considering all mentioned suggestions as well as parameters such as smoothness and skewness, hexahedron grid discretization was applied for each computational domain by using one of the commercial CFD mesh generation software. Overall grid distribution was performed using hyperbolic tangent function  $\tanh$ . Grid distribution on building surfaces is shown in figure (5.11). There are 16040 cells (i.e., nodes:  $54 \times 51 \times 66$ ) on building surfaces that interact with wind flow for the domains of CD0 and CD45 study cases. For the study case CD0R, this value is 15422. (i.e., nodes:  $54 \times 51 \times 62$ ). These surface distributions were found to be optimum to satisfy the suggestions of a 1.3 stretching ratio and  $y^+ = 1$ . While figure (5.12) shows the overall grid distribution for each study case, figure (5.13), figure (5.14), and figure (5.15) illustrate meshing strategy on the x-y plane in a way to meet the suggestions mentioned above with reasonable numerical costs. Thomas-Middlecoff and Steger-Sorenson control functions were used to increase the grid quality in the regions where the strategy followed around the building, which are also shown in these figures. As a result of this mentioned strategy, computational domains were discretized with the parameters given in tables (5.2) and (5.3).

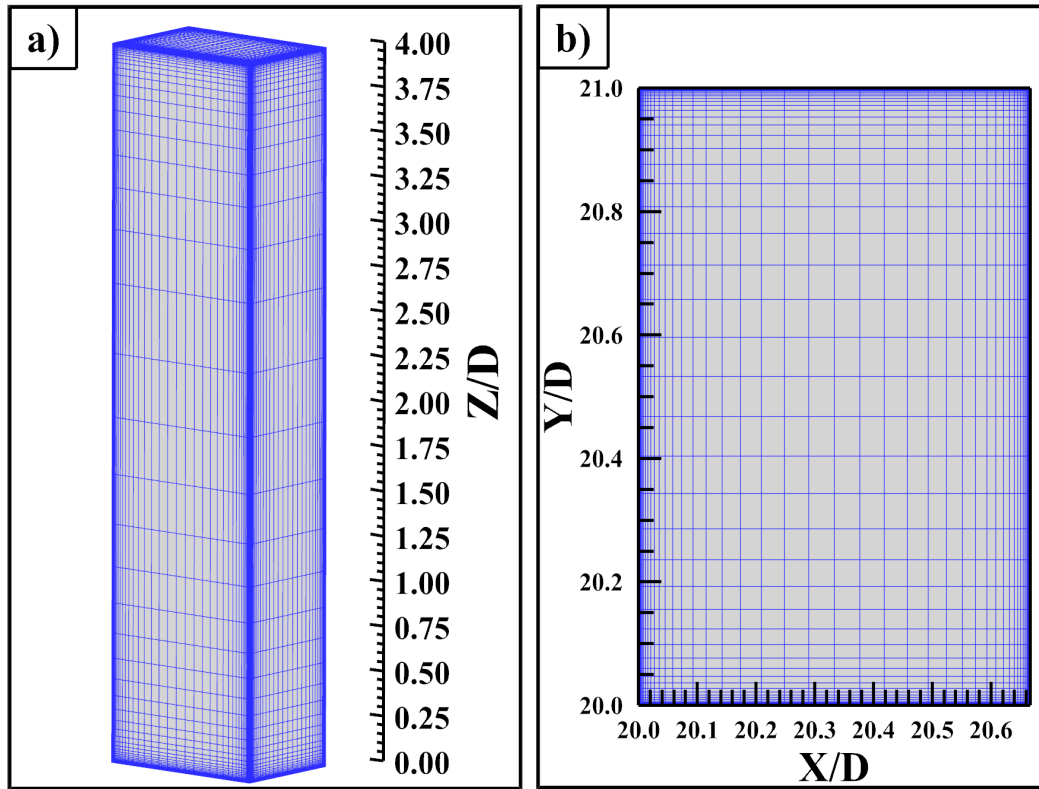


Figure 5.11. Grid distribution on building surfaces  
a) Front view of CD0-CD45~CD0R, b) Top view of CD0-CD45~CD0R

Table 5.2 Total grid points and hexahedron cells of computational domains

Domain	<i>Stretching Ratio (In general)</i>	<i>Maximum Stretching Ratio</i>	<i>Number of Grid Points</i>	<i>Number of Hexahedron Cells</i>
CD0	1.2	1.3	256x224x128	7221855
CD0R	1.3	1.3	240x208x112	5491503
CD45	1.2	1.3	256x224x128	7221855

Table 5.3 Meshing parameters about computational domains

Domain	<i>Maximum Skewness</i>	<i>Minimum Included Angle</i>
CD0	0.538	41.54°
CD0R	0.519	43.25°
CD45	0.528	43.23°

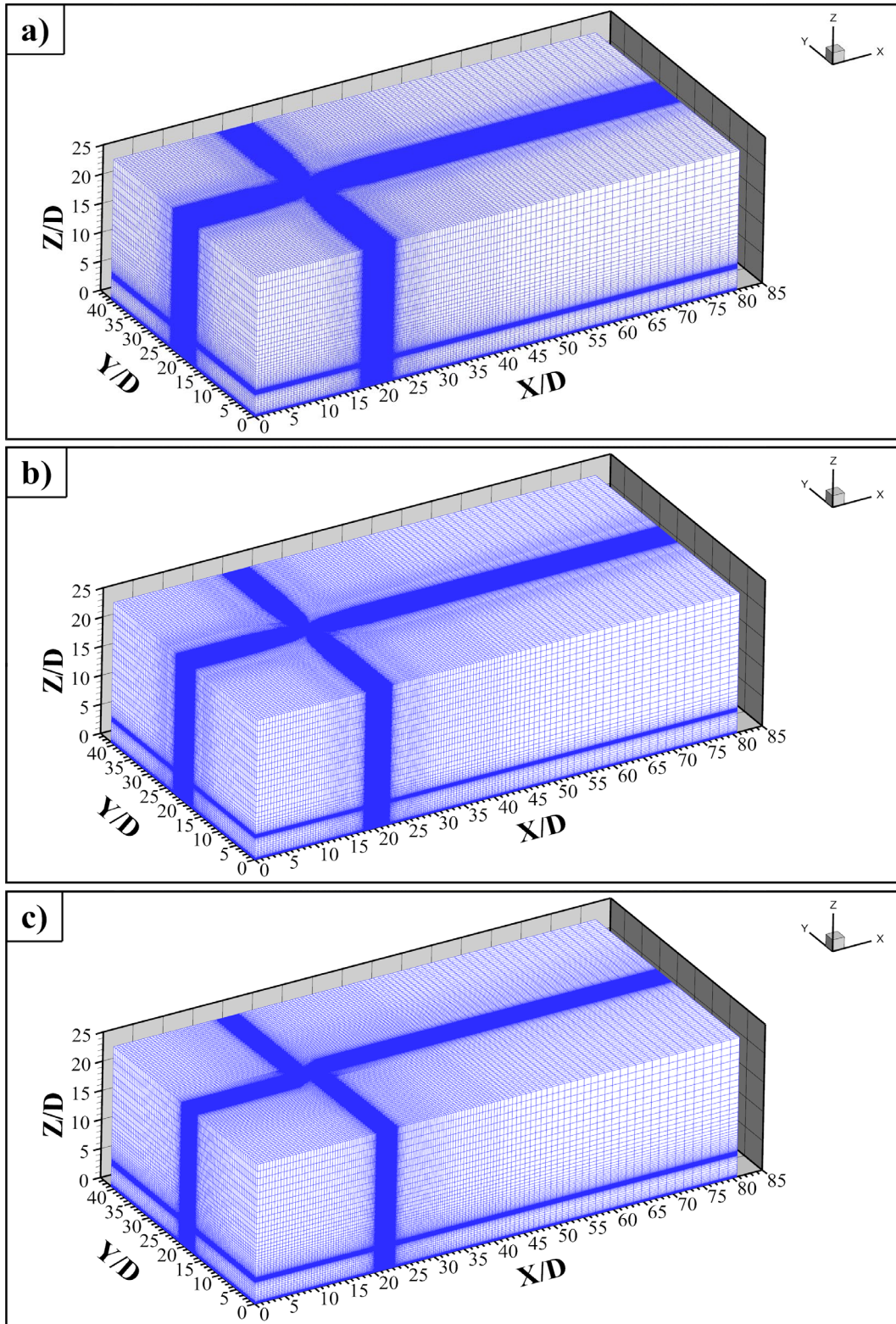


Figure 5.12. Overall grid distribution of computational domains  
a) CD0 (256x224x128), b) CD0R (240x208x112), c) CD45 (256x224x128)

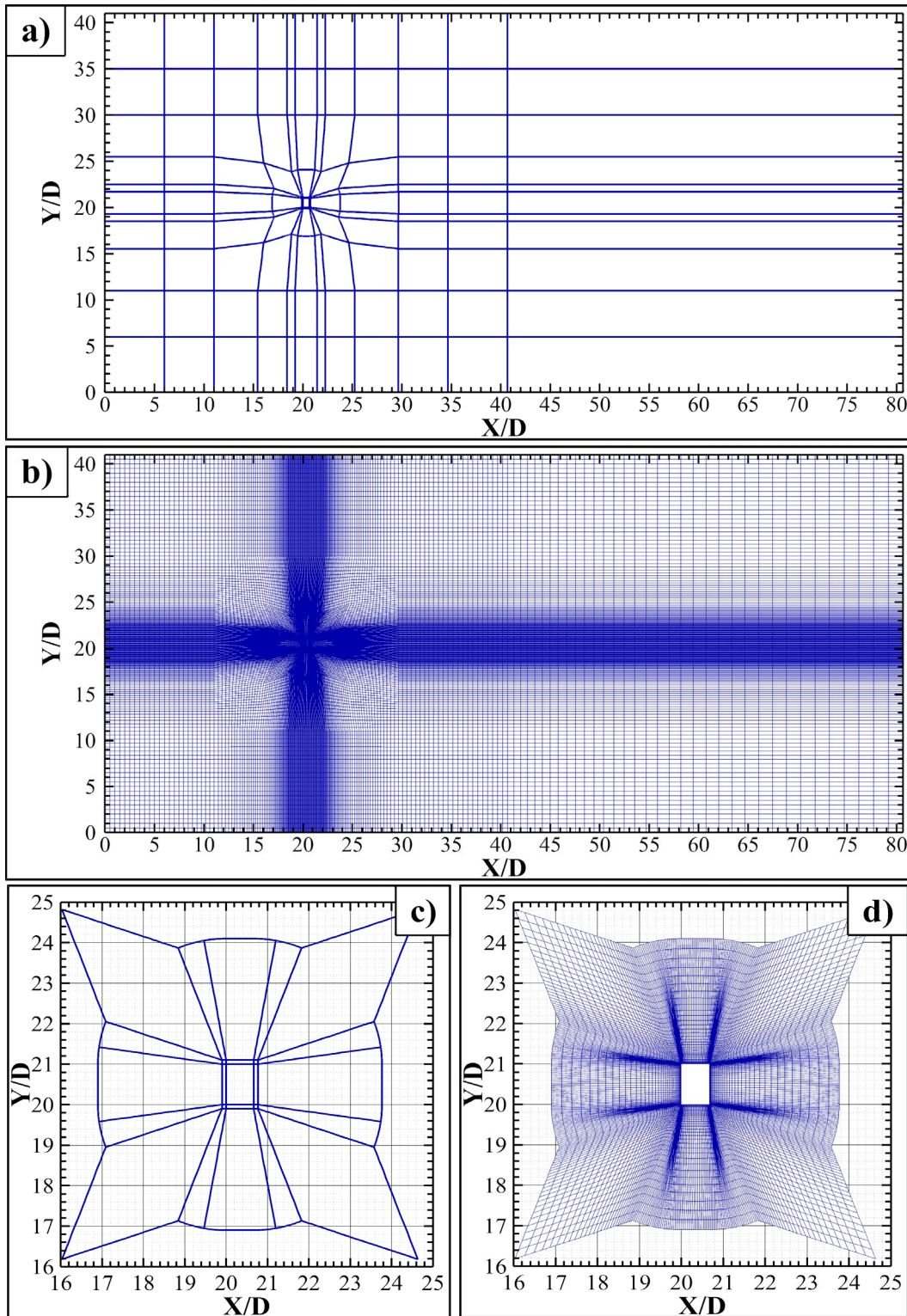


Figure 5.13. Meshing strategy for CD0  
 a) Overall connectors, b) Overall grid distribution in x-y plane  
 c) Connectors around the building, d) Grid distribution around the building

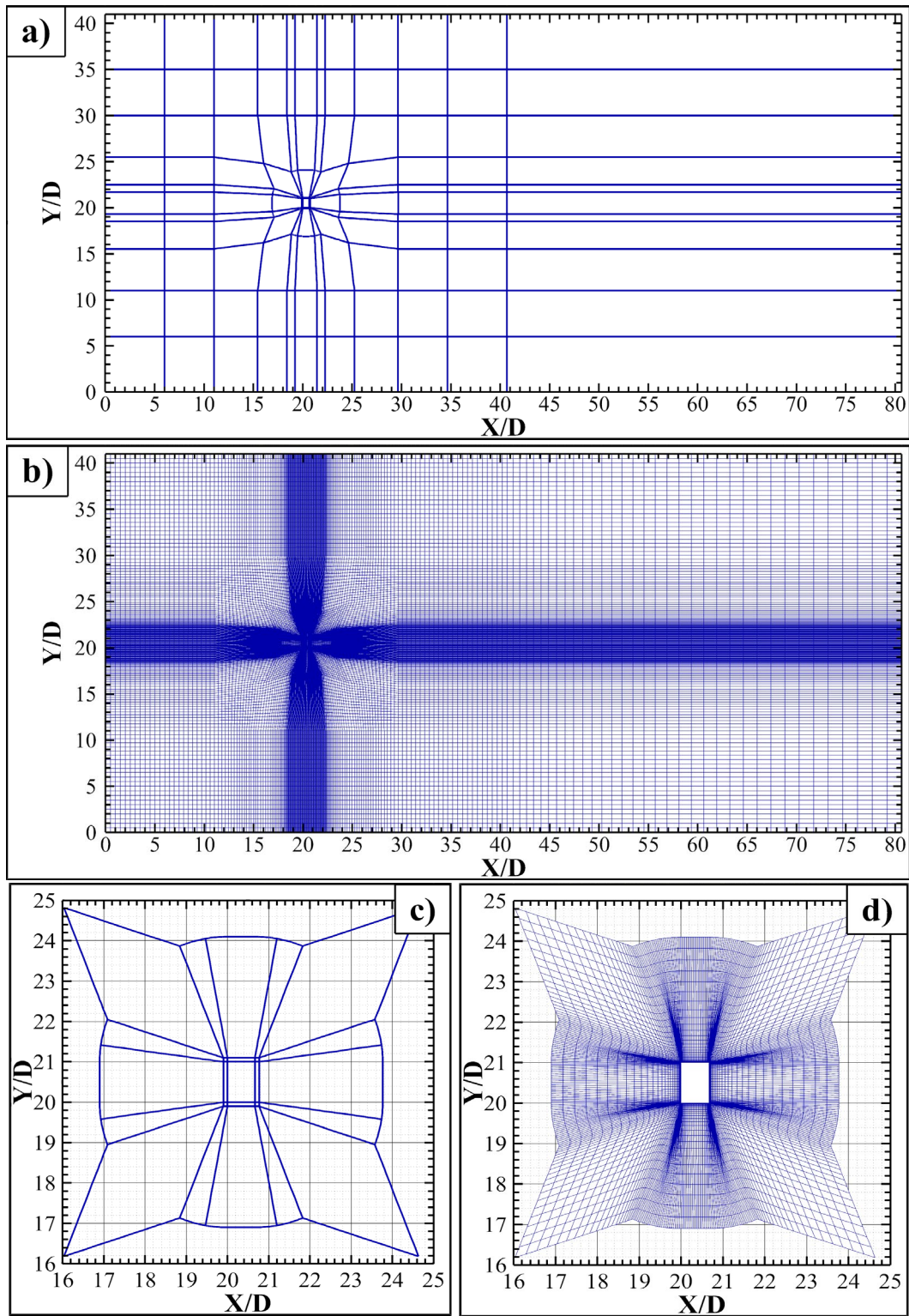


Figure 5.14. Meshing strategy for CD0R  
 a) Overall connectors, b) Overall grid distribution in x-y plane  
 c) Connectors around the building, d) Grid distribution around the building

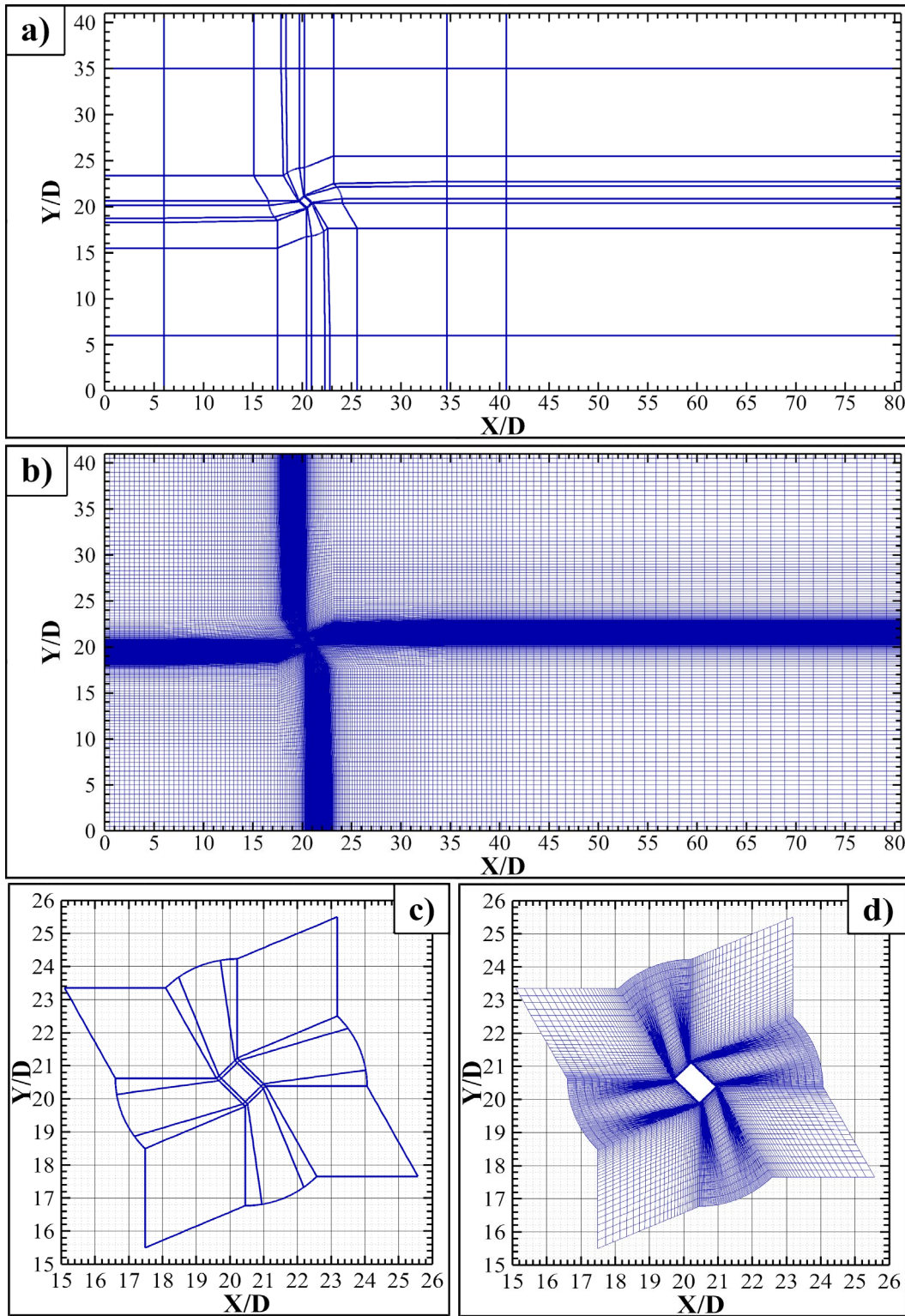


Figure 5.15. Meshing strategy for CD45  
 a) Overall connectors, b) Overall grid distribution in x-y plane  
 c) Connectors around the building, d) Grid distribution around the building

## 5.5 Boundary Conditions

The inflow boundary conditions for the computational domains were generated using CDRFG, as explained in Section (5.2) with reference velocity, power-law coefficient, integral turbulence length scales, and turbulence intensities. These parameters were directly taken for isolated tall building case from the reference numerical study conducted by Elshaer et al. in 2016. All surfaces of the target building and ground of the domains were assigned as a no-slip boundary condition, which implies that fluid velocity is zero relative to the boundary or, in other words, the tangential velocity components are zero. The symmetrical condition (i.e., symmetrical surface boundary condition) in which the normal velocity components and shear stresses are assumed to be zero were applied to the domains' lateral boundaries. The symmetrical boundary condition was also applied to the computational domains' upper boundaries considering that this condition does not affect the results with the distance of  $5H$ . However, different boundary conditions will be tested on this boundary in further studies. Figure (5.16) shows the boundary conditions applied in this study.

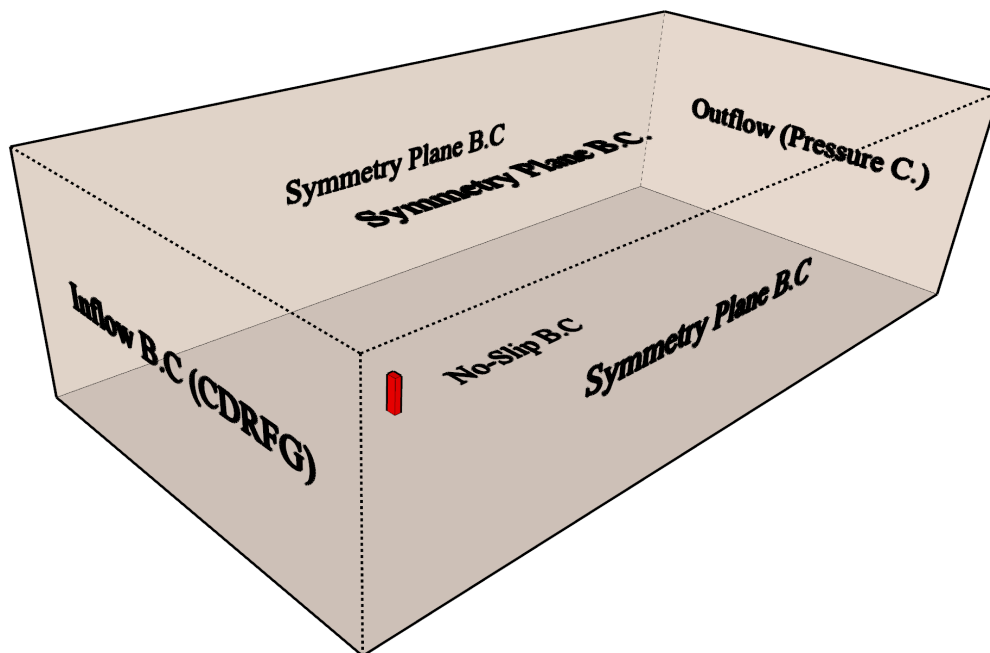


Figure 5.16. Assigned boundary conditions for computational domains

In the reference numerical study, validation of the numerical model for aerodynamic analysis of CAARC building with a geometric scale of 1:400 was performed considering the results of an experimental study that was conducted by Dragoiescu et al. in 2006 with using the RWDI wind tunnel, which had dimensions of 2.4 m wide and 2 m high. The CAARC standard tall building model under open terrain wind conditions had been analyzed with both individual and environmental buildings configurations. In this study, obtained results for the isolated CAARC tall building model under open terrain wind conditions using the numerical model and synthetic inflow turbulence generator that were mentioned in sections (5.1) and (5.2) were compared with these reference studies taking the same mean velocity, turbulence intensity, and length scale profiles. These parameters required for inflow generation were provided by Elshaer et al. (2016) and defined as follows.

- Mean Velocity Profile:

$$\bar{u}(z) = \bar{u}(z_B) \left( z / z_B \right)^\alpha \quad (5.5.1)$$

Where  $z_B$  is reference height, which is taken as the height of the building.  $\alpha$  is a power-law coefficient and equals 0.17 for this study. The mean wind velocity at building height  $\bar{u}(z_B)$  is 10 m/s.

- Turbulence intensities for each direction:

$$I_j(z) = I_j(z_B) \left( z / z_B \right)^{-d_j} \quad (5.5.2)$$

$I_j(z_B)$  refers to the turbulence intensity at the reference height for the  $j$  direction. For  $j=1, 2$  and  $3$ , this value was taken as 0.197 (i.e., 19.7%), 0.167 (i.e., 16.7%), and 0.145 (i.e., 14.5%) while the coefficient  $d_j$  was defined as 0.232, 0.154 and 0.007 respectively.

- Integral turbulence length scale profiles for each direction:

$$L_j(z) = L_j(z_B) \left( z / z_B \right)^{\epsilon_j} \quad (5.5.3)$$

$L_j(z_B)$  represents the integral turbulence length scales at the reference height for the  $j$  direction. For  $j=1, 2,$  and  $3,$  this value was provided as  $0.563$  m,  $0.147$  m, and  $0.186$  m, while the coefficient  $\varepsilon_j$  was defined as  $0.133, 0.154,$  and  $0.187$  in order.

As previously mentioned in Sub-section (5.2.2) and Section (5.4), the study cases' simulations were carried out using non-dimensional parameters within the numerical model. Therefore, reference mean wind speed velocity, turbulence length scales, were made non-dimensionalized by the  $D,$  and  $U_m.$  Furthermore, frequencies were adjusted with respect to them. These non-dimensional parameters used in this study are given in table (5.4) with reference values. Although these values are provided here for informational purposes, calculation processes of them are performed within the algorithm of CDRFG as shown in figure (5.6) and procedures which are given with (5.2.26) and (5.2.27).

Table 5.4 Parameters used for the generation of the turbulent velocity field

Parameter	Reference numerical study (Elshaer et al., 2016)	Current Study (CD0-CD0R-CD45)
$z_B, \bar{u}(z_B)$	0.4572m – 10 m/s	4 – 0.8638
$L_u(z_B), L_v(z_B), L_w(z_B)$	0.563m – 0.147m – 0.186m	4.926 – 1.286 – 1.627
$\varepsilon_1 - \varepsilon_2 - \varepsilon_3$	0.133 – 0.154 – 0.178	0.133 – 0.154 – 0.178
$I_u(z_B), I_v(z_B), I_w(z_B)$	19.7% – 16.7% – 14.5%	19.7% – 16.7% – 14.5%
$d_1 - d_2 - d_3$	0.232 – 0.154 – 0.007	0.232 – 0.154 – 0.007
$f_{m,\min}, f_{m,\max}, \Delta f$	1Hz – 100Hz – 1Hz	0.01Hz – 0.99Hz – 0.01Hz
M	100	100
N	50	50
$C_c$	10	10
Tuning distance	$z_B / 2$	$z_B / 2$

Target mean wind velocity, integral length scale, and intensity profiles obtained from these reference parameters are shown in figure (5.17). The synthesized velocity field at  $t=24$  sec is given in figure (5.18) to illustrate instant inflow boundary conditions.

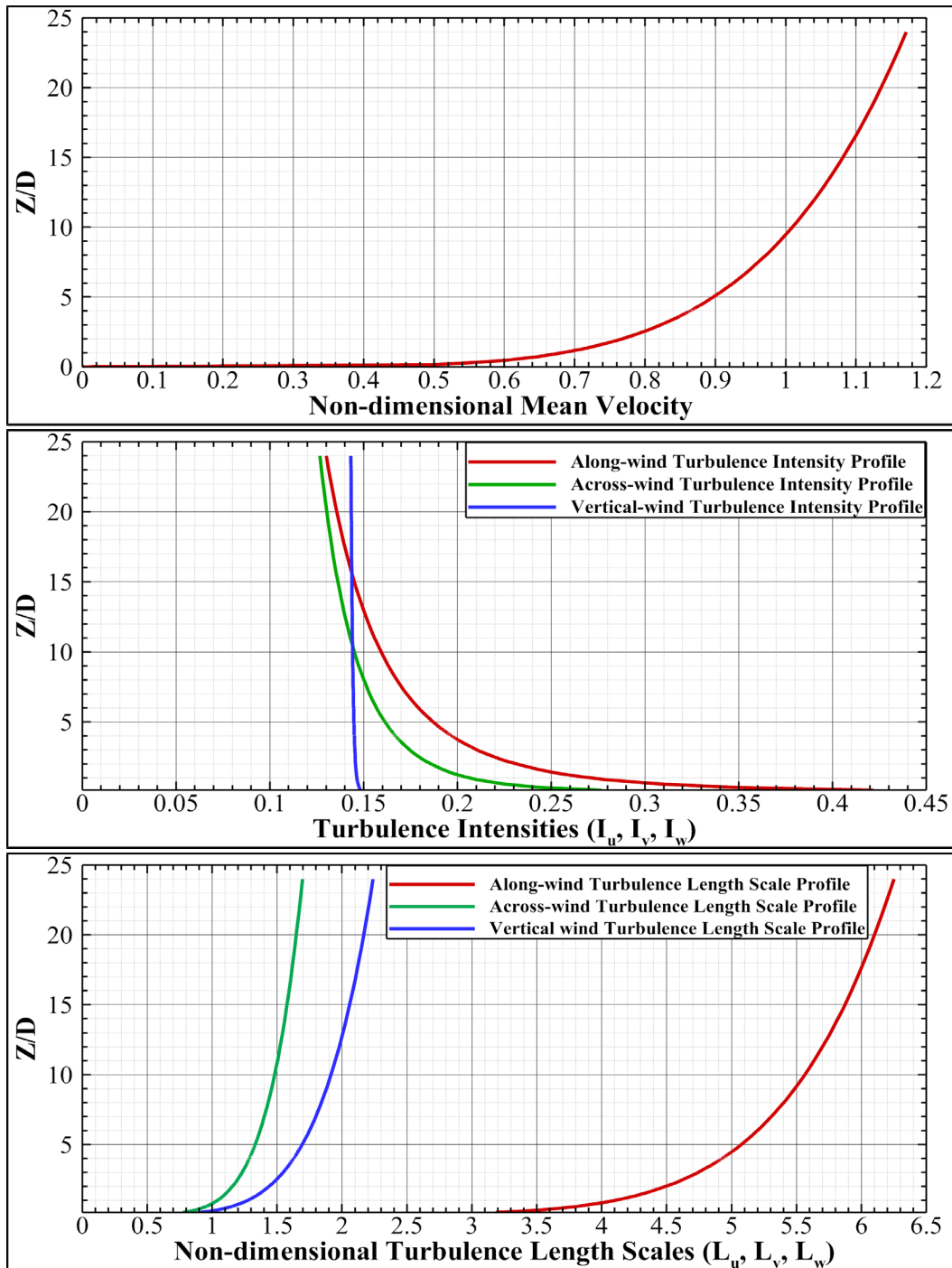


Figure 5.17. Profiles used for generation of the turbulent velocity field

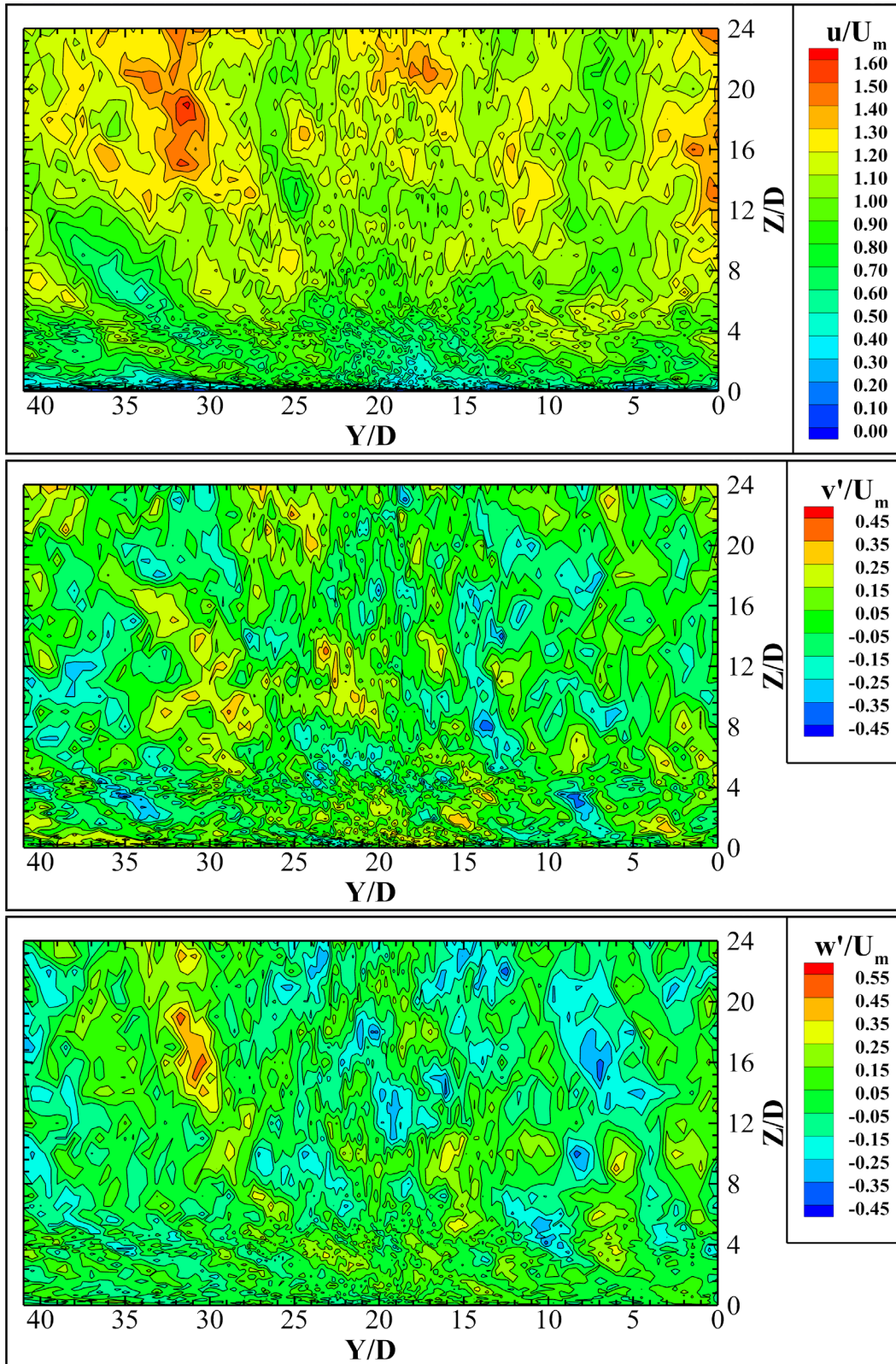


Figure 5.18. The synthesized velocity field at  $t=24 D/U$

### 5.5.1 Decomposition of Synthesized Turbulent Velocity Fields

For the inflow boundary condition, each study case's turbulent velocity fields were synthesized for 100 D/U with a 0.1 D/U sampling time step. To illustrate whether the synthesized turbulent velocities during a specified period are in good agreement with target spectra, mean velocity profile, and turbulence intensity profiles or not, three points at the building height in the region where the building coincides on the inflow plane were chosen. These points are abbreviated as ‘‘SOP’’ in this study. As long as a point's position is the same in the inflow plane for each study case, synthesized velocities have the same statistical properties since it was generated with the same parameters and seeds. Therefore, these points were selected such that their locations are the same for the study cases CD0 and CD0R. On the other hand, due to the differences in grid distribution between computational domains, these points were selected very close as much as possible to these two cases for case CD45. The purpose of this selection is to observe and show the consistency between the study cases. Table (5.5) provides the locations of these points with their statistical descriptors.

Table 5.5 Statistical observation points and their statistical descriptors

Study Case	SOP	X/D	Y/D	Z/D	$\bar{u}(z_B)$	$I_u(\%)$	$I_v(\%)$	$I_w(\%)$
Target	-	-	-	-	0.8638	19.70	16.70	14.50
	SOP-1	0.000	20.972	4.000	0.8771	21.28	13.95	14.31
CD0	SOP-2	0.000	20.523	4.000	0.8684	21.49	13.66	13.07
	SOP-3	0.000	20.028	4.000	0.8588	21.77	14.46	13.34
	SOP-1	0.000	20.972	4.000	0.8771	21.28	13.95	14.31
CD0R	SOP-2	0.000	20.523	4.000	0.8684	21.49	13.66	13.07
	SOP-3	0.000	20.028	4.000	0.8588	21.77	14.46	13.34
	SOP-1	0.000	20.976	4.000	0.8772	21.29	13.96	14.32
CD45	SOP-2	0.000	20.519	4.000	0.8682	21.49	13.67	13.07
	SOP-3	0.000	20.028	4.000	0.8587	21.77	14.46	13.34

From the observation points given in table (5.5), SOP-1 corresponds to the upper left corner, SOP-2 to the upper-middle, and SOP-3 to the upper right corner of the building for CD0 and CD0R when viewed from the along-wind direction. Figures (5.19) and (5.20) show the synthesized velocity-time histories in each direction at the SOP-1 for study cases. If these two figures with the table (5.5) are examined, one may conclude that the synthesized velocities are almost identical for each study case. This typical situation is directly related to the point's height since target spectrums, intensities, length scales, and mean velocities are defined based on the elevation, as mentioned in Sub-chapter (5.2). Small differences between obtained mean velocities and intensities at these points in study cases are due to the locations of points in the across-wind direction. Correspondingly, also considering the same domain dimensions and grid distributions, it can be stated that CD0, CD0R, and CD45 study cases have the same inflow boundary conditions. Therefore, the following figures from (5.21) to (5.26) are given to represent all study cases. On the other hand, it is observed in figures (5.19) and (5.20) that obtained mean values deviate slightly from the target mean values because of the small contributions of the velocity fluctuations in the along-wind direction. Although these components must not have mean values considering their definitions given in Sub-section (2.2.2), these deviations are due to summation of the round-off errors that occur while calculating each of  $M \times N$  frequencies' contributions to the instantaneous velocity at a certain time. Besides, truncation errors that arise from solving non-linear equations for wavenumber corrections and accuracy of the RNG techniques used in the generation induce that divergence. Even if there is the possibility of detecting these errors on a point-by-point basis and introducing additional conditions that can reduce them as much as possible, it is thought that these procedures would disrupt the chaotic nature of turbulence in the synthesized velocity field. For this reason, such procedures were not included in the algorithm used in this study.

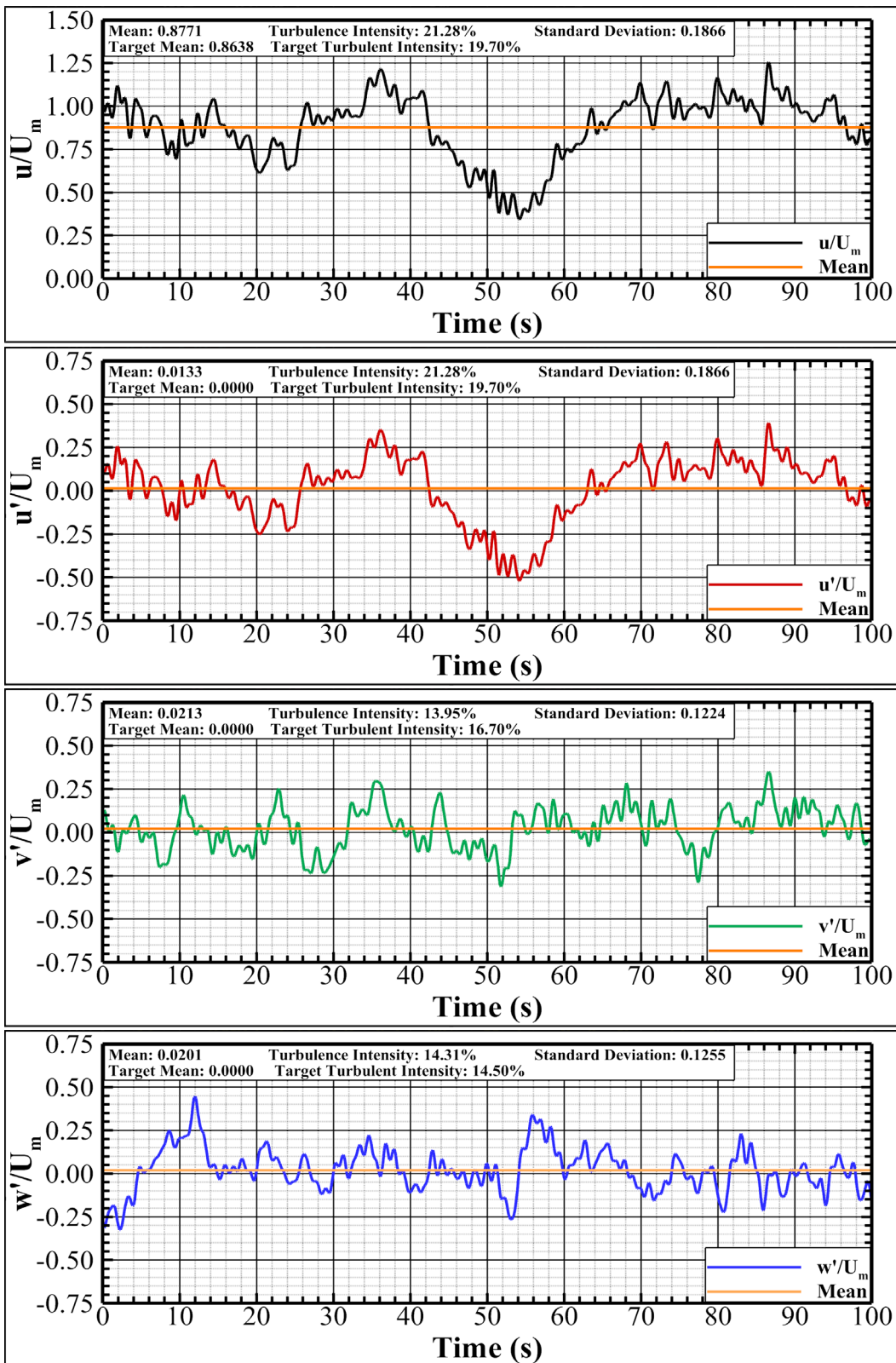


Figure 5.19. Velocity-time histories at SOP-1 for CD0 and CD0R

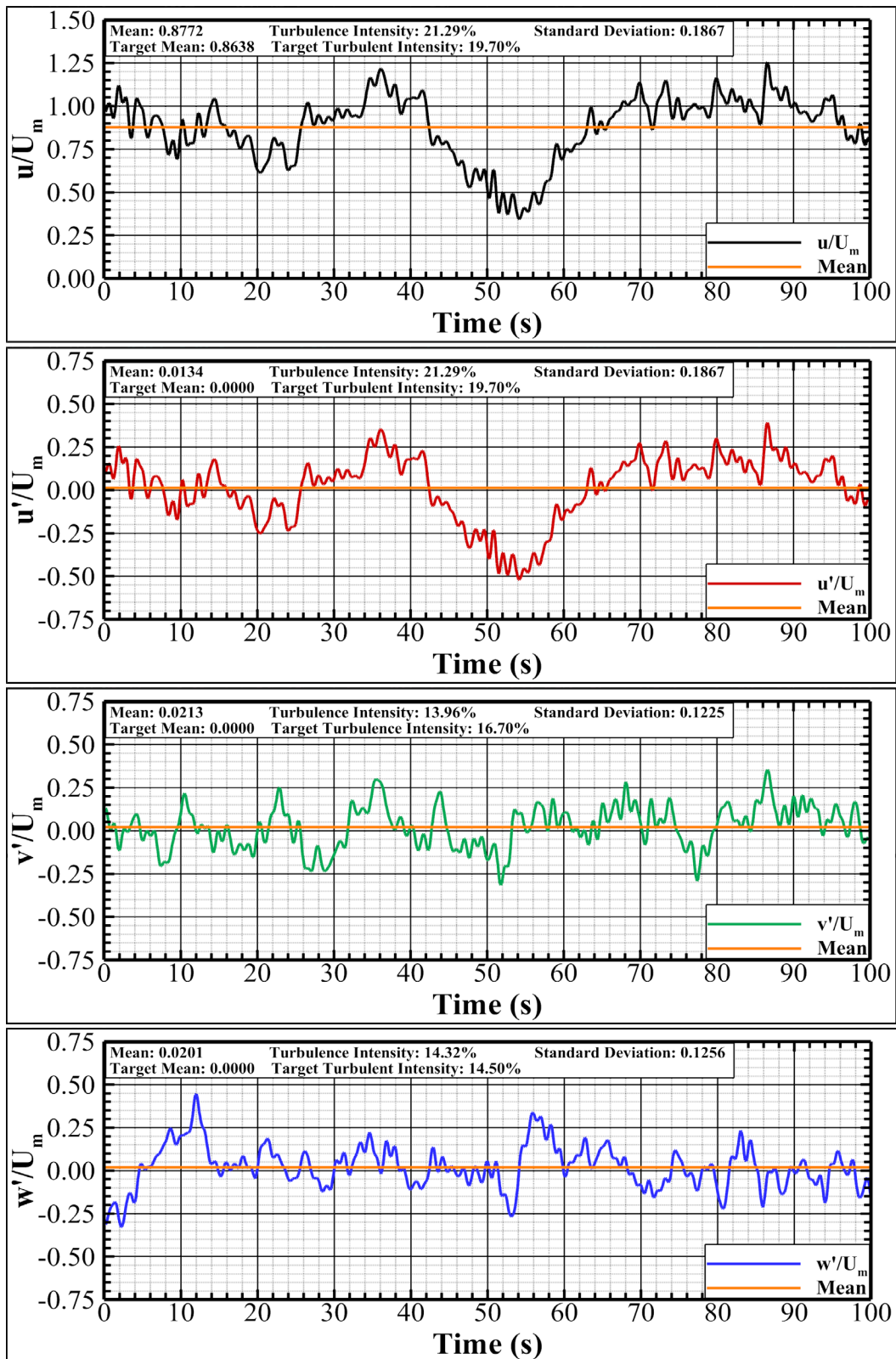


Figure 5.20. Velocity-time histories at SOP-1 for CD45

The mean velocity profiles in the along-wind direction obtained over the vertical lines passing through the selected points are demonstrated in figure (5.21). It is seen that they follow the target velocity profile with acceptable accuracy, although there are some deviations from point to point due to the aforementioned reasons.

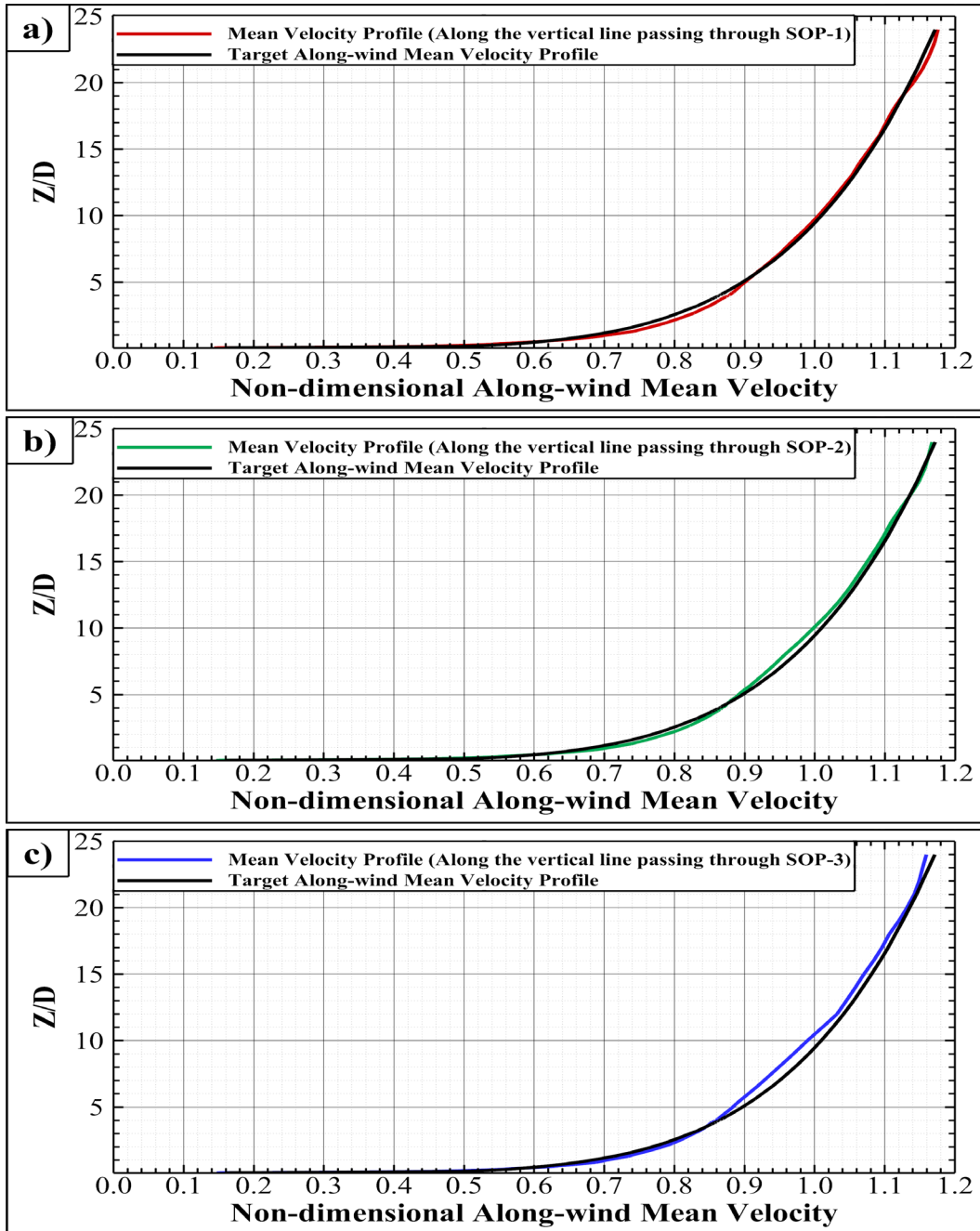


Figure 5.21. Comparison of along-wind mean velocity profiles Along the vertical line passing through a) SOP-1, b) SOP-2, c) SOP-3

The synthesized velocities at selected points are compared with each other in figure (5.22). Although their frequency sets and heights correspondingly desired mean velocities, turbulence intensities, length scales, and spectrums are the same, the phase shifts and amplitude differences (i.e., vertical shifts) at any instant are seen clearly between selected points. The phase shift and vertical shift can be defined as parameters that indicate how far the signal or harmonic function differs from its general position horizontally or vertically in order. In this figure, the reason for these shifts is due to the positions of observation points (i.e., SOP) in the across-wind direction. However, if the algorithm given in figure (5.6) is examined, one may conclude that wavenumber distribution, location, decay coefficient, and especially target correlation have great importance in how the velocities are distributed during the synthesizing. Nevertheless, when phase and vertical shifts are ignored, it is observed that the synthesized velocities in each direction have similar tendencies within themselves at similar time intervals. These tendencies are directly related to the selected frequency range and frequency bandwidth to represent the target spectrum. Figure (5.22) also indicates the uniqueness of the synthesized velocities in each direction at any point on the inflow plane.

Obtained turbulence intensity profiles over the vertical lines passing through the selected observation points in each direction are given in figure (5.23). It is observed that obtained intensities differ partially from the target value with an accuracy that varies depending on the point's elevation. This may be caused by round-off errors in mean velocities and frequency-based oscillations on target spectra that alter based on the point's vertical location. Synthesized spectrums are calculated with the equation (5.5.4) and given for selected points in figures from (5.24) to (5.26).

$$S_i(f_{m,n}) = (u_{i,rms}^2 N) / \Delta f \quad (5.5.4)$$

In general, it can be stated that obtained intensities and spectrums are in good agreement with target profiles and spectra. Besides, the promising accuracy of the CDRFG used in this study can be further increased in the light of long-term studies due to the variety of parameters required for synthesizing.

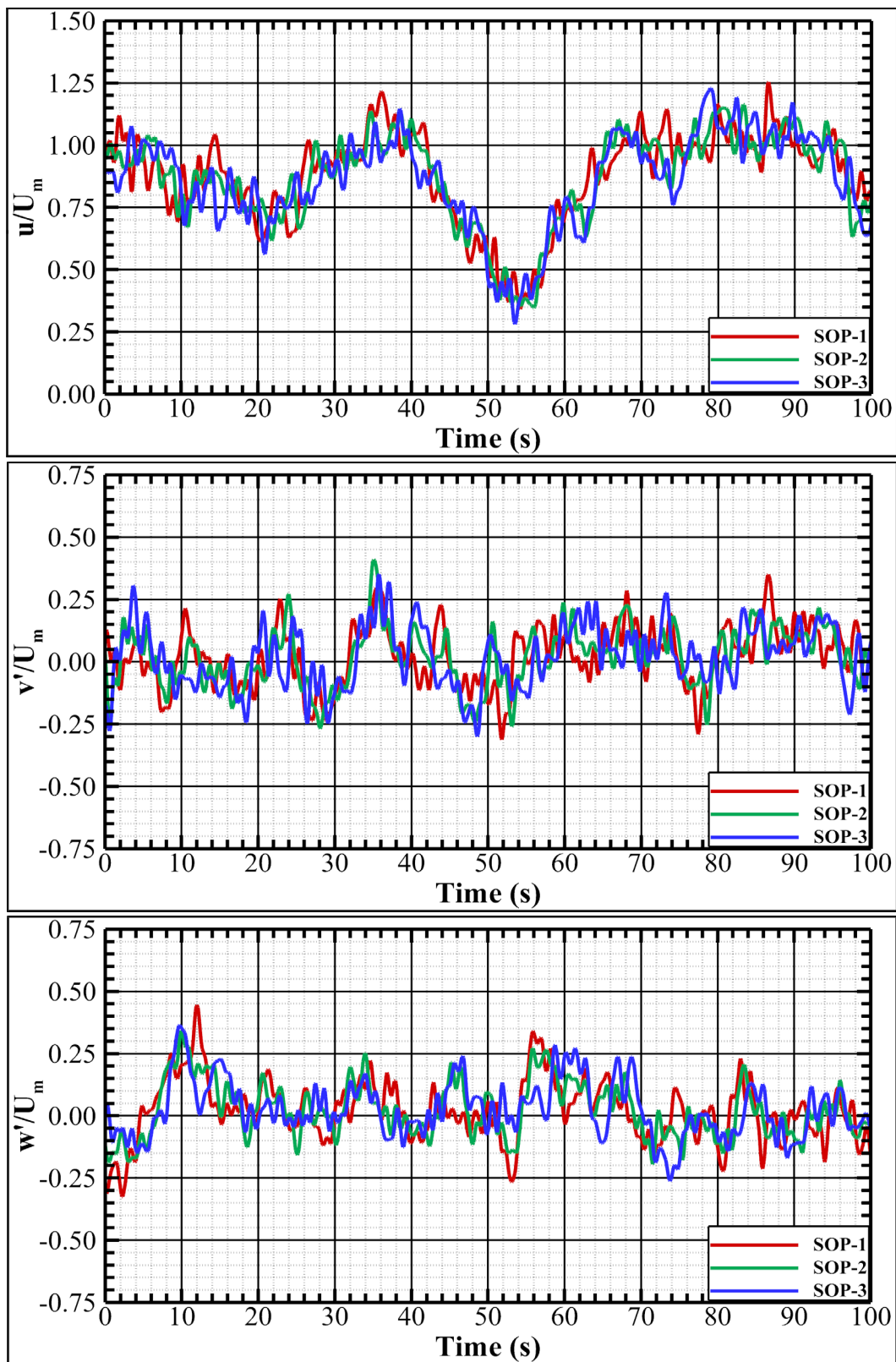


Figure 5.22. Comparison of velocity-time histories

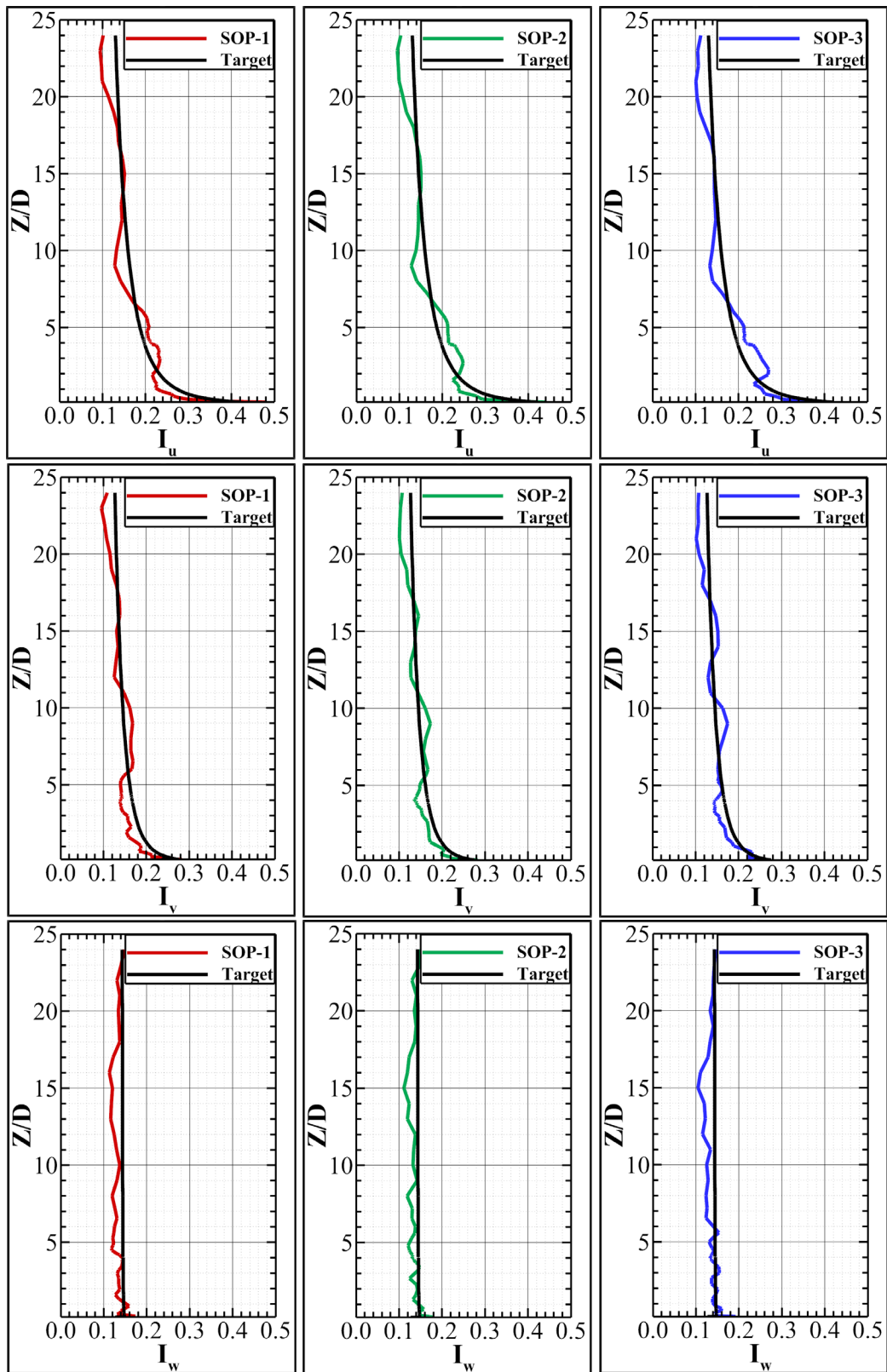


Figure 5.23. Comparison of turbulence intensity profiles

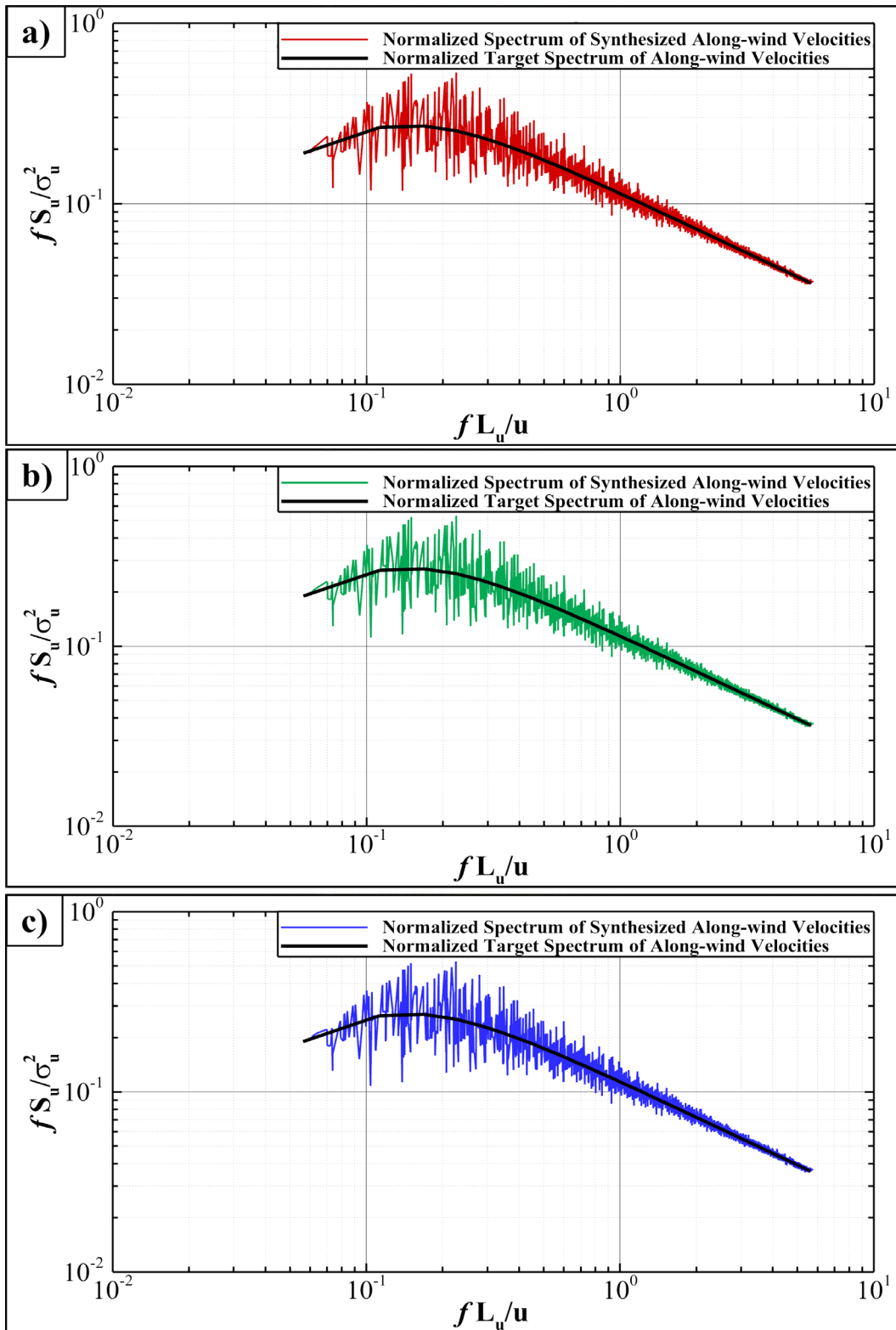


Figure 5.24. Comparison of along-wind spectra with von Karman spectrum  
a) At SOP-1, b) At SOP-2, c) At SOP-3

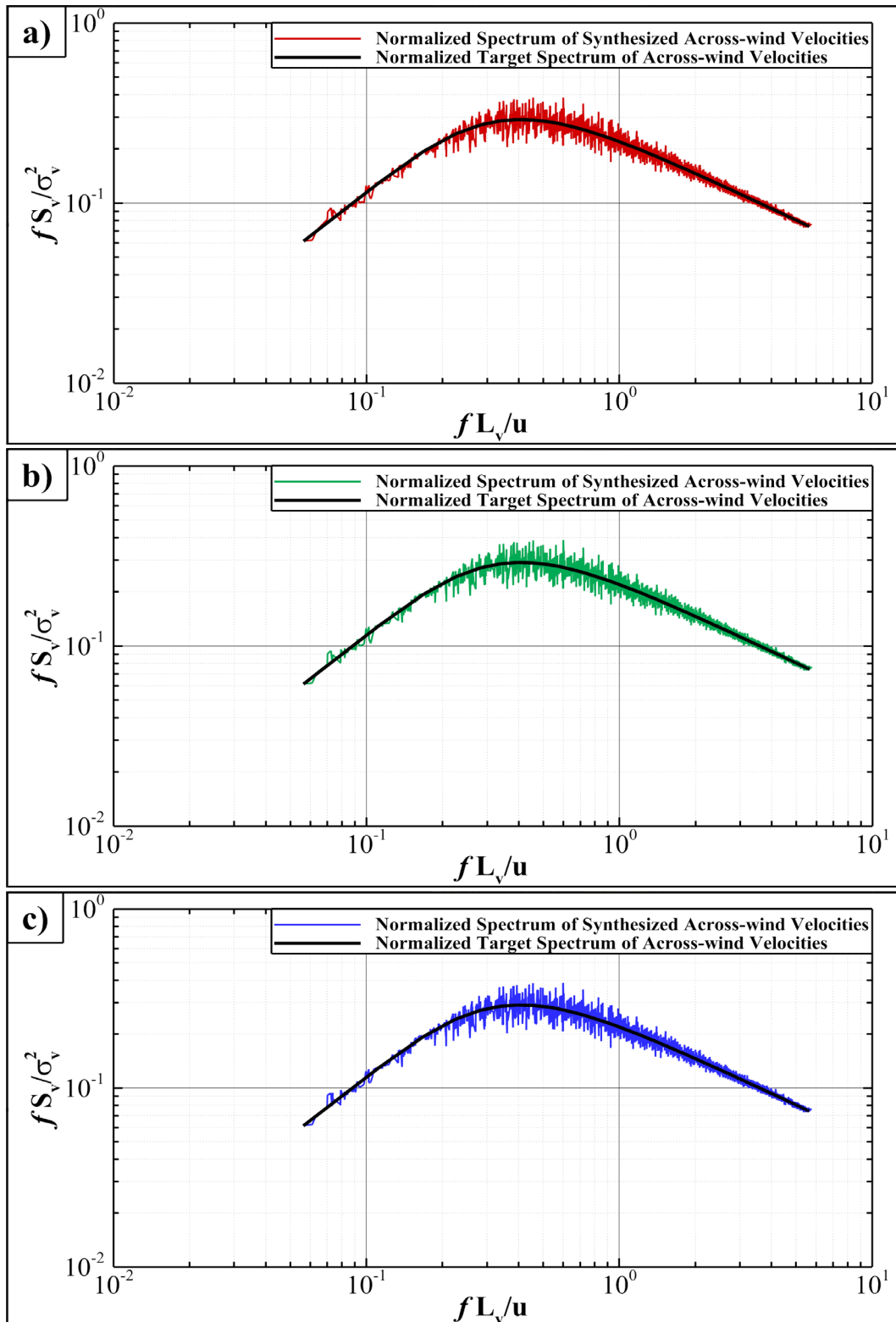


Figure 5.25. Comparison of across-wind spectra with von Karman spectrum  
a) At SOP-1, b) At SOP-2, c) At SOP-3

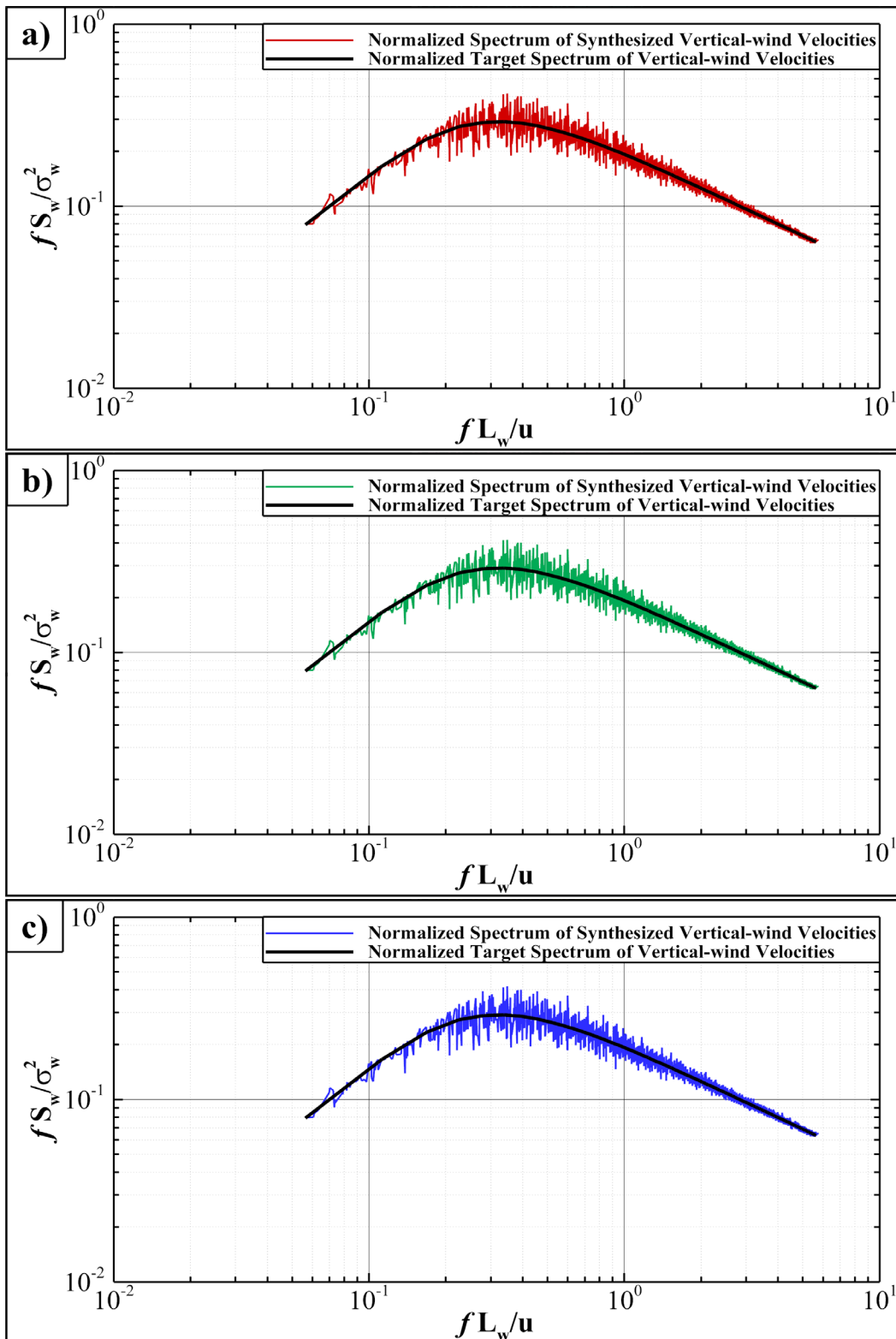


Figure 5.26. Comparison of vertical-wind spectra with von Karman spectrum  
 a) At SOP-1, b) At SOP-2, c) At SOP-3

## CHAPTER 6

### RESULTS AND DISCUSSION

In this chapter, the results of the simulations performed under the boundary conditions given in Section (5.5) are examined and presented. After conducting a mesh independence study with CD0 and CD0R study cases, obtained pressure coefficients on CAARC building model for CD0 case were compared with the results obtained from reference experimental and numerical studies, which were provided by Elshaer et al. in 2016. In order to observe the effects of the numerical model's accuracy on obtained results, flow fields obtained from the S-A RANS and S-A DES models for study case CD0 were compared, and results are presented. Furthermore, the effects of wind angle of attack on both pressure coefficients on the building surfaces and the flow patterns around the building are analyzed by comparing the results of CD0 and CD45 study cases.

#### 6.1 Grid Independence Study

In order to confirm whether the simulations are dependent or independent of the grid, simulations were conducted with a coarser computational domain CD0R and finer computational domain CD0. The meshing strategies and detailed information about these domains are provided in Section (5.4). As a result of these simulations, obtained velocity fields around the building by using S-A based DES model are given in figure (6.1) for CD0R (a) and CD0 (b). In this figure, positive velocities near the building's windward surface are observed, while negative velocities occur near the leeward surface. On the top surface, negative velocities are captured within the reverse flow (i.e., tip vortex formation), and the shear layer is also seen. When these velocity fields are compared, it is concluded that simulations are independent of the grids. Numerical costs of these simulations are provided in Sub-section (6.5).

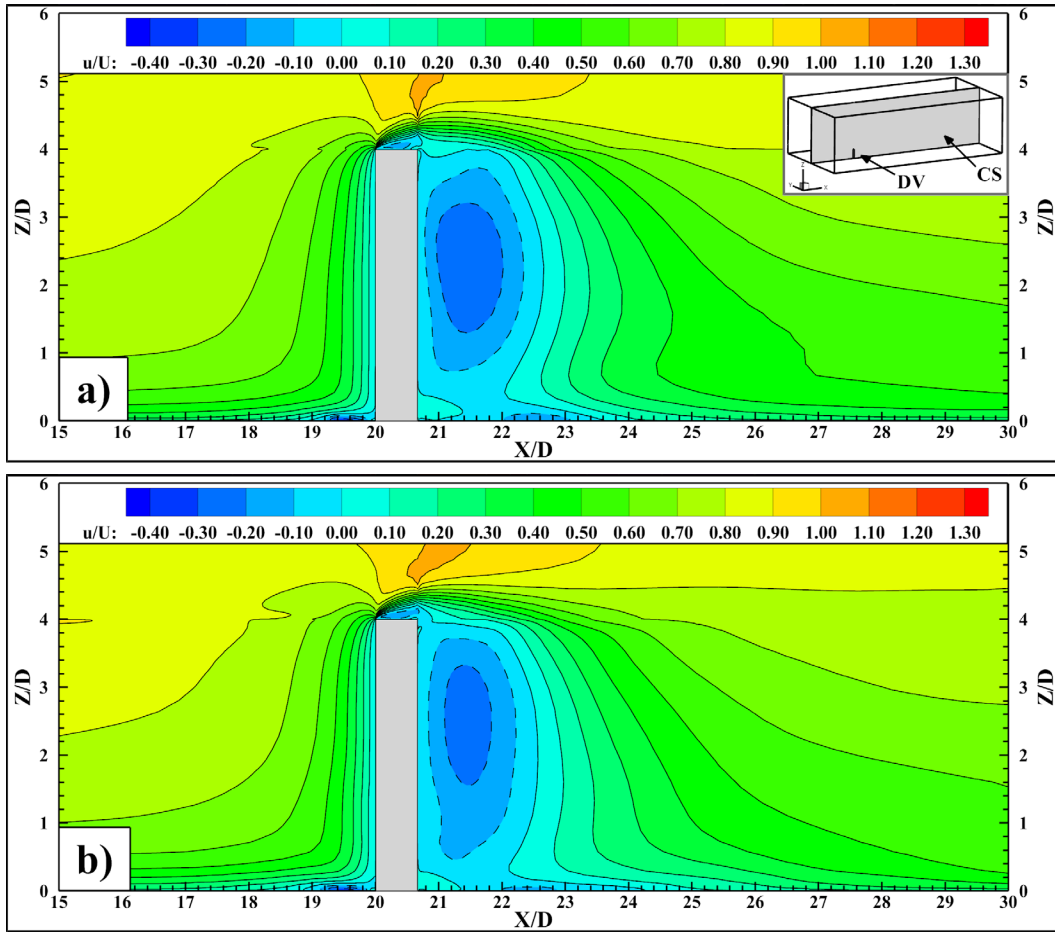


Figure 6.1. Non-dimensional mean velocity field of CD0 (a) and CD0R (b)

## 6.2 Analysis of Mean and RMS Pressure Coefficients

### 6.2.1 Mean Pressure Coefficients: Study Case CD0 (0° AOA)

As a common practice, measured pressure values on building surfaces are provided in terms of non-dimensional pressure coefficients  $C_p$  by normalizing them with reference mean dynamic pressure. (Simiu & Yeo, 2019) This parameter is obtained as given below.

$$C_p = \frac{P - P_0}{(0.5)\rho(\bar{u}(z_B))^2} \quad (6.2.1)$$

In the equation (6.2.1),  $P$  is time-averaged static pressure on building surface,  $P_0$  is reference static pressure taken far enough from the building,  $\rho$  is the air density taken as  $1.225 \text{ kg/m}^3$ , and  $\bar{u}(z_B)$  is reference mean wind speed at the building height. Figure (6.2) shows distributions of mean pressure coefficients on the building's windward surface for study case of CD0 obtained using S-A RANS (a) and S-A DES (b) numerical models.

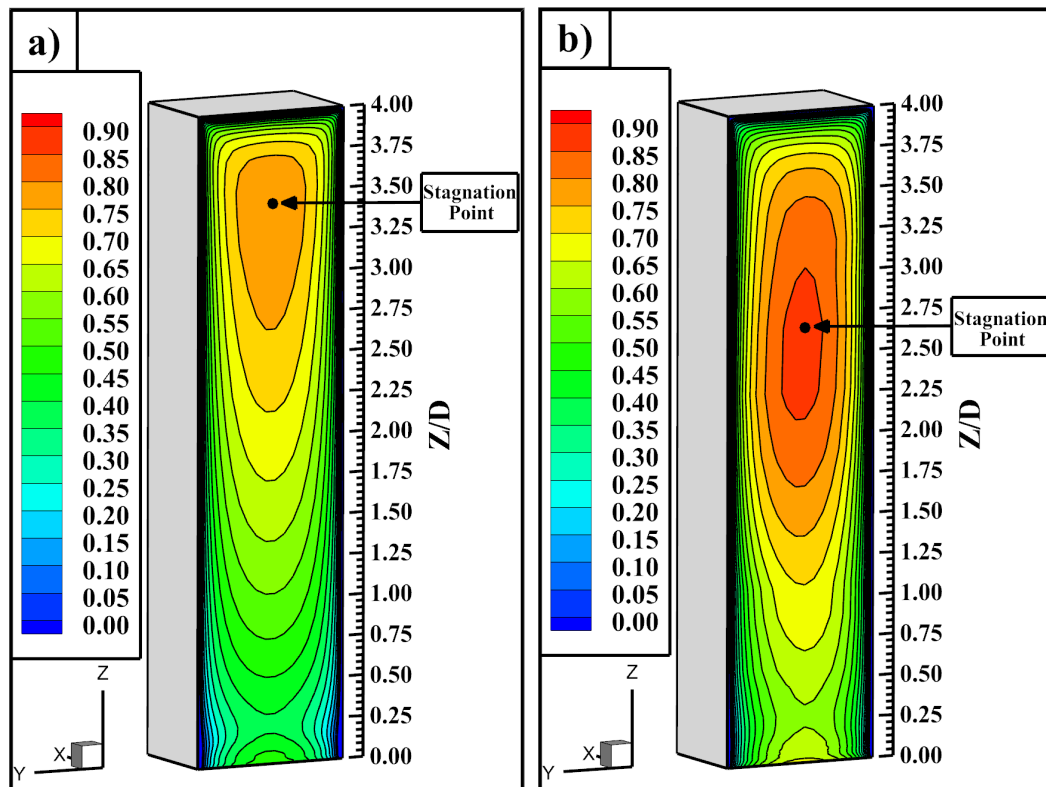


Figure 6.2. Mean  $C_p$  distributions on the windward surface ( $0^\circ$  AOA)  
a) obtained by using S-A RANS, b) obtained by using S-A DES

As highlighted in Section (4.3), one of the inferences made from the articles reviewed on this topic is that mean pressure coefficients on the building's front (windward) surface mainly depend on the mean velocity profile. When the given distributions are examined by considering that inference, it is concluded that they have a similar pattern for both numerical models. On the other hand, it is observed that the pressure coefficients obtained with the S-A RANS model are relatively less, while the

location of the stagnation point is higher with respect to the S-A DES model. Since these simulations are performed using the same mean wind velocity profiles, the variation in the stagnation point's height is seen directly related to the numerical model's accuracy. In principle, DES models provide more accurate results than RANS models. In figure (6.3), current S-A RANS and S-A DES solutions are compared with experimental (BLWT) and numerical results provided by Elshaer et al. (2016). As a result of this comparison, one may observe that S-A RANS model provides a similar pattern with slightly underestimated mean pressures compared to the reference numerical study, which was conducted by using LES with CDRFG. It is also noticed that the stagnation point's location is higher than the reference experimental study for both of these cases. On the other hand, obtained pressure coefficients with current S-A DES model appear to be closer to the experimental study.

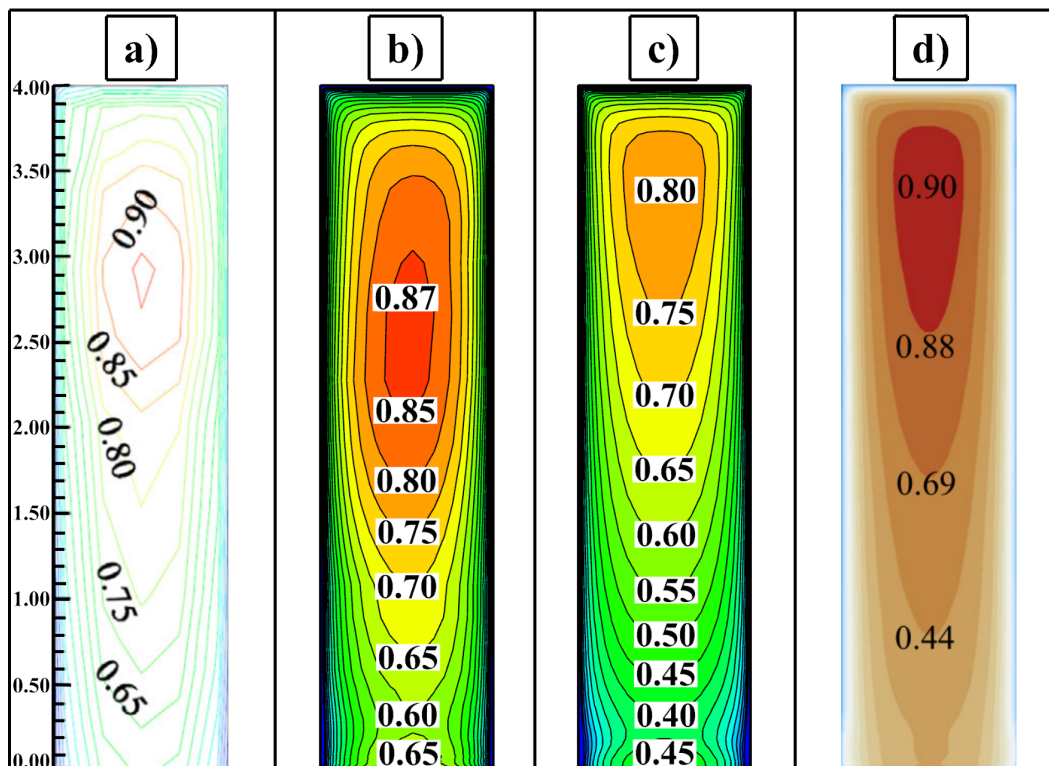


Figure 6.3. Comparison of mean  $C_p$  on the windward surface ( $0^\circ$  AOA)  
a) Reference experimental study (Dragoiescu et al., 2006), b) Current S-A DES  
c) Current S-A RANS, d) Reference numerical study (Elshaer et al., 2016)

According to Elshaer et al. (2016), the main reason for the discrepancy between the experimental and the LES model, especially on the stagnation point, was linked to the prescribed frequency range for the numerical simulation that may differ with the wind tunnel due to the BLWT wind tunnel's incapability to produce lower frequencies (i.e., Larger eddies). However, with the same input data used in S-A DES model, it is shown that better agreement with the experimental results can be reached. The height of the stagnation point corresponds to  $2.625Z/D$  for S-A DES, while this value is roughly  $2.9Z/D$  in the wind tunnel. Although this point's position is a bit lower for S-A DES, it is clear that the pressure coefficients obtained with S-A DES and CDRFG on front face of the building are promising and even more accurate than the reference numerical study compared with the experimental study. Besides, based on these results, it is recognized that solving viscous sublayer directly instead of certain wall treatments leads to a noticeable accuracy increase on obtained mean pressure coefficients at lower heights of the building. Several studies to support this observation are included in Sub-section (4.2.2)

Similar to mean pressure distribution on the building's windward side, negative pressure distributions on the leeward (rear) side also depend on mean velocity profile. As mentioned in Section (4.3), several studies referred that these negative pressure coefficients are also sensitive to turbulence intensities. In figure (6.4), obtained negative pressure coefficients with both S-A RANS and S-A DES models are compared with the reference numerical and experimental studies. In the light of this comparison, one may observe that S-A RANS model appears insufficient to capture negative pressures while S-A DES model provides closer results to the reference numerical study. Although all models predict negative pressures less with respect to the reference experimental study, it is seen that S-A DES model cannot provide better accuracy than the reference numerical study. It is believed that any improvement to the accuracy of CDRFG compiled for this study will increase the performance of the DES model in capturing negative pressure coefficients.

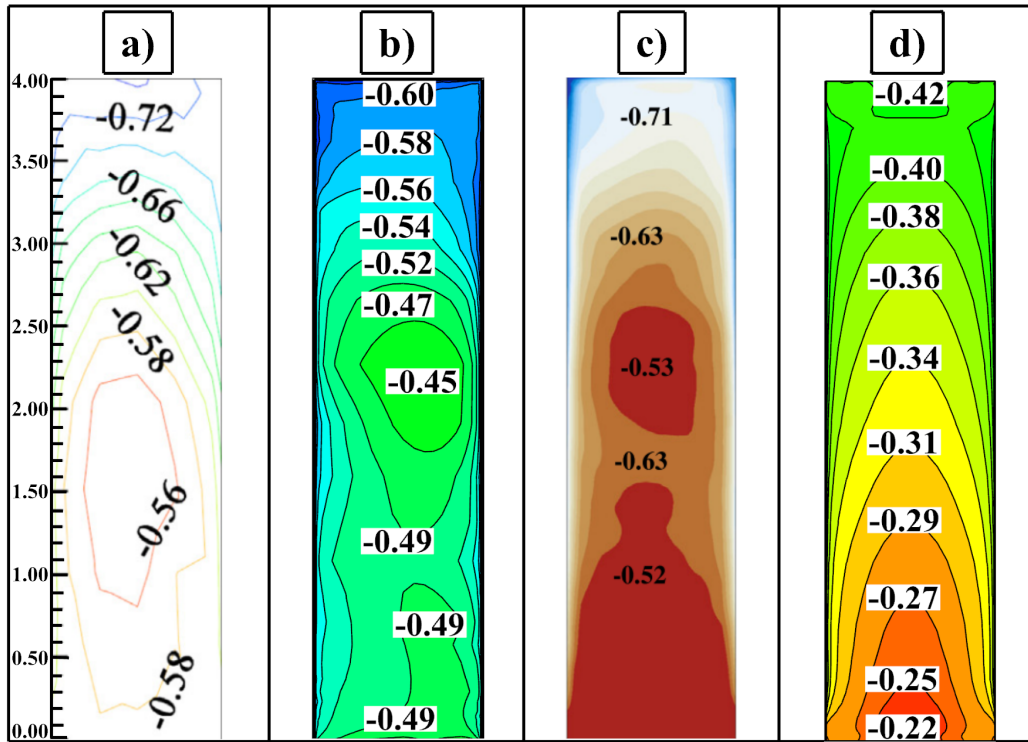


Figure 6.4. Comparison of mean  $C_p$  on the leeward surface ( $0^\circ$  AOA)  
 a) Reference experimental study (Dragoiescu et al., 2006), b) Current S-A DES  
 c) Reference numerical study (Elshaer et al., 2016), d) Current S-A RANS

In the literature, comparison and validation of numerical and experimental studies on tall buildings' aerodynamics are generally carried out based on the pressure coefficients around target building at the height of  $2H/3$  (i.e., the height of stagnation point), where  $H$  is the building height. Accordingly, figure (6.5) demonstrates the comparison of obtained pressure coefficients around CAARC tall building at this height with the reference studies. If the interval between  $0$  and  $1.5x/D$  that indicates positive pressures on the building's windward (front) surface at this level is examined, one may notice that S-A DES model with CDRFG provides almost the same pressure coefficients as the wind tunnel. It also appears that the reference numerical study (LES+CDRFG) overestimated the positive pressure coefficients, while S-A RANS model underestimates them. Considering S-A RANS model's performance in this range, it is seen that the effect of the synthesized velocity field (i.e., incoming flow) together with the accuracy of the numerical model is very important to predict pressure coefficients on the building.

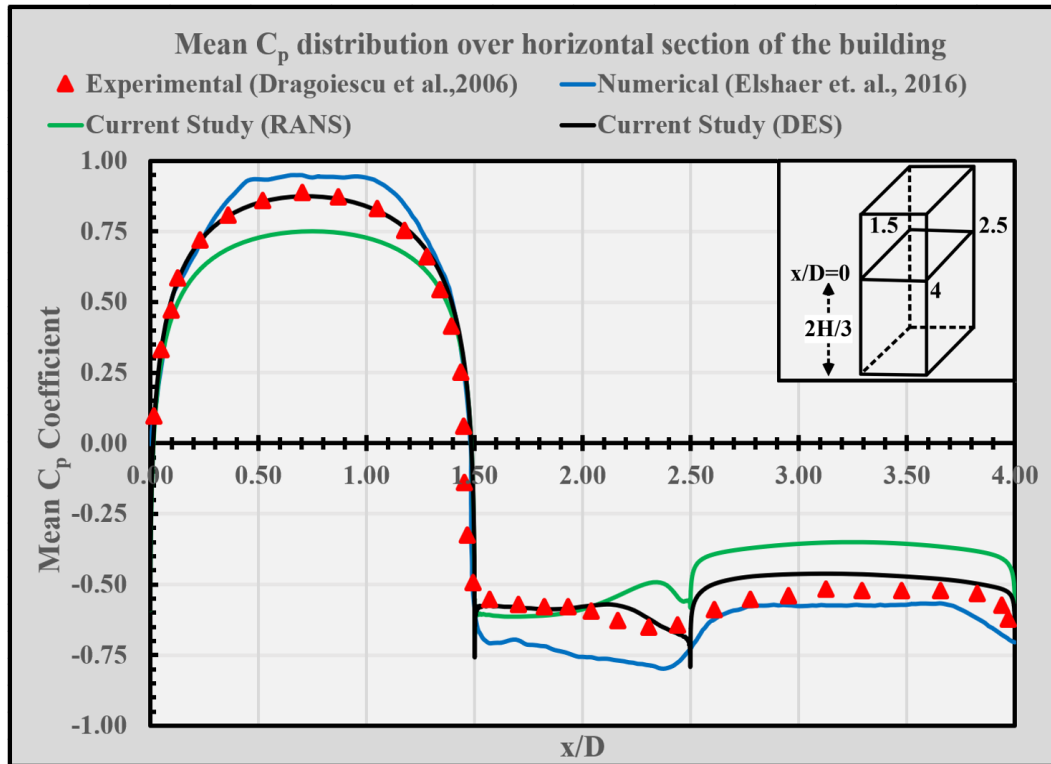


Figure 6.5. Mean  $C_p$  distributions over the horizontal section ( $0^\circ$  AOA)

Obtained negative pressure coefficients with S-A DES on the building's side surface represented by the interval between  $1.5x/D$  and  $2.5x/D$  are in good agreement with the wind tunnel data. Therefore, it is deduced that S-A DES model with CDRFG resolves the flow separation resulting from sharp corners and edges quite well. As mentioned in Section (4.3), if it is considered that the numerical studies in the literature generally do not provide the same accuracy on the side and rear walls as estimating positive pressures on windward surface of the building, obtained results are very promising.

In the interval between  $2.5x/D$  and  $4x/D$ , which depicts negative pressures on leeward (rear) side of the building, the same inferences made based on figure (6.4) are valid. Nevertheless, it is noticed that negative pressure coefficients obtained with S-A DES model are closer to the reference experimental study at this height than they appear in figure (6.4).

## 6.2.2 The Effects of AOA on Mean Pressure Coefficients

The building surfaces are named as given in figure (6.6) to convey the effects of wind angle of attack on mean pressure coefficients obtained on these surfaces.

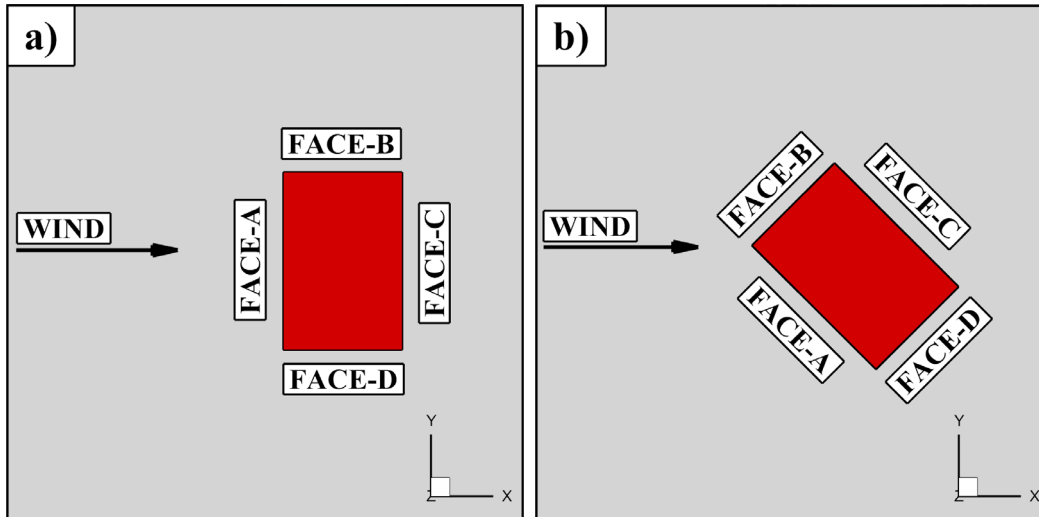


Figure 6.6. Nomenclature of building surfaces for  $0^\circ$ AOA (a) and  $45^\circ$ AOA (b)

Based on this nomenclature, mean pressure coefficients obtained on Face-A (windward surface for  $0^\circ$  AOA) and Face-B (crosswind left side for  $0^\circ$  AOA), which are directly exposed to the wind at an angle of  $45^\circ$ , are given in figure (6.7) for both study cases. It is noticed that positive pressure coefficients obtained on Face-A in the study case of  $0^\circ$  AOA (CD0) are higher than the study case of  $45^\circ$  AOA (CD45), and their distribution is concentrated in the middle zone of that face since the wind approaches the surface directly. Maximum pressure coefficients are approximately at the height of  $2.625Z/D$  for CD0 while at the height of  $2.27Z/D$  for CD45, and its value is 0.87 for wind incidence angle of  $0^\circ$  while it is 0.73 at an incidence angle of  $45^\circ$ . As a result of a change in the wind incidence angle, positive pressure coefficients are observed on Face-B in contrast to negative pressure coefficients (suction) observed on the same plane at a wind incidence angle of  $0^\circ$ . Besides, higher positive pressure coefficients in  $45^\circ$  AOA are concentrated along the windward edge between Face-A and Face-B. The surfaces directly exposed to the wind have positive

pressure coefficients. Therefore, the building configuration is quite important at these pressure coefficients. At both incidence angles of wind, it is seen that positive pressure coefficients increase with the height up to the level of stagnation point and then begin to decrease towards the tip of the building.

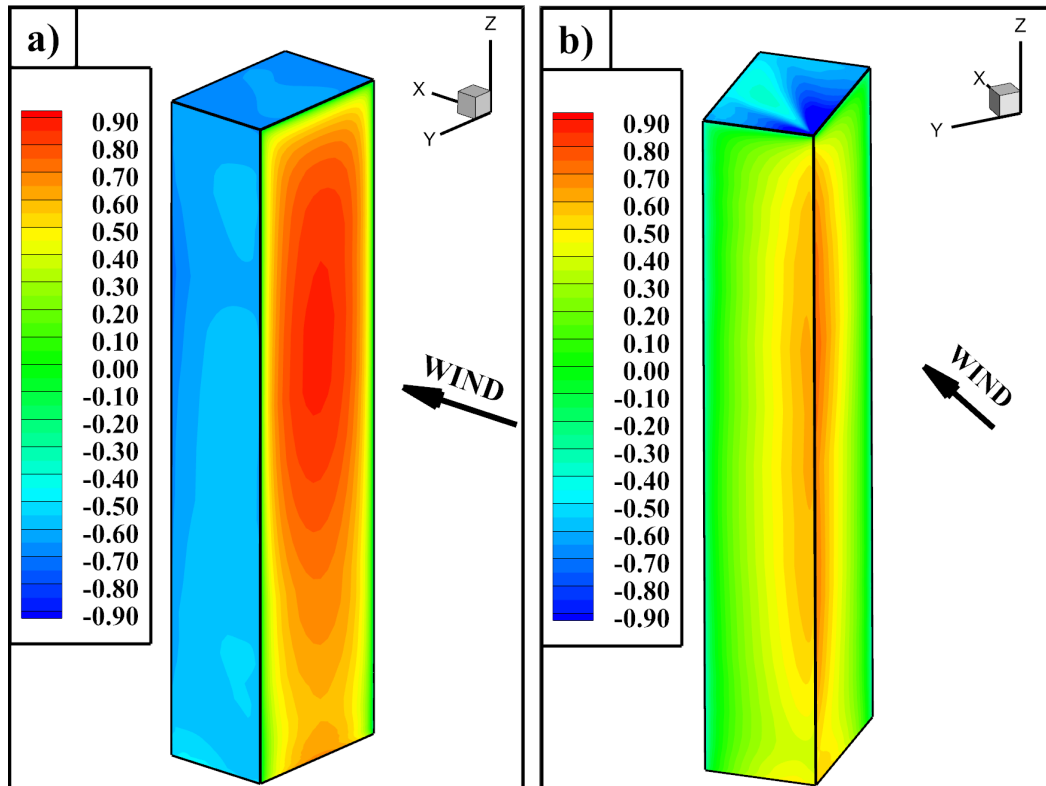


Figure 6.7. The effect of AOA on positive pressure coefficients  
a)  $0^\circ$  AOA obtained by S-A DES, b)  $45^\circ$  AOA obtained by S-A DES

Figure (6.8) depicts obtained negative pressure coefficients on Face-C (windward side for  $0^\circ$  AOA) and Face-D (crosswind right side for  $0^\circ$  AOA) for incidence angles of  $0^\circ$  and  $45^\circ$ . When the wind approaches the building with an angle of  $0^\circ$ , B and D faces have almost the same negative pressure coefficients and distribution. Therefore, these faces show the same characteristics, and although negative pressure coefficients increase towards the windward edge of Face-B, their distribution is almost uniform. On the other hand, it is observed that the distribution of negative pressure coefficients takes shape depending on the width of the faces C and D at an incidence angle of  $45^\circ$ .

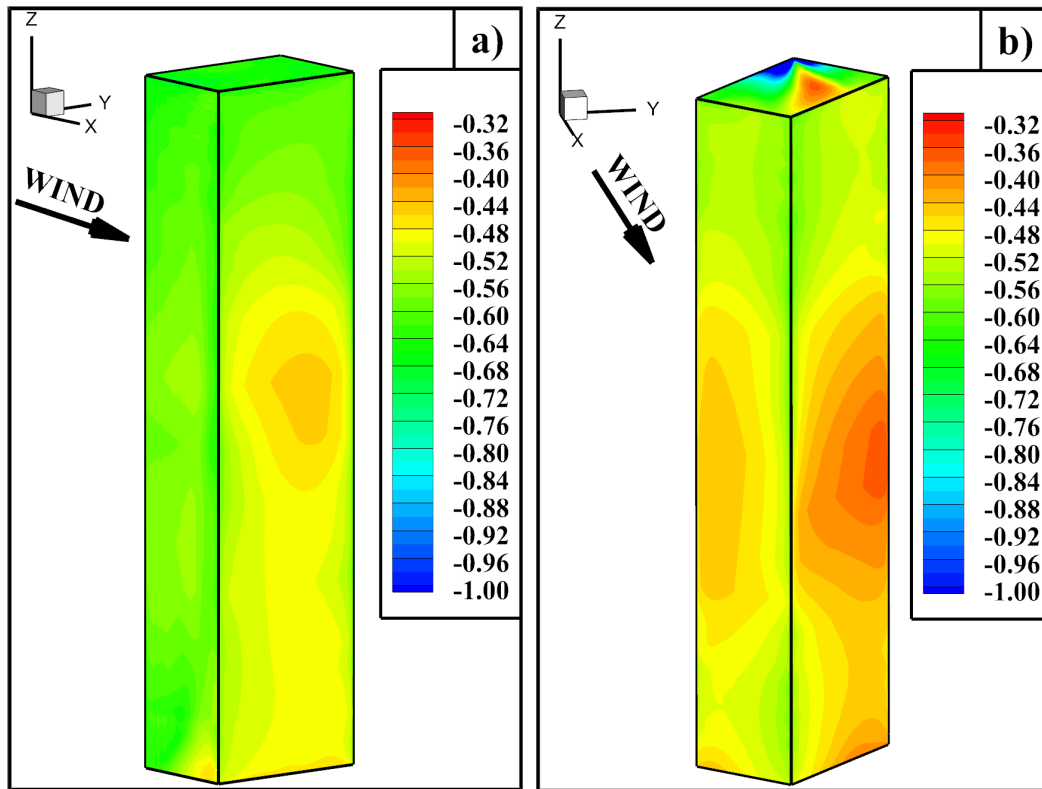


Figure 6.8. The effect of AOA on negative pressure coefficients  
a) 0°AOA obtained by S-A DES, b) 45°AOA obtained by S-A DES

For 0° AOA, negative pressure coefficients decrease from the tip of the building to the center of Face-C (at the height of  $2.2Z/D$ ) and then increase to the bottom of that surface. The variation of these coefficients depending on the height is noticeably smaller than the variation of positive pressure coefficients. Similar behavior is noticed on both Face-C and Face-D at an incidence angle of 45°. However, it is seen that minimum negative pressure coefficients are concentrated near the windward edges of these surfaces at the height of  $1.7Z/D$  rather than the center of the surfaces. In addition, obtained negative pressure coefficients on faces C and D are relatively smaller than negative pressure coefficients at an incidence angle of 0°. Correspondingly, obtained minimum negative pressure coefficient is 0.42 for 0° AOA while it is 0.37 for 45° AOA. Therefore, although it may be deduced that negative pressures decrease depending on incidence angle, this statement is required to be studied and observed from more than two angles.

When the building top surface is examined at a wind incidence angle of  $0^\circ$ , an almost uniform distribution is observed, although there is a slight decrease in the negative pressure coefficients towards the center of the surface. On the contrary, at an incidence angle of  $45^\circ$ , an increase in negative pressure coefficients on the top surface's windward corner is seen since it is exposed directly to the wind. This is related to the formations of two separate tip vortices observed in this case. Furthermore, negative pressure coefficients relatively decrease to the leeward edge towards Face-C compared to the  $0^\circ$  AOA.

Within this sub-section, many of the observations and inferences made on obtained pressure coefficients in this study depending on the variation of wind angle of attack are quite similar to the experimental study conducted by Verma in 2016 on a square tall building under different incidence angles from  $0^\circ$  to  $90^\circ$  with an angle of  $15^\circ$  increments. Furthermore, similar distributions of pressure coefficients on building surfaces for both incident angles of  $0^\circ$  and  $45^\circ$  can be found within the numerical study performed by Elshaer et al. in 2017.

### 6.2.3 RMS Pressure Coefficients: Study Case CD0 ( $0^\circ$ AOA)

Fluctuating (RMS) pressure coefficients are calculated with the equation (6.2.2). Obtained pressure coefficients in the  $0^\circ$  angle of attack are compared with the reference experimental and numerical study in figure (6.9). In this figure, the left three columns (a) demonstrate the RMS pressure coefficients on the windward surface, while the right three columns (b) show the building's leeward surface.

$$C_{p_{rms}} = \frac{\sqrt{(\overline{P'})^2}}{0.5\rho(\overline{u}(z_B))^2} \quad (6.2.2)$$

According to this comparison, it is noticed clearly that the obtained RMS pressure coefficients are unacceptably higher than both reference experimental and numerical studies. As given in Section (4.3), several studies in the literature emphasized that

RMS pressure coefficients are very sensitive to the turbulence intensities rather than the mean velocity profile. Therefore, these results are directly related to the CDRFG code compiled for this study.

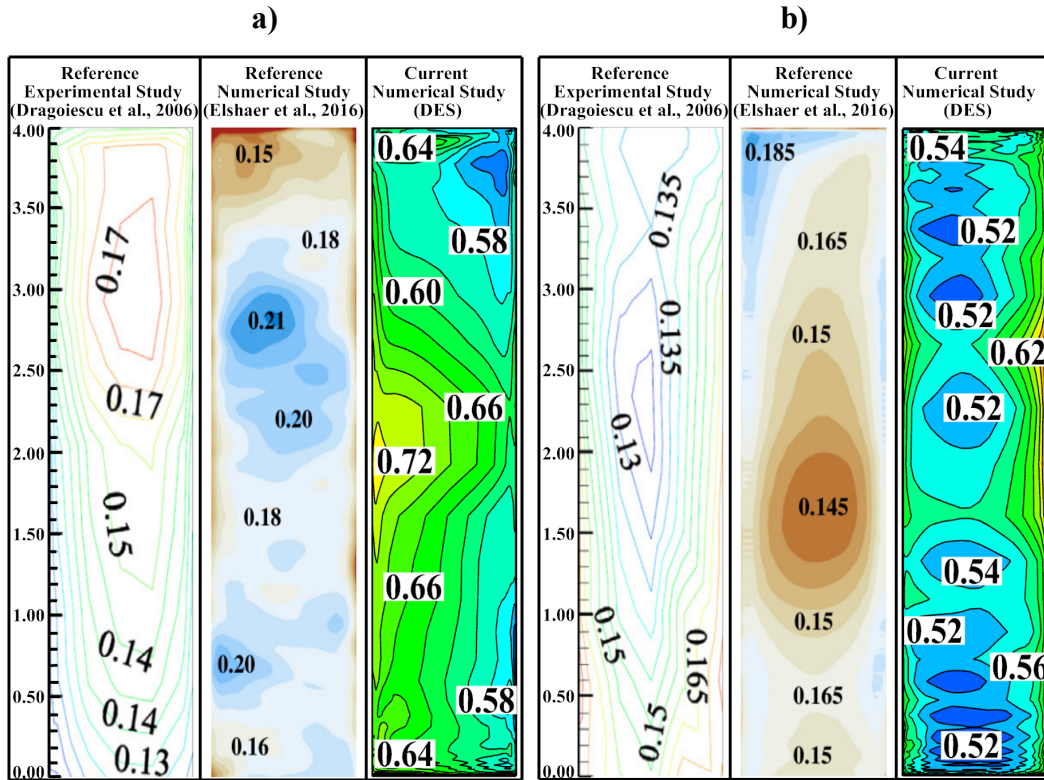


Figure 6.9. Comparison of RMS  $C_p$  distributions ( $0^\circ$  AOA)  
a) on windward surface of the building, b) on leeward surface of the building

In Sub-section (5.5.1), it is mentioned that obtained turbulence intensities from synthesized velocities over the vertical lines passing through the observation points taken from the right, left, and middle of the building differ partially from the target intensity profiles. (Please see figure (5.23).) Obtained along-wind turbulence intensities are less than the target intensities for up to half of the building height, while they are more than the target intensities from this level to the top of the building. In the across-wind direction, obtained turbulence intensities are mainly less than the target intensities throughout the building. On the other hand, vertical turbulence intensities do not deviate much from the target profile up to building height. However, these deviations are not seen as the major reason why these RMS

pressure coefficients are so high from the acceptable range, although these deviations affect the obtained RMS pressure coefficients. The basis of this idea is the distribution of RMS pressure coefficients around the building for  $0^\circ$  AOA at the height of  $2H/3$ . This distribution is given in figure (6.10a) with the RMS coefficients that were obtained from reference numerical and experimental studies.

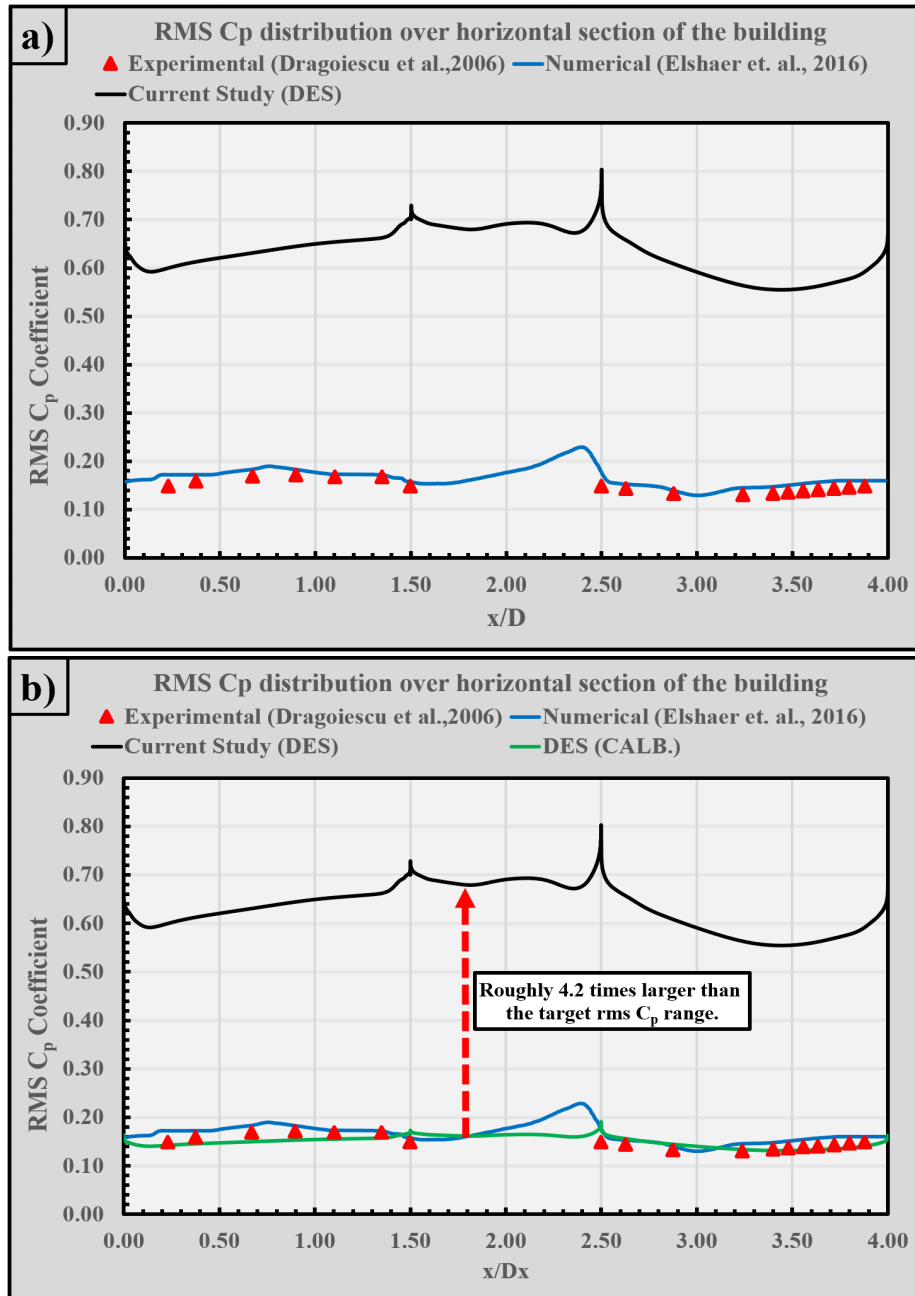


Figure 6.10. RMS  $C_p$  distributions over the horizontal section ( $0^\circ$  AOA)

It is noticed that the obtained RMS pressure coefficients around the building roughly 4.2 times higher than target RMS pressures. Once this ratio is applied to the obtained RMS coefficients, which is given with a green plot called “DES CALB.” in figure (6.10b), it is seen that the target range is obtained with acceptable accuracy. It was mentioned by Thordal et al. (2019) that any inconsistency of inflow boundary conditions may lead to unacceptable results, especially in RMS pressure coefficients compared to mean pressure coefficients. To support this statement, obtained RMS pressure coefficients from several numerical and experimental studies are provided by them and given in figure (6.11) in this study.

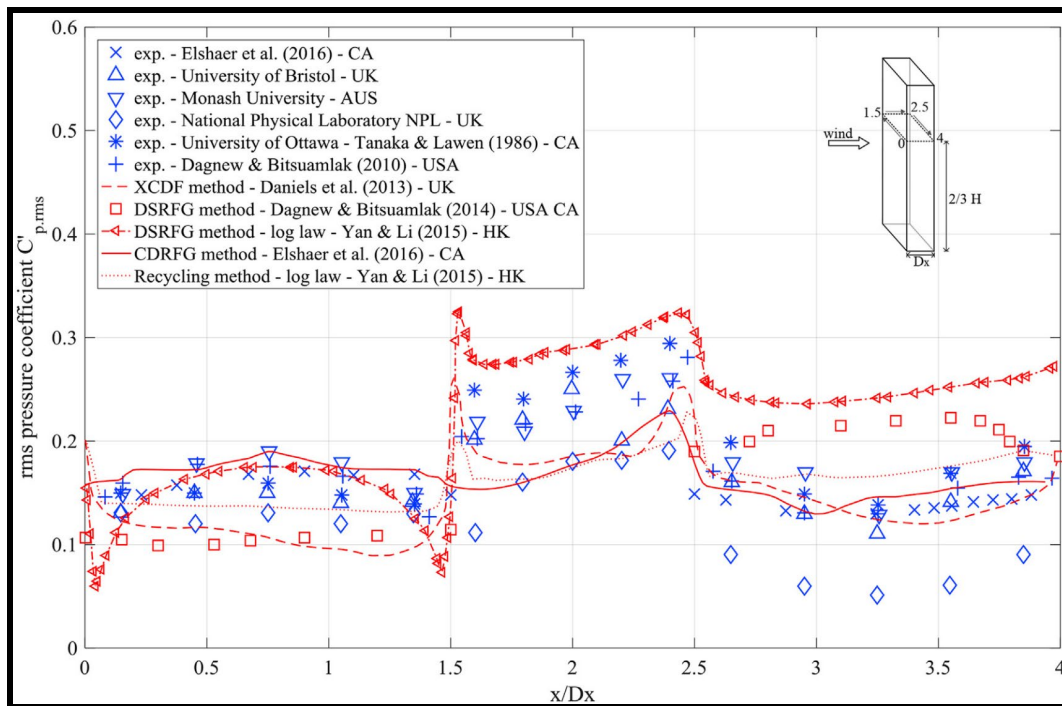


Figure 6.11. RMS pressure coefficient distributions from several studies

Note: Reprinted from “Review for practical application of CFD for the determination of wind load on high-rise buildings” by Authors M.S. Thordal, J.C. Bennetsen, and H. Koss, 2019, *Journal of Wind Engineering and Industrial Aerodynamics*, 186, 155-168, Copyright 2019 by Elsevier

There is more than one parameter in the algorithm of CDRFG that may affect RMS pressure coefficients, such as the difference in obtained RMS pressure coefficients. The main ones are the coherency decay coefficient, target coherency, the target spectrum's resolution, or frequency bandwidth. In several background studies, it was

observed that RMS pressure coefficients vary with an order of square root of the differentiation of amplitudes  $p_i^{m,n} - q_i^{m,n}$  that are determined for each frequency during the synthesizing. For instance, in one of these background studies performed by synthesizing over half of the target spectrum at each point, RMS pressure coefficients were obtained approximately 1.41 times less. However, as can be expected, when the spectrum changes, the flow characteristics also change. Therefore, the frequency bandwidth, which is another parameter that will lead to the same effect without changing prescribed flow characteristics, may cause higher RMS pressure coefficients. This parameter directly affects resolution of the spectrum throughout selected frequency range. Depending on frequency bandwidth, the normal distribution of random frequencies and correspondingly sub-frequencies generated for segment frequencies are changed. In order to increase resolution of the target spectrum without changing frequency range, the number of segment frequencies (i.e.,  $M$ ) is required to be increased. Besides, the tuning factor and tuning distance may also cause such RMS pressure coefficients. Therefore, it is concluded that further studies are necessary to examine the effects of these parameters and to find why the obtained RMS pressure coefficients are higher than normal.

### **6.3 Flow Characteristics Around the Building**

#### **6.3.1 Study Case CD0: 0° Angle of Attack**

When the studies are reviewed in Chapter-4, one may conclude that characteristic features of the flow obtained around tall buildings and similar structures depend on various conditions such as dimensions of the target building, corner types, façade designs, presence of surrounding buildings, approaching wind speed and incidence angle. Therefore, these features are too complicated to generalize. Several flow patterns around the building at an incidence angle of 0° captured by S-A RANS (a) and S-A DES (b) models are given in figure (6.12) with 3D streamlines.

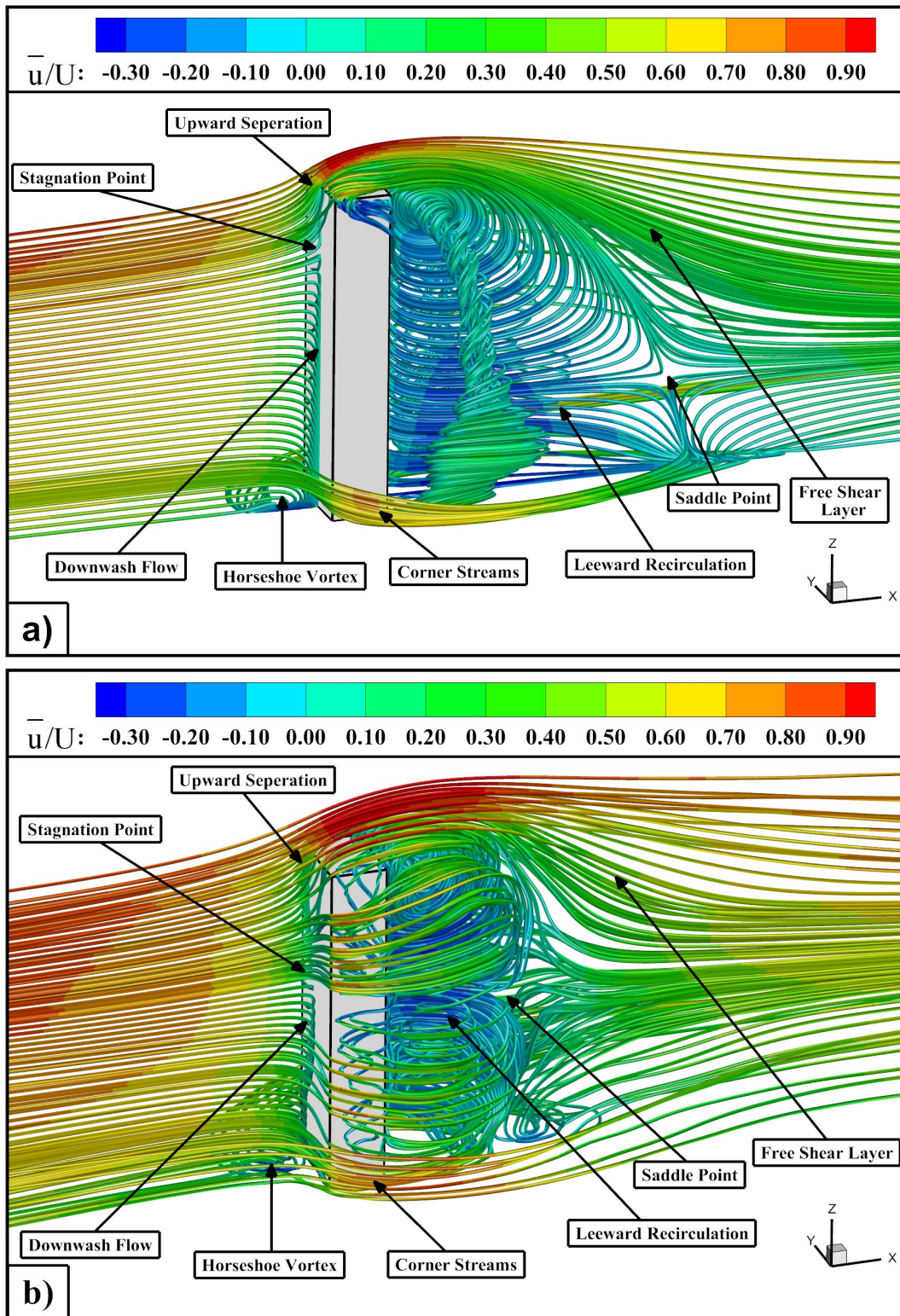


Figure 6.12. Characteristic mean flow patterns around the building (0° AOA)  
 a) captured by S-A RANS, b) captured by S-A DES

In both models, stagnation point, separations, downwash flow, and horseshoe vortex formation are observed on windward surface of the building, while recirculation zone, free shear layer, and saddle point are seen on leeward side of the building. Corner streams, vortices near the building's crosswind side, and tip vortices are noticed. Besides, these flow patterns obtained from S-A RANS and S-A DES models differ noticeably compared to each other due to their accuracies. The captured flow patterns are given as streamlines with pressure contours on a plane passing through the middle of the building in figure (6.13) for S-A RANS (a) and S-A DES (b).

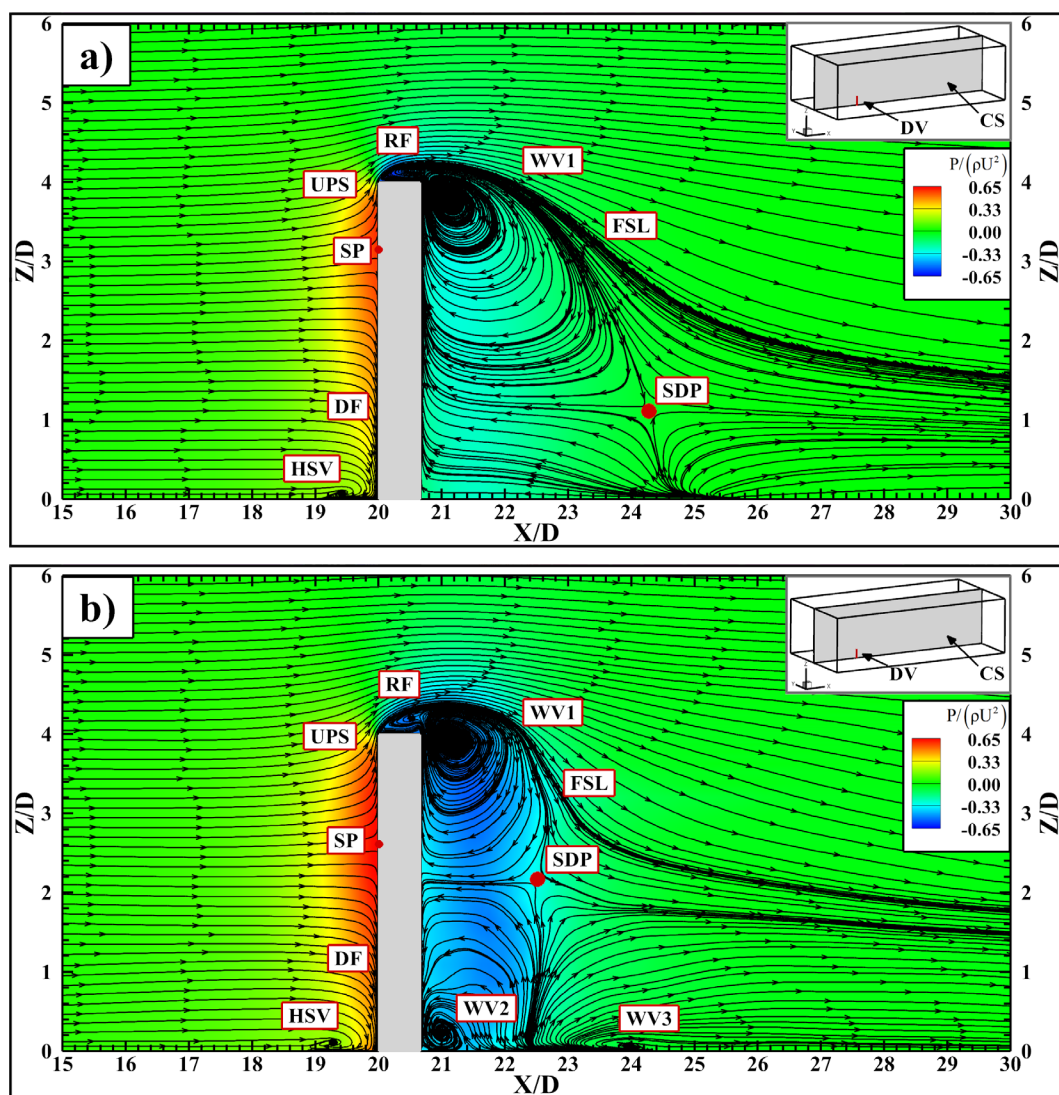


Figure 6.13. Mean streamline patterns with pressure distribution ( $0^\circ$  AOA)  
a) obtained by S-A RANS, b) obtained by S-A DES

In figure (6.13), the stagnation point where velocities are zero and correspondingly the pressure is maximum is abbreviated as SP. In both models, it is seen that the positive pressures on the front surface of the building are concentrated at the location of this point. It is observed that S-A RANS model predicts the height of SP higher than normal, and both positive and negative pressures around the building are less than S-A DES model. At the location of SP, flow is separated into downward, upward and sideward directions on the windward surface of the building. Therefore, depending on the SP's height, the distances where downwash (i.e., downward) and upward flows are seen along the windward surface vary. In parallel with this, downwash flow is observed over a longer distance in S-A RANS model than S-A DES model. Downwash flow (DF) is the flow directed by the building to the ground in three directions with the contribution of pressure distribution around stagnation point along the building's windward surface when exposed to the wind. It is a relatively slow flow that merges with the approaching wind at lower heights of the building. Separation of the flow along the bottom wall at the upstream of the building causes the formation of a horseshoe-like structure that wraps around the building. This formation is known as the horseshoe vortex, and it is denoted HSV in figure (6.13). Peterka et al. (1985) stated that the flow near corners accelerates to similar velocities at  $3H/4$  of the building due to the effects of sharp corners and relatively slow down just after the corners. When figure (6.12) is examined, this flow motion is partially observed in the numerical models. On the other hand, the flow velocity near the corners is seen slightly less in S-A RANS model than the corner streams in S-A DES model. Horseshoe vortex and relatively faster wind flow around the building's corners are essential, especially for pedestrian wind comforts (at 2m). Although both numerical models capture this flow pattern, it is noticed that the center of this vortex in S-A RANS model is slightly lower and closer to the building than the HSV in S-A DES model. The flow directed from stagnation point to the top of the building separates from the building's windward surface with an increasing velocity due to the effect of upper edge of the windward surface. This movement is called upward separation (UPS) and creates reverse flow (RF), resulting in negative

pressures on the building's top surface. These aforementioned flow patterns are observed more clearly in figure (6.14).

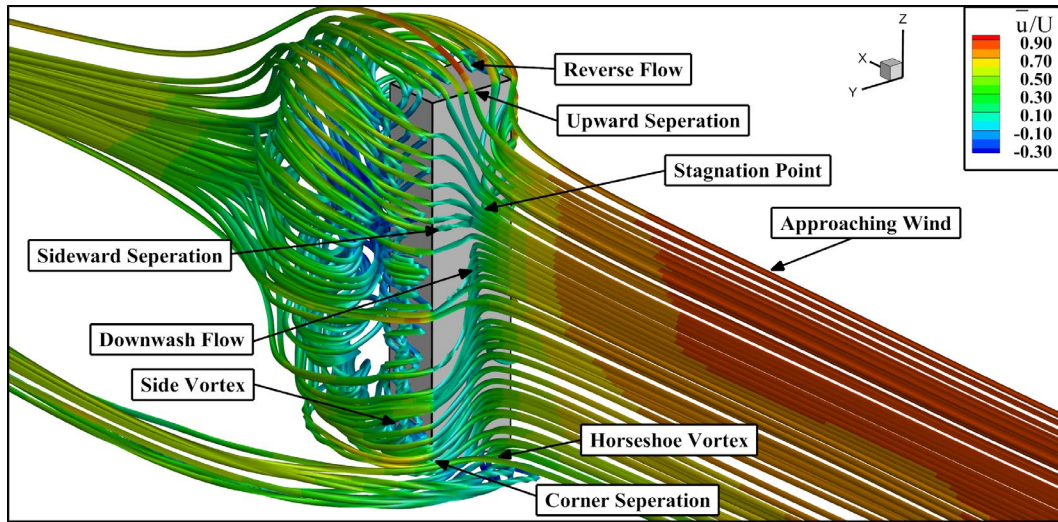


Figure 6.14. Separations and corner streams captured by S-A DES ( $0^\circ$  AOA)

Figure (6.15) depicts wake flow patterns with mean vertical velocities captured by S-A RANS (a) and S-A DES (b). In this figure, slower vertical velocity of downwash and comparatively smaller tip vortex formation are noticed in S-A RANS model than the flow captured by S-A DES.

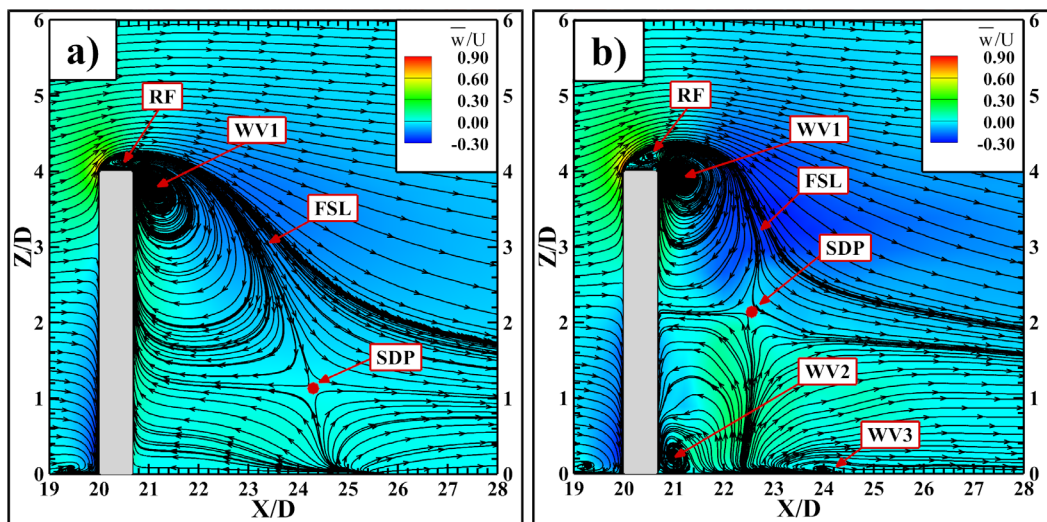


Figure 6.15. Comparison of wake flow patterns ( $0^\circ$  AOA)  
a) captured by S-A RANS, b) captured by S-A DES

Separated flows near the building's side and top surfaces move towards the region where low pressure (suction) zone occurs behind the building. The differences between these flows' velocities lead to the generation of saddle point (SDP) behind the building. This point, also known as *elevated free stagnation point*, is defined as the point where the flows coming from the building surfaces balance each other. (Addepalli & Pardyjak, 2015) The saddle point is located at (24.3 X/D, 1.175 Z/D) in S-A RANS model and at (22.59 X/D, 2.175Z/D) in S-A DES model. Above this point, an upper wake vortex (WV1) formation in which the flow rotates in the clockwise direction is seen near the building's leeward surface. This formation differs in numerical models depending on the model's accuracy in determining the saddle point's position. Therefore, in S-A RANS model, WV1 is observed from the height of 1.175Z/D to the building's tip throughout a distance of 3.63X/D from the building's leeward surface. On the contrary, WV1 is seen to be smaller in S-A DES model than S-A RANS model and recognized from the height of 1.825 Z/D to the building's tip throughout a distance of 1.92 X/D from the building's leeward surface. It is also noticed that the WV1 rotates slower in S-A RANS model compared to S-A DES model. Under saddle point, wake vortex WV2 in which the flow rotates in the counterclockwise direction is captured by S-A DES. With the effect of the WV1 and WV2 vortices, the pressures obtained on the building's leeward surface are minimal at the height of SDP while increasing from that point to the building's tip and bottom, as shown in figure (6.13). There is also a third vortex WV3 observed along the bottom wall at the downstream of the building in S-A DES simulation. On the other hand, S-A RANS model cannot capture the formations of WV2 and WV3, and the flow moves upwards along the building surface in the region of WV2. With the absence of the WV2 vortex, a uniform increase in negative pressures from bottom to top of the building is observed in the wake. As a result, it is concluded that the numerical model's accuracy is important to define flow patterns, especially behind the building with the location of a saddle point.

In figure (6.16), mean flow patterns with along-wind velocities around the building at the heights of  $H/3$  and  $2H/3$  are given for S-A RANS (a-c) and S-A DES (b-d). It is noticed that recirculation zone and reattachment lengths are predicted to be longer in S-A RANS compared to S-A DES model. In both models, shear layer formations are observed throughout the building's height due to sideward separation of the flow and its interaction with relatively slow flow near the building's crosswind sides. In S-A DES model, a faster flow is seen in shear layers than in S-A RANS model. The velocity of shear layer flows increases as the mean wind speed increases throughout the building's height in both models. Besides, the formations of vortices are identified between these layers and the building's crosswind sides. These vortices lose their coherence in these regions with increasing height. However, while these vortices are still visible at the building height in S-A DES model, they are not fully resolved in S-A RANS model.

There are two recirculating eddies at the downstream of the building, which are crosswind left vortex (CWL<sub>V</sub>) and crosswind right vortex (CWR<sub>V</sub>), both in S-A RANS and S-A DES solutions of the mean flow. The size of these vortices is larger in S-A RANS model compared to S-A DES model. In S-A RANS simulation, these vortices' size decreases as getting away from the bottom wall, whereas their size is almost constant through the building height in S-A DES simulation.

It is noticed that in the mean flow, CWL<sub>V</sub> and CWR<sub>V</sub> are slightly asymmetrical in S-A DES model due to the asymmetry generated as a result of the synthesized inflow boundary conditions, as mention in Sub-section (5.5.1). Observed mean flow patterns such as primary wake vortex VW<sub>1</sub>, secondary wake vortex VW<sub>2</sub>, and locations of stagnation and saddle points given in figures (6.13), (6.15), and (6.16) are quite similar to the results of the study conducted by S. Huang et al. in 2007 to analyze wind effects on a CAARC tall building model with using LES and RANS numerical models.

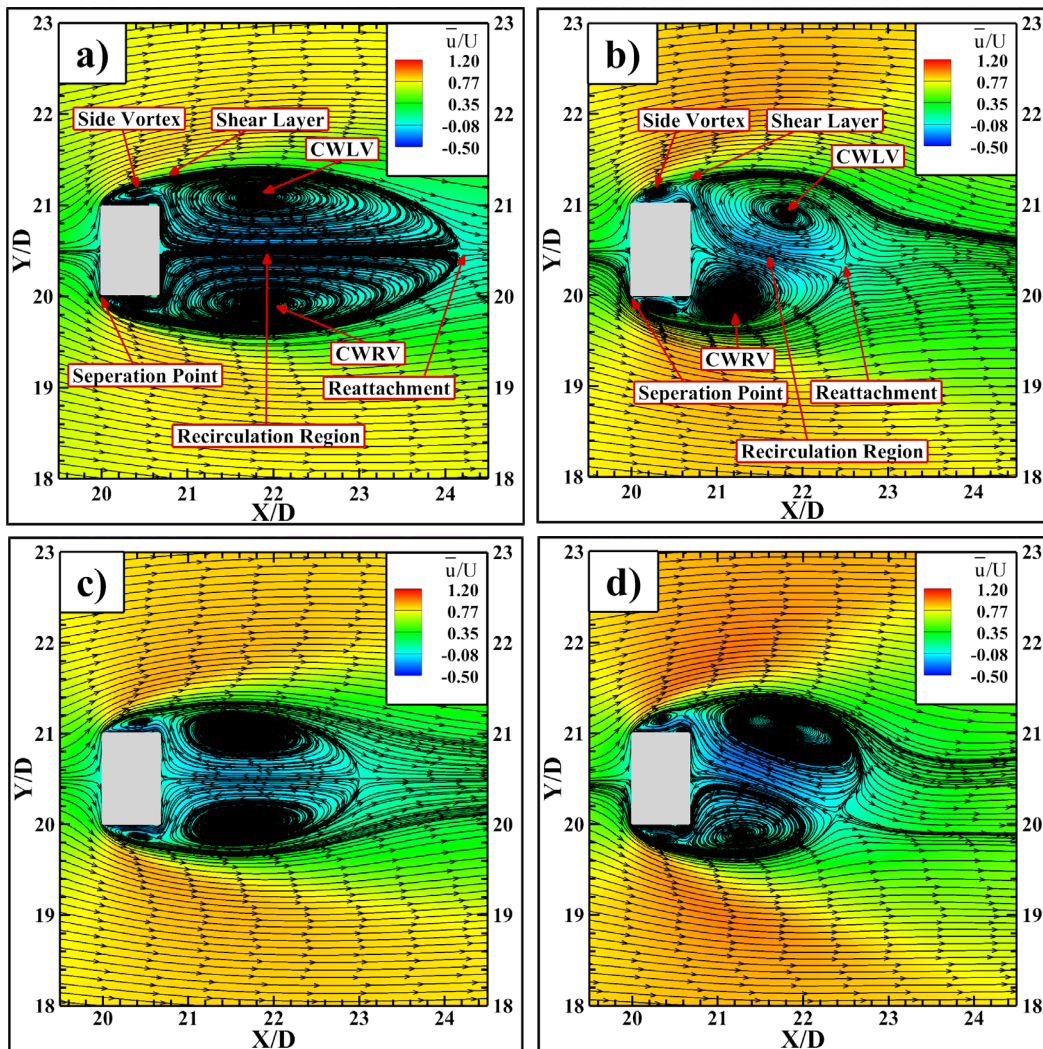


Figure 6.16. Comparison of mean flow patterns ( $0^\circ$  AOA)  
 a) at  $H/3$  captured by S-A RANS, b) at  $H/3$  captured by S-A DES  
 c) at  $2H/3$  captured by S-A RANS, d) at  $2H/3$  captured by S-A DES

Figure (6.17) demonstrates out-of-plane vorticity contours at the heights of  $H/3$  (a),  $2H/3$  (b), and  $H$  (c). Shear layers are clearly visible from the amplified out-of-plane vorticity contours in these figures. Besides, small vortices occurring near the building's leeward corners are also identified, and it is noticed that they lose their coherence at the building level.

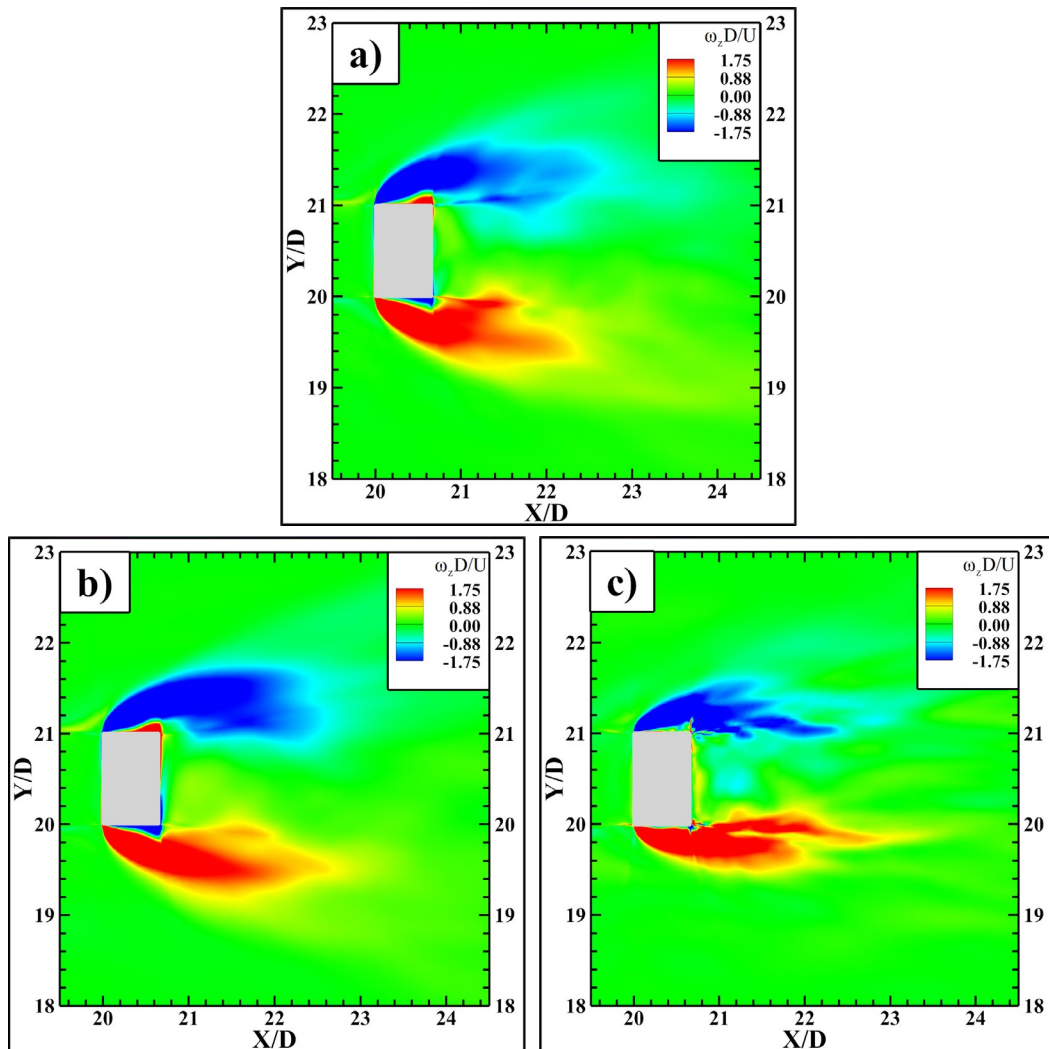


Figure 6.17. Mean out-of-plane vorticities obtained by S-A DES ( $0^\circ$  AOA)  
 a) at  $H/3$ , b) at  $2H/3$ , c) at  $H$

Figure (6.18) demonstrates turbulence kinetic energy contours at the heights of  $H/3$  (a),  $2H/3$  (b), and on a vertical plane passing through the middle of the building (c). It is seen that the turbulence kinetic energy is amplified along the shear layers forming on the sides and also at the wake of the building.

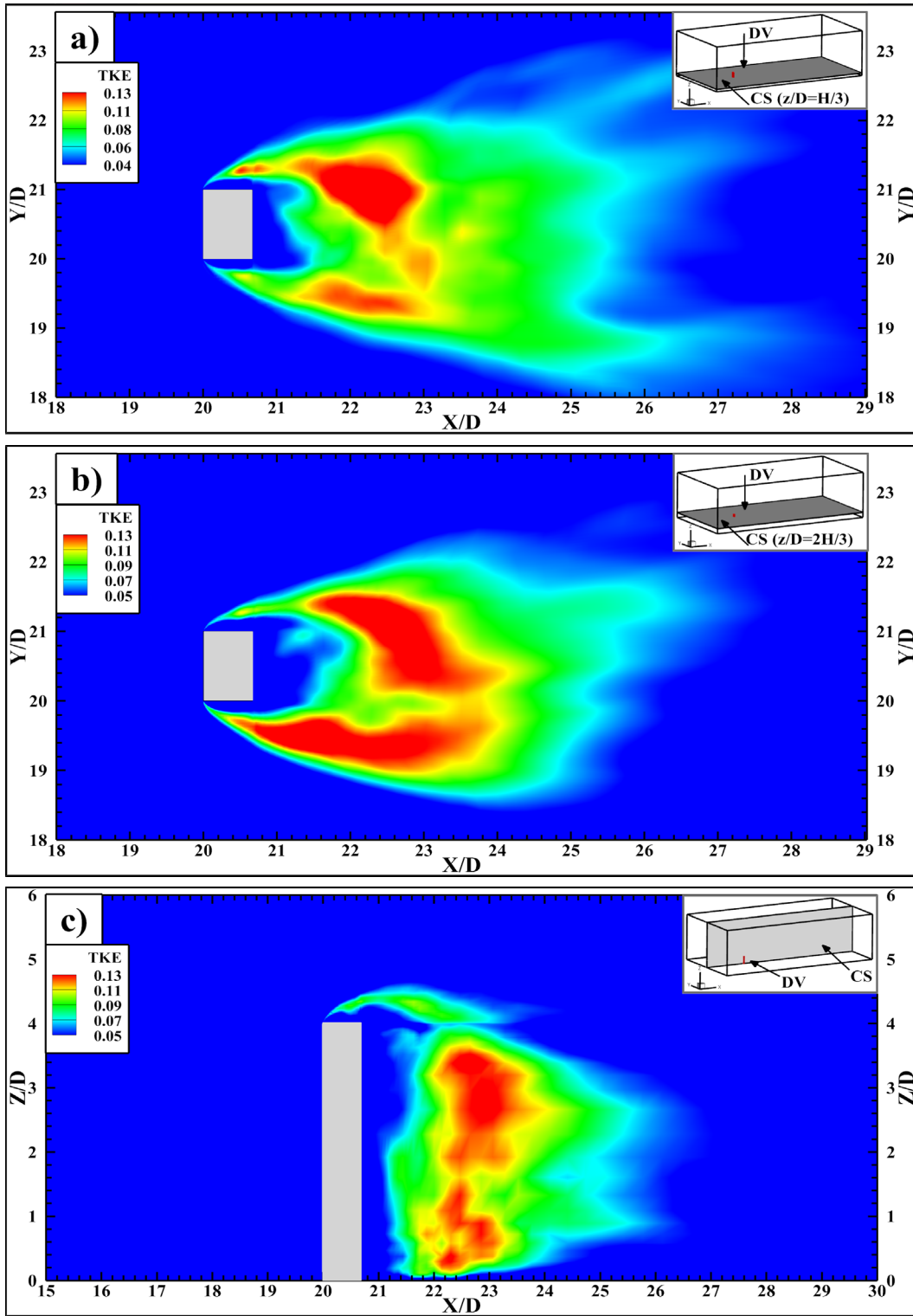


Figure 6.18. Non-dimensional TKE distributions ( $0^\circ$  AOA) obtained by S-A DES a) at  $H/3$ , b) at  $2H/3$  c) on a vertical plane passing through the middle of the building

### 6.3.2 Study Case CD45: 45° Angle of Attack

In order to observe the effect of incidence angle of wind on the flow around the building, obtained flow patterns for 0° AOA (a) and 45° AOA (b) are given in figure (6.19). The notation given for the building surfaces in figure (6.6) is also used in this sub-section. Approaching flow at an angle of 45° hits the faces A and B of the building. Although stagnation point is not clear for 45° AOA in this figure, upward separation is observed in the upper edges of faces A and B. The formation of a horseshoe vortex is also noticed in front of the building, similar to the study case 0° AOA. Due to the sideward separations near the leeward edges of faces A and B, corner and edge streams in the flow at an angle of 45° accelerate more than the flow at an angle of 0°. Besides, separated flow moves directly to the circulation zone without causing side vortex formations near the building. Saddle point and free shear layer patterns are observed with two wake vortices. It is also seen that these vortices in the leeward circulation zone are shaped behind the building depending on the incidence angle of the wind and the dimensions of the building surfaces.

In figure (6.20), flow patterns with pressure contours are shown on a plane passing through the middle of the building are given for incident angle of 0° (a) and incident angle of 45° (b). The stagnation point is identified approximately at  $2.27Y/D$  for the flow at an angle of 45°, and it is noticed that the height of the stagnation point is shifted below compared to the flow at an angle of 0°. Accordingly, it is concluded that the position of stagnation point changes with respect to the wind angle of attack. Consequently, in study case 45° AOA, a shorter downwash flow is observed along the building's windward edge between faces A and B. The horseshoe vortex's center has a slightly lower position than the horseshoe vortex that occurs in the flow at an incidence angle of 0°.

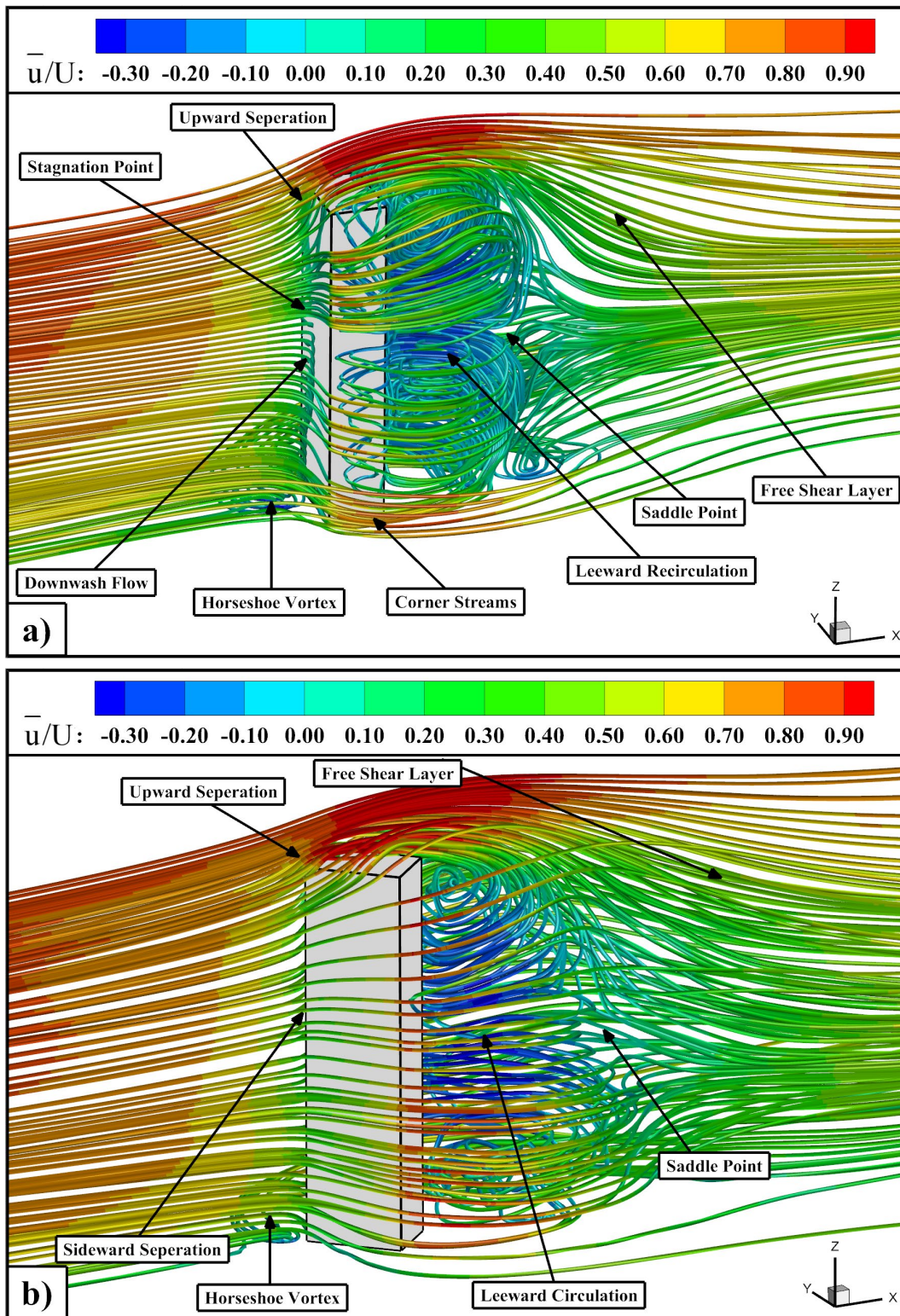


Figure 6.19. The effect of AOA on mean flow patterns around the building  
 a) captured by S-A DES at 0° AOA, b) captured by S-A DES at 45° AOA

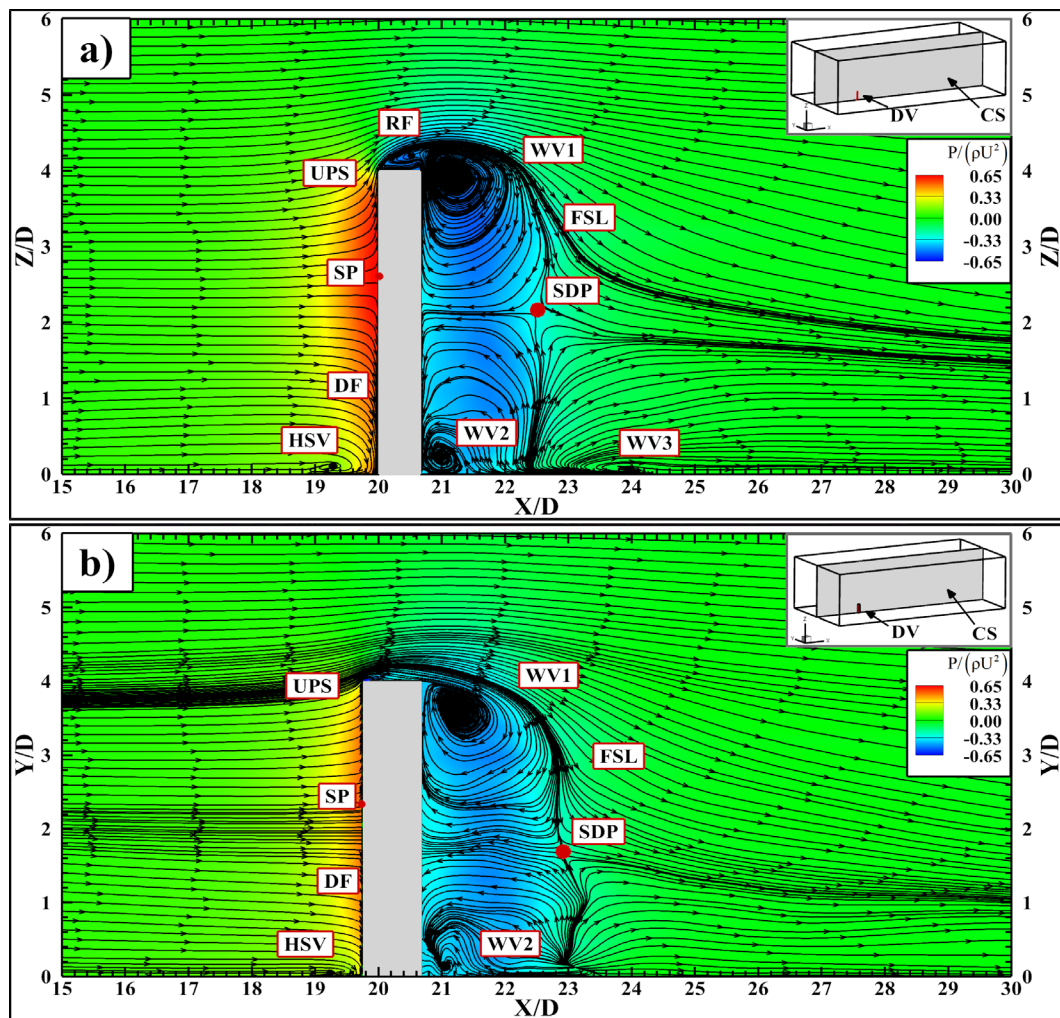


Figure 6.20. Comparison of mean flow patterns with pressure distributions  
a) 0° AOA, b) 45° AOA

No visible reversed flow is identified with this point of view in the flow at an angle of 45°. However, the formations of two tip vortices due to the upward separation, which occurs in both upper edges of faces A and B, are demonstrated using the Q criterion in the figure (6.21). It should be noted that in the 0° angle of attack case, there is only one bigger tip vortex covering the entire width of the building's top surface. In this figure, the horseshoe vortex formation in the flow at an incidence angle of 45° (b-d) is also noticed to be longer than the horseshoe vortex in the flow with an 0° angle of attack (a-c). Furthermore, it is observed that the HSV is separated into two branches towards right crosswind surface of the building in case of 0° AOA.

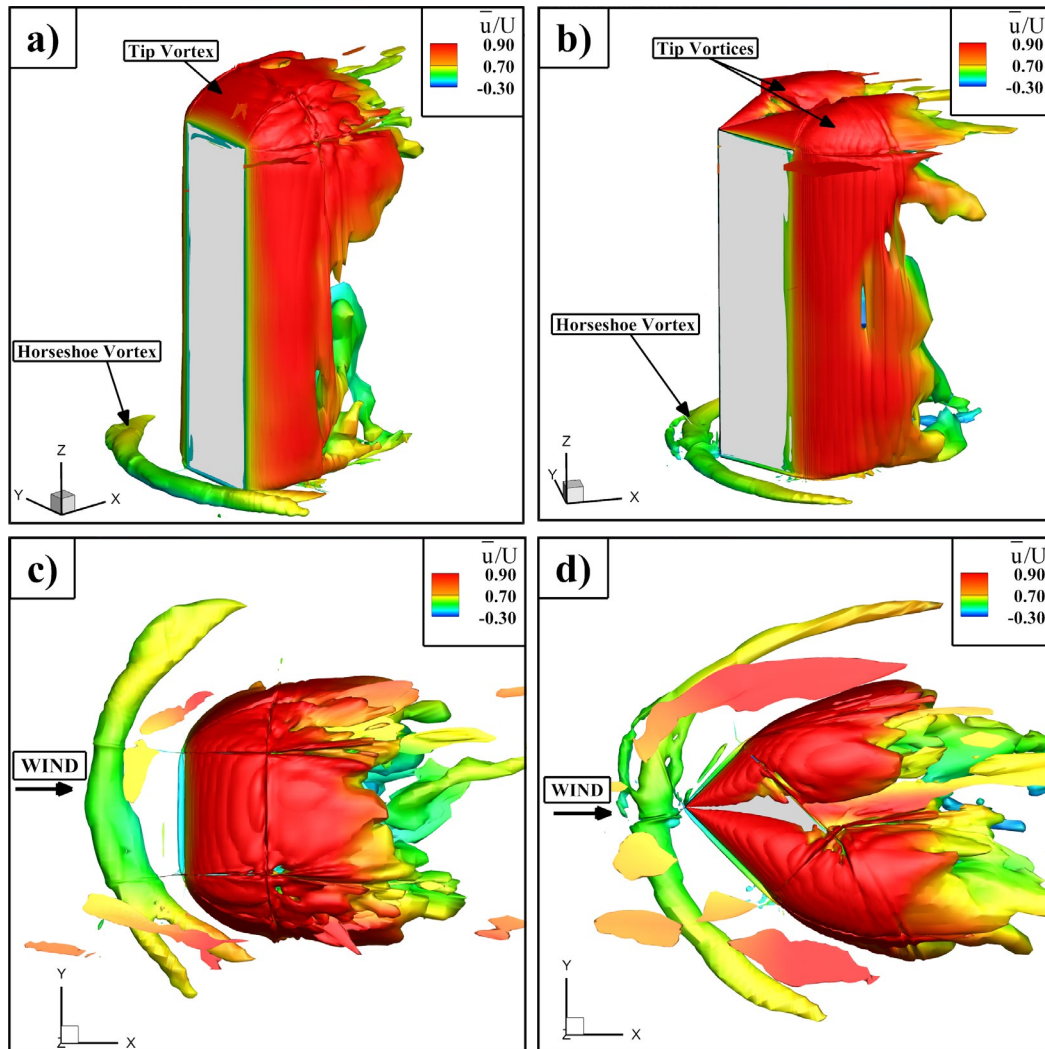


Figure 6.21. Isosurface plots of mean vortices captured by S-A DES  
a)  $0^\circ$ AOA Side view, b)  $45^\circ$ AOA Side view  
c)  $0^\circ$ AOA Top view, d)  $45^\circ$ AOA Top view

In figure (6.22), the flow patterns captured behind the building for the flow at an incidence angle of  $0^\circ$  (a) and the flow at an incidence angle of  $45^\circ$  (b) are depicted together with the mean vertical velocity contours. WV1 and VW2 vortices' formations are also observed in the flow with an incidence angle of  $45^\circ$ . The saddle point (SP) is located at  $(22.9 X/D, 1.7 Z/D)$ . Accordingly, it is seen that the location of this point is farther away from the building and occurs at a lower height with respect to the flow at an angle of  $0^\circ$ . With the change of the saddle point's position, it is noticed that the height of the clockwise rotating WV1 throughout the building

increases while the height of the counterclockwise rotating WV2 decreases in the flow at an angle of  $45^\circ$ . Besides, WV3 is not seen behind the building in this flow.

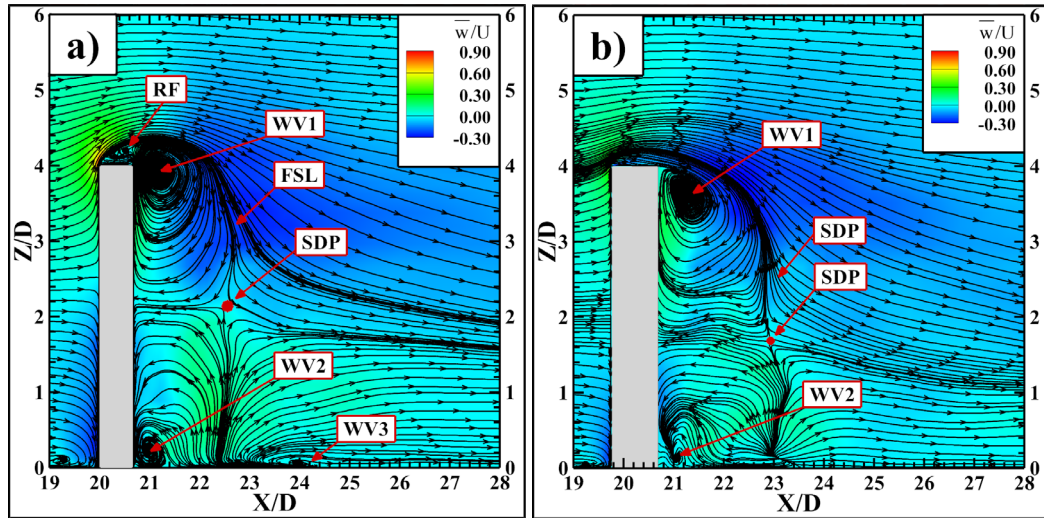


Figure 6.22. Comparison of wake flow patterns with mean vertical velocities captured by S-A DES at a)  $0^\circ$  AOA, b)  $45^\circ$  AOA

Figure (6.23) shows the comparison of the flow patterns in these flows at heights of  $H/3$  (a-b) and  $2H/3$  (c-d). It is noticed that the recirculation region and consequently the reattachment length is longer in the flow at an incidence angle of  $45^\circ$  with respect to the flow with an incidence angle of  $0^\circ$ . Furthermore, it is observed that flow behind the building is separated on the building's leeward corners and leads to formations of vortices in these corners in the case of  $0^\circ$  AOA. On the other hand, the flow behind the building is separated along the edge between faces C and D in the case of  $45^\circ$  AOA. Within the region where this separation occurs, a vortex forms near the edge of face-D at the height of  $H/3$ , and it loses its coherence as the height increases. In figure (6.23), it is also noticed that the velocity of the flow between the vortices CWLV and CWLR is higher in the flow at an incidence angle of  $45^\circ$  than the flow at an incidence angle of  $0^\circ$ . In both cases, shear layer formation is observed near the corners where the flow is separated.

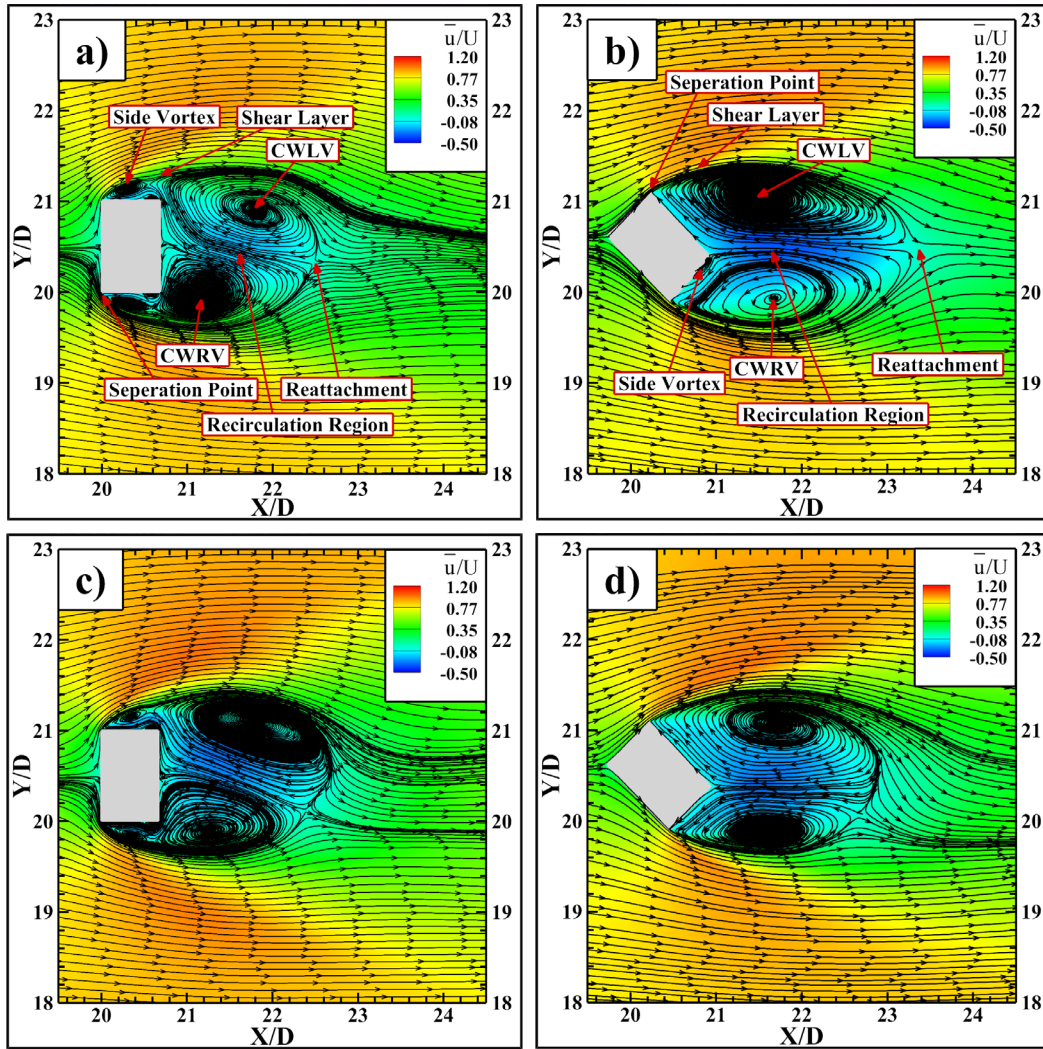


Figure 6.23. The effect of incidence angle on flow patterns captured by DES  
 a) at  $H/3$  ( $0^\circ$  AOA), (b) at  $H/3$  ( $45^\circ$  AOA),  
 c) at  $2H/3$  ( $0^\circ$  AOA), d) at  $2H/3$  ( $45^\circ$  AOA)

In figure (6.24), out-of-plane vorticities are given at the heights of the  $H/3$  (a),  $2H/3$  (b), and  $H$  (c) for the flow at an incidence angle of  $45^\circ$ . There are two shear layer formations observed between the building's leeward corner due to the flow between tip vortices on the building's top surface.

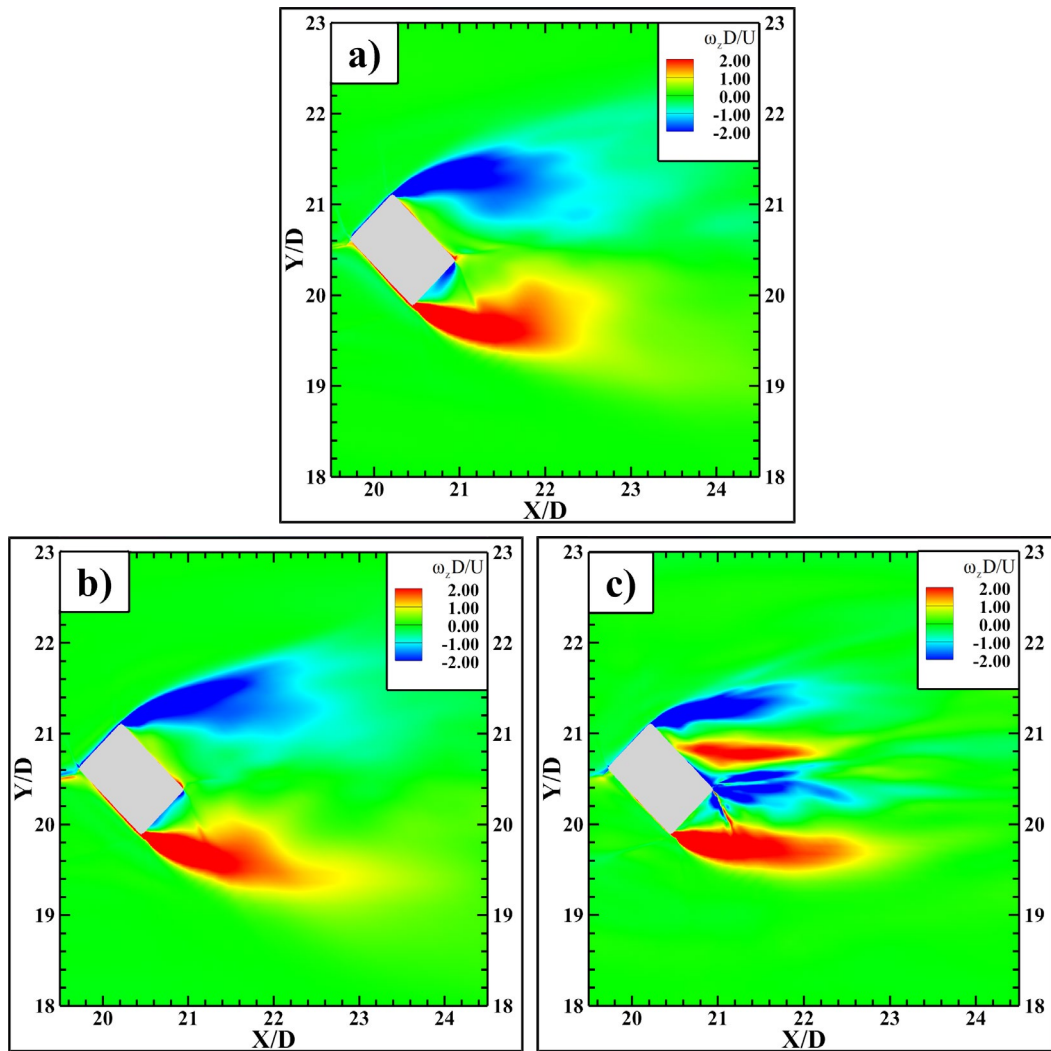


Figure 6.24. Mean out-of-plane vorticities obtained by S-A DES ( $45^\circ$  AOA)  
a) at  $H/3$ , b) at  $2H/3$ , c) at  $H$

Figure (6.25) demonstrates turbulence kinetic energy contours for the case of  $45^\circ$  AOA at the heights of  $H/3$  (a),  $2H/3$ (b), and on a vertical plane passing through the middle of the building (c). It is noticed that the kinetic energy of the flow behind the Face-C decreases as the height increases while the kinetic energy of the flow behind the Face-D increases with the height.

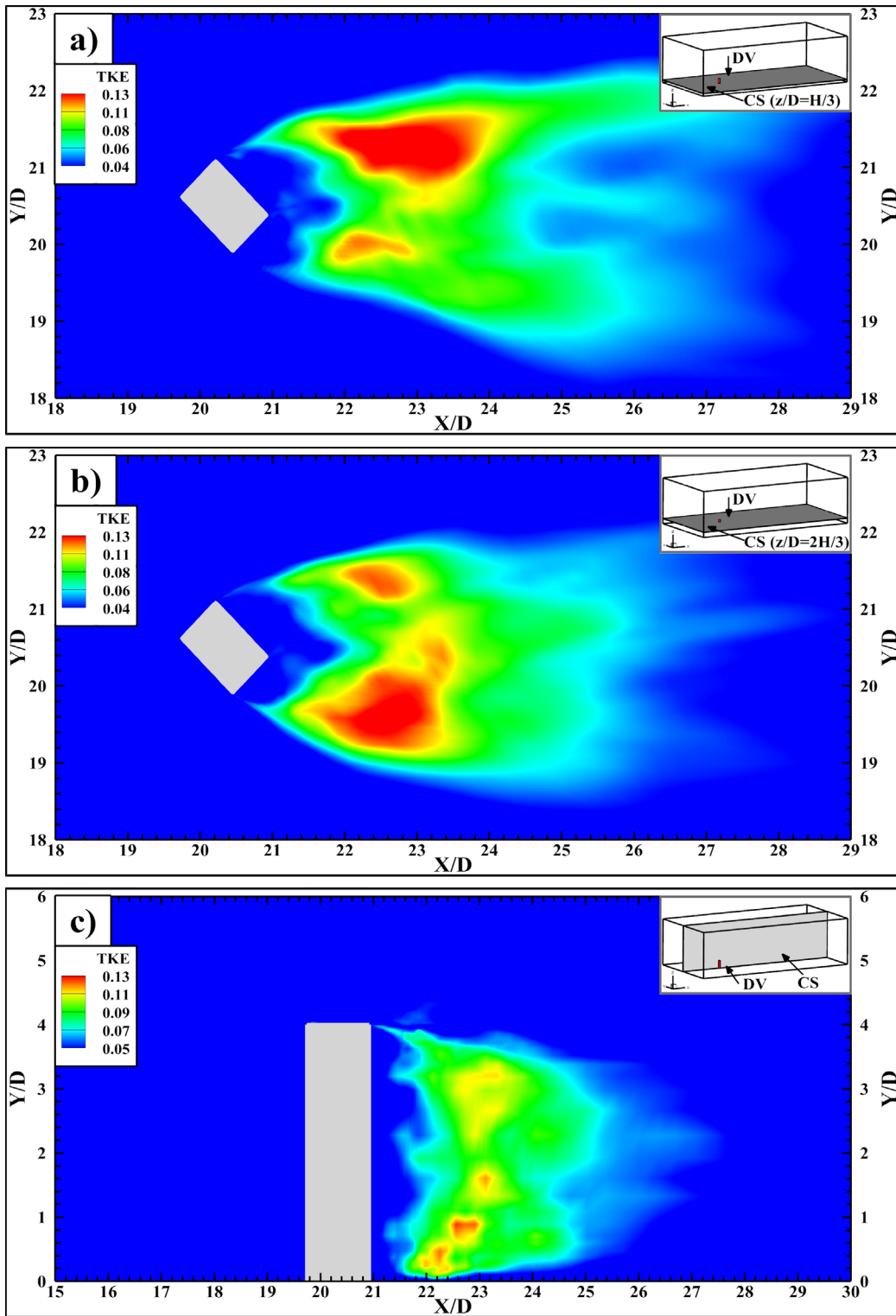


Figure 6.25. Non-dimensional TKE distribution ( $45^\circ$  AOA) obtained by S-A DES a) at height of  $H/3$ , b) at height of  $2H/3$  c) on a vertical plane passing through the middle of the building

## 6.4 Summary and Conclusions

Spalart-Allmaras based Detached Eddy Simulation (S-A DES) model with high resolution, and S-A based RANS models were used to simulate flows around the CAARC tall building model under  $0^\circ$  and  $45^\circ$  angles of wind attack at the open-terrain conditions. As a result of this study, it has been shown that very good results can also be obtained by using DES models that were less preferred compared to RANS and LES models in the analysis of the flow around the tall buildings in the literature. It is also intended to reveal that synthetic inflow boundary generation techniques can also be developed for hybrid models with possible improvements by using the CDRFG technique with the DES model. The results and several conclusions are given briefly below.

- When the obtained mean pressure coefficients by S-A RANS model on a tall building model in the flow field with an incidence angle of  $0^\circ$  are examined, it is seen that this model provides slightly less positive pressure coefficients on the building's windward surface compared to the reference wind tunnel data. Besides, it is noticed that S-A RANS model underestimates negative pressure coefficients on leeward surface of the building noticeably.
- With S-A DES model, an excellent agreement with the wind tunnel data was obtained on the building's windward and crosswind surfaces. Similar but slightly underestimated negative pressure coefficients were obtained on leeward surface with this numerical model compared to the wind tunnel and corresponding reference numerical study of Elshaer et al. (2016). It is thought that the accuracy of the results on this surface may be improved with the improvement of the accuracy of CDRFG code, which was compiled for this study.
- It is observed that solving viscous sublayer directly instead of utilizing wall functions increases the accuracy of results, especially in predicting the location of stagnation point and pressure coefficients.

- When the RMS pressure coefficients are compared with the reference studies, it is noticed that obtained RMS values are roughly 4.2 times higher than the target range. This situation is directly related to the CDRFG code used in this study, and it may be associated with the insufficient resolution of the prescribed spectrum while synthesizing the velocities. Therefore, further studies are required to observe the effects of segment frequencies, frequency bandwidth, decay coefficient, tuning factor, and tuning distance on the results.
- When the effects of different wind angles of attack on mean pressure coefficients are examined, it is noticed that the surfaces that are exposed to wind directly have positive pressure coefficients, and the distribution of pressure coefficients varies significantly depending on the incidence angle.
- After comparing the flow fields obtained by S-A RANS and S-A DES models, it is observed that flow patterns such as upper and lower wake vortices noticeably differ.
- As a result of the comparison of flow fields simulated under the  $0^\circ$  and  $45^\circ$  angles of wind attack, it is noticed that formations of several flow patterns such as recirculation, tip vortices, and shear layer formations are directly shaped with the building's dimensions and the wind's incidence angle.
- Although S-A RANS models are widely used in simulating flows around buildings, S-A DES model that does not use wall functions gives more realistic results in capturing pressure coefficients on the buildings and the unsteady flow dynamics.

## **6.5 Challenges of This Study**

This study's main difficulty was the determination of the frequency ranges within the framework of the target normalized spectrum to provide the same mean velocity profile, turbulence intensities, and turbulence integral turbulence length scales with the reference studies when working on different geometric scales. There is no direct

answer to how the frequency ranges, the sampling time step, and duration are determined in the literature. Besides, detailed studies based on these parameters could not be found.

During the compiling phase of the CDRFG for this study, only synthesized spectrums and intensities were checked to decide whether the synthesis process was correct or not. The reason for that, only one point-based data was provided rather than detailed profiles with respect to height by several studies that were conducted by using one of the synthetic inflow turbulence generation techniques in the literature. In other words, since profiles similar to the provided ones in figures (5.21) and (5.23) were not given in the literature, it was not possible to compare synthesized fields statistically along with the target height. When the authors of certain articles/studies were reached, it was understood that they did not want to share these key pieces of information. Therefore, it is thought that the accuracy of the compiled CDRFG can be increased and even improved by using any wind tunnel data.

During the compiling phase, parallelization of the CDRFG technique was not carried out until the synthesized velocity fields met certain criteria. The main reason for this was to prevent possible coding errors that may occur in the use of OpenMP and MPI libraries from being jumbled together with possible computational errors caused by the algorithm. The compiling phase of the CDRFG was started with a computer that had 4 cores/8 threads Intel i7 6700K (4.40 GHz overclocked and water-cooled), 32 GB 2133 GHz DDR4 ram, and 512 Gb M2 SSD (writing speed: 3000Mb/s, reading speed 3500 Mb/s). The first trial-error stages of the CDRFG code took about 4-5 days with this computer for 0.1 seconds synthesizing duration with 0.0002 seconds sampling time step at eleven test points in order to increase accuracy while using MPI libraries and also to examine certain characteristic behaviors of processors such as the tendency to generate the same random numbers as described in Sub-section (5.2.2). While the duration for synthesizing was kept shorter to save time for simple runs, this option was not used when analyzing the obtained data's behavior statistically in different time intervals. Upon deciding on the optimum RNG procedures and non-linear solving algorithms with MPI libraries, much time was also

spent on memory optimizations due to the increase in memory requirement of allocated arrays within the CDRFG algorithm depending on the parallel use. The flowchart given in figure (5.6) is the optimum structure of the CDRFG that was found at the end of excessive studies. This stage took about eight months. After completing the parallelization of the compiled code with OpenMP and MPI, the CDRFG code's behavior depending on the input values and the synthesized velocities were examined to prevent all possible errors for two months. The computer used in this compiling stage was decided to be insufficient, and a new one was set up. The final optimization of the CDRFG was finished by using this computer, which has 16 core/32threads Intel i9 7960x processor (2.8 GHz to 4.2 GHz water-cooled), 64 Gb 3200 MHz DDR4 ram, and 512 Gb M2 SSD (writing speed: 3000Mb/s, reading speed 3500 Mb/s). When this processor uses all of the cores with its threads, a constant 3.6GHz is acquired in each core. The time spent on synthesizing velocity fields for each study case in this study by utilizing CDRFG with this hardware is given in table (6.1).

Table 6.1 Time spent on synthesizing velocity fields for each study case

<i>Inflow Plane</i>	<i>Number of grid points</i>	<i>Sampling Time</i>	<i>Sampling Time Step</i>	<i>Number of Core/Thread</i>	<i>Duration of Synthesizing</i>
CD0	1x224x128	100 D/U	0.1 D/U	16C/32T	78.55 min
CD0R	1x208x112	100 D/U	0.1 D/U	16C/32T	67.05 min
CD45	1x224x128	100 D/U	0.1 D/U	16C/32T	78.59 min

The computational cost of the CDRFG varies considerably based on different frequency ranges, sampling time steps, and the computational domain's inflow plane. This situation is related to the iterative non-linear solver (Trust-region) algorithm used to correlate wavenumbers. Therefore, speedup calculations generally made in MPI-based codes were not performed. When the time spent on synthesizing velocity fields with the CDRFG code compiled in this study is examined, 65.82% of the total time is taken by wavelength correction (Trust-region algorithm), while 20.58% of this duration is spent for synthesizing process using the equation (5.2.1) with

generated random number domains. 1.08% of the total duration is taken for MPI communication, and 12.52% of it is spent for writing the synthesized data. It is seen that a considerable amount of time is spent on a non-linear solver. The accuracy criteria defined for this algorithm are quite high. By lowering this criterion, the computational cost of the CDRFG can be reduced significantly. On the other hand, it was decided to increase the accuracy criterion for this study since the synthesizing process took a short time. After boundary conditions were synthesized, simulations were carried out with the S-A RANS and S-A DES numerical model using the provided computational resources, which are 128 cores (Intel Xeon E5 2680 V3) with 1TB storage by TUBITAK ULAKBIM High Performance and Grid Computing Center. For 21600 iterations with a 0.025 D/U time step, the study case CD0R with queue time lasted 12 days. This duration was 19 days for CD0 and 16 days for CD45. These durations were valid when there is not much demand for TRUBA ULAKBIM resources and varied depending on the waiting times. It is important to inform that there are six different blending modules to be queued and run within the S-A DES model's high accuracy numerical scheme. Therefore, 16 cores were used to wait less in clusters. In table (6.2), the average number of iterations resolved on an hourly basis for S-A DES model is given, considering that it is more decisive. RANS simulations lasted 1-2 days for study cases.

Table 6.2 Time spent on S-A DES simulations for each study case

Study Case	<i>Number of Hexahedron Cells</i>	<i>Number of Iterations</i>	<i>Time Step</i>	<i>Iterations Per Hour</i>	<i>Number of Core</i>
CD0	7221855	256x224x128	0.025 D/U	67	16C
CD0R	5491503	240x208x112	0.025 D/U	95	16C
CD45	7221855	256x224x128	0.025 D/U	67	16C

In conclusion, detailed studies on parameters such as frequency bandwidth and tuning factor to examine their effects on results could not be done due to the limited time.

## **6.6 Future Studies**

After conducting parametric studies on the obtained RMS pressure coefficients, it is planned to investigate environmental buildings' effect on the wind flow around the target building and the pressure coefficients. In addition, the building with and without surrounding buildings can be examined more comprehensively under different wind incidence angles. It is also possible to examine the variations of wind flow conditions around the building with an urban area development depending on the years. Finally, the aerodynamic analysis of different structures such as stadiums, bridges, wind turbines may be performed.

## REFERENCES

- Aboshosha, H., Elshaer, A., Bitsuamlak, G. T., & El Damatty, A. (2015). Consistent inflow turbulence generator for LES evaluation of wind-induced responses for tall buildings. *Journal of Wind Engineering and Industrial Aerodynamics*, *142*, 198–216. <https://doi.org/10.1016/j.jweia.2015.04.004>
- Addepalli, B., & Pardyjak, E. R. (2015). A study of flow fields in step-down street canyons. *Environmental Fluid Mechanics*, *15*(2), 439–481. <https://doi.org/10.1007/s10652-014-9366-z>
- Allegrini, J., & Carmeliet, J. (2017). Evaluation of the Filtered Noise Turbulent Inflow Generation Method. In *Flow, Turbulence and Combustion* (Vol. 98, Issue 4). <https://doi.org/10.1007/s10494-016-9798-2>
- Alminhana, G. W., Braun, A. L., & Loredou-Souza, A. M. (2018). A numerical-experimental investigation on the aerodynamic performance of CAARC building models with geometric modifications. *Journal of Wind Engineering and Industrial Aerodynamics*. <https://doi.org/10.1016/j.jweia.2018.07.001>
- Arany, L., Bhattacharya, S., Macdonald, J., & Hogan, S. J. (2015). Simplified critical mudline bending moment spectra of offshore wind turbine support structures. *Wind Energy*, *18*(12), 2171–2197. <https://doi.org/https://doi.org/10.1002/we.1812>
- Baker, C., Johnson, T., Flynn, D., Hemida, H., Quinn, A., Soper, D., & Sterling, M. (2019). Computational techniques. In *Train Aerodynamics* (pp. 53–71). Elsevier. <https://doi.org/10.1016/B978-0-12-813310-1.00004-6>
- Balendra, T., Anwar, M. P., & Tey, K. L. (2005). Direct measurement of wind-induced displacements in tall building models using laser positioning technique. *Journal of Wind Engineering and Industrial Aerodynamics*, *93*(5), 399–412. <https://doi.org/10.1016/j.jweia.2005.03.003>

- Bandi, E. K., Tamura, Y., Yoshida, A., Chul Kim, Y., & Yang, Q. (2013). Experimental investigation on aerodynamic characteristics of various triangular-section high-rise buildings. *Journal of Wind Engineering and Industrial Aerodynamics*, 122, 60–68. <https://doi.org/10.1016/j.jweia.2013.07.002>
- Bazdidi-Tehrani, F., Kiamansouri, M., & Jadidi, M. (2016). Inflow turbulence generation techniques for large eddy simulation of flow and dispersion around a model building in a turbulent atmospheric boundary layer. *Journal of Building Performance Simulation*, 9(6), 680–698. <https://doi.org/10.1080/19401493.2016.1196729>
- Benhamadouche, S., Jarrin, N., Addad, Y., & Laurence, D. (2006). Synthetic turbulent inflow conditions based on a vortex method for large-eddy simulation. *Progress in Computational Fluid Dynamics*, 6(1–3), 50–57. <https://doi.org/10.1504/PCFD.2006.009482>
- Benoit, R. (1977). On the Integral of the Surface Layer Profile-Gradient Functions. *Journal of Applied Meteorology*, 16, 859–860. [https://doi.org/10.1175/1520-0450\(1977\)016<0859:OTIOTS>2.0.CO;2](https://doi.org/10.1175/1520-0450(1977)016<0859:OTIOTS>2.0.CO;2)
- Bensow, R., Fureby, C., Liefvendahl, M., & Persson, T. (2006). A Comparative Study of RANS, DES and LES. *26th ONR Symposium on Naval Hydrodynamics, January 2017*, 17–22.
- Blackmore, P. A. (1985). A comparison of experimental methods for estimating dynamic response of buildings. *Journal of Wind Engineering and Industrial Aerodynamics*, 18(2), 197–212. [https://doi.org/10.1016/0167-6105\(85\)90098-4](https://doi.org/10.1016/0167-6105(85)90098-4)
- Blocken, B. (2015). Computational Fluid Dynamics for urban physics: Importance, scales, possibilities, limitations and ten tips and tricks towards accurate and reliable simulations. *Building and Environment*, 91, 219–245. <https://doi.org/10.1016/j.buildenv.2015.02.015>

- Blocken, B. (2018). LES over RANS in building simulation for outdoor and indoor applications: A foregone conclusion? In *Building Simulation* (Vol. 11, Issue 5). <https://doi.org/10.1007/s12273-018-0459-3>
- Blocken, B., Stathopoulos, T., & Carmeliet, J. (2007). CFD simulation of the atmospheric boundary layer: wall function problems. *Atmospheric Environment*, *41*(2), 238–252. <https://doi.org/10.1016/j.atmosenv.2006.08.019>
- Braun, A. L., & Awruch, A. M. (2009). Aerodynamic and aeroelastic analyses on the CAARC standard tall building model using numerical simulation. *Computers and Structures*, *87*(9–10), 564–581. <https://doi.org/10.1016/j.compstruc.2009.02.002>
- Britannica, T. Editors of Encyclopaedia (2020, February 12). Atmospheric circulation. Encyclopedia Britannica. <https://www.britannica.com/science/atmospheric-circulation>
- Businger, J. A., Wyngaard, J. C., Izumi, Y., & Bradley, E. F. (1971). Flux-Profile Relationships in the Atmospheric Surface Layer. *Journal of the Atmospheric Sciences*, *28*(2), 181–189. [https://doi.org/10.1175/1520-0469\(1971\)028<0181:FPRITA>2.0.CO;2](https://doi.org/10.1175/1520-0469(1971)028<0181:FPRITA>2.0.CO;2)
- Castro, H. G., Paz, R. R., & Sonzogni, V. E. (2011). Generation of Turbulent Inlet Velocity Conditions for Large Eddy Simulations. *Mecánica Computacional*, *XXX*(November 2015), 2275–2288. <https://doi.org/10.4155/CMT.11.53>
- Cermak, J. E. (2003). Wind-tunnel development and trends in applications to civil engineering. *Journal of Wind Engineering and Industrial Aerodynamics*, *91*(3), 355–370. [https://doi.org/10.1016/S0167-6105\(02\)00396-3](https://doi.org/10.1016/S0167-6105(02)00396-3)
- Cochran, L., & Derickson, R. (2005). Low-rise Buildings and Architectural Aerodynamics. *Architectural Science Review*, *48*, 265–276. <https://doi.org/10.3763/asre.2005.4833>

- Constantinescu, G., Koken, M., & Zeng, J. (2011). The structure of turbulent flow in an open channel bend of strong curvature with deformed bed: Insight provided by detached eddy simulation. *Water Resources Research*, 47(5), 1–17. <https://doi.org/10.1029/2010WR010114>
- Constantinescu, G., & Squires, K. (2004). Numerical investigations of flow over a sphere in the subcritical and supercritical regimes. *Physics of Fluids*, 16(5), 1449–1466. <https://doi.org/10.1063/1.1688325>
- Counihan, J. (1975). Adiabatic atmospheric boundary layers: A review and analysis of data from the period 1880-1972. *Atmospheric Environment (1967)*, 9(10), 871–905. [https://doi.org/10.1016/0004-6981\(75\)90088-8](https://doi.org/10.1016/0004-6981(75)90088-8)
- Dagnew, A. K., Bitsuamalk, G. T., & Merrick, R. (2009). Computational evaluation of wind pressures on tall buildings. *11th Americas Conference on Wind Engineering, January*.
- Dagnew, A. K., & Bitsuamlak, G. T. (2010). LES evaluation of wind pressures on a standard tall building with and without a neighboring building. *The Fifth International Symposium on Computational Wind Engineering (CWE2010) Chapel Hill, North Carolina, USA, 2007*.
- Dagnew, A. K., & Bitsuamlak, G. T. (2013). Computational evaluation of wind loads on buildings: A review. *Wind and Structures, An International Journal*, 16(6), 629–660. <https://doi.org/10.12989/was.2013.16.6.629>
- Dagnew, A. K., & Bitsuamlak, G. T. (2014). Computational evaluation of wind loads on a standard tall building using les. *Wind and Structures, An International Journal*, 18(5), 567–598. <https://doi.org/10.12989/was.2014.18.5.567>
- Daniels, S. J., Castro, I. P., & Xie, Z. T. (2013). Peak loading and surface pressure fluctuations of a tall model building. *Journal of Wind Engineering and Industrial Aerodynamics*, 120, 19–28. <https://doi.org/10.1016/j.jweia.2013.06.014>

- Davenport, A.G. (1971). The response of six building shapes to turbulent wind. *Philosophical Transactions of the Royal Society of London. Series A, Mathematical and Physical Sciences*, 269(1199), 385–394. <https://doi.org/10.1098/rsta.1971.0039>
- Davenport, A.G. (1995). How can we simplify and generalize wind loads? *Journal of Wind Engineering and Industrial Aerodynamics*, 54–55(C), 657–669. [https://doi.org/10.1016/0167-6105\(94\)00079-S](https://doi.org/10.1016/0167-6105(94)00079-S)
- Davenport, Alan G. (1960). *Rationale for Determining Design Wind Velocities*.
- Davidson, L. (2007). Using isotropic synthetic fluctuations as inlet boundary conditions for unsteady simulations. *Advances and Applications in Fluid Mechanics*, 1(1), 1–35.
- di Mare, L., Klein, M., Jones, W. P., & Janicka, J. (2006). Synthetic turbulence inflow conditions for large-eddy simulation. *Physics of Fluids*, 18(2). <https://doi.org/10.1063/1.2130744>
- Dragoiescu, C., Garber, J., & Kumar, K. S. (2006). A comparison of force balance and pressure integration techniques for predicting wind-induced responses of tall buildings. *Proceedings of the Structures Congress and Exposition, 2006*, 14. [https://doi.org/10.1061/40889\(201\)14](https://doi.org/10.1061/40889(201)14)
- Druault, P., Lardeau, S., Bonnet, J. P., Coiffet, F., Delville, J., Lamballais, E., Largeau, J. F., & Perret, L. (2004). Generation of Three-Dimensional Turbulent Inlet Conditions for Large-Eddy Simulation. *AIAA Journal*, 42(3), 447–456. <https://doi.org/10.2514/1.3946>
- Elshaer, A., Aboshosha, H., Bitsuamlak, G., El Damatty, A., & Dagnew, A. (2016). LES evaluation of wind-induced responses for an isolated and a surrounded tall building. *Engineering Structures*, 115, 179–195. <https://doi.org/10.1016/j.engstruct.2016.02.026>

- Elshaer, A., Gairola, A., Adamek, K., & Bitsuamlak, G. (2017). Variations in wind load on tall buildings due to urban development. *Sustainable Cities and Society*. <https://doi.org/10.1016/j.scs.2017.06.008>
- Emes, M. J., Arjomandi, M., Kelso, R. M., & Ghanadi, F. (2016). Integral length scales in a low-roughness atmospheric boundary layer. *Proceedings of the 18th Australasian Wind Engineering Society Worksho, July, 1–4*. <http://hdl.handle.net/2440/109454>
- Engineering Science Data Unit (ESDU) 74030. (2010). *Characteristics of atmospheric turbulence near the ground-Part I: Definitions and General Information*.
- Engineering Science Data Unit (ESDU) 82026. (2002). *Strong winds in the atmospheric boundary layer - Part I: hourly-mean wind speeds*.
- Engineering Science Data Unit (ESDU) 84011. (1993). *Wind speed profiles over terrain with roughness changes*.
- Engineering Science Data Unit (ESDU) 85020. (2001). *Characteristics of atmospheric turbulence near the ground - Part II: single point data for strong winds (neutral atmosphere)*.
- Farell, C., & Iyengar, a. (1997). Experimental determination of roughness length and integral length scale in atmospheric boundary layer simulations. *2nd European and African Conference on Wind Engineering, 89, 1–9*. [https://doi.org/10.1016/S0167-6105\(01\)00099-X](https://doi.org/10.1016/S0167-6105(01)00099-X)
- Foken, T. (2017). *Micrometeorology*. Springer. <https://link.springer.com/book/10.1007/978-3-642-25440-6>
- Franke, J., Hellsten, A., Schlünzen, H., & Carissimo, B. (2007). Best Practice Guideline for the Cfd Simulation of Flows in the Urban Environment. Cost 732: Quality Assurance and Improvement of Microscale Meteorological Models. In *BEST PRACTICE GUIDELINE FOR THE CFD SIMULATION OF FLOWS IN THE URBAN ENVIRONMENT, COST Action 732* (Issue May).

- Garratt, J. R. (1994). *The atmospheric boundary layer*. Cambridge University Press.
- Gatski, T. B., & Bonnet, J.-P. (2013). Compressible Turbulent Flow. In *Compressibility, Turbulence and High Speed Flow*. <https://doi.org/10.1016/b978-0-12-397027-5.00003-4>
- Goliger, A. M., & Milford, R. V. (1988). Sensitivity of the CAARC standard building model to geometric scale and turbulence. *Journal of Wind Engineering and Industrial Aerodynamics*, *31*(1), 105–123. [https://doi.org/10.1016/0167-6105\(88\)90190-0](https://doi.org/10.1016/0167-6105(88)90190-0)
- Hanson, T., Smith, F., Summers, D., & Wilson, C. B. (1982). Computer simulation of wind flow around buildings. *Computer-Aided Design*, *14*(1), 27–31. [https://doi.org/https://doi.org/10.1016/0010-4485\(82\)90008-2](https://doi.org/https://doi.org/10.1016/0010-4485(82)90008-2)
- Hanson, T., Summers, D. M., & Wilson, C. B. (1986). A three-dimensional simulation of wind flow around buildings. *International Journal for Numerical Methods in Fluids*, *6*(3), 113–127. <https://doi.org/10.1002/flid.1650060303>
- He, J., & Song, C. C. S. (1997). A numerical study of wind flow around the TTU building and the roof corner vortex. *Journal of Wind Engineering and Industrial Aerodynamics*, *67–68*, 547–558. [https://doi.org/10.1016/S0167-6105\(97\)00099-8](https://doi.org/10.1016/S0167-6105(97)00099-8)
- Hémon, P., & Santi, F. (2007). Simulation of a spatially correlated turbulent velocity field using biorthogonal decomposition. *Journal of Wind Engineering and Industrial Aerodynamics*, *95*(1), 21–29. <https://doi.org/10.1016/j.jweia.2006.04.003>
- Hirt, C. W., Ramshaw, J. D., & Stein, L. R. (1978). Numerical simulation of three-dimensional flow past bluff bodies. *Computer Methods in Applied Mechanics and Engineering*, *14*(1), 93–124. [https://doi.org/https://doi.org/10.1016/0045-7825\(78\)90014-2](https://doi.org/https://doi.org/10.1016/0045-7825(78)90014-2)
- Holmes, J. D. (John D. (2001). *Wind loading of structures*. London ; New York : Spon Press.

- Huang, M. F., Lau, I. W. H., Chan, C. M., Kwok, K. C. S., & Li, G. (2011). A hybrid RANS and kinematic simulation of wind load effects on full-scale tall buildings. *Journal of Wind Engineering and Industrial Aerodynamics*, 99(11), 1126–1138. <https://doi.org/10.1016/j.jweia.2011.09.003>
- Huang, S. H., Li, Q. S., & Wu, J. R. (2010). A general inflow turbulence generator for large eddy simulation. *Journal of Wind Engineering and Industrial Aerodynamics*. <https://doi.org/10.1016/j.jweia.2010.06.002>
- Huang, S., Li, Q. S., & Xu, S. (2007). Numerical evaluation of wind effects on a tall steel building by CFD. *Journal of Constructional Steel Research*, 63(5), 612–627. <https://doi.org/10.1016/j.jcsr.2006.06.033>
- Huang, S., Li, R., & Li, Q. S. (2013). Numerical simulation on fluid-structure interaction of wind around super-tall building at high reynolds number conditions. *Structural Engineering and Mechanics*, 46(2), 197–212. <https://doi.org/10.12989/sem.2013.46.2.197>
- Irwin, J. S. (1979). A theoretical variation of the wind profile power-law exponent as a function of surface roughness and stability. *Atmospheric Environment (1967)*, 13(1), 191–194. [https://doi.org/https://doi.org/10.1016/0004-6981\(79\)90260-9](https://doi.org/https://doi.org/10.1016/0004-6981(79)90260-9)
- Ishizaki, H., & Nishimura, H. (1992). Wind tunnel experiments on the vibrations of flexible models of a tall building. *Journal of Wind Engineering and Industrial Aerodynamics*, 42(1), 1065–1072. [https://doi.org/https://doi.org/10.1016/0167-6105\(92\)90113-O](https://doi.org/https://doi.org/10.1016/0167-6105(92)90113-O)
- Jamieson, N. J., Carpenter, P., & Cenek, P. D. (1992). Wind induced external pressures on a tall building with various corner configurations. *Journal of Wind Engineering and Industrial Aerodynamics*, 44(1–3), 2401–2412. [https://doi.org/10.1016/0167-6105\(92\)90032-6](https://doi.org/10.1016/0167-6105(92)90032-6)

- Jarrin, N., Benhamadouche, S., Laurence, D., & Prosser, R. (2006). A synthetic-eddy-method for generating inflow conditions for large-eddy simulations. *International Journal of Heat and Fluid Flow*, 27(4), 585–593. <https://doi.org/10.1016/j.ijheatfluidflow.2006.02.006>
- Jarrin, N., Prosser, R., Uribe, J. C., Benhamadouche, S., & Laurence, D. (2009). Reconstruction of turbulent fluctuations for hybrid RANS/LES simulations using a Synthetic-Eddy Method. *International Journal of Heat and Fluid Flow*, 30(3), 435–442. <https://doi.org/10.1016/j.ijheatfluidflow.2009.02.016>
- Jayanti, S. (2018). Computational Fluid Dynamics for Engineers and Scientists. In *Computational Fluid Dynamics for Engineers and Scientists*. <https://doi.org/10.1007/978-94-024-1217-8>
- Johansson, P. S., & Andersson, H. I. (2004). Generation of inflow data for inhomogeneous turbulence. *Theoretical and Computational Fluid Dynamics*, 18(5), 371–389. <https://doi.org/10.1007/s00162-004-0147-z>
- Justus, C. G., Hargraves, W. R., & Mikhail, A. (1976). *Reference wind speed distributions and height profiles for wind turbine design and performance evaluation applications. [USA]*. <https://doi.org/10.2172/7216073>
- Kaimal, J. C., & Finnigan, J. J. (1994). *Atmospheric boundary layer flows : their structure and measurement*. Oxford University Press.
- Kawai, H. (1998). Effect of corner modifications on aeroelastic instabilities of tall buildings. *Journal of Wind Engineering and Industrial Aerodynamics*, 74–76, 719–729. [https://doi.org/10.1016/S0167-6105\(98\)00065-8](https://doi.org/10.1016/S0167-6105(98)00065-8)
- Kempf, A. M., Wysocki, S., & Pettit, M. (2012). An efficient, parallel low-storage implementation of Klein’s turbulence generator for LES and DNS. *Computers and Fluids*, 60, 58–60. <https://doi.org/10.1016/j.compfluid.2012.02.027>
- Khanduri, A. C., Stathopoulos, T., & Bédard, C. (1998). Wind-induced interference effects on buildings - A review of the state-of-the-art. *Engineering Structures*, 20(7), 617–630. [https://doi.org/10.1016/S0141-0296\(97\)00066-7](https://doi.org/10.1016/S0141-0296(97)00066-7)

- Kim, Y. C., Bandi, E. K., Yoshida, A., & Tamura, Y. (2015). Response characteristics of super-tall buildings - Effects of number of sides and helical angle. *Journal of Wind Engineering and Industrial Aerodynamics*, *145*, 252–262. <https://doi.org/10.1016/j.jweia.2015.07.001>
- Kim, Y., Castro, I. P., & Xie, Z. T. (2013). Divergence-free turbulence inflow conditions for large-eddy simulations with incompressible flow solvers. *Computers and Fluids*, *84*, 56–68. <https://doi.org/10.1016/j.compfluid.2013.06.001>
- Klein, M., Sadiki, A., & Janicka, J. (2003). A digital filter based generation of inflow data for spatially developing direct numerical or large eddy simulations. *Journal of Computational Physics*, *186*(2), 652–665. [https://doi.org/10.1016/S0021-9991\(03\)00090-1](https://doi.org/10.1016/S0021-9991(03)00090-1)
- Koken, M., & Constantinescu, G. (2011). Flow and turbulence structure around a spur dike in a channel with a large scour hole. *Water Resources Research*, *47*(12), 1–19. <https://doi.org/10.1029/2011WR010710>
- Kraichnan, R. H. (1970). Diffusion by a random velocity field. *Physics of Fluids*, *13*(1), 22–31. <https://doi.org/10.1063/1.1692799>
- Kröger, H., & Kornev, N. (2018). Generation of divergence free synthetic inflow turbulence with arbitrary anisotropy. *Computers and Fluids*, *165*, 78–88. <https://doi.org/10.1016/j.compfluid.2018.01.018>
- Kwon, D. K., & Kareem, A. (2013). Comparative study of major international wind codes and standards for wind effects on tall buildings. *Engineering Structures*, *51*, 23–35. <https://doi.org/10.1016/j.engstruct.2013.01.008>
- Lateb, M., Meroney, R. N., Yataghene, M., Fellouah, H., Saleh, F., & Boufadel, M. C. (2016). On the use of numerical modelling for near-field pollutant dispersion in urban environments – A review. *Environmental Pollution*, *208*(September 2015), 271–283. <https://doi.org/10.1016/j.envpol.2015.07.039>

- Leon Lyles, Lowell A. Disrud, & R. K. Krauss. (1971). Turbulence Intensity as Influenced by Surface Roughness and Mean Velocity in a Wind-Tunnel Boundary Layer. *Transactions of the ASAE*, 14(2), 0285–0289. <https://doi.org/10.13031/2013.38277>
- Lim, H. C., Thomas, T. G., & Castro, I. P. (2009). Flow around a cube in a turbulent boundary layer: LES and experiment. *Journal of Wind Engineering and Industrial Aerodynamics*, 97(2), 96–109. <https://doi.org/10.1016/j.jweia.2009.01.001>
- Liu, J., & Niu, J. (2016). CFD simulation of the wind environment around an isolated high-rise building: An evaluation of SRANS, LES and DES models. *Building and Environment*, 96, 91–106. <https://doi.org/10.1016/j.buildenv.2015.11.007>
- Lu, C. L., Li, Q. S., Huang, S. H., Chen, F. B., & Fu, X. Y. (2012). Large eddy simulation of wind effects on a long-span complex roof structure. *Journal of Wind Engineering and Industrial Aerodynamics*, 100(1), 1–18. <https://doi.org/10.1016/j.jweia.2011.10.006>
- Lund, T. S., Wu, X., & Squires, K. D. (1998). Generation of Turbulent Inflow Data for Spatially-Developing Boundary Layer Simulations. *Journal of Computational Physics*, 140(2), 233–258. <https://doi.org/10.1006/jcph.1998.5882>
- Manwell, J. F., McGowan, J. G., & Rogers, A. L. (2011). *Wind energy explained: theory, design and application*. Wiley.
- Melaku, A., Bitsuamlak, G., Elshaer, A., & Aboshosha, H. (2017). Synthetic inflow turbulence generation methods for LES study of tall building aerodynamics. *2017 Americas Conference on Wind Engineering, ACWE 2017, May*.
- Melbourne, W. H. (1980). Comparison of measurements on the CAARC standard tall building model in simulated model wind flows. *Journal of Wind Engineering and Industrial Aerodynamics*, 6(1–2), 73–88. [https://doi.org/10.1016/0167-6105\(80\)90023-9](https://doi.org/10.1016/0167-6105(80)90023-9)

- Mendis, P., Ngo, T., Haritos, N., Hira, A., Samali, B., & Cheung, J. (2007). Wind loading on tall buildings. *Electronic Journal of Structural Engineering*, 7, 41–54.
- Meng, F. Q., He, B. J., Zhu, J., Zhao, D. X., Darko, A., & Zhao, Z. Q. (2018). Sensitivity analysis of wind pressure coefficients on CAARC standard tall buildings in CFD simulations. *Journal of Building Engineering*, 16(January), 146–158. <https://doi.org/10.1016/j.jobe.2018.01.004>
- Mochida, A., Murakami, S., Shoji, M., & Ishida, Y. (1993). Numerical Simulation of Flowfield around Texas Tech Building by Large Eddy Simulation. In S. B. T.-C. W. E. 1 Murakami (Ed.), *Computational Wind Engineering 1* (pp. 455–460). Elsevier. <https://doi.org/10.1016/B978-0-444-81688-7.50050-4>
- Mochida, Akashi, & Lun, I. Y. F. (2008). Prediction of wind environment and thermal comfort at pedestrian level in urban area. *Journal of Wind Engineering and Industrial Aerodynamics*, 96(10–11), 1498–1527. <https://doi.org/10.1016/j.jweia.2008.02.033>
- Mohotti, D., Wijesooriya, K., & Dias-da-Costa, D. (2019). Comparison of Reynolds Averaging Navier-Stokes (RANS) turbulent models in predicting wind pressure on tall buildings. *Journal of Building Engineering*, 21(August 2018), 1–17. <https://doi.org/10.1016/j.jobe.2018.09.021>
- Monin, A. S., & Obukhov, A. M. (1954). *Basic laws of turbulent mixing in the surface layer of the atmosphere*.
- Montazeri, H., Blocken, B., Janssen, W. D., & van Hooff, T. (2013). CFD evaluation of new second-skin facade concept for wind comfort on building balconies: Case study for the Park Tower in Antwerp. *Building and Environment*, 68, 179–192. <https://doi.org/10.1016/j.buildenv.2013.07.004>
- Murakami, S. (1990). Computational wind engineering. *Journal of Wind Engineering and Industrial Aerodynamics*, 36(PART 1), 517–538. [https://doi.org/10.1016/0167-6105\(90\)90335-A](https://doi.org/10.1016/0167-6105(90)90335-A)

- Murakami, S. (1993). Comparison of various turbulence models applied to a bluff body. *Journal of Wind Engineering and Industrial Aerodynamics*, 46–47(C), 21–36. [https://doi.org/10.1016/0167-6105\(93\)90112-2](https://doi.org/10.1016/0167-6105(93)90112-2)
- Murakami, S. (1998). Overview of turbulence models applied in CWE-1997. *Journal of Wind Engineering and Industrial Aerodynamics*. [https://doi.org/10.1016/S0167-6105\(98\)00004-X](https://doi.org/10.1016/S0167-6105(98)00004-X)
- Murakami, Shuzo, & Mochida, A. (1988). 3-D numerical simulation of airflow around a cubic model by means of the model. *Journal of Wind Engineering and Industrial Aerodynamics*, 31(2–3), 283–303. [https://doi.org/10.1016/0167-6105\(88\)90009-8](https://doi.org/10.1016/0167-6105(88)90009-8)
- Murakami, Shuzo, Mochida, A., & Sakamoto, S. (1997). CFD analysis of wind-structure interaction for oscillating square cylinders. *Journal of Wind Engineering and Industrial Aerodynamics*, 72(1–3), 33–46. [https://doi.org/10.1016/S0167-6105\(97\)00245-6](https://doi.org/10.1016/S0167-6105(97)00245-6)
- Nozawa, K., & Tamura, T. (2002). Large eddy simulation of the flow around a low-rise building immersed in a rough-wall turbulent boundary layer. *Journal of Wind Engineering and Industrial Aerodynamics*, 90(10), 1151–1162. [https://doi.org/10.1016/S0167-6105\(02\)00228-3](https://doi.org/10.1016/S0167-6105(02)00228-3)
- Nozu, T., Tamura, T., Okuda, Y., & Sanada, S. (2008). LES of the flow and building wall pressures in the center of Tokyo. *Journal of Wind Engineering and Industrial Aerodynamics*, 96(10–11), 1762–1773. <https://doi.org/10.1016/j.jweia.2008.02.028>
- Obasaju, E. D. (1992). Measurement of forces and base overturning moments on the CAARC tall building model in a simulated atmospheric boundary layer. *Journal of Wind Engineering and Industrial Aerodynamics*, 40(2), 103–126. [https://doi.org/10.1016/0167-6105\(92\)90361-D](https://doi.org/10.1016/0167-6105(92)90361-D)

- Pamiès, M., Weiss, P. É., Garnier, E., Deck, S., & Sagaut, P. (2009). Generation of synthetic turbulent inflow data for large eddy simulation of spatially evolving wall-bounded flows. *Physics of Fluids*, 21(4). <https://doi.org/10.1063/1.3103881>
- Panneer Selvam, R. (1996). Computation of flow around Texas Tech building using  $k$ - $\epsilon$  and Kato-Launder  $k$ - $\epsilon$  turbulence model. *Engineering Structures*, 18(11), 856–860. [https://doi.org/10.1016/0141-0296\(95\)00156-5](https://doi.org/10.1016/0141-0296(95)00156-5)
- Panofsky, H. A., Blackadar, A. K., & McVehil, G. E. (1960). The diabatic wind profile. *Quarterly Journal of the Royal Meteorological Society*, 86(369), 390–398. <https://doi.org/10.1002/qj.49708636911>
- Parv, B., Hulea, R., & Zoicas, R. (2012). Comparative study of wind effects on tall buildings using international codes and CFD. *ECCOMAS 2012 - European Congress on Computational Methods in Applied Sciences and Engineering, e-Book Full Papers, January*, 6857–6866.
- Patruno, L., & Ricci, M. (2017). On the generation of synthetic divergence-free homogeneous anisotropic turbulence. *Computer Methods in Applied Mechanics and Engineering*, 315, 396–417. <https://doi.org/10.1016/j.cma.2016.11.005>
- Patruno, L., & Ricci, M. (2018). A systematic approach to the generation of synthetic turbulence using spectral methods. *Computer Methods in Applied Mechanics and Engineering*, 340, 881–904. <https://doi.org/10.1016/j.cma.2018.06.028>
- Pavlidis, D., Gorman, G. J., Gomes, J. L. M. A., Pain, C. C., & ApSimon, H. (2010). Synthetic-eddy method for urban atmospheric flow modelling. *Boundary-Layer Meteorology*, 136(2), 285–299. <https://doi.org/10.1007/s10546-010-9508-x>
- Peterka, J. A., Meroney, R. N., & Kothari, K. M. (1985). Wind flow patterns about buildings. *Journal of Wind Engineering and Industrial Aerodynamics*, 21(1), 21–38. [https://doi.org/10.1016/0167-6105\(85\)90031-5](https://doi.org/10.1016/0167-6105(85)90031-5)
- Plate, E. J. (1971). *Aerodynamic characteristics of atmospheric boundary layers*. U.S. Atomic Energy Commission, Division of Technical Information.

- Poletto, R., Craft, T., & Revell, A. (2013). A new divergence free synthetic eddy method for the reproduction of inlet flow conditions for les. *Flow, Turbulence and Combustion*, *91*(3), 519–539. <https://doi.org/10.1007/s10494-013-9488-2>
- Poletto, R., Revell, A., Craft, T., & Jarrin, N. (2011). Divergence free synthetic eddy method for embedded les inflow boundary conditions. *7th International Symposium on Turbulence and Shear Flow Phenomena, TSFP 2011, 2011-July*(1).
- Pope, S. B. (2000). *Turbulent Flows*. Cambridge University Press. <https://doi.org/10.1017/CBO9780511840531>
- Ricci, M., Patruno, L., Kalkman, I., de Miranda, S., & Blocken, B. (2018). Towards LES as a design tool: Wind loads assessment on a high-rise building. *Journal of Wind Engineering and Industrial Aerodynamics*, *180*(June 2017), 1–18. <https://doi.org/10.1016/j.jweia.2018.07.009>
- Sakamoto, S., Murakami, S., & Mochida, A. (1993). Numerical study on flow past 2D square cylinder by Large Eddy Simulation: Comparison between 2D and 3D computations. *Journal of Wind Engineering and Industrial Aerodynamics*, *50*(C), 61–68. [https://doi.org/10.1016/0167-6105\(93\)90061-R](https://doi.org/10.1016/0167-6105(93)90061-R)
- Salim, S. M., & Ong, K. C. (2013). Performance of RANS, URANS and LES in the prediction of airflow and pollutant dispersion. *Lecture Notes in Electrical Engineering*, *170 LNEE*, 263–274. [https://doi.org/10.1007/978-94-007-4786-9\\_21](https://doi.org/10.1007/978-94-007-4786-9_21)
- Schlünzen, K. H., Grawe, D., Bohnenstengel, S. I., Schlüter, I., & Koppmann, R. (2011). Joint modelling of obstacle induced and mesoscale changes-Current limits and challenges. *Journal of Wind Engineering and Industrial Aerodynamics*, *99*(4), 217–225. <https://doi.org/10.1016/j.jweia.2011.01.009>
- Selvam, R. P. (1992). Computation of pressures on Texas Tech Building. *Journal of Wind Engineering and Industrial Aerodynamics*, *43*(1–3), 1619–1627. [https://doi.org/10.1016/0167-6105\(92\)90572-R](https://doi.org/10.1016/0167-6105(92)90572-R)

- Senthooran, S., Lee, D.-D., & Parameswaran, S. (2004). A computational model to calculate the flow-induced pressure fluctuations on buildings. *Journal of Wind Engineering and Industrial Aerodynamics*, 92(13), 1131–1145. <https://doi.org/10.1016/j.jweia.2004.07.002>
- Sharma, A., Mittal, H., & Gairola, A. (2019). Detached-eddy simulation of interference between buildings in tandem arrangement. *Journal of Building Engineering*, 21(July 2018), 129–140. <https://doi.org/10.1016/j.jobee.2018.10.004>
- Simiu, E., & Yeo, D. (2019). *Wind Effects on Structures: Modern Structural Design for Wind*. <https://doi.org/10.1002/9781119375890>
- Smirnov, A., Shi, S., & Celik, I. (2001). Random Flow Generation Technique for Large Eddy Simulations and Particle-Dynamics Modeling. *Journal of Fluids Engineering*, 123(2), 359. <https://doi.org/10.1115/1.1369598>
- Solsvik, J., & Jakobsen, H. A. (2016). A review of the statistical turbulence theory required extending the population balance closure models to the entire spectrum of turbulence. *AIChE Journal*, 62(5), 1795–1820. <https://doi.org/https://doi.org/10.1002/aic.15128>
- Spalart, P. R., Allmaras, S. R., & Reno, J. (1992). One-Equation Turbulence Model for Aerodynamic Flows Boeing. *Aiaa*, 23.
- Spalart, P. R., Jou, W. H., Strelets, M. K., & Allmaras, S. R. (1997). Comments on the feasibility of LES for wings and on a hybrid RANS/LES approach. *Advances in DNS/LES*, 1(JANUARY), 4–8.
- Spera, D. A. (2009). *Wind Turbine Technology: Fundamental Concepts in Wind Turbine Engineering, Second Edition*. ASME.
- Spera, D., & Richards, T. (1979). *Modified power law equations for vertical wind profiles*.

- Stathopoulos, T. (1985). Wind environmental conditions around tall buildings with chamfered corners. *Journal of Wind Engineering and Industrial Aerodynamics*, 21(1), 71–87. [https://doi.org/10.1016/0167-6105\(85\)90034-0](https://doi.org/10.1016/0167-6105(85)90034-0)
- Stathopoulos, Ted. (2006). Pedestrian level winds and outdoor human comfort. *Journal of Wind Engineering and Industrial Aerodynamics*, 94(11), 769–780. <https://doi.org/10.1016/j.jweia.2006.06.011>
- Stull, R. (2017). *Practical Meteorology: An Algebra-based Survey of Atmospheric Science* (version 1.). AVP International, University of British Columbia.
- Stull, R. B. (1988). *An introduction to boundary layer meteorology*. Kluwer Academic.
- Sutton, O. G. (1977). *Micrometeorology : a study of physical processes in the lowest layers of the earth's atmosphere*. Krieger.
- Tamura, T., Miyagi, T., & Kitagishi, T. (1998). Numerical prediction of unsteady pressures on a square cylinder with various corner shapes. *Journal of Wind Engineering and Industrial Aerodynamics*, 74–76, 531–542. [https://doi.org/10.1016/S0167-6105\(98\)00048-8](https://doi.org/10.1016/S0167-6105(98)00048-8)
- Tanaka, H., & Lawen, N. (1986). Test on the CAARC standard tall building model with a length scale of 1 : 1000. *Journal of Wind Engineering and Industrial Aerodynamics*, 25(1), 15–29. [https://doi.org/10.1016/0167-6105\(86\)90102-9](https://doi.org/10.1016/0167-6105(86)90102-9)
- Tanaka, Hideyuki, Tamura, Y., Ohtake, K., Nakai, M., & Chul Kim, Y. (2012). Experimental investigation of aerodynamic forces and wind pressures acting on tall buildings with various unconventional configurations. *Journal of Wind Engineering and Industrial Aerodynamics*, 107–108, 179–191. <https://doi.org/10.1016/j.jweia.2012.04.014>
- Tang, U. F., & Kwok, K. C. S. (2004). Interference excitation mechanisms on a 3DOF aeroelastic CAARC building model. *Journal of Wind Engineering and Industrial Aerodynamics*, 92(14–15), 1299–1314. <https://doi.org/10.1016/j.jweia.2004.08.004>

- Taylor, G. I. (1938). The Spectrum of Turbulence. *Proceedings of the Royal Society A: Mathematical, Physical and Engineering Sciences*, 164(919), 476–490. <https://doi.org/10.1098/rspa.1938.0032>
- Tennekes, H., & Lumley, J. L. (1972). *A first course in turbulence*. The MIT Press.
- Thepmongkorn, S., Wood, G. S., & Kwok, K. C. S. (2002). Interference effects on wind-induced coupled motion of a tall building. *Journal of Wind Engineering and Industrial Aerodynamics*, 90(12), 1807–1815. [https://doi.org/https://doi.org/10.1016/S0167-6105\(02\)00289-1](https://doi.org/https://doi.org/10.1016/S0167-6105(02)00289-1)
- Thordal, M. S., Bennetsen, J. C., Capra, S., & Koss, H. H. H. (2020). Towards a standard CFD setup for wind load assessment of high-rise buildings: Part 1 – Benchmark of the CAARC building. *Journal of Wind Engineering and Industrial Aerodynamics*, 205(May), 104283. <https://doi.org/10.1016/j.jweia.2020.104283>
- Thordal, M. S., Bennetsen, J. C., Capra, S., Kragh, A. K., & Koss, H. H. H. (2020). Towards a standard CFD setup for wind load assessment of high-rise buildings: Part 2 – Blind test of chamfered and rounded corner high-rise buildings. *Journal of Wind Engineering and Industrial Aerodynamics*, 205(March), 104282. <https://doi.org/10.1016/j.jweia.2020.104282>
- Thordal, M. S., Bennetsen, J. C., & Koss, H. H. H. (2019). Review for practical application of CFD for the determination of wind load on high-rise buildings. *Journal of Wind Engineering and Industrial Aerodynamics*, 186, 155–168. <https://doi.org/10.1016/j.jweia.2018.12.019>
- Tominaga, Y. (2015). Flow around a high-rise building using steady and unsteady RANS CFD: Effect of large-scale fluctuations on the velocity statistics. *Journal of Wind Engineering and Industrial Aerodynamics*, 142, 93–103. <https://doi.org/10.1016/j.jweia.2015.03.013>

- Tominaga, Y., Mochida, A., Murakami, S., & Sawaki, S. (2008). Comparison of various revised k- $\epsilon$  models and LES applied to flow around a high-rise building model with 1:1:2 shape placed within the surface boundary layer. *Journal of Wind Engineering and Industrial Aerodynamics*, 96(4), 389–411. <https://doi.org/10.1016/j.jweia.2008.01.004>
- Tominaga, Y., Mochida, A., Yoshie, R., Kataoka, H., Nozu, T., Yoshikawa, M., & Shirasawa, T. (2008). AIJ guidelines for practical applications of CFD to pedestrian wind environment around buildings. *Journal of Wind Engineering and Industrial Aerodynamics*, 96(10), 1749–1761. <https://doi.org/https://doi.org/10.1016/j.jweia.2008.02.058>
- Tsuchiya, M., Murakami, S., Mochida, A., Kondo, K., & Ishida, Y. (1997). Development of a new k- $\epsilon$  model for flow and pressure fields around bluff body. *Journal of Wind Engineering and Industrial Aerodynamics*, 67–68, 169–182. [https://doi.org/10.1016/S0167-6105\(97\)00071-8](https://doi.org/10.1016/S0167-6105(97)00071-8)
- Tutar, M., & Oguz, G. (2002). Large eddy simulation of wind flow around parallel buildings with varying configurations. *Fluid Dynamics Research*, 31(5–6), 289–315. [https://doi.org/10.1016/S0169-5983\(02\)00127-2](https://doi.org/10.1016/S0169-5983(02)00127-2)
- Veloudis, I., Yang, Z., McGuirk, J. J., Page, G. J., & Spencer, A. (2007). Novel implementation and assessment of a digital filter based approach for the generation of les inlet conditions. *Flow, Turbulence and Combustion*, 79(1), 1–24. <https://doi.org/10.1007/s10494-006-9058-y>
- Verma, S. K. (2016). *Effect of wind incidence angle on wind pressure distribution on square plan tall buildings*. 6(04), 45–52. [http://www.jairjp.com/MAY2013/04 VERMA.pdf](http://www.jairjp.com/MAY2013/04%20VERMA.pdf)
- Versteeg, H. K., & Malalasekera, W. (2007). *An Introduction to Computational Fluid Dynamics The Finite Volume Method* (2nd ed.). Pearson Education. <https://books.google.com.tr/books?id=Gc4AWPJqb4AC>

- Weerasuriya, A. U. (2013). Computational Fluid Dynamic (CFD) simulation of flow around tall buildings. *Engineer: Journal of the Institution of Engineers, Sri Lanka*, 46(3), 43. <https://doi.org/10.4038/engineer.v46i3.6784>
- Wieringa, J. (1992). Updating the Davenport roughness classification. *Journal of Wind Engineering and Industrial Aerodynamics*, 41(1), 357–368. [https://doi.org/https://doi.org/10.1016/0167-6105\(92\)90434-C](https://doi.org/https://doi.org/10.1016/0167-6105(92)90434-C)
- Wijesooriya, K., Mohotti, D., Chauhan, K., & Dias-da-Costa, D. (2019). Numerical investigation of scale resolved turbulence models (LES, ELES and DDES) in the assessment of wind effects on supertall structures. *Journal of Building Engineering*, 25(February), 100842. <https://doi.org/10.1016/j.jobe.2019.100842>
- Xiao, F., Dianat, M., & McGuirk, J. J. (2017). An LES Turbulent Inflow Generator using A Recycling and Rescaling Method. In *Flow, Turbulence and Combustion* (Vol. 98, Issue 3). Flow, Turbulence and Combustion. <https://doi.org/10.1007/s10494-016-9778-6>
- Xie, J. (2014). Aerodynamic optimization of super-tall buildings and its effectiveness assessment. *Journal of Wind Engineering and Industrial Aerodynamics*, 130, 88–98. <https://doi.org/10.1016/j.jweia.2014.04.004>
- Xie, Z., & Castro, I. P. (2006). LES and RANS for turbulent flow over arrays of wall-mounted obstacles. *Flow, Turbulence and Combustion*, 76(3), 291–312. <https://doi.org/10.1007/s10494-006-9018-6>
- Xie, Z. T., & Castro, I. P. (2008). Efficient generation of inflow conditions for large eddy simulation of street-scale flows. *Flow, Turbulence and Combustion*, 81(3), 449–470. <https://doi.org/10.1007/s10494-008-9151-5>
- Xie, Z. T., & Castro, I. P. (2009). Large-eddy simulation for flow and dispersion in urban streets. *Atmospheric Environment*, 43(13), 2174–2185. <https://doi.org/10.1016/j.atmosenv.2009.01.016>

- Yan, B., & Li, Q. (2016). Large-eddy simulation of wind effects on a super-tall building in urban environment conditions. *Structure and Infrastructure Engineering*, 12(6), 765–785. <https://doi.org/10.1080/15732479.2015.1051997>
- Yan, B. W., & Li, Q. S. (2015). Inflow turbulence generation methods with large eddy simulation for wind effects on tall buildings. *Computers and Fluids*, 116, 158–175. <https://doi.org/10.1016/j.compfluid.2015.04.020>
- Yan, B. W., & Li, Q. S. (2017). Detached-eddy and large-eddy simulations of wind effects on a high-rise structure. *Computers and Fluids*, 150, 74–83. <https://doi.org/10.1016/j.compfluid.2017.02.009>
- Yang, Q., Zhou, T., Yan, B., Van Phuc, P., & Hu, W. (2020). LES study of turbulent flow fields over hilly terrains — Comparisons of inflow turbulence generation methods and SGS models. *Journal of Wind Engineering and Industrial Aerodynamics*, 204(July). <https://doi.org/10.1016/j.jweia.2020.104230>
- Yoshie, R., Mochida, A., Tominaga, Y., Kataoka, H., Harimoto, K., Nozu, T., & Shirasawa, T. (2007). Cooperative project for CFD prediction of pedestrian wind environment in the Architectural Institute of Japan. *Journal of Wind Engineering and Industrial Aerodynamics*, 95(9–11), 1551–1578. <https://doi.org/10.1016/j.jweia.2007.02.023>
- Yu, Y., Yang, Y., & Xie, Z. (2018). A new inflow turbulence generator for large eddy simulation evaluation of wind effects on a standard high-rise building. *Building and Environment*, 138(November 2017), 300–313. <https://doi.org/10.1016/j.buildenv.2018.03.059>
- Zhang, Y., Habashi, W. G., & Khurram, R. A. (2015). Predicting wind-induced vibrations of high-rise buildings using unsteady CFD and modal analysis. *Journal of Wind Engineering and Industrial Aerodynamics*, 136, 165–179. <https://doi.org/10.1016/j.jweia.2014.11.008>
- Zhang, Z., Quan, Y., Gu, M., & Xiong, Y. (2013). Effects of corner chamfering and rounding modification on aerodynamic coefficients of square tall buildings. *Tumu Gongcheng Xuebao/China Civil Engineering Journal*, 46(9), 12–20.